Machine Learning Methods for Tau Lepton Identification and Search for the Supersymmetric Partner of the Tau Lepton Using CMS Run 2 Data

Dissertation

zur Erlangung des Doktorgrades an der Fakultät
für Mathematik, Informatik und Naturwissenschaften
Fachbereich Physik
der Universität Hamburg

vorgelegt von

Mykyta Shchedrolosiev

geboren in Cherson, Ukraine

Hamburg
2025

Gutachter/innen der Dissertation: Dr. Isabell Melzer-Pellmann
                                                               Prof. Dr. Elisabetta Gallo-Voss

Zusammensetzung der Prüfungskommission: Prof. Dr. Gregor Kasieczka
                                                               Prof. Dr. Jan Louis
                                                               Prof. Dr. Elisabetta Gallo-Voss
                                                               Dr. Alexei Raspereza
                                                               Dr. Isabell Melzer-Pellmann

Vorsitzende/r der Prüfungskommission: Prof. Dr. Gregor Kasieczka

Datum der Disputation: 23.05.2025

Vorsitzender des Fach-Promotionsausschusses PHYSIK: Prof. Dr. Wolfgang J. Parak

Leiter des Fachbereichs PHYSIK: Prof. Dr. Markus Drescher

Dekan der Fakultät MIN: Prof. Dr.-Ing. Norbert Ritter

Declaration on oath

I hereby declare and affirm that this doctoral dissertation is my own work and that I have not used any aids and sources other than those indicated.

If electronic resources based on generative artificial intelligence [1, 2, 3] (gAI) were used in the course of writing this dissertation, I confirm that my own work was the main and value-adding contribution and that complete documentation of all resources used is available in accordance with good scientific practice. I am responsible for any erroneous or distorted content, incorrect references, violations of data protection and copyright law or plagiarism that may have been generated by the gAI.

Hamburg, April 16, 2025.   Mykyta Shchedrolosiev

Abstract

Gauge-mediated supersymmetry breaking models provide a compelling framework for the search for a supersymmetric partner of the tau lepton ($\widetilde{\tau}$) with a macroscopic lifetime. In such scenarios, $\widetilde{\tau}$ can decay to tau lepton displaced from the primary proton-proton interaction vertex. Standard tau reconstruction and identification techniques at the Compact Muon Solenoid (CMS) experiment are not designed for these displaced signatures, motivating the development of specialised approaches.

This thesis begins by improving the existing CMS tau identification algorithms for prompt taus using modern machine learning techniques. Building on this foundation, a graph-based neural network is introduced to reliably identify displaced tau leptons, where large displacements pose unique detection challenges. Leveraging this dedicated displaced-tau identification, the first search for the direct production of moderately long-lived $\widetilde{\tau}$ particles (decaying within the tracker volume) with hadronic taus in the final state is performed using proton-proton collision data at $\sqrt{s} = 13\,\text{TeV}$. The analysis is based on a dataset corresponding to an integrated luminosity of $138\,\text{fb}^{-1}$, collected by the CMS experiment from 2016 to 2018. This work significantly enhances sensitivity to $\widetilde{\tau}$ decay lengths of the order of centimetres or more, expanding the experimental coverage of gauge-mediated supersymmetry breaking scenarios.

Zusammenfassung

Modelle mit eichvermittelter Supersymmetriebrechung bieten einen überzeugenden Rahmen für die Suche nach einem supersymmetrischen Partner des Tau-Leptons ($\widetilde{\tau}$) mit makroskopischer Lebensdauer. In solchen Szenarien kann $\widetilde{\tau}$ in Tau-Leptonen zerfallen, deren Zerfallsvertex gegenüber dem primären Proton-Proton-Wechselwirkungsvertex deutlich räumlich versetzt sind. Die Standardmethoden zur Rekonstruktion und Identifizierung von Tau-Leptonen am Compact Muon Solenoid (CMS)-Experiment sind für solche Signaturen nicht ausgelegt, was die Entwicklung spezialisierter Verfahren erforderlich macht.

Diese Doktorarbeit beginnt mit der Verbesserung bestehender CMS-Tau-Identifikationsalgorithmen für prompte Tau-Leptonen mithilfe moderner Methoden des maschinellen Lernens. Aufbauend auf diesem Fundament wird ein graphbasiertes neuronales Netzwerk vorgestellt, das Tau-Leptonen auch bei großen Zerfallsverschiebungen zuverlässig identifiziert, die in einem Sekundärvertex entstehen, der einen makroskopischen Abstand zum Primärvertex hat.. Mithilfe dieser spezialisierten Identifikation wird erstmals eine Suche nach der direkten Produktion mäßig langlebiger $\widetilde{\tau}$-Teilchen (die innerhalb des Tracker-Volumens zerfallen) mit hadronischen Tau-Endzuständen unter Verwendung von Proton-Proton-Kollisionsdaten bei $\sqrt{s} = 13\,\text{TeV}$ durchgeführt. Die Analyse basiert auf einem Datensatz mit einer integrierten Luminosität von $138\,\text{fb}^{-1}$, der vom CMS-Experiment in den Jahren 2016 bis 2018 aufgezeichnet wurde. Diese Arbeit verbessert die Empfindlichkeit auf $\widetilde{\tau}$-Zerfallslängen im Zentimeterbereich oder darüber hinaus erheblich und erweitert die experimentelle Abdeckung von Szenarien mit eichvermittelter Supersymmetriebrechung.

Contents

Introduction

Since the dawn of civilisation, humanity has been driven by a deep desire to understand the nature of matter. Every generation has tried to unravel the layers of the physical world and understand nature's matter and fundamentals at a deeper level.

Today, the Standard Model (SM) of particle physics is one of the most significant achievements of this long historical pursuit. It successfully describes the known elementary particles and three of the four forces that govern them. One of the most outstanding achievements of the SM is its successful prediction of the Higgs boson [4, 5], a milestone discovery confirmed in 2012 that fundamentally validated our understanding of electroweak symmetry breaking. Despite its remarkable successes, the SM remains incomplete, as it does not incorporate gravity, offers no explanation for dark matter or dark energy, and cannot explain the observed matter-antimatter asymmetry and the measured Higgs boson mass. To address these and other unanswered questions, researchers have proposed theories that extend the SM and push our current understanding into new territory.

One possible theoretical framework that addresses this is Supersymmetry (SUSY). It introduces a new symmetry that pairs each known particle with a companion called a superpartner, potentially explaining various mysteries of the SM. For instance, supersymmetric models can help stabilise the mass of the Higgs boson, unify forces at very high energies, and provide a suitable candidate for dark matter. In particular SUSY scenarios, the superpartner of the third-generation lepton ($\widetilde{\tau}$) can be lighter than the superpartner of the other leptons [6]. The search for such a scenario, particularly with tau leptons in the final state, which are expected to have stronger coupling to their superpartners than first- and second-generation leptons [7], is particularly compelling for new-physics searches. However, unlike electrons or muons, studying tau leptons in the final state is associated with the necessity of specialised reconstruction and identification methods to capture their decays to hadrons. Moreover, scenarios such as gauge mediated supersymmetry breaking (GMSB) predict long-lived $\widetilde{\tau}$ states whose decay into taus can occur centimetres away from the primary interaction point (displaced decays), an exotic signature requiring specialised reconstruction techniques.

A key objective of this thesis is to develop and refine standard and displaced tau identification techniques, which are crucial for the central analysis presented here: the search for the pair production of long-lived $\widetilde{\tau}$ with hadronically decaying tau leptons in the final state. The data collected at $\sqrt{s} = 13\,\text{TeV}$ from 2016 to 2018, corresponding to an integrated luminosity of 138fb^{-1}, are utilized in this analysis. Leveraging the newly developed displaced tau identification method, stringent upper limits are set on the production cross section of pair-produced long-lived $\widetilde{\tau}$, significantly advancing previous results.

Chapter 1 outlines the foundational aspects of the SM and highlights the possibilities of its extension that motivate the data analysis performed in this thesis. Chapter 2 introduces the Large Hadron Collider (LHC) and the Compact Muon Solenoid (CMS) experiment, providing an overview of their main components. Chapter 3 explains how CMS reconstructs key physics objects used in the data analysis.

Chapter 4 contains the advanced techniques for reconstructing and identifying τ leptons at CMS. The task of the τ lepton reconstruction is challenging because of the necessity to distinguish genuine τ leptons from fakes in a crowded particle environment. Furthermore, the chapter outlines the contribution to the state-of-the-art machine learning-based identification of hadronically decaying τ leptons (τ_{h}) in the CMS experiment, exemplified by the DeepTau algorithm [8]. It details the sophisticated data preprocessing techniques and domain adaptation methods, which have substantially enhanced the classification efficiency and minimised the discrepancies in predicted score distributions between data and simulation.

Chapter 5 describes the development of the displaced τ signature reconstruction, which previously was not explored within CMS. Adopting ParticleNet [9] for identifying displaced τ_{h} helps to develop the algorithm that successfully captures the internal characteristics of the signal and can separate displaced τ_{h} from the other SM jets.

The main focus of this thesis is the search for long-lived $\widetilde{\tau}$ pair production in the final state with two hadronically decaying tau leptons, described in Chapter 6. The analysis relies on the new displaced tau reconstruction algorithm. It targets events with large missing transverse momentum ($p_{\mathrm{T}}^{\mathrm{miss}}$), which stems from both the neutrinos in the tau decays and the lightest SUSY particles, which are neutral, weakly interacting, and cannot be detected. A $p_{\mathrm{T}}^{\mathrm{miss}}$ trigger is employed to record these events, and an entirely data-driven background prediction method is used to model the relevant SM processes accurately. This strategy significantly enhances previous results [10] by extending the exclusion range for $\widetilde{\tau}$ pair production scenarios with macroscopic $\widetilde{\tau}$ proper decay length ($c\tau_0$) of order $\mathcal{O}(\mathrm{cm-m})$. In the maximally mixed scenario, when the supersymmetric partners of the left- and right-handed τ leptons ($\widetilde{\tau}_{\mathrm{L}}$ and $\widetilde{\tau}_{\mathrm{R}}$) are equally mixed, this analysis excludes $\widetilde{\tau}$ masses from about $100\,\mathrm{GeV}$ to $300\,\mathrm{GeV}$, covering $c\tau_0$ values from $10\,\mathrm{mm}$ to a few hundred millimetres. In the mass-degenerate scenario, when the two $\widetilde{\tau}$ mass eigenstates have nearly the same mass, the exclusion extends up to nearly $450\,\mathrm{GeV}$, covering the proper decay length of a few mm to about $30\,\mathrm{cm}$. These results illustrate how a dedicated displaced τ_{h} reconstruction approach can significantly boost sensitivity to long-lived particles, expanding the exclusion region and strengthening constraints on $\widetilde{\tau}$ production in GMSB.

Chapter 1

Fundamentals of particle physics

The research presented in this thesis is based on the theoretical frameworks of particle physics. Their fundamental principles are outlined in this chapter to set the stage for this thesis work.

1.1 The Standard Model

The SM of particle physics is one of modern science's most successful theoretical frameworks. It is based on quantum field theory (QFT), established in the 20th century [11] to describe physics at high energies. It accounts for relativistic effects as well as processes involving particle decay, creation, and annihilation. In QFT, fundamental particles are excitations of their corresponding fields. Interactions between them are mediated by gauge fields, which, in a perturbative description, can be understood as the exchange of virtual particles associated with specific interactions. Developed over several decades, the SM unifies the electromagnetic, weak, and strong interactions within a single theoretical structure, leaving gravity as the only fundamental force not included. The list of SM particles is shown in Fig. 1.1 with their electric charge, spin and mass.

The Standard Model (SM) is built upon several key principles that govern elementary particles' fundamental interactions and explain the nature of matter.

The SM is invariant under *Lorentz transformations*, ensuring that the laws of physics remain unchanged in all inertial reference frames. This requirement constrains the form of the Lagrangian and ensures consistency with special relativity.

At its core, the SM is based on *local gauge symmetry* given by the group structure:

$$SU(3)_C \otimes SU(2)_L \otimes U(1)_Y \,.$$

The three gauge groups correspond to different fundamental interactions: $SU(3)_C$ represents the strong interaction, $SU(2)_L$ is associated with the weak isospin, and $U(1)_Y$ determines the weak hypercharge, which contributes to the electroweak interaction.

A crucial feature of the SM is the *spontaneous symmetry breaking* via the Brout–Englert–Higgs [13, 14, 15] mechanism. This process generates masses for the weak bosons ($W^\pm$ and Z) while keeping the photon (γ) massless, resulting in the separation of the electromagnetic and weak interactions. The original gauge symmetry

Standard Model of Elementary Particles
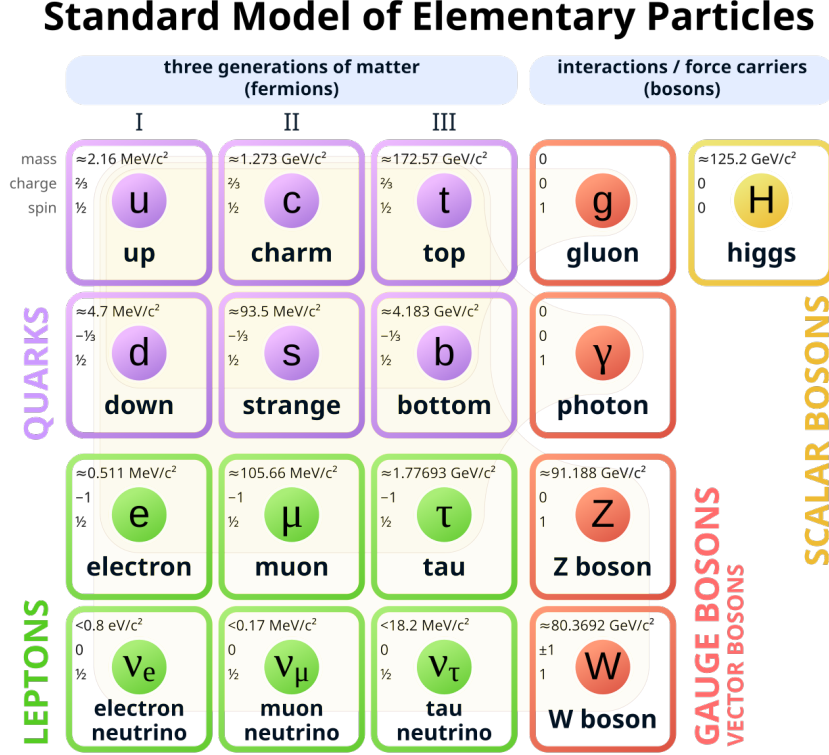
Figure 1.1: The particles in the Standard Model of particle physics [12].

$SU(3)_C \otimes SU(2)_L \otimes U(1)_Y$ is spontaneously broken down to

$$SU(3)_C \otimes U(1)_{EM}.$$

The SM maintains *gauge invariance*, which helps ensure its renormalizability by allowing divergences in physical predictions to be systematically controlled within perturbative quantum field theory. It also incorporates *parity violation* in weak interactions, meaning that weak interactions distinguish between left- and right-handed particles. This is experimentally confirmed by the observation that, in the SM, only left-handed chiral neutrinos and right-handed chiral antineutrinos participate in weak interactions.

The SM assumes that neutrinos are *massless* in its original formulation. However, experimental evidence of neutrino oscillations suggests that neutrinos have mass, implying the need for physics beyond the Standard Model.

The SM includes three generations of leptons: the electron (e), muon (μ), and tau (τ), along with their corresponding neutrinos (ν_e, ν_μ, ν_τ). Similarly, there are six types of quarks, grouped into three generations: the up-type quarks (up u, charm c, and top t) and the down-type quarks (down d, strange s, and bottom b).

1.1.1 Basic constituents of the Standard Model

In the context of QFT, the key structure used to describe a system's dynamics is the Lagrangian density $\mathcal{L}$ (further referred to as Lagrangian), which depends on the fundamental

fields and allows for the description of their interactions and fundamental symmetries. The action is then defined as the spacetime integral of the Lagrangian density $\mathcal{L}$:

$$S = \int d^4x\, \mathcal{L} \,. \tag{1.1}$$

After this, the equations of motion of a system can be derived from the *principle of least action* ($\delta S = 0$.).

The main components of the SM Lagrangian are the gauge fields, which mediate fundamental interactions; the fermion fields, representing matter particles; the Higgs field, responsible for mass generation; and the interaction terms that govern the dynamics between these fields. Below, the form of the corresponding fields is detailed:

- The SM includes three generations of fermions (quarks and leptons) that are spin-$\frac{1}{2}$ particles. Quarks carry colour charge and have fractional electric charge. They are arranged in the SM as left-handed doublets and right-handed singlets under $SU(2)_L$. Left-handed quark doublets (weak isospin doublets) participate in the weak interaction and are written as follows:

$$Q_1 = \begin{pmatrix} u \\ d \end{pmatrix}_L \,, \quad Q_2 = \begin{pmatrix} c \\ s \end{pmatrix}_L \,, \quad Q_3 = \begin{pmatrix} t \\ b \end{pmatrix}_L \,.$$

These doublets contain the up-type quarks (u, c, t) with charge $+\frac{2}{3}e$ and the down-type quarks (d, s, b) with charge $-\frac{1}{3}e$. The third component of the weak isospin for quarks in the upper and lower component of the isospin doublet is $I_3 = \frac{1}{2}$ and $I_3 = -\frac{1}{2}$ correspondingly.

Right-handed quark singlets do not participate in the weak interaction but still carry colour and electric charges. These fields are organised as right-handed components of up- or down-type quarks:

$$U_1 = u_R \,, \quad U_2 = c_R \,, \quad U_3 = t_R \,.$$

$$D_1 = d_R \,, \quad D_2 = s_R \,, \quad D_3 = b_R \,.$$

The right-handed quark singlets do not form a weak doublet. Their third component of weak isospin is $I_3 = 0$.

Each quark field carries a colour index, which can be represented as a vector:

$$q = \begin{pmatrix} q_r \\ q_g \\ q_b \end{pmatrix} \,,$$

where the indices r, g, b correspond to the three colour charges: red, green, and blue.

Leptons as fermions do not carry colour charge but can carry electric charge and are represented as left-handed lepton doublets that participate in the weak interaction:

$$L_1 = \begin{pmatrix} \nu_e \\ e \end{pmatrix}_L \,, \quad L_2 = \begin{pmatrix} \nu_\mu \\ \mu \end{pmatrix}_L \,, \quad L_3 = \begin{pmatrix} \nu_\tau \\ \tau \end{pmatrix}_L \,,$$

where neutrinos (ν_e, ν_μ, ν_τ) have zero electric charge and leptons (e, μ, τ) have charge $-1e$. At the same time, right-handed lepton singlets that do not participate in the weak interaction can be notated as:

$$E_1 = e_R, \quad E_2 = \mu_R, \quad E_3 = \tau_R.$$

Analogously to $Q_{1,2,3}$ doublets, I_3 in the upper and lower component of the isospin doublet is $I_3 = \frac{1}{2}$ and $I_3 = -\frac{1}{2}$ correspondingly.

- The Higgs field is the spin-0 scalar field that introduces the mechanism of spontaneous symmetry breaking. It is represented as a doublet:

$$H = \begin{pmatrix} \phi^+ \\ \phi^0 \end{pmatrix}, \tag{1.2}$$

with a vacuum expectation value:

$$\langle H \rangle = \frac{1}{\sqrt{2}} \begin{pmatrix} 0 \\ v \end{pmatrix}. \tag{1.3}$$

The Higgs mechanism generates the masses for the weak bosons and fermions using a spontaneous symmetry-breaking mechanism as shown in Section 1.1.3.

- The SM contains three sets of gauge spin-1 fields that correspond to the fundamental interactions:

    1. Gluons (G_μ^a) are the carriers of the strong interaction. They are spin-1 gauge bosons transforming in the octet representation of the colour group $SU(3)_C$, meaning they carry colour charges as colour-anticolour pairs. Unlike quarks, gluons have zero electric charge and do not participate in weak interactions.

    2. Weak bosons ($W_\mu^\pm$) mediate the charged current weak interaction. They are spin-1 bosons and interact with particles that carry weak isospin. The Z-boson (Z_μ) is the neutral weak boson that mediates the neutral current weak interaction. It is a massive spin-1 boson with zero electric charge but interacts with fermions.

    3. Photons (A_μ) are the massless spin-1 bosons responsible for electromagnetic interactions. They interact with all charged particles but do not interact via the strong or weak forces.

1.1.2 Electroweak sector

The electroweak sector of the SM describes the unification of electromagnetism and the weak nuclear force at high energies within a single theoretical framework. This approach was formulated by Glashow [16], Weinberg [17], and Salam [18]. The theory was experimentally confirmed in 1983 by discovering the W and Z bosons at CERN at the UA1 [19] and UA2 [20] experiments. The electroweak sector is formulated in the gauge theory based on the $SU(2)_L \otimes U(1)_Y$ symmetry group, which is spontaneously broken via the Higgs mechanism, giving mass to the W and Z bosons.

Following the gauge principle allows us to extend the theory with gauge bosons. The electroweak interaction is governed by the $SU(2)_L \otimes U(1)_Y$ gauge symmetry, with the corresponding gauge fields:

- The $SU(2)_L$ symmetry is associated with three weak isospin gauge bosons: $V_\mu^1, V_\mu^2, V_\mu^3$.
- The $U(1)_Y$ symmetry is associated with the hypercharge gauge boson B_μ.

The Lagrangian of the electroweak interaction after requiring gauge symmetry can be expressed as:

$$\mathcal{L}_{\text{EW}} = \mathcal{L}_g + \mathcal{L}_f + \mathcal{L}_h + \mathcal{L}_y \,. \tag{1.4}$$

The term $\mathcal{L}_g$ describes the interaction between the three V vector bosons and the B vector bosons.

$$\mathcal{L}_g = -\frac{1}{4} V_a^{\mu\nu} V_{\mu\nu}^a - \frac{1}{4} B^{\mu\nu} B_{\mu\nu} \,, \tag{1.5}$$

$$B_{\mu\nu} = \partial_\mu B_\nu - \partial_\nu B_\mu \,, \tag{1.6}$$

$$V_{\mu\nu}^i = \partial_\mu V_\nu^i - \partial_\nu V_\mu^i + g\,\epsilon^{ijk} V_\mu^j V_\nu^k \,. \tag{1.7}$$

$\mathcal{L}_f$ is the kinetic term for the SM fermions.

$$\mathcal{L}_f = i\overline{L}_n \gamma^\mu \partial_\mu L_n + i\overline{E}_n \gamma^\mu \partial_\mu E_n + i\overline{Q}_n \gamma^\mu \partial_\mu Q_n + i\overline{U}_n \gamma^\mu \partial_\mu U_n + i\overline{D}_n \gamma^\mu \partial_\mu D_n \,. \tag{1.8}$$

The regular derivative should be extended to be covariant to include fermion interactions with the gauge bosons. The covariant derivative considering weak isospin and hypercharge fields is defined as:

$$\partial_\mu \to \mathcal{D}_\mu = \left(\partial_\mu - ig \sum_{i=1}^{3} T_W^i V_\mu^i - ig' \frac{Y_f}{2} B_\mu \right) \,, \text{ (for } L_n, Q_n, H) \tag{1.9}$$

$$\partial_\mu \to \mathcal{D}_\mu = \left(\partial_\mu - ig' \frac{Y_f}{2} B_\mu \right) \,, \text{ (for } E_n, U_n, D_n) \tag{1.10}$$

where g and g' are the $SU(2)_L$ and $U(1)_Y$ gauge couplings, Y_f is hypercharge of the corresponding field, T_W^i is the generator of the $SU(2)_L$ group. The Higgs field's Lagrangian is expressed as

$$\mathcal{L}_H = \mathcal{D}_\mu H^+ \mathcal{D}^\mu H - V(H^+ H) \,, \tag{1.11}$$

with $V(H^+ H)$ is the Higgs potential, and the Higgs field acts as an isospin doublet of the $SU_L(2)$ group as notated in Eq. (1.2).

The Lagrangian that describes the interaction between fermionic fields and the Higgs field is expressed as follows:

$$\mathcal{L}_{\text{int}} = - \left(Y^l_{mn} \overline{L}_m H E_n + Y^d_{mn} \overline{Q}_m H D_n + Y^u_{mn} \overline{Q}_m \tilde{H} U_n + \text{h.c.} \right) , \qquad (1.12)$$

where $\tilde{H} = i\sigma_2 H^*$ (σ_2 is the second Pauli matrix). Within the framework of the spontaneous symmetry breaking described in Section 1.1.3, the fermions are gaining mass, which can be expressed as follows:

$$m_f = \frac{Y_f \cdot v}{\sqrt{2}} , \qquad (1.13)$$

where Y_f is the Yukawa coupling for a given fermion and v is the Higgs vacuum expectation value. The hierarchy of fermion masses arises from the different values of Y_f across quarks and leptons.

The Cabibbo–Kobayashi–Maskawa (CKM) matrix, which describes the mixing of quark flavours in weak interactions, arises naturally from the diagonalisation of the Yukawa coupling matrices. After diagonalising the Yukawa couplings for the up-type and down-type quarks, the resulting mismatch between the mass eigenstates and the weak interaction eigenstates gives rise to the CKM matrix, provided by:

$$V_{\text{CKM}} = \begin{bmatrix} V_{ud} & V_{us} & V_{ub} \\ V_{cd} & V_{cs} & V_{cb} \\ V_{td} & V_{ts} & V_{tb} \end{bmatrix} \approx \begin{bmatrix} 0.974 & 0.225 & 0.003 \\ 0.225 & 0.973 & 0.041 \\ 0.009 & 0.040 & 0.999 \end{bmatrix} ,$$

where each element represents the probability amplitude for a transition between quark flavours under the weak interaction.

1.1.3   Electroweak symmetry breaking

The Brout-Englert-Higgs mechanism is a cornerstone of the SM of particle physics. Proposed independently in 1964 by Robert Brout and François Englert [13], Peter Higgs [14] and Gerald Guralnik, C. R. Hagen, and Tom Kibble [15], the mechanism explains how the weak gauge bosons (the W and Z bosons specifically) acquire masses. Through this mechanism, the vacuum state no longer respects the full electroweak symmetry, leading to the emergence of massive W and Z bosons, while the photon remains massless. This process is crucial for ensuring consistency with experimental observations of particle masses while maintaining the fundamental principles of gauge theory.

The Higgs potential $V(H^+ H)$ is chosen to be of the form:

$$V(H^+ H) = -\mu^2(H^+ H) + \lambda(H^+ H)^2 .$$

This choice of potential is motivated, first, by the fact that in our $(3 + 1)$-dimensional space, a scalar field theory with a potential containing terms $\sim \varphi^n$ (where $n \geq 4$) is non-renormalizable and, therefore, unphysical. Second, the considered potential exhibits

invariance under discrete transformations, $V(\varphi) = V(-\varphi)$. The parameter λ in the potential $V(\varphi)$ must be positive because, for $\lambda < 0$, the potential becomes negative at large field values φ. In such a case, the system would tend toward a state with arbitrarily low energy, $E \to -\infty$ as $\varphi \to \infty$. This situation is unphysical since an infinite negative energy cannot characterise a stable ground state of the system. Therefore, the conditions $\lambda > 0$ and $\mu^2 < 0$ must be satisfied. The shape of this potential is shown in Fig. 1.2.
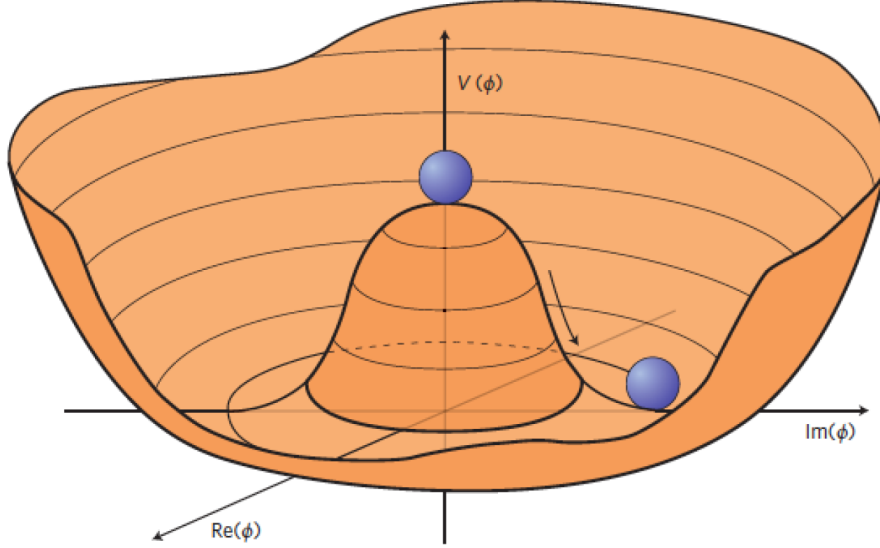
Figure 1.2: Shape of the Higgs potential for $\mu^2 < 0$ [21].

Electroweak symmetry breaking (EWSB) occurs when the Higgs field acquires a nonzero vacuum expectation value (VEV), spontaneously breaking the $SU(2)_L$ symmetry

$$\langle \Phi \rangle = \frac{1}{\sqrt{2}} \begin{pmatrix} 0 \\ v \end{pmatrix}. \tag{1.14}$$

After symmetry breaking:

- The fields transform under mixing relations:
$$\begin{pmatrix} A_\mu \\ Z_\mu \end{pmatrix} = \begin{pmatrix} \cos\theta & \sin\theta \\ -\sin\theta & \cos\theta \end{pmatrix} \begin{pmatrix} B_\mu \\ V_\mu^3 \end{pmatrix}, \tag{1.15}$$
  where θ is the Weinberg angle.

- The charged boson states are defined as:
$$W_\mu^\pm = \frac{V_\mu^1 \mp i V_\mu^2}{\sqrt{2}}. \tag{1.16}$$

- The **W and Z bosons** acquire masses:
$$M_W = \frac{gv}{2}, \quad M_Z = \frac{\sqrt{g^2 + g'^2}\,v}{2}, \tag{1.17}$$
  where g and g' are the $SU(2)_L$ and $U(1)_Y$ gauge couplings.

- The **photon** remains massless, preserving the symmetry of electromagnetism.
- The fermions acquire masses through the Yukawa interaction.

1.1.4 Quantum chromodynamics

Quantum chromodynamics (QCD) describes the strong interaction within the framework of the SM. The theoretical framework was established in the early 1970s by the physicists Murray Gell-Mann, Harald Fritzsch, Heinrich Leutwyler [22, 23] and David Gross, Frank Wilczek [24], David Politzer [25], who demonstrated asymptotic freedom in non-Abelian gauge theories. QCD is based on the gauge group $SU(3)_C$, which, based on the principle described above, allows the inclusion of the gluon gauge fields in theory. Requiring gauge invariance, the covariant derivative is defined as follows:

$$\partial_\mu \to \mathcal{D}_\mu = \left(\partial_\mu - ig_s \sum_{a=1}^{8} T_C^a G_\mu^a \right) ,$$

where G_μ^a is the gluon field with the index $a = 1..8$, T_C^a are the Gell-Mann matrices, g_s is the gauge constant of the $SU(3)_C$ group. Then, additional kinetic terms are added to the Lagrangian:

$$L_{kin}^{\text{QCD}} = -\frac{1}{4} G_{\mu\nu}^a G_a^{\mu\nu} ,$$

$$G_{\mu\nu}^a = \partial_\mu G_\nu^a - \partial_\nu G_\mu^a + g_s f^{abc} G_\mu^b G_\nu^c ,$$

where f^{abc} are the structure constants of the $SU(3)_C$ group.

One of the key features of QCD is asymptotic freedom, where the coupling g_s decreases at high energies due to the negative beta function:

$$\beta(g_s) = -\frac{g_s^3}{(4\pi)^2} \left(11 - \frac{2}{3} n_f \right) , \tag{1.18}$$

where n_f is the number of quark flavours. This implies that quarks behave as nearly free particles at high energies. Then the effective coupling of QCD evolves with the energy scale μ, described by the running coupling constant:

$$\alpha_s(\mu) = \frac{12\pi}{(33 - 2n_f) \ln(\mu^2/\Lambda^2)} , \tag{1.19}$$

where Λ is the QCD scale parameter, this running behaviour underpins the transition from asymptotic freedom to confinement. The dependence of α_s on the energy scale is crucial in high-energy experiments, such as deep inelastic scattering and collider physics.

1.2 Beyond the Standard Model

Currently, the SM remains the most consistent theory up to a certain energy scale [26]. It has made accurate predictions, including the existence of the Higgs boson, which was

confirmed in 2012 [4, 5] at the LHC. However, despite its success, the SM is known to be incomplete. A few unresolved issues are listed below, suggesting the need for physics beyond the Standard Model.

1. **Gravity**: The SM does not include gravity, as a quantum field theory does not describe general relativity.

2. **Dark matter and dark energy**: Cosmological observations indicate that a significant portion of the universe's matter is dark matter, which does not interact electromagnetically and, according to current observational constraints [27], does not exhibit significant interactions through the strong nuclear force [28]. This type of matter is not explained by the framework of the SM. Additionally, dark energy, responsible for the universe's accelerating expansion, is not explained within the SM framework [29].

3. **Matter-antimatter asymmetry**: The observable universe mainly consists of matter, even though theories predict that equal quantities of matter and antimatter should have emerged during the Big Bang. The current sources of CP violation recognised in the Standard Model, especially in weak interactions, fail to explain the observed baryon asymmetry sufficiently.

4. **Neutrino masses**: The SM does not include neutrino mass terms. This contradicts the observation of neutrino oscillations, which can happen only with nonzero masses.

5. **Hierarchy problem**: The hierarchy problem refers to the large discrepancy between the electroweak scale ($\sim 10^2$ GeV) and the Planck scale ($\sim 10^{19}$ GeV). The Higgs boson mass m_H receives large quantum corrections from loop diagrams, particularly from top quarks, gauge bosons, and other virtual particles. A dominant one-loop correction from a heavy fermion to m_H^2 is given by:

$$\Delta m_H^2 \approx \frac{Y_f}{16\pi^2}\Lambda^2 \,,$$

where Λ represents the high-energy cutoff, potentially the Planck scale, and Y_f is the Yukawa coupling. This leads to a higher expected Higgs mass than the observed value (~ 125 GeV). To maintain a low Higgs mass, an unnatural fine-tuning of parameters is needed, which seems highly coincidental and lacks a deeper underlying reason [30].

1.2.1 Supersymmetric extension

In the search for the possible extension of the SM that can resolve existing inconsistencies, a supersymmetric extension was developed [31, 32, 33]. The minimal supersymmetric SM (MSSM) is the theory that considers the minimal number of parameters for the symmetrisation of the SM. While being a natural extension of the SM, it can potentially explain the following aspects:

- SUSY helps to **resolve the hierarchy problem**, which arises from large quadratic corrections to the Higgs boson mass in the Standard Model. Supersymmetry mitigates this issue by linking scalars to fermions through a symmetry that ensures their quantum corrections cancel out. Since fermion masses receive only logarithmic corrections, this cancellation protects the Higgs mass from excessive divergence. The Higgs vacuum expectation value is tied to a negative scalar mass term in the Lagrangian, implying that superpartner masses should remain near the electroweak scale ($\sim 100\,\text{GeV}$) to maintain naturalness.

- SUSY suggests that the three gauge couplings of the SM that correspond to the $SU(3)_C$, $SU(2)_L$, and $U(1)_Y$ gauge groups evolve with energy in a way that allows them to meet at a single unification scale, named M_{GUT}, associated with a grand unifying theory (GUT). The **unification of gauge couplings** indicates a potential single underlying force at high energies.

- SUSY can **provide a dark matter candidate**. The lightest supersymmetric particle (LSP), typically the neutralino or gravitino, is stable and interacts weakly, making it a compelling Weakly Interacting Massive Particle (WIMP) candidate for dark matter. The stability of the LSP is ensured by R-parity conservation, which is defined as:

$$R_p = (-1)^{3(B-L)+2S},$$

where B is the baryon number, L is the lepton number, and S is the spin.

Below, the basics of the MSSM and its hypothetical experimental implications that can be observed at the LHC are discussed.

1.2.2 The minimal supersymmetric standard model

The MSSM [34, 35, 36] is the simplest theoretical framework that extends the SM of particle physics by introducing supersymmetry. The MSSM particles include superpartners for every SM particle with a spin difference of $1/2$. Two Higgs doublets are required for anomaly cancellation and fermion mass generation, unlike in the SM, which contains only one Higgs doublet. If SUSY is spontaneously broken, a goldstino ($\tilde{G}_{1/2}$) emerges, which in supergravity (SUGRA) gets absorbed by the gravitino. The superpartners of the standard model particles are listed in Table 1.1. After electroweak symmetry breaking, similarly to how V and the B fields mix to produce the physical Z^0 and γ fields, the corresponding supersymmetric fields mix to produce a zino ($\tilde{Z}^0$) and a massless photino.

Table 1.1: Particle content of the MSSM showing the SM particles and their supersymmetric partners (superpartners) along with their spin and R-parity values.

Particle	Symbol	Spin	R-Parity	Superpartner	Symbol	Spin	R-Parity
Quark	q	$\frac{1}{2}$	$+1$	Squark	$\tilde{q}$	0	-1
Lepton	ℓ	$\frac{1}{2}$	$+1$	Slepton	$\tilde{\ell}$	0	-1
W boson	$\mathcal{W}$	1	$+1$	Wino	$\tilde{\mathcal{W}}$	$\frac{1}{2}$	-1
B boson	$\mathcal{B}$	1	$+1$	Bino	$\tilde{\mathcal{B}}$	$\frac{1}{2}$	-1
Gluon	g	1	$+1$	Gluino	$\tilde{g}$	$\frac{1}{2}$	-1
Higgs	H_u, H_d	0	$+1$	Higgsinos	$\tilde{H}_u, \tilde{H}_d$	$\frac{1}{2}$	-1

The MSSM is the standard SUSY framework for phenomenological studies [34]. Its Lagrangian consists of kinetic terms for chiral superfields, gauge kinetic terms, and the superpotential, which is at most cubic in chiral superfields and includes Yukawa interactions and the Higgsino mass term. The superpotential for MSSM can be expressed as follows [35]:

$$W_{\text{MSSM}} = \overline{u}\mathbf{y}_u Q H_u - \overline{d}\mathbf{y}_d Q H_d - \overline{e}\mathbf{y}_e L H_d + \mu H_u H_d \,. \tag{1.20}$$

The objects H_u, H_d, Q, L, u, d, e correspond to chiral superfields. The dimensionless Yukawa coupling parameters $\mathbf{y}_u, \mathbf{y}_d, \mathbf{y}_e$ are 3×3 matrices in family space. The "μ term" can be expressed as $\mu(H_u)_\alpha(H_d)_\beta \epsilon^{\alpha\beta}$, where $\epsilon^{\alpha\beta}$ is used to contract $SU(2)_L$ weak isospin indices $\alpha, \beta = 1, 2$. The term $\overline{u}\mathbf{y}_u Q H_u$ can be written more explicitly as $(\overline{u})^{ci}(\mathbf{y}_u)_{ij}(Q_L)^{ja\alpha}(H_u)_\beta \epsilon^{\alpha\beta}$ where $i, j = 1, 2, 3$ are family indices, and $a = 1, 2, 3$ is a color index of $SU(3)_C$.

The MSSM Lagrangian incorporates all supersymmetric interactions consistent with $SU(3)_C \otimes SU(2)_L \otimes U(1)_Y$ gauge invariance, with coupling strengths constrained only by supersymmetry and gauge invariance, but not by additional theoretical assumptions. An explicit soft-SUSY-breaking term is introduced to account for SUSY breaking, avoiding quadratic divergences and ensuring energy scales remain at the electroweak level. Since no universal spontaneous SUSY-breaking mechanism exists, it is externally imposed to maintain phenomenological viability.

In the SM, fermions have chirality (left or right) and transform differently under $SU(2) \otimes U(1)$, carrying distinct quantum numbers. Hence, they belong to separate chiral supermultiplets: $(\tilde{f}_L, f_L)$ and $(\tilde{f}_R, f_R)$. Their scalar superpartners $\tilde{f}_L$ and $\tilde{f}_R$ do not have chirality but are labelled as left and right for distinction. These states mix, producing mass eigenstates $\tilde{f}_1, \tilde{f}_2$. For example, to incorporate third-generation sleptons, the simplified model requires modification where the left-handed and right-handed τ superpartners undergo mixing, expressed as

$$\begin{pmatrix} \tilde{\tau}_1 \\ \tilde{\tau}_2 \end{pmatrix} = \begin{pmatrix} \cos\theta_{\tilde{\tau}} & \sin\theta_{\tilde{\tau}} \\ -\sin\theta_{\tilde{\tau}} & \cos\theta_{\tilde{\tau}} \end{pmatrix} \begin{pmatrix} \tilde{\tau}_L \\ \tilde{\tau}_R \end{pmatrix} \,, \tag{1.21}$$

where $\tilde{\tau}_1$ and $\tilde{\tau}_2$ are the mass eigenstates arranged in order from the lighter to the heavier and $\theta_{\tilde{\tau}}$ is $\tilde{\tau}$ mixing parameter. The $\tilde{\tau}$ mass matrix in the basis $(\tilde{\tau}_L, \tilde{\tau}_R)$ is given by:

$$M_{\tilde{\tau}}^2 = \begin{pmatrix} m_{\tilde{\tau}_L}^2 & m_{\tilde{\tau}_{LR}}^2 \\ m_{\tilde{\tau}_{LR}}^{2*} & m_{\tilde{\tau}_R}^2 \end{pmatrix} \,, \tag{1.22}$$

with the mass terms defined as follows:

$$m^2_{\tilde{\tau}_L} = \tilde{m}^2_{\tilde{\tau}_L} + m^2_\tau + M^2_Z \cos 2\beta \left(-\frac{1}{2} - \sin \theta^2_W \right), \tag{1.23}$$

$$m^2_{\tilde{\tau}_R} = \tilde{m}^2_{\tilde{\tau}_R} + m^2_\tau + M^2_Z \cos 2\beta(-\sin \theta^2_W), \tag{1.24}$$

$$m^2_{\tilde{\tau}_{LR}} = -m_\tau(\mu \tan \beta + A^*_\tau), \tag{1.25}$$

where $\tilde{m}^2_{\tilde{\tau}_L}, \tilde{m}^2_{\tilde{\tau}_R}$ are the soft SUSY-breaking squared masses for left- and right-handed staus, m_τ is the tau lepton mass, M_Z is the mass of the Z boson, $\tan \beta = v_u/v_d$ is the ratio of Higgs vacuum expectation values, θ_W is the weak mixing angle, μ is the Higgsino mass parameter, A_τ is the trilinear soft SUSY-breaking coupling for the $\tilde{\tau}$. Mass eigenstates $\tilde{\tau}_1$ and $\tilde{\tau}_2$ can be obtained through a diagonalization of $M^2_{\tilde{\tau}}$ matrix. For the small values of $\tan \beta$, the mixing is minimal, and mass eigenstates are relatively close to the gauge eigenstates. For larger values of $\tan \beta$, the mixing between the left- and right-handed $\tilde{\tau}$ states becomes more pronounced, leading to mass eigenstates that can be significantly lighter than the sleptons of the first and second generations. As a result, the $\tilde{\tau}$ often emerges as the lightest slepton.

Similarly to sleptons, the neutral fermionic states, which include neutral gauginos and neutral Higgsinos, do not form mass eigenstates. These states are mixed due to electroweak symmetry breaking, forming mass eigenstates known as neutralinos. The neutralino mass matrix in the basis $(\tilde{B}, \tilde{W}^0, \tilde{H}^0_d, \tilde{H}^0_u)$ is given by:

$$M_{\tilde{\chi}^0} = \begin{pmatrix} M_1 & 0 & -M_Z c_\beta s_W & M_Z s_\beta s_W \\ 0 & M_2 & M_Z c_\beta c_W & -M_Z s_\beta c_W \\ -M_Z c_\beta s_W & M_Z c_\beta c_W & 0 & -\mu \\ M_Z s_\beta s_W & -M_Z s_\beta c_W & -\mu & 0 \end{pmatrix}, \tag{1.26}$$

where, M_1 and M_2 are the soft SUSY-breaking masses for the bino $(\tilde{B})$ and wino $(\tilde{W}^0)$, μ is the Higgsino mass parameter, M_Z is the mass of the Z boson, $s_W = \sin \theta_W$ and $c_W = \cos \theta_W$ are the sine and cosine of the weak mixing angle, $s_\beta = \sin \beta$ and $c_\beta = \cos \beta$, where $\tan \beta = v_u/v_d$ is the ratio of Higgs vacuum expectation values. The physical neutralino mass eigenstates $\tilde{\chi}^0_i$ ($i = 1, 2, 3, 4$) are obtained by diagonalizing corresponding neutralino mass matrix.

A more detailed description of the constituents of the MSSM Lagrangian can be found in Ref. [37].

1.2.3   Gauge mediated supersymmetry breaking

SUSY must be broken because no supersymmetric particles have yet been observed at current experimental energies. This means their masses must be much higher than those of the SM particles. GMSB [38, 39, 40, 41] is one possible way to achieve this. In GMSB, SUSY breaking happens first in a hidden sector, and then messenger particles transmit this breaking to the visible sector. Unlike gravity-mediated SUSY breaking (such as minimal supergravity (mSUGRA)), which transmits SUSY breaking via Planck-suppressed interactions, GMSB relies on gauge interactions, making it a flavour-blind

mediation mechanism. In the GMSB, the gravitino ($\widetilde{G}$) is the LSP for low SUSY-breaking scales, making it a viable dark matter candidate.

The scale of SUSY breaking ($\langle F_S \rangle$) determines the mass of the gravitino [34]:

$$M_{\widetilde{G}} = \frac{\langle F_S \rangle}{\sqrt{3} M_{\mathrm{Pl}}} \approx 2.5 \left(\frac{\langle F_S \rangle}{(100 \text{ TeV})^2} \right) \text{eV}, \tag{1.27}$$

where M_{Pl} is Plank scale. The $\widetilde{\tau}$ becomes next to lightest SUSY particle (NLSP), which decays to gravitino by the following reaction:

$$\widetilde{\tau}_1^\pm \rightarrow \tau^\pm + \widetilde{G} . \tag{1.28}$$

This decay is significantly suppressed due to the large values of M_{Pl}. This leads to $\widetilde{\tau}$ acquiring a macroscopic decay length, which leads to its distinct signature. The $\widetilde{\tau}$ proper decay length ($c\tau_0$) can be expressed as follows [39]:

$$c\tau_0 \approx 100 \mu m \left(\frac{100 \text{ GeV}}{m_{\widetilde{\tau}}} \right)^5 \left(\frac{\sqrt{\langle F_S \rangle}}{100 \text{ TeV}} \right)^4 . \tag{1.29}$$

In the aforementioned equation, the following regimes can be noted:

- If $\sqrt{\langle F_S \rangle}$ is small, the $\widetilde{\tau}$ decays quickly.
- If $\sqrt{\langle F_S \rangle}$ is large, the $\widetilde{\tau}$ can be long-lived, travelling macroscopic distances before decaying.
- For sufficiently high values of $\sqrt{\langle F_S \rangle}$, the $\widetilde{\tau}$ may behave like a meta-stable heavy charged particle.

This long-lived $\widetilde{\tau}$ can be detected through displaced lepton signatures in colliders, providing an experimental handle on GMSB models.

1.2.4 Simplified models

Simplified SUSY models [42, 43] focus on the sparticles and interactions most relevant to a specific decay chain or production mode, avoiding the extensive complexity of the full SUSY spectrum, which initially contains a large number of parameters. By restricting the free parameters to just a few masses and branching fractions, these models simplify the interpretation of data, facilitating comparisons across different analyses. Simplified models are characterised by minimal field content to reduce the number of unknown mass and coupling parameters.

A simplified model describing $\widetilde{\tau}$ pair production is used in this thesis. It includes only the $\widetilde{\tau}$ and LSP as SUSY particles, assuming that all other SUSY particles are too heavy to be produced. The LSP is often a $\widetilde{\chi}_1^0$ or a $\widetilde{G}$, which is assumed stable, conserving R-parity.

The primary decay mode is $\widetilde{\tau} \rightarrow \tau + \widetilde{G}$, which could be revealed in a collider experiment through the decay products of the τ lepton and an energy imbalance in the event due to $\widetilde{G}$ escaping detection. The simplified diagram of such a process is shown in Fig. 1.3.
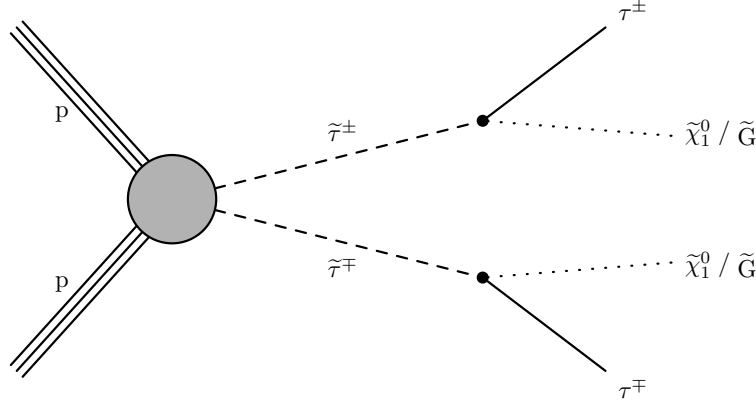
Figure 1.3: Diagram of direct $\widetilde{\tau}$ pair production.

A scan is performed over $(m_{\widetilde{\tau}}, c\tau_0(\widetilde{\tau}))$, keeping the LSP mass fixed at $1\,\text{GeV}$ throughout this thesis. This explores regions characterised by various proper lifetimes. In GMSB models, the gravitino typically serves as a very light LSP, and varying the $\widetilde{\tau}$ lifetime helps probe different phenomenological decay scenarios.

The total cross-section for left-handed sleptons (including $\widetilde{\tau}$) is generally larger than for right-handed sleptons due to their stronger coupling to electroweak gauge bosons. Signal production cross sections are calculated at next-to-leading order (NLO) with next-to-leading logarithmic (NLL) soft-gluon resummation [44].

When the $\widetilde{\tau}$ mixing angle is maximised, the lighter mass eigenstate ($\widetilde{\tau}_1$) is an equal mixture of left- and right-handed components. For this configuration, the cross-section is near minimal for lighter $\widetilde{\tau}$ masses but slightly higher than minimal for heavier masses. In cases where both $\widetilde{\tau}$ mass eigenstates ($\widetilde{\tau}_1$ and $\widetilde{\tau}_2$) are nearly degenerate, the overall cross-section is influenced by both eigenstates, but the primary impact of degeneracy is seen in decay kinematics, resulting in distinct experimental signatures.

Calculated cross sections for various mixing scenarios are presented in Fig. 1.4.

1.2.5 Experimental constraints

The latest SUSY searches from A Toroidal LHC Apparatus (ATLAS) and CMS have established stringent constraints on a wide range of SUSY models using 13 TeV collision data with integrated luminosities up to 139 fb^{-1} at ATLAS and 137 fb^{-1} at CMS. The summary plots are shown in Figs. 1.5 and 1.6 and illustrate the most up-to-date mass exclusion limits for squarks, gluinos, and electroweakinos, as well as searches for long-lived particles. These results significantly restrict the possible parameter space for supersymmetry, particularly in simplified models, and highlight the continued absence of a clear SUSY signal. Future analyses with larger datasets and improved search techniques will further refine these constraints.

The search for supersymmetric particles in the long-lived sector is particularly important. Many beyond the Standard Model (BSM) scenarios — such as GMSB discussed above, R-parity violating SUSY, and other extensions — predict new particles with macroscopic
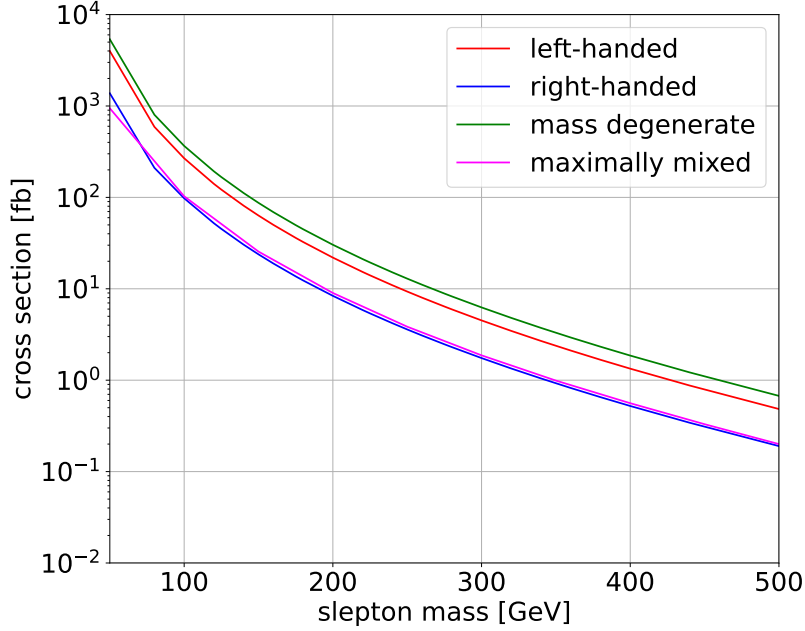
Figure 1.4: Cross section of $\widetilde{\tau}$ pair production as a function of $m_{\widetilde{\tau}}$ [45].

decay lengths. Typically, displaced lepton searches focus on identifying a lepton accompanied by additional tracks or objects, relying on the reconstruction of the displaced secondary vertex. However, significant interest also exists towards the case of *solitary displaced leptons*, which originate from a displaced vertex where the decay produces only one visible lepton and an invisible particle [39]. Searches based on such detector signatures are challenging to detect. A solitary displaced lepton lacks accompanying signatures, making it harder to reconstruct the decay and distinguish it from backgrounds. Tracking algorithms are often optimised for prompt particles, with reconstruction tuned for tracks that originate close to the interaction point.

On the other hand, existing prompt SUSY searches are not sensitive to moderately displaced signatures. These searches usually apply strict impact parameter vetoes, effectively removing events where sleptons decay at a measurable displacement from the primary vertex. As a result, *solitary displaced leptons* remain undetected in standard prompt searches.

In the context of long-lived $\widetilde{\tau}$ searches, the most stringent limits on displaced τ are in the degenerate production of the two mass eigenstates $\widetilde{\tau}_1$ and $\widetilde{\tau}_2$, which results in a larger cross section than the production of $\widetilde{\tau}_1$ alone. The CMS and ATLAS limits demonstrate the most stringent constraints for these scenarios, as shown in Figs. 1.7. The strongest exclusions are observed for lifetimes of $\tau_0 \sim 10^{-2} - 10\,\text{ns}$, covering a broad mass range up to $300\,\text{GeV}$ for $\widetilde{\tau}$ pair production scenarios.

The pair production of the lighter stau eigenstate, $\widetilde{\tau}_1$, is investigated under the assumption of maximal mixing between the $\widetilde{\tau}_\text{L}$ and $\widetilde{\tau}_\text{R}$ components, characterized by a mixing angle of $\pi/4$. This choice of mixing is motivated by its close kinematic properties and production cross section to those predicted in GMSB scenarios. In such scenarios, a nearly massless gravitino is the lightest supersymmetric particle, while the $\widetilde{\tau}_1$ serves as the next-to-lightest
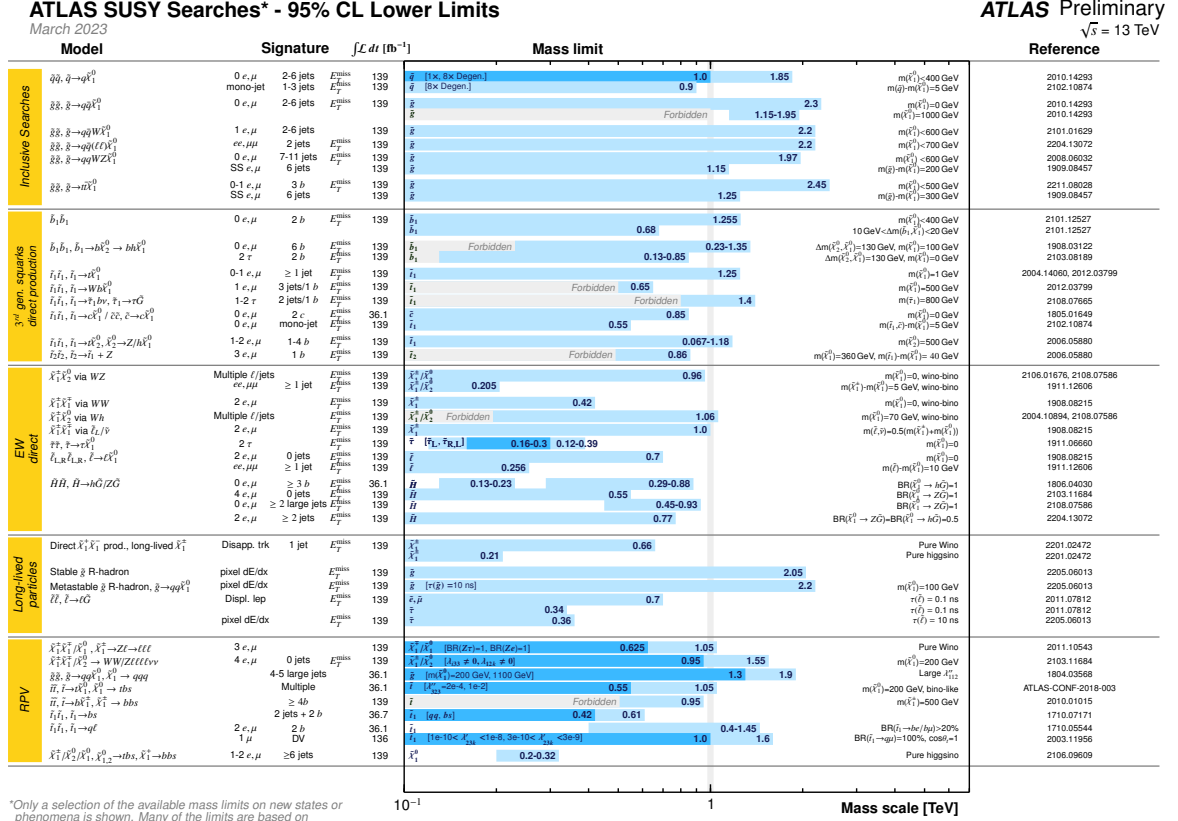
Figure 1.5: ATLAS SUSY summary exclusion limits [46].

supersymmetric particle. The suppressed coupling of the $\widetilde{\tau}$ to the gravitino results in a finite but non-negligible lifetime, allowing for displaced decay within a few centimetres. Existing experimental limits from Ref. [10], illustrated in Fig. 1.8, exclude scenarios of pair production for proper decay lengths up to approximately 0.1 mm. The primary objective of this analysis is to explore scenarios featuring substantially longer lifetimes.

It is worth mentioning that a displaced τ signature arises in a wide variety of BSM scenarios in addition to the GMSB model described above. For instance, certain dark matter models can incorporate heavy neutral leptons that couple weakly to the SM, resulting in long-lived particles that decay into τ leptons [50]. In other scenarios, vector-like leptons may produce long-lived bosons that travel some distance before decaying, giving rise to displaced τ signatures [51]. Likewise, leptoquarks - proposed as mediators between quarks and leptons - can be embedded in models with parameter choices that lead to displaced τ final states [52]. Finally, hidden sector models with dark bound states may also yield long-lived particles that decay visibly inside the detector, including final states with displaced τ leptons [53]. The shared experimental signature of a displaced τ vertex thus provides a unifying strategy to search for multiple classes of exotic phenomena.

1.3 Monte Carlo simulation

The research conducted in this thesis relies on precise theoretical predictions of both signal and background event topologies. These predictions are obtained through simulations
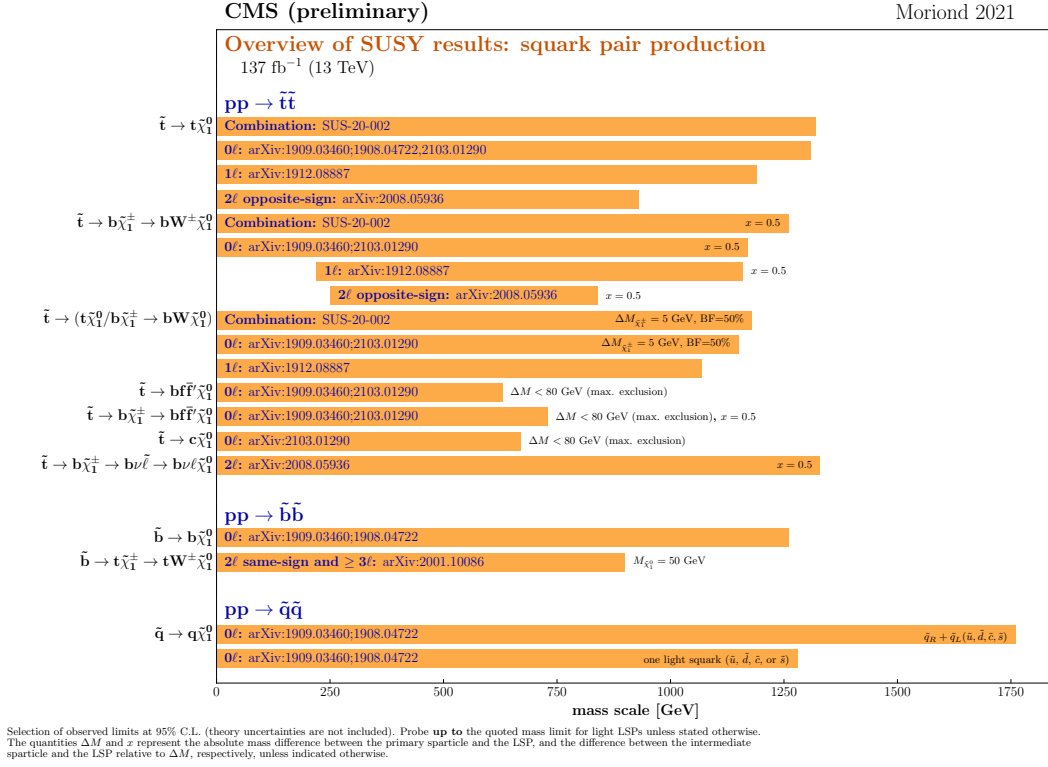
Figure 1.6: CMS SUSY summary exclusion limits [47].

of the underlying physics processes, commonly called Monte Carlo (MC) simulations. By reproducing the entire chain of particle interactions from the hard-scattering process through the detector response, MC allows us to compare observed data with theoretical expectations.

A simulation starts with the *matrix element (ME)* generator such as MAD-GRAPH5_aMC@NLO [54]. The ME generator calculates the probability of particular partonic interactions (e.g. quark-antiquark or gluon fusion processes) at leading order (LO) or NLO in perturbative QCD. The parton distribution functions (PDFs), such as the NNPDF3.1 set, are used to specify how quarks and gluons are distributed inside the proton at the relevant factorisation scales. Once the momenta and flavours of the outgoing partons have been generated, a *parton shower (PS)* algorithm (as implemented in PYTHIA [55]) simulates additional soft and collinear radiation of gluons or quarks, thereby producing more realistic final-state kinematics and jet multiplicities. Afterwards, the *hadronisation* phase describes how coloured partons become colour-neutral hadrons, using phenomenological models such as the Lund string [56] or cluster model [57]. After this, all unstable hadrons and resonances decay according to measured branching ratios. Then, particles propagate through the CMS detector using simulation tools such as GEANT4 [58]. In CMS simulations, the standard process for simulating all particle interactions with matter using GEANT4 is referred to as Full Simulation (FullSim). In contrast, certain detector effects can be parameterised for larger MC samples without using GEANT4 to save computational time. This approach is known as Fast Simulation (FastSim).

Signal and background processes are modelled using MC simulation. In the analysis de-

Figure 1.7: Expected (dashed) and observed (solid) 95% CL exclusion contours for $\tilde{e}$ NLSP, $\tilde{\mu}$ NLSP, $\tilde{\tau}$ NLSP, and co-NLSP production as a function of the slepton mass and lifetime. The CMS results [48] (left) and ATLAS results [49] (right) are shown. Selectrons ($\tilde{e}_{L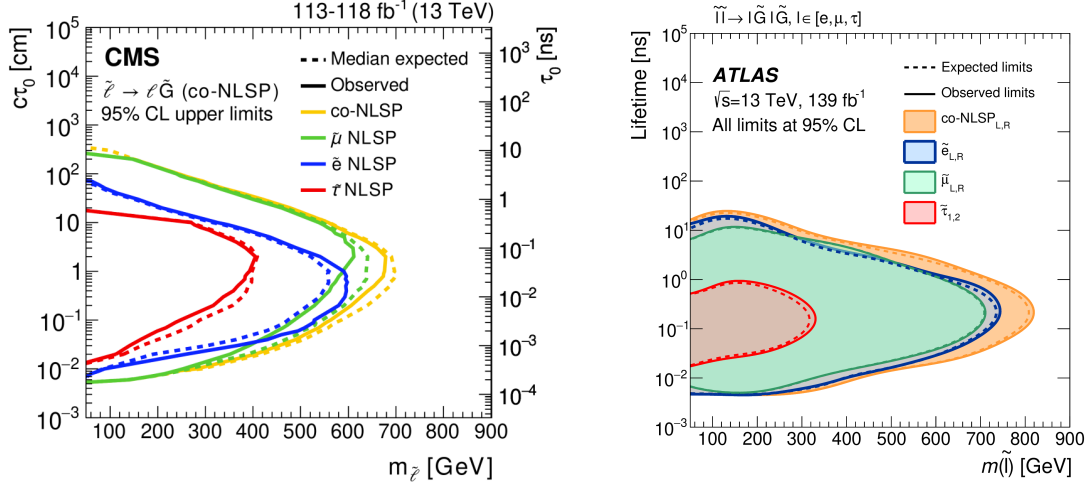,R}$) and smuons ($\tilde{\mu}_{L,R}$) are superpartners of left- and right-handed electrons and muons, while staus ($\tilde{\tau}_{1,2}$) are mixed states of the left- and right-handed tau superpartners, with $\sin\theta_{\tilde{\tau}} = 0.95$. The limits assume a 100% branching ratio for $\tilde{\ell} \to \ell + \tilde{G}$. The observed exclusion region is to the left of the solid curves, while the dashed lines indicate expected limits.

scribed in Chapter 6, the backgrounds are primarily estimated from control regions in data. However, MC simulations remain essential to validate and tune the analysis strategy and test the background estimation methods' accuracy. For generating the relevant MC samples, MadGraph5_aMC@nlo is utilised for processes involving Drell-Yan (DY) production associated with jets, W+jets, $t\bar{t}$, diboson, and QCD multijet. For single top production, which demands NLO accuracy and proper matching to parton showers, POWHEG is employed. The proton parton distribution functions (PDFs) from the NNPDF 2.3 set are used for the 2016 simulation samples, while the updated NNPDF 3.1 PDFs are adopted for the 2017 and 2018 simulation campaigns. Additionally, Pythia8 is implemented as the PS and hadronisation algorithm, providing the transition from parton-level to stable particle-level final states. A comprehensive overview of all simulated background samples used in the analysis is summarised in Table A.2.

The generation of models involving direct $\tilde{\tau}$ pair production and the subsequent production of τ leptons is performed using MadGraph5_aMC@nlo event generators (version 2.4.2) at LO precision. These event generators simulate promptly decaying $\tilde{\tau}$ sleptons up to the production of τ leptons. The decay of τ leptons is handled by pythia 8.2. Models with $\tilde{\tau}$ proper decay length ranging from $c\tau_0 = 0.01$ to $10\,\mathrm{m}$ are explored. The $\tilde{\tau}$ is considered, with $\tilde{\tau}$ masses ranging from 90 to $500\,\mathrm{GeV}$. The generated parameters are listed in Tables A.3 and A.3. The CP5 event tune [59] is applied. For PDFs, the NNPDF3.1 NLO PDFs are used. Showering and hadronisation of partons are conducted with pythia, while detailed simulation of the CMS detector relies on the Geant4 FullSim that is implemented inside CMSSW [60] framework.
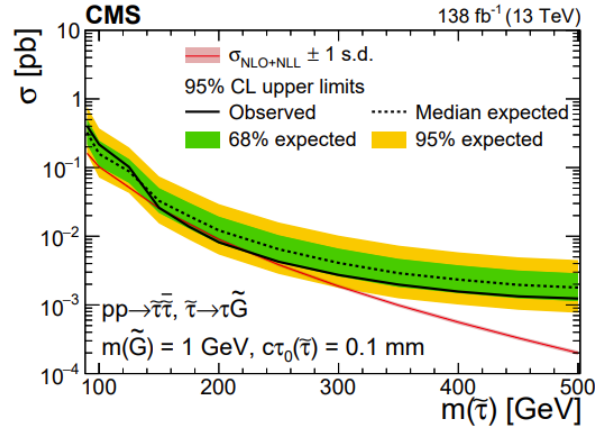
Figure 1.8: Expected and observed 95% CL cross section upper limits as functions of the $\widetilde{\tau}$ mass for long-lived $\widetilde{\tau}$ in the maximally mixed scenario for an LSP mass of $1\,\mathrm{GeV}$, and for $c\tau_0$ value of $0.1\,\mathrm{mm}$. The inner (green) band and the outer (yellow) band indicate the regions containing 68 and 95%, respectively, of the distribution of limits expected under the background-only hypothesis. The red line and thin shaded band indicate the NLO+NLL prediction for the signal production cross section [10].

Chapter 2

The CMS Experiment

The analysis described in the thesis is based on the proton-proton (pp) collision data recorded at CMS [61]. The CMS detector, located at the LHC [62], is one of the world's most advanced particle physics detectors. The CMS detector is designed to study a wide range of phenomena, from the Higgs boson production to the search for new physics beyond the SM, such as supersymmetry. This chapter focuses on the technical aspects of the CMS detector. It provides a detailed overview of its key components, including the silicon tracker, electromagnetic and hadronic calorimeters, and the muon system. The data utilised in this analysis were collected by the CMS experiment from 2016 to 2018 at a centre-of-mass energy of 13 TeV.

2.1   The Large Hadron Collider

The LHC is a circular superconducting hadron accelerator placed within a 27 km long tunnel, initially built for the infrastructure of the Large Electron-Positron (LEP) [63] collider. The LHC is part of the European Organization for Nuclear Research (CERN) infrastructure, shown in Fig. 2.1. Located up to 170 m underground, the LHC's design capitalises on pre-existing civil engineering structures while also requiring the construction of new underground and surface facilities designed for experiments such as CMS. Initially conceived for a centre-of-mass energy of 14 TeV, the LHC underwent subsequent upgrades to achieve 13.6 TeV during Run 3.

Before the injection into the LHC, the protons undergo a series of accelerations, progressively increasing their energy from ionisation to their final injection in the LHC. The chain of acceleration is as follows:

- **Proton Source**: Ionization of hydrogen gas to create protons.
- **LINAC4** [65]: A linear accelerator that speeds up the protons to the energies of 160 MeV.
- **Proton Synchrotron Booster (PSB)** [66]: Increases the proton energy from 160 MeV to 2 GeV.
- **Proton Synchrotron (PS)** [67]: Accelerates protons from 2 GeV to 26 GeV.
- **Super Proton Synchrotron (SPS)** [68]: Further accelerates protons from 26 GeV to 450 GeV.
- **Transfer Lines (TI2, TI8)**: Injects protons into the LHC.
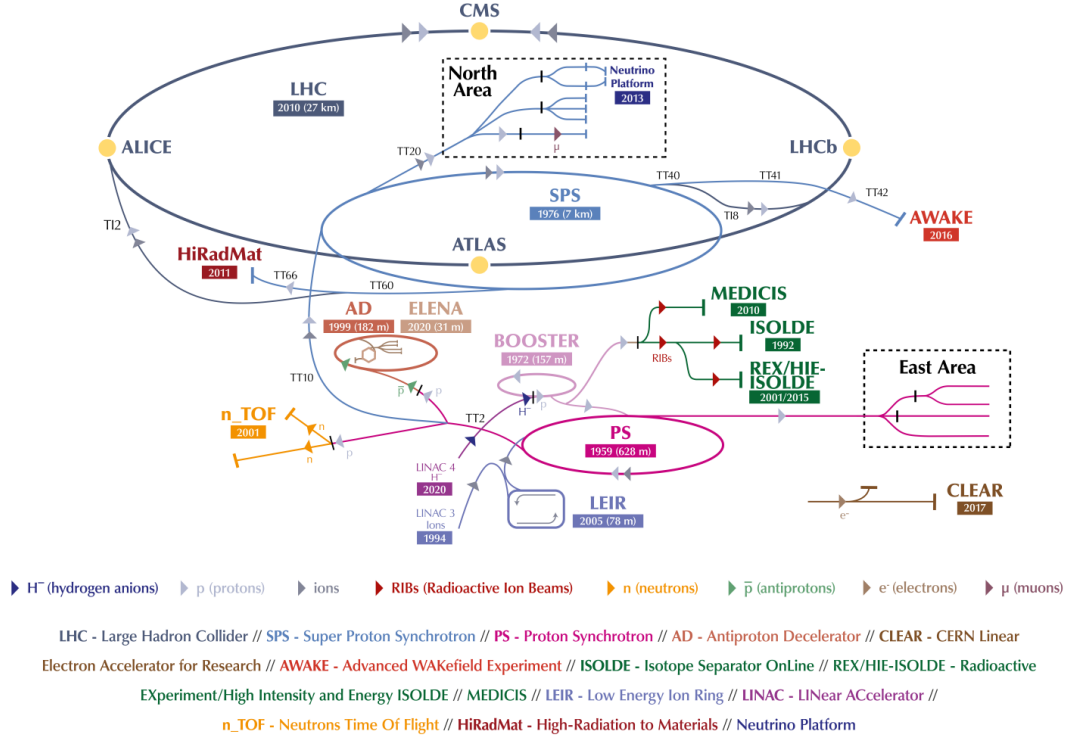
Figure 2.1: The CERN accelerator complex [64].

- **LHC**: Final acceleration to 6.5 TeV (or more, depending on the run period) per proton for collisions.

2.1.1 Experiments at the Large Hadron Collider

The LHC is built to explore some of the most fundamental questions in particle physics, including the study of the Higgs boson's properties and the search for new physics BSM. The main experiments located at LHC are as follows:

- **A Toroidal LHC Apparatus (ATLAS):** The ATLAS [69] detector is a large, complex design measuring 46 m in length and 25 m in diameter. It includes silicon trackers, calorimeters, and muon chambers, all enclosed in a toroidal magnetic field. This setup is optimised for precision tracking, energy measurement, and particle identification.

- **Compact Muon Solenoid (CMS):** The CMS [61] is a general-purpose detector, smaller and denser than ATLAS. It features a large solenoid magnet producing a 3.8 T magnetic field. Its design includes a silicon tracker, a crystal-based electromagnetic calorimeter, and muon detectors, all designed for high precision in identifying and measuring particles, especially muons.

- **Large Hadron Collider beauty (LHCb):** LHCb [70] has a unique forward geometry, optimised for studying particles produced at small angles relative to the beamline. Unlike the cylindrical designs of ATLAS and CMS, LHCb's forward detector configuration is ideal for analysing the decays of beauty quarks, using advanced tracking and vertex detectors for high-precision measurements

of quarks.

- **A Large Ion Collider Experiment (ALICE):** ALICE [71] is designed to handle the extreme conditions of heavy-ion collisions. It uses specialised detectors like a Time Projection Chamber (TPC) to track thousands of particles produced in lead-lead collisions. ALICE focuses on high particle multiplicity and heavy-ion physics, making its ability to reconstruct dense particle environments distinct.

- Complementary LHC Experiments: **TOTal Elastic and diffractive cross section Measurement (TOTEM)** [72] measures the total proton-proton cross-section and studies diffractive scattering at the LHC; **Monopole and Exotics Detector at the LHC (MoEDAL)** [73] is dedicated to searching for magnetic monopoles and other exotic particles beyond the Standard Model; **Forward Search Experiment (FASER)** [74] is designed to detect long-lived BSM particles, such as dark photons and other weakly interacting particles; **Large Hadron Collider forward (LHCf)** [75] supports studies of high-energy cosmic rays by measuring particles produced in the very forward region of LHC collisions.

2.1.2 Luminosity and pileup

One goal of the LHC is to investigate physics beyond the Standard Model by reaching the highest possible centre-of-mass energies, up to 14 TeV, and high luminosity. Higher centre-of-mass energy enables the study of more massive particles and rare phenomena, while increased luminosity boosts the collision rate, offering a larger dataset for statistical analysis. The number of events produced per second in LHC collisions can be expressed as:

$$N_{\text{event}} = L\sigma_{\text{event}} \,,$$

where σ_{event} is the cross section of the event under investigation, and L is the machine luminosity. The luminosity, which describes the event rate, depends on various beam parameters and is defined for a Gaussian beam distribution as [62]:

$$L = \frac{N_b^2 n_b f_{\text{rev}} \gamma_r F}{4\pi \epsilon_n \beta^\star} \,,$$

where, N_b is the number of particles per bunch, n_b is the number of bunches per beam, f_{rev} is the revolution frequency, γ_r is the relativistic gamma factor, ϵ_n is the normalized transverse beam emittance, $\beta^\star$ is the beta function at the collision point, F is the geometric luminosity reduction factor due to the crossing angle, given by:

$$F = \left(1 + \left(\frac{\theta_c \sigma_z}{2\sigma^\star}\right)^2\right)^{-1/2} \,,$$

where θ_c is the full crossing angle at the interaction point (IP), σ_z is the root mean square (RMS) bunch length, and $\sigma^\star$ is the transverse RMS beam size at the IP.

Integrated luminosity represents the total number of collision events in data collected over an interval of time. The larger the dataset available for statistical analysis, the bigger the chances of observing rare processes. It is defined as the time integral of the instantaneous luminosity, $L_{Int}(t) = \int L(t) \, dt$. Integrated luminosity is measured in units of inverse femtobarns (fb^{-1}) or picobarns (pb^{-1}).

The LHC operates high-luminosity experiments like ATLAS and CMS, targeting a peak luminosity of $L = 10^{34} \, \text{cm}^{-2} \, \text{s}^{-1}$ for proton-proton collisions. The other experiments require a lower luminosity.

To achieve the required luminosity at the LHC, it is necessary to increase the number of particles in each bunch, increase the number of bunches, and tightly focus the beams at the collision points using advanced superconducting magnets. The LHC design implements opposite magnet fields in one magnet for the two counter-rotating proton beams, eliminating the possibility of using antiparticle beams. The machine consists of twin-bore magnets with two sets of coils and beam channels housed within the same mechanical structure. Figure 2.2 illustrates the cross-section of the cryodipole magnet and the beam line, through which two pp beams travel. The whole ring houses 1232 main dipole magnets.
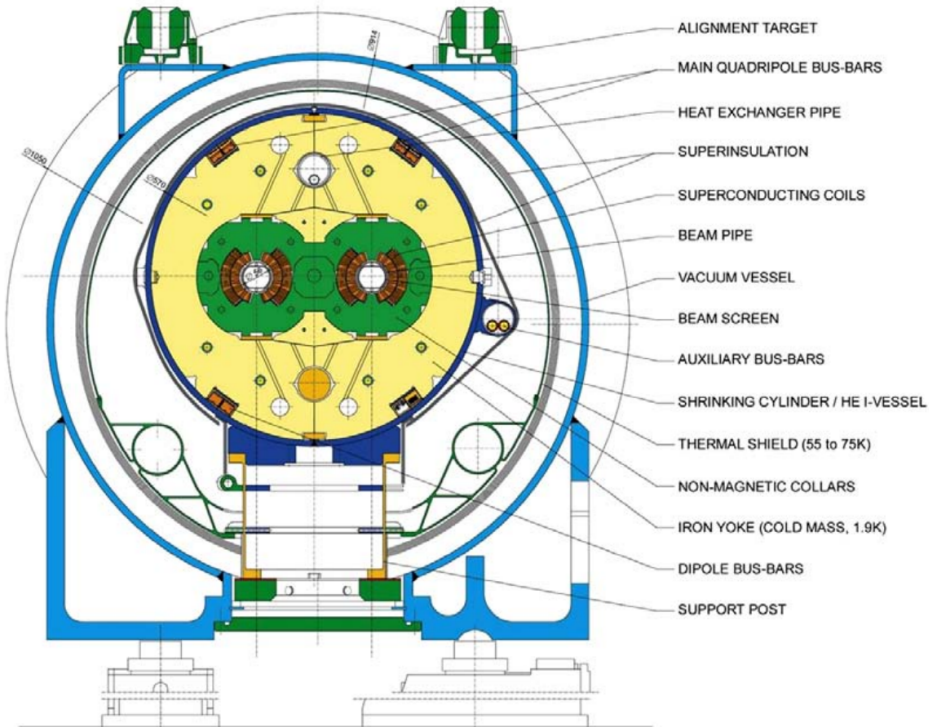
Figure 2.2: Cross-section of cryodipole margent [62].

The "dipole cold mass" is the core of the cryodipole, housing components cooled by superfluid helium. Located inside the shrinking cylinder/He II vessel (see Figure 2.2), it features two apertures for the cold bore tubes where proton beams circulate. Operating at the temperature of $1.9 \, \text{K}$, each dipole cold mass is about $15 \, \text{m}$ long, $570 \, \text{mm}$ in diameter,

and weighs about 27.5 tons with a slight curvature with an apical angle of 5.1 mrad, aligning with the particle trajectory and a curvature radius of approximately 2812 m at room temperature.

The high luminosity at the LHC helps to target the very rear processes. However, it is associated with specific features, such as more than one parallel proton-proton interaction in the same bunch crossing. Such parallel pp interactions are called pileup. Its frequency increases with the increase of luminosity. A typical event with numerous parallel pp interactions is shown in Fig. 2.3
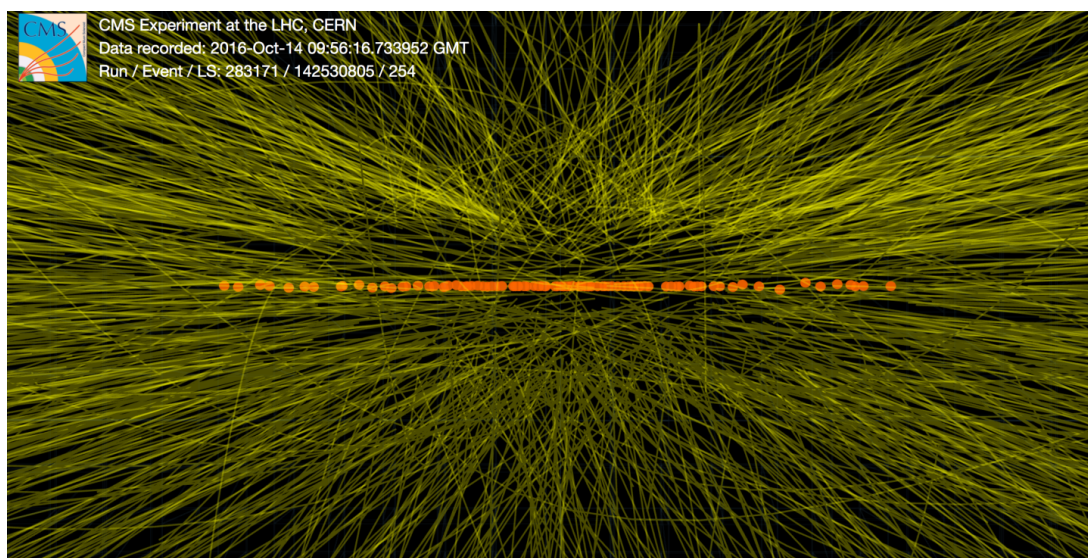
Figure 2.3: Collisions recorded by the CMS detector on October 14 2016 during the high pileup fill [76]. The events are from isolated bunches with an average pileup of roughly 100.

Pileup can be problematic in certain detector regions where particles from different interactions overlap. It also affects the trigger system, which must efficiently select events in real time. Advanced algorithms for pileup subtraction and enhanced tracking techniques help reduce pileup effects [77]. As the LHC moves toward higher luminosity, especially with the High-Luminosity LHC (HL-LHC), where pileup could exceed 200 interactions per bunch crossing, this challenge requires detector upgrades and analysis technique improvements.

2.1.3 Operation schedule

In its first operational phase, the LHC produced pp collisions at a centre-of-mass energy of 7 TeV, later increasing to 8 TeV. This period culminated on July 4, 2012, when the ATLAS and CMS experiments announced the discovery of the Higgs boson. The LHC restarted in 2015 with upgraded components, enabling collisions at increased centre-of-mass energy of 13 TeV. To extend these capabilities further, the LHC is undergoing an extensive upgrade to transform into the HL-LHC, scheduled for completion in the 2030s. The HL-LHC will increase the collision rate by a factor of ten, enabling more data collection. The schedule of LHC, including HL-LHC, is shown in Fig. 2.4.
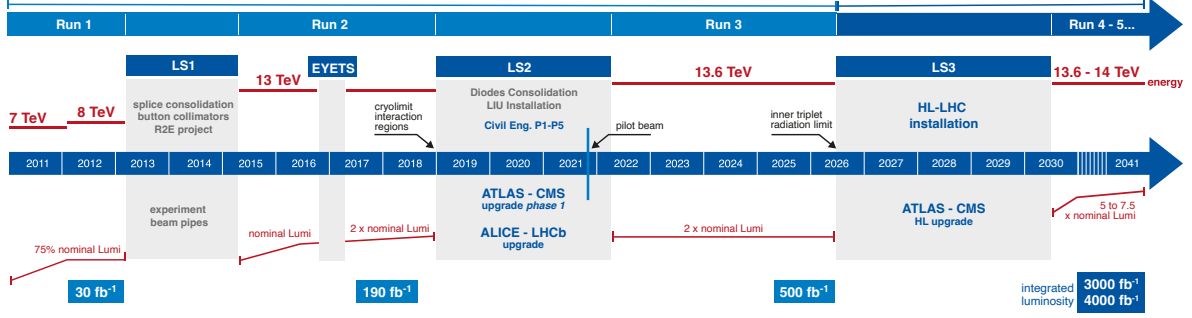
Figure 2.4: The planned timeline [78] for the LHC as of January 2025.

2.2   The Compact Muon Solenoid

The search for BSM physics, presented in this thesis, uses data collected by the CMS experiment. The CMS detector follows a standard particle detector architecture, as shown in Fig. 2.6, designed to detect and reconstruct all particle types produced in collisions efficiently. At its core, CMS consists of a high-field superconducting solenoid that encases several key sub-detector systems.

Starting from the interaction point, the silicon tracker records the trajectories of charged particles, providing precise momentum measurement and vertex reconstruction before the particles interact with the dense calorimeter material. The Electromagnetic Calorimeter (ECAL), made of lead-tungstate crystals, measures the energy of electrons and photons through electromagnetic showers. Following this, the Hadronic Calorimeter (HCAL), composed of brass-scintillator layers, captures the energy of hadrons. The Muon System, positioned at the outermost layer within the iron flux-return yoke, consists of four stations of muon detectors that ensure full 4π solid angle coverage, enabling robust muon identification.

CMS also features forward calorimeters, extending the pseudorapidity coverage up to $|\eta| \leq 5$, providing high hermeticity for missing energy measurements. The overall detector dimensions are $21.6\,\text{m}$ in length, $14.6\,\text{m}$ in diameter, and a total weight of $12500\,\text{tons}$, making it the heaviest particle detector in the world. These components work together to ensure efficient particle detection and precision measurements in high-energy collisions. A schematic representation of the CMS detector is shown in Fig. 2.5, with further details provided in the sections below.

The CMS detector uses a right-handed Cartesian coordinate system to describe physical properties. The origin is at the interaction point, the **z-axis** is aligned with the beamline (proton collision axis), the **x-axis** points radially inward toward the centre of the LHC, and the **y-axis** points upward.

In addition, cylindrical coordinates are commonly used:

- r is the radial distance from the beamline,
- ϕ is the azimuthal angle in the transverse plane (x-y plane),
- θ is the polar angle relative to the z-axis.

Instead of the polar angle θ, the **pseudorapidity** η is used because particle production is constant as a function of rapidity and because differences in rapidity are Lorentz invariant
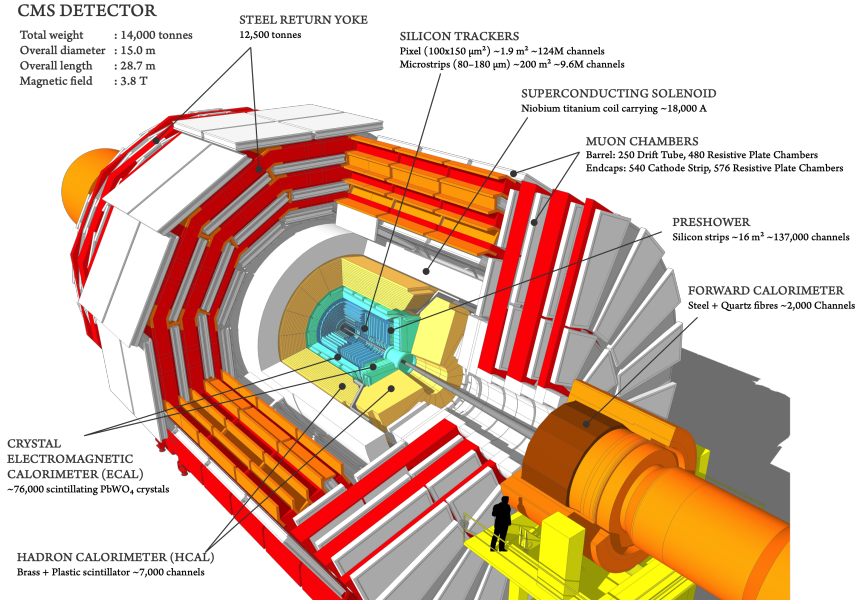
Figure 2.5: The Compact Muon Solenoid [79].

under boosts along the longitudinal axis. It is defined as:

$$\eta = -\ln\left(\tan\frac{\theta}{2}\right)$$
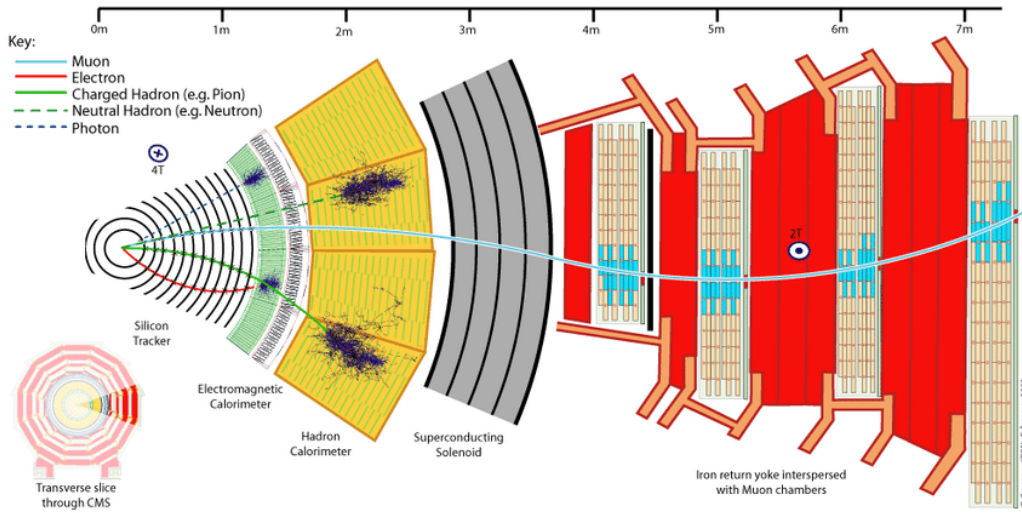
Figure 2.6: The transverse cross-section of the Compact Muon Solenoid [80].

2.2.1 Superconducting solenoid magnet

At CMS, particle reconstruction relies on a powerful superconducting solenoid magnet, generating a magnetic field of 3.8 T. This field bends the trajectory of charged particles, allowing precise momentum measurement. The magnet has an inner radius of 2.9 m and an outer of 3.8 m with a length of 12.9 m. The magnet's superconducting coils are cooled to $-268.5°$ C, reaching a superconductivity state and a current of up to 18 kA, creating a stronger field than conventional magnets. The experiment is named compact due to

the magnet's small form factor and large magnetic field. Inside the solenoid, the tracker and calorimeters are located. At the same time, the muon detectors are embedded in a 12-sided iron return yoke with a radius of 7 m and a length of 21.6 m, which keeps the magnetic field contained within the experiment and filters particles, letting only muons and weakly interacting particles pass through.

2.2.2 Tracking detectors

The tracker is the crucial subsystem that precisely measures the trajectory of the charged particles in the magnetic solenoid's field. The ability to reconstruct particle paths allows for identifying particle types and measuring their momentum. In this thesis, the reconstruction of displaced τ leptons relies heavily on the accurate tracking of their decay products. The detailed layout of the tracker is shown in Fig. 2.7. CMS adopts an all-silicon detector, which is split into two parts:
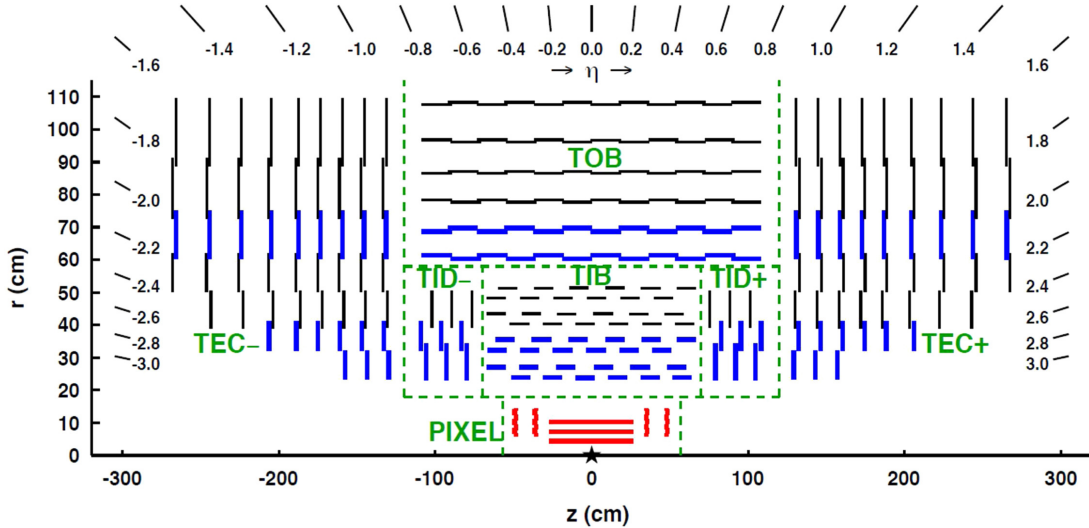
Figure 2.7: Longitudinal view of the CMS Phase-0 tracker detector [81].

The Silicon Pixel Detector

The Silicon Pixel Detector (SPD) is the part of the tracking system closest to the interaction region. It is responsible for achieving a small impact parameter resolution, which is essential for good secondary vertex reconstruction. This detector has a high granularity with a pixel size of $100 \times 150\ \mu\mathrm{m}^2$ and can operate in a region with a high density of particles. During the Phase-1 upgrade after the 2016 data-taking period, the Pixel detector was replaced by an upgraded version that contains one more barrel layer and endcap disk, as shown in Fig. 2.8.

The CMS Phase-1 pixel detector layout is updated for four-hit coverage over the pseudorapidity range $|\eta| < 2.5$, improved pattern recognition and track reconstruction, and added redundancy to handle hit losses. It contains less material, reducing multiple scattering, as demonstrated in Fig. 2.9, and updated readout chips improve processing at the high event collision rate.

The four-barrel layers have radii of 29, 68, 109 and 160 mm, covering the area of $-27 < z < 27$ cm along the beamline. The six end disks with a radius in the range of 45-110 mm
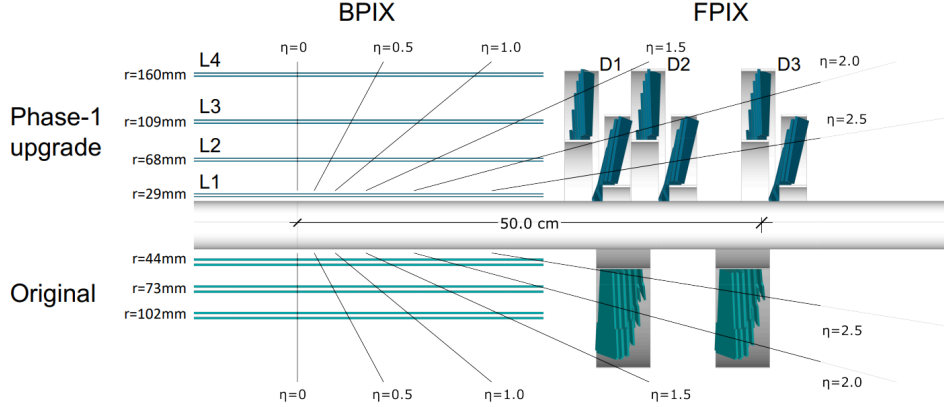
Figure 2.8: Layout of the CMS Phase-1 pixel detector compared to the original detector layout, in longitudinal view [82].
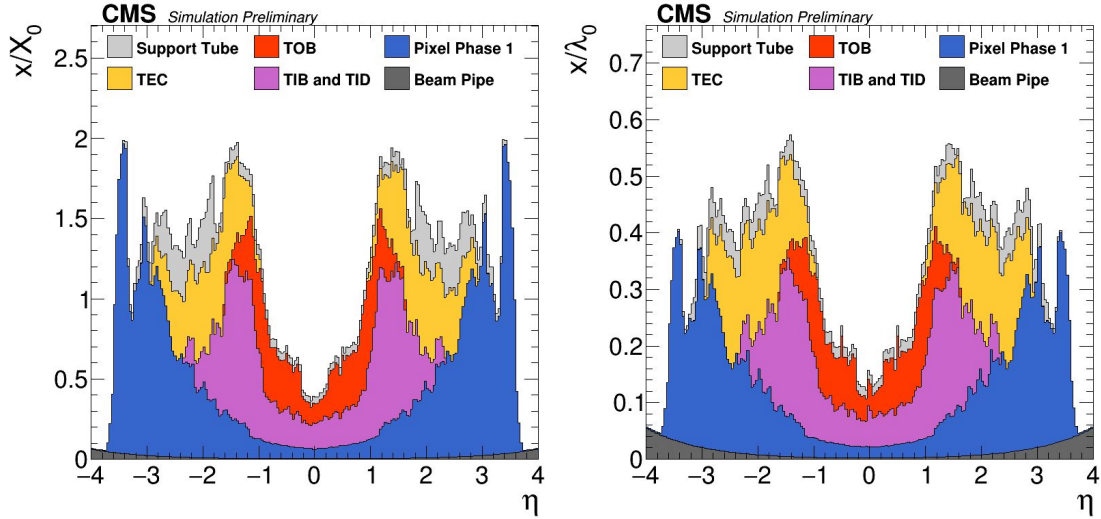
Figure 2.9: Material budget shown as the number of radiation lengths (x/X_0, right) and hadronic interaction lengths (x/λ_0, left) as a function of η [83].

for the inner ring and 96-161 for the outer ring are placed at $|z|$ of 338 (D1 inner ring), 309 (D1 outer ring), 413 (D1 inner ring), 384 (D1 outer ring), 508 (D1 inner ring) and 479 mm (D1 outer ring). The primary task of the pixel detector is to provide excellent vertex resolution, enabling the reconstruction of short-lived particles that decay within millimetres of their production point.

The Silicon Strip Detector

The Silicon Strip Detector (SSD) covers the broader volume between the pixel detector and calorimeters. The strip detector is responsible for measuring particles' position over a broader area in smaller densities of particles in comparison to the pixel tracker. The detector is segmented into thin silicon strips, with strip lengths varying between 10-20 cm, depending on the detector layer. The CMS tracker is composed of several key components: the Tracker Inner Barrel (TIB), Tracker Inner Disks (TID), Tracker Outer Barrel (TOB), and Tracker Endcaps (TEC). Together, they provide comprehensive coverage for tracking

charged particles across a wide range of pseudorapidity.

- The **TIB** consists of four cylindrical layers of silicon strip sensors located between 20 cm and 55 cm from the beam axis. These layers are designed to capture particle trajectories at intermediate radii. The silicon strips in the TIB vary in length across the layers to optimise spatial resolution while minimising the material budget.

- The **TID** comprises three forward-mounted disk structures on either side of the TIB, covering the transition between the barrel and forward regions. The TID extends the tracker's reach into the forward region with a pseudorapidity coverage of up to $|\eta| \approx 2.5$. Its wedge-shaped silicon strip sensors are designed to handle particles emerging at steeper angles, thus ensuring continuous tracking from the barrel to the endcaps.

- The **TOB** is the outermost component of the barrel tracker, consisting of six layers of silicon strip detectors that extend radially from 55 cm to 116 cm from the beam axis. Compared to the TIB, the longer silicon strips in the TOB are optimised for tracking particles at larger radii. The TOB is essential in improving momentum resolution for high-momentum particles by providing extended lever arms that enable precise measurement of track curvature.

- The **TEC** is located at the ends of the CMS tracker, covering the forward and backwards regions with high pseudorapidity values. Each TEC consists of nine disks arranged in concentric rings, with silicon strip sensors mounted on each. The TEC covers a radial distance from approximately 22 cm to 113 cm from the beamline, tracking particles emerging at small angles relative to the beam axis.

2.2.3 The calorimeter system

The calorimeters in high-energy physics experiments are designed to measure the energy of the particles produced in collisions. The basic principle is that particles that reach the calorimeter volume interact in dense environments, creating a cascade of secondary particles. After this, the readout system converts the secondary particle energy into an electric signal.

The calorimeters in CMS can be separated into two types: the ECAL and the HCAL. The ECAL calorimeters aim to reconstruct electrons, positrons and photons. The particles that interact electromagnetically create a shower, preferably through bremsstrahlung, pair production, Compton scattering and Photoelectric Effects. As shown in Fig. 2.6, the ECAL is located between the tracker and HCAL. The HCAL calorimeters aim to measure the energy of the massive particles that are much more penetrating and deposit, in most cases, only a tiny amount of energy in the ECAL, such as hadrons. This shower in HCAL is produced by inelastic scattering, nuclear spallation, and electromagnetic interactions mentioned previously. The HCAL is installed inside the solenoid to ensure the best possible energy measurement material. The technical details of the two calorimetric systems are given below:

Electromagnetic calorimeter

The ECAL is a hermetic, homogeneous calorimeter which uses lead tungstate ($PbWO_4$)
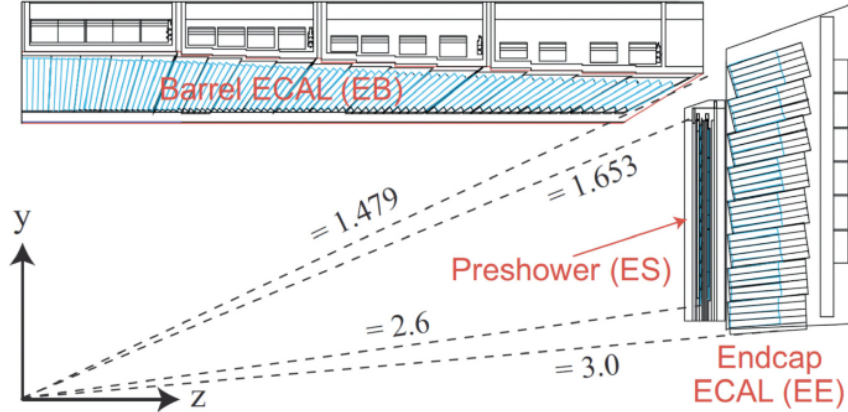
Figure 2.10: Longitudinal view of the quarter of ECAL [84].

crystals, which are opaque to x-ray light but transparent to visible light. These scintillating material have a relatively short radiation length ($X_0 = 0.89$ cm) and Moliére radius (2.2 cm) and low scinillating time (15 ns). The crystals are truncated pyramid-shaped and are grouped into towers with 5×5 crystals each. ECAL consists of 61200 crystals in the central barrel region and 7324 in each endcap. The detailed view of ECAL is shown in Fig. 2.10.

Avalanche Photodiodes (APDs) are utilised as photodetectors in the barrel section (EB) of the CMS ECAL. At the same time, Vacuum Phototriodes (VPTs) are used in the endcaps (EE) to handle the high-radiation density environment. To enhance π^0/γ discrimination, a pre-shower detector (ES) is installed in front of the endcap crystals. This detector, composed of two orthogonal layers of silicon micro-strip sensors, covers the pseudorapidity range $1.65 < |\eta| < 2.6$, improving particle identification before the particles reach the calorimeter.

The energy resolution of calorimeters is typically expressed as:

$$\left(\frac{\sigma_E}{E}\right)^2 = \left(\frac{S}{\sqrt{E}}\right)^2 + \left(\frac{N}{E}\right)^2 + C^2\,, \tag{2.1}$$

where S, N, and C represent the stochastic, noise, and constant terms, respectively.

- The stochastic term $S/\sqrt{E}$ arises from statistical fluctuations in shower development, photostatistics, and energy deposited in the pre-shower. For CMS, the measured value is $S \approx 2.8\% \, \mathrm{GeV}^{1/2}$.
- The noise term N/E results from electronics, digitisation, and pileup noise and is measured for the ECAL as $N \approx 12\% \, \mathrm{GeV}$.
- The constant term C accounts for factors such as light collection non-uniformity, inter-calibration errors, and leakage from the back of the calorimeter. For CMS, $C \approx 0.3\%$.

These values were determined in test beams, showing excellent agreement with measured resolutions in the energy range of 20 to 250 GeV.

Hadronic calorimeter
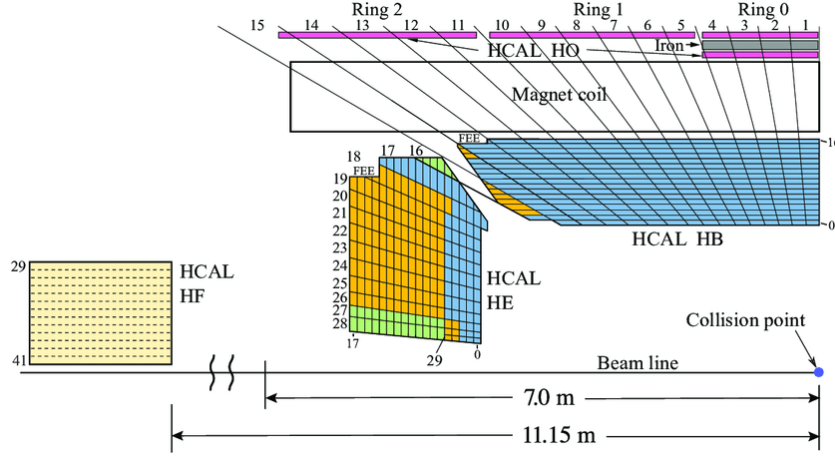
Figure 2.11: Longitudinal view of the quarter of HCAL [85].

The HCAL is constructed using layers of dense absorber material, such as brass or steel, interleaved with plastic scintillator tiles to capture hadrons. The light produced by the scintillators is collected through Wavelength Shifting (WLS) fibres and read out using Silicon Photomultipliers (SiPMs). The HCAL is divided into several sections: the Hadron Barrel (HB), Hadron Outer (HO), Hadron Endcap (HE), and the Hadron Forward (HF) calorimeters. The HB, which covers the pseudorapidity range $|\eta| < 1.3$, comprises brass absorbers arranged into 18 wedges, each weighing 26 tons, that form half a barrel. These halves are assembled into five rings to complete the entire barrel. Positioned outside the magnetic coil, the HO calorimeter captures most energy leakage from the HB. The HE calorimeter, which covers the pseudorapidity range $1.3 < |\eta| < 3.0$, also uses brass absorbers combined with plastic scintillators to sample energy. The HF calorimeter, covering the pseudorapidity range $3.0 < |\eta| < 5.2$, consists of Cherenkov detectors built from steel absorbers with quartz fibres running longitudinally through the material. The detailed view scheme of HCAL is shown in Fig. 2.11.

The resolution in HCAL varies significantly depending on the part of the detector. For the HB and HE, the coefficients in the Eq. (2.1) are around $S = 100\% \, \text{GeV}^{1/2}$ for the stochastic term and $C = 5\%$ for the constant term. In contrast, the noise term in the CMS HCAL energy resolution is often approximated as zero because its contribution is minimal. At the high energies typically measured by the HCAL, the noise from electronics, digitisation, and pileup becomes negligible compared to the signal. Additionally, the advanced design of the SiPMs and efficient signal processing techniques further reduce noise. For the HF, the coefficients in the Eq. (2.1) are $S = 170\% \, \text{GeV}^{1/2}$ for the stochastic term and $C = 10\%$ for the constant term.

2.2.4 Muon chambers

The CMS muon system [86] employs three types of gaseous detectors: Drift Tubes (DTs), Cathode Strip Chambers (CSCs), and Resistive Plate Chambers (RPCs), each optimised for specific regions of the detector.

The DTs are located in the barrel region ($|\eta| < 1.2$), where the magnetic field is relatively uniform and radiation levels are low. The DT system is organised into four concentric
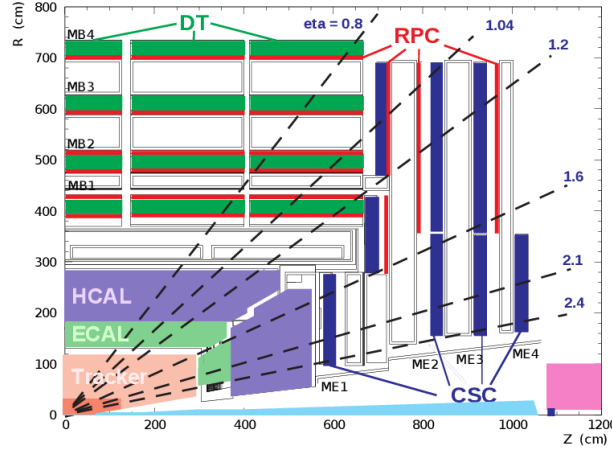
Figure 2.12: Layout of one quadrant of CMS. The four DT stations in the barrel (MB1-MB4, green), the four CSC stations in the endcap (ME1-ME4, blue), and the RPC stations (red) are shown [87].

cylindrical stations. Each station contains rectangular drift cells filled with a gas mixture of 85% Argon and 15% CO_2, providing a spatial resolution of approximately 100 μm. DTs measure muon tracks in both the bending plane (r-ϕ) and the longitudinal direction (z). Additionally, DTs contribute to the first-level muon trigger by delivering fast timing information and position measurements.

The CSCs are used in the endcap region ($0.9 < |\eta| < 2.4$), where the magnetic field is more substantial, less uniform, and has higher radiation levels. CSCs are multi-wire proportional chambers, each composed of six layers of anode wires interleaved with cathode planes and segmented into radial strips. This configuration provides high spatial resolution down to 75 micron in certain regions, such as ME1, and ensures excellent pattern recognition in high-radiation environments. The CSCs are critical in high-resolution 3D track reconstruction, precise timing, and triggering.

The RPCs operate in both the barrel and endcap regions, providing fast timing information with a time resolution of approximately 1 ns. The RPCs consist of double-gap parallel plates operating in avalanche mode and are primarily used for muon triggering. Six layers of RPCs are integrated with the DT system in the barrel, while in the endcap, they are paired with CSCs. The RPCs cover the pseudorapidity range up to $|\eta| < 1.6$ and are essential for identifying the correct bunch crossing and contributing to the first-level trigger system.

2.2.5   Trigger and data collection

Due to the high intensity of collisions at CMS, recording all the collision data is impossible due to the enormously high flow and size of information. However, not all events are relevant for physics purposes. Most events produced in proton-proton collisions at the LHC involve soft QCD interactions with little relevance to the primary research goals, obscuring the rare, high-energy interactions of interest. The trigger system [88, 89] is implemented to store events with potential signatures of interest. The CMS trigger system comprises two levels: the Level 1 (L1) trigger, implemented in custom hardware, and the High Level Trigger (HLT), a software-based system running on a processor farm.

The **L1 trigger** processes inputs from the calorimeters and muon detectors, identifying high-interest events such as leptons, photons, jets, and missing transverse energy (E_T^{miss}) within $4\,\mu$s. It consists of two main components for the calorimeter: the Regional Calorimeter Trigger (RCT), which handles regional information, and the Global Calorimeter Trigger (GCT), which calculates global quantities and classifies jets. The L1 system integrates data from DTs, CSCs, and RPCs for muons, using pattern recognition to form muon candidates with high redundancy and spatial accuracy.

The **HLT** utilises software algorithms to enhance the initial L1 data selection, further decreasing the data rate to $400\,$Hz for storage purposes. Operating on a farm of standard processors, the HLT reconstructs physics objects and applies advanced selection criteria similar to those used in offline analysis. It features builder and filter units that assemble events and carry out reconstruction and filtering on an event-by-event basis.

The complexity of the detector and the data collection process necessitated a flexible data model to meet the diverse needs of various physics analyses. Consequently, CMS data is organised into different tiers. The most important ones for end users are the RECO and AOD tiers. The RECO data tier includes a comprehensive set of reconstructed object information essential for analysis, while the Analysis Object Data (AOD) tier is a subset of RECO. It is optimised to provide the crucial information required for most CMS analyses, with a reduced data size of about $140\,$kB per event. Both formats are designed to balance performance and flexibility in reconstruction, although they are not ideally suited for direct end-user analysis.

A more analysis-friendly data format is derived from AOD, such as *MiniAOD*, which is designed to balance data size and physics content for efficient analysis. The typical data size for MiniAOD is $\sim 30 - 50\,$kB per event, significantly smaller than the original AOD. This format retains high-level reconstructed physics objects (e.g., electrons, muons, jets, and MET) while preserving some lower-level information, such as particle flow candidates and secondary vertices.

For even more compact storage and faster processing, *NanoAOD* is used, which contains only high-level reconstructed objects essential for final-stage statistical analyses. The standard *NanoAOD* size is $\sim 1 - 3\,$kB per event, making it highly suitable for large-scale physics studies where detailed event-level information is not required.

However, due to the necessity of precise information on jet constituents and the inclusion of the `DisTau` tagger output (described in Section 5), a customised NanoAOD format, *NanoAOD-distau*, is designed for the following analysis. This specialised format retains additional physics content while maintaining a compact structure, resulting in a typical size of $\sim 8 - 9\,$kB per event.

Chapter 3

Object reconstruction in CMS

This section describes the fundamentals of object reconstruction algorithms in CMS. Reconstruction algorithms at CMS are essential for transforming raw detector data into meaningful physics objects to be analysed. Various objects are targeted in CMS, covering a substantial phase space of possible particle physics analyses. In the current study, well-identified objects, i.e. leptons and jets, are used for various analysis regions. It is essential to highlight that while the reconstruction is reliable for prompt objects, the CMS detector also allows the reconstruction of displaced objects produced at a substantial distance from the centre of collisions. Hypothetical long-lived BSM particles might produce such particles, and the good reconstruction of their decay products is essential to study various hypothetical new-physics processes. The mechanisms used for object reconstruction in this analysis are described below.

3.1   Track reconstruction

When particles pass the silicon layers in the tracker, they create hits in the silicon. Each hit represents a spatial point where a particle passed through. The particle may pass through multiple adjacent pixels or strips, depositing charge in each one. Adjacent signals are combined into clusters of charge. After forming clusters, the position of the particle crossing point within the detector is estimated from the cluster properties [90]. Because track reconstruction is performed on the level of detector coordinates, it is essential to translate the local sensor coordinates of the hits into the global detector coordinate system. This mapping accounts for misalignment between the expected and actual position of the sensor, as well as deformation of the surface of the detector. This process is known as tracker alignment [91].

Track reconstruction in CMS is performed iteratively. Each iteration follows a four-step procedure. The first step is seeding, where initial track candidates, or seeds, are created to provide an estimate of the trajectory parameters. These proto-candidates are then propagated through the tracker layers using a Kalman filter, identifying compatible hits at each layer and updating the track parameters in a building process. Afterwards, tracks are fitted by combining all associated hits to refine their parameters, and finally, they undergo a selection process where quality criteria are checked to identify reliable tracks.

The key aspect of track building involves recognising patterns and constructing a candidate trajectory by selecting its hits from all hits in the event. The combinatorial Kalman

filter (CKF) in track reconstruction is an iterative algorithm that estimates a particle's trajectory by propagating an initial seed through detector layers. At each layer, it predicts the track's location and searches for compatible hits within a defined window. When a hit is found, it is added to the trajectory, refining the track parameters and reducing uncertainty. If multiple hits are compatible, multiple candidates are created, but only the best are retained based on quality criteria. The process continues until stopping conditions are met, providing an optimised track estimate that balances measurement precision with material effects. The illustration of the building step is shown in Fig. 3.1.
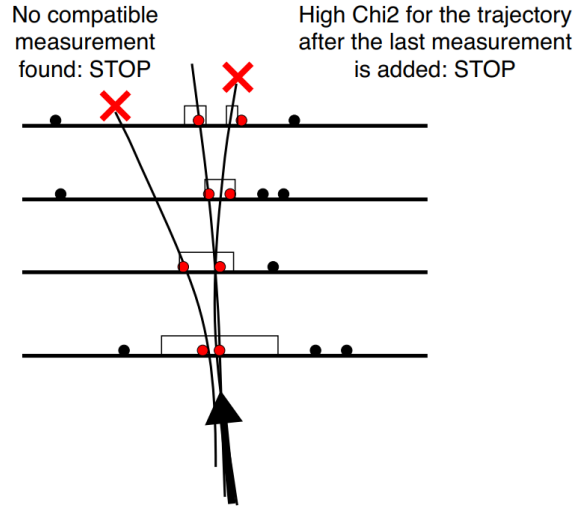
Figure 3.1: The building of the track based on the hits' compatibility with the predicted trajectory [92].

In 2017, the track reconstruction algorithms were updated [93] to leverage the upgraded pixel detector's improved features and an increased number of tracks originating from the pileup interactions. The seeding procedure was updated using the cellular automation technique [94] to create track seeds. As was mentioned before, tracking in CMS is performed iteratively. Each iteration has its specific seed and targets different signatures going from the centre to the outer layers, progressively reducing the number of hits to analyse. In the context of long-lived particles, the essential iteration steps that form the track seeds are based on the triplets in the TIB, TIDs and TECs layers (PixelLess iteration), as well as triplets and hit pairs in the TOB and TEC parts of the strip detector (TobTec iteration). This step potentially increases sensitivity to the particles whose decay vertices are significantly displaced from the centre of the detector over a distance of 10-60 cm. The description of each iteration step is given below:

1. **Initial step**: Targets high-p_T tracks originating very close to the interaction point, using four hits in the pixel detector to constrain the track's direction and ensure quick and accurate reconstruction.

2. **HighPtTriplet**: Similar to the initial step but using three-pixel hits instead of four, it can recover tracks where one hit may be missing while still focusing on high-p_T tracks produced close to the beamline.

3. **LowPtQuad**: Similar to the initial step, this iteration loosens the p_{T} threshold, aiming to capture lower-p_{T} tracks but requiring four pixel hits.

4. **LowPtTriplet**: This iteration also targets low-p_{T} tracks but require only three-pixel hits, following a similar configuration as **HighPtTriplet**, with a focus on capturing tracks with smaller p_{T}.

5. **DetachedQuad**: Uses four-pixel hits and allows for more significant displacement from the interaction point, targeting tracks that originate moderately far from the primary vertex (PV).

6. **DetachedTriplet**: Complements the **DetachedQuad** iteration, using three hits and focusing on tracks with slight displacement from the PV.

7. **PixelPair**: Pairs of pixel hits are constrained by known PV positions to reconstruct tracks in regions where inactive pixel modules overlap. This helps recover tracks that may otherwise be missed due to detector gaps.

8. **MixedTriplet**: Designed for moderately displaced tracks, using combinations of hits from both the inner pixel layers and the first layers of the strip detector, thereby improving tracking for particles decaying further from the vertex.

9. **PixelLess**: Targets highly displaced tracks that may not produce hits in the pixel detector, instead using hits in the strip detector for seed formation.

10. **TobTec**: Focuses on reconstructing highly displaced tracks using both hit triplets and hit pairs within the outer strip detector (TOB and TEC), ensuring coverage for tracks originating far from the PV.

11. **JetCore**: Restricts tracking to regions around high-energy jets (over $100\,\mathrm{GeV}$), using narrow search windows in η-ϕ space. This iteration helps reconstruct dense track environments within jets.

12. **Muon inside-out**: Aims to improve the precision of muon tracks by using information from muon detectors to refine track parameters, especially for muons with $p_{\mathrm{T}} > 2\,\mathrm{GeV}$. If the muon track can match a pre-existing track in the inner detector, the track is refit with looser constraints, potentially improving accuracy.

13. **Muon outside-in**: For high-p_{T} muons ($p_{\mathrm{T}} > 10\,\mathrm{GeV}$) detected in the muon system, seeds are formed in the outer layers of the tracker and then propagated inward. The first three outer layers need up to three hits each to generate seeds, facilitating the initial stages of pattern recognition.

After the construction of the tracks, ensuring that only high-quality tracks are used for analysis is essential. Track candidates are evaluated based on criteria such as the number of layers with hits, the goodness of fit (χ^2/dof), and their compatibility with the PV. Initially, a "loose" selection filters out poor candidates. This is followed by "tight" and "high-purity" selections, where progressively stricter criteria are enforced. Additional constraints on transverse and longitudinal impact parameters enhance selection reliability,

especially under high-luminosity conditions. These selection criteria collectively minimise fake tracks and improve precision.

The efficiency of reconstructing tracks from t$\bar{\text{t}}$ events is illustrated in Fig. 3.2. Efficiency is defined as the ratio of matched reconstructed tracks to the total number of simulated tracks. For a reconstructed track to be considered a match with a simulated track, more than 75% of the hits on the reconstructed track must originate from the simulated track. The corresponding MC study demonstrates the importance of PixelLess and TobTec iterations for reconstructing displaced tracks.
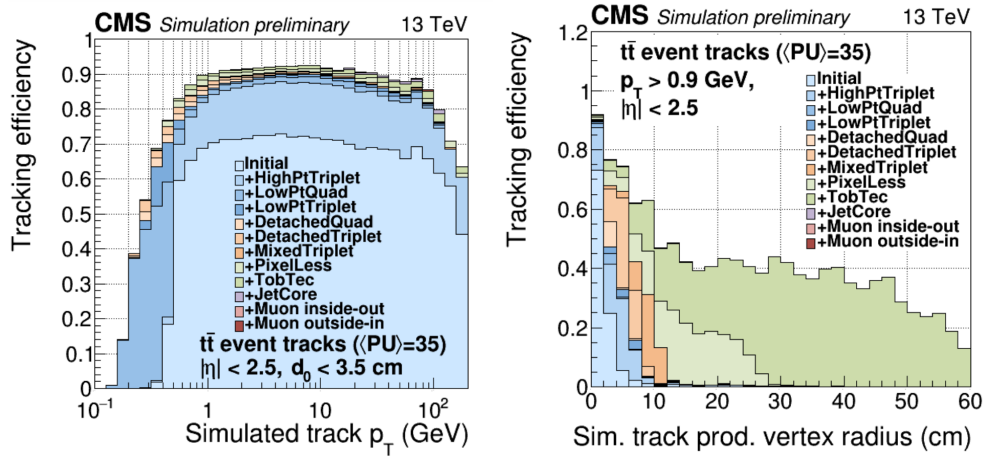
Figure 3.2: Track reconstruction efficiency per tracking iteration as a function of simulated track p_{T} (left) and the simulated track production vertex (right) for the Phase-1 tracker [95].

A comparison of tracker performance at different pileup levels is shown in Fig. 3.3 to demonstrate the robustness of the tracking technique. This demonstrates reliable data quality even as pileup increases in high-luminosity environments. The fake rate is the number of non-matched reconstructed tracks divided by the total number of reconstructed tracks. This demonstrates a potential increase in background fake rates for a case of high-impact parameters, which is expected for displaced vertices.

3.2 Vertex Reconstruction in CMS

Vertex reconstruction in CMS aims to determine the precise positions of all proton-proton interaction points (vertices) within an event. After tracks are selected according to the aforementioned procedure, two additional steps are performed: track clustering and vertex fitting.

Selected tracks are clustered based on their z-positions. It uses the deterministic annealing (DA) algorithm for track clustering. The DA algorithm iteratively minimises an energy function E, which considers both track proximity and track weight, helping to identify multiple vertices in high-pileup conditions. The energy function is:

$$E = \sum_i w_i \cdot \exp\left(-\frac{(z_i - z_{\text{vertex}})^2}{2\sigma_z^2}\right) ,$$
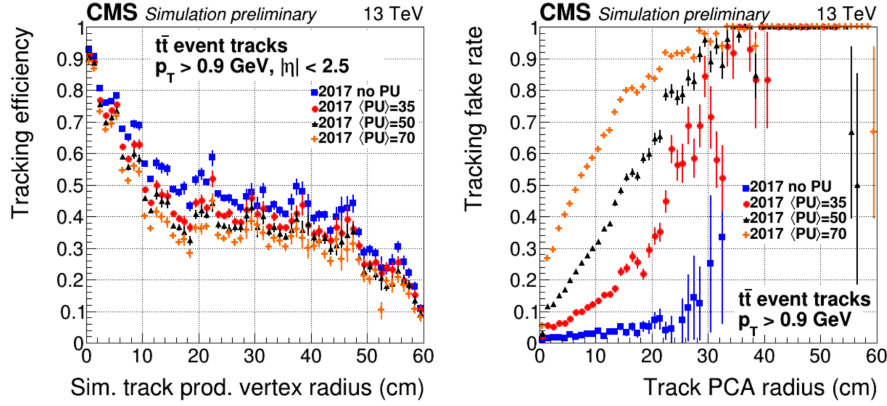
Figure 3.3: The efficiency of track reconstruction is analysed based on the simulated track production vertex radius (left), while the fake rate is examined with respect to the radius of the point of closest approach to the beamline of the reconstructed track (right). This analysis is conducted for the Phase-1 tracker under various pileup conditions [95].

where w_i is the weight for each track i, z_i is the track's z-position, z_{vertex} is the estimated vertex position, and σ_z is the uncertainty in the z-direction. The DA algorithm's annealing schedule adjusts these weights to balance the precision of vertex resolution with the separation of nearby vertices.

For each cluster of tracks, the final vertex position is determined using a vertex fitting algorithm, often with adaptive weights for each track to improve robustness. The vertex position $\vec{V} = (x, y, z)$ is obtained by minimizing the sum of squared residuals:

$$\chi^2 = \sum_i w_i \left(\frac{(\vec{r}_i - \vec{V})^2}{\sigma_i^2} \right),$$

where $\vec{r}_i$ is the position of track i at its point of closest approach, and σ_i is the uncertainty in the track position. This fitting procedure defines the 3D vertex location with typical uncertainties of 10–12 micron for high-multiplicity events.

The secondary vertex (SV) associated with long-lived particles is computed with selection variations, particularly regarding impact parameter criteria. While deterministic annealing can also be used to cluster tracks for SV, searching for clusters significantly displaced from the PV undergoes adaptation to identify tracks that deviate considerably from the primary interaction region.

3.3 Calorimeter clustering

To use information from the HCAL and ECAL calorimeters, it is essential to turn raw, distributed signals into higher-level objects. For this purpose, clustering [96, 97] is used with further calibration and noise suppression, aiming for a precise estimation of the energy and position of the deposited particle.

The clustering algorithm in ECAL starts by forming a "basic cluster" around the local maxima of the energetic deposit. A supercluster (SC) is formed by adding "basic clusters" along ϕ to account for radiation spread due to the magnetic field. Various corrections are

applied to account for geometry, material effects, and differences between electron and photon showers. Due to the differing geometric arrangements of crystals in the barrel and endcap regions, distinct clustering algorithms are applied to each region [60].

For the clustering in HCAL, similar to ECAL, high-energy cells are identified as seeds. Neighbouring cells around the seed are added to the cluster if they meet specific energy and spatial continuity criteria. In the HCAL, various depths or layers are combined to capture the entirety of the hadronic shower, accounting for the broad distribution of energy that occurs in these showers. After this, energy scale calibrations based on isolated hadrons are implemented, considering the nonlinearities in their response, ensuring accurate energy measurements for particles passing through the calorimeter.

3.4   The particle flow algorithm

In CMS, the particle-flow algorithm (PF) algorithm [98] converts tracks and clusters obtained from previous steps into physics objects. This algorithm is an essential step in reconstructing stable, final-state particles.

The algorithm starts with a procedure called linking. This procedure connects PF objects, such as inner tracks, preshower, ECAL and HCAL energy clusters and muon system information into PF blocks. The algorithm tests any pairs of PF elements to determine if they originate from the same particle. The pairs of elements evaluated by the link procedure are limited to the nearest neighbours within η and ϕ coordinates, which are considered to reduce computational complexity. For the linking, a k-dimensional tree [99] is used. The conditions needed to connect two elements depend on the object's nature. A jet consisting of five particles is illustrated in Fig. 3.4, detailing their paths, energy deposits in the ECAL and HCAL, and the associated reconstructed clusters and tracks.
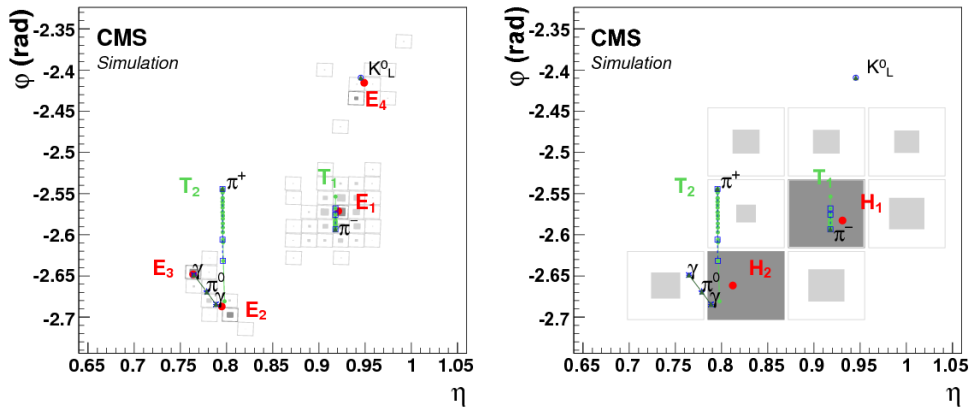
Figure 3.4: An example of five particles shown on the ECAL (bottom left) and HCAL (bottom right) surfaces in the (η, ϕ) plane. The K_L^0 and π^-, along with photons from the π^0 decay, form four distinct ECAL clusters labelled $E_{1,2,3,4}$, while the π^+ leaves no ECAL cluster. The charged pions create tracks $T_{1,2}$, shown as vertical lines in the (η, ϕ) view, pointing to HCAL clusters $H_{1,2}$. ECAL and HCAL cells are displayed as squares with shading proportional to the logarithm of cell energy. Cluster positions are marked by dots, simulated particles by dashed lines, and their calorimeter impacts by open markers.

After linking, the algorithm identifies the particles based on the established blocks.

1. **Photons**, such as those from π^0 decays or electron bremsstrahlung, are identified as energy clusters in the ECAL that are not associated with the extrapolation of any charged particle trajectory to the ECAL.

2. **Electrons**, such as those resulting from photon conversions in the tracker material or semileptonic decays of B hadrons, are identified as primary charged particle tracks. These electrons may also correspond to several energy clusters in the ECAL, which are linked to the track's extrapolation into the ECAL and to any potential bremsstrahlung photons emitted while passing through the tracker material.

3. **Muons** from hadron semileptonic decays are identified as tracks in the central tracker. These tracks are consistent with either a single track or multiple hits in the muon system and are associated with calorimeter deposits that are compatible with the muon hypothesis.

4. **Charged hadrons** are identified as charged particle tracks that are neither classified as electrons nor as muons.

5. **Neutral hadrons** are identified as energy clusters in the HCAL that are not linked to any charged hadron trajectories or as a combined excess of energy in the ECAL and HCAL beyond what is expected from the charged hadron energy deposit.

The energy of photons is measured using the ECAL. For electrons, energy is calculated by combining the track momentum at the primary interaction vertex, the energy from the ECAL cluster, and the total energy of all bremsstrahlung photons associated with the track. The energy of muons is determined solely based on their track momentum. For charged hadrons, energy is determined by combining track momentum with the energies from both ECAL and HCAL, with corrections applied based on how the calorimeters respond to hadronic showers. Finally, the energy of neutral hadrons is derived from the corrected energies provided by both the ECAL and HCAL.

3.5 Electron and photon reconstruction

Both electrons and photons deposit most of their energy in ECAL. Electrons and photons can mutually convert through bremsstrahlung or e^+e^- pair production as they move through the tracker layers. Because of the magnetic field, this cascade of particles is spread in the ϕ direction. As mentioned in Section 3.3, clusters in ECAL are connected within SC to merge the particle and associated radiation. The illustration of the SC in ECAL is shown in Fig. 3.5.

The track is reconstructed using a dedicated Gaussian Sum Filter (GSF) [101] tracking algorithm to account for energy loss due to the radiation. Then, electron reconstruction begins with a seeding step, which can be ECAL-driven or tracker-driven.

1. The ECAL-driven seeding: superclusters are matched to track seeds by ensuring spatial consistency in the barrel and forward tracker regions.
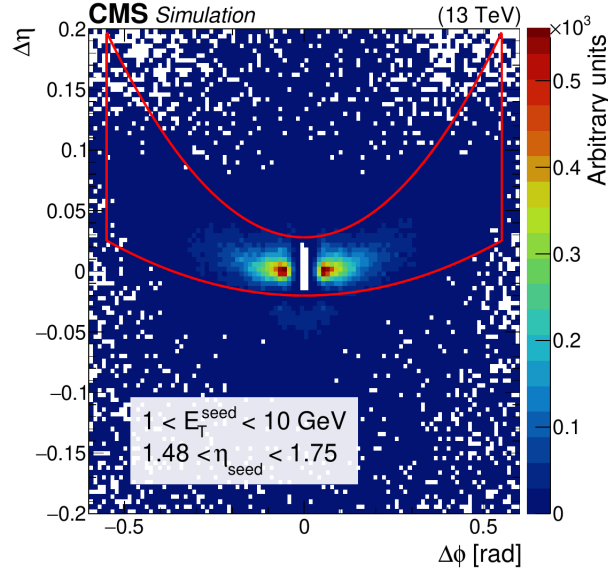
Figure 3.5: Distribution $\Delta\eta = \eta_{\text{seed-cluster}} - \eta_{\text{cluster}}$ versus $\Delta\phi = \phi_{\text{seed-cluster}} - \phi_{\text{cluster}}$ for simulated electrons with $1 < E_{\text{T}}^{\text{seed}} < 10\,\text{GeV}$ and $1.48 < \eta_{\text{seed}} < 1.75$. The shape of the supercluster selected by the moustache algorithm is shown with the red contour [100].

    2. Tracker-driven seeding: starts with the generic track in the inner tracker, which is then matched to ECAL clusters.

The ECAL-driven seeding is effective for high-energy electrons, while the tracker-driven allows the recovery of low-p_{T} and non-isolated electrons.

Photon reconstruction begins directly with energy deposits in the ECAL. Clusters in the ECAL are grouped into superclusters using the moustache algorithm, which captures all energy deposits related to the photon and its possible conversions. In photon conversion to e^+e^- pairs, the conversion recovery algorithm links the secondary tracks to the photon supercluster to ensure accurate energy measurement. Photons are then identified based on their isolation in the ECAL and the absence of associated hadronic or tracker activity.

Electron and photon identification uses cut-based and boosted decision tree (BDT) techniques for background rejection. The cut-based method uses variables like shower shape, isolation, and the ratio of energy deposited in the hadronic calorimeter to that in the electromagnetic calorimeter. Electron identification includes additional checks like track-cluster matching in the electromagnetic calorimeter. Photon identification focuses on isolation and shower shape to distinguish prompt photons from those originating from meson decays.

3.6 Muon reconstruction

Muon reconstruction in CMS is performed independently in different subdetectors [102]. Three major reconstruction approaches are utilized [103, 104]:

- **Standalone Muons:** These are reconstructed solely from hits in the muon system. Using the hit patterns in the muon chambers, tracks are identified and

fitted, with their momentum estimated from the track curvature in the magnetic field. While this method provides the initial reconstruction, its resolution is less precise compared to combined approaches.

- **Global Muons:** Tracks from the muon system are matched to those reconstructed in the silicon tracker. A combined fit is performed, integrating hits from both the tracker and the muon system, significantly enhancing the resolution and quality of the reconstructed tracks. This method is particularly effective for high-p_T muons, where the additional lever arm of the muon system improves the precision.

- **Tracker Muons:** Reconstructed using only silicon tracker hits, these muons are identified if their tracks extrapolate to a consistent pattern in the muon system or meet specific quality criteria. This approach is particularly effective for low-p_T muons or in regions where the muon system coverage is incomplete.

In addition to reconstruction, muon identification is used to reduce background faking muons, ensuring accurate classification for physics analyses. The process utilises the quality of reconstructed trajectories and specific muon properties, such as their compatibility with hits in the inner tracker and muon chambers, as well as the overall fit quality of the global track.

The Muon ID involves several key criteria:

- The number of hits recorded in the inner tracker and muon chambers.
- The degree of matching between the inner tracker and standalone muon tracks.
- The goodness-of-fit (χ^2) of the reconstructed track.

An important component of muon identification is isolation, which quantifies the activity of other particles around the muon. This is evaluated in a cone of $\Delta R = 0.4$ around the muon direction. The relative isolation (I_rel^μ) is defined as:

$$I_\mathrm{rel}^\mu = \frac{\sum E_T(\mathrm{charged}) + \max\left(\sum E_T(\mathrm{neutral}) - 0.5\sum E_T(\mathrm{charged, PU}), 0\right)}{p_T^\mu} \,,$$

where p_T^μ is the transverse momentum of the muon, $\sum E_T(\mathrm{charged})$ represents the transverse energy of charged hadrons within the isolation cone, $\sum E_T(\mathrm{neutral})$ includes contributions from neutral hadrons and photons, $\sum E_T(\mathrm{charged, PU})$ accounts for pileup contributions from charged particles. To correct for pileup effects, the neutral energy term is reduced by $0.5\sum E_T(\mathrm{charged, PU})$. Any negative values resulting from this correction are set to zero using the max function, ensuring that the isolation remains physically meaningful.

CMS employs several working points (WPs) for muon identification, tailored to different track quality and analysis requirements:

- **Loose Muon ID:** A basic selection identifying muons using either the tracker or global reconstruction algorithms.
- **Medium Muon ID:** Extends the loose selection by requiring hits from at least 80% of the layers traversed by the muon track in the inner tracker.

- **Tight Muon ID:** A stricter criterion based on the medium ID, requiring at least six hits in the inner tracker (including one in the pixel detector) and imposing constraints on the transverse and longitudinal impact parameters (d_0 and d_z).

These working points allow for flexibility in analysis, balancing efficiency and purity. For instance, the tight muon ID is optimised for high-purity samples required in precision measurements and rare process searches.

3.7 Jets

Quarks and gluons cannot exist as free particles and undergo hadronisation and fragmentation processes. When quarks or gluons have substantial momentum, they create a collimated spray of secondary particles, named **jet**. Corresponding jet objects can be reconstructed using a clustering algorithm that groups final-state particles. Such an algorithm must satisfy two fundamental requirements:

1. *Infrared safety:* In QCD, soft gluon emission can occur at any stage of a particle showering. If reconstructable jet properties were sensitive to such radiation, this would make the calculation physically meaningless because such emissions are unavoidable. The requirement of not being sensitive to adding or removing a very soft particle is called *infrared safety.*

2. *Collinear safety:* During the showering, particles can split into nearly collinear pairs. For instance, a quark can radiate a gluon or a gluon can split into two gluons. The resulting calculation of jet properties should not be sensitive to these collinear splittings. The corresponding requirement is called *collinear safety.*

This study used hadronic jets clustered with the infrared and collinear safe anti-k_T algorithm [105, 106] with a distance parameter of 0.4. The algorithm clusters PF candidates described in Section 3.4. The algorithm operates iteratively, following these steps:

1. Estimate the distance of each possible pair of particles d_{ij} and the distance to the beamline d_{iB}. The particle-particle distance parameter d_{ij} has the following form:

$$d_{ij} = \min\left(\frac{1}{p_{\mathrm{T},i}^2}, \frac{1}{p_{\mathrm{T},j}^2}\right) \frac{\Delta R_{ij}^2}{R^2}, \qquad (3.1)$$

   where R is the jet radius parameter, $\Delta R_{ij}^2 = (\eta_i - \eta_j)^2 + (\phi_i - \phi_j)^2$ is the squared distance between particles i and j in (η, ϕ) space, $p_{\mathrm{T},i}$ is the transverse momentum of the particle i. The distance of the particle to the beamline is represented as follows:

$$d_{iB} = \frac{1}{p_{\mathrm{T},i}^2}. \qquad (3.2)$$

2. Start with the smallest distance, if the distance is $d_{ij} < d_{iB}$, particles are merged into a single "proto-jet" by summing their momenta. If the smallest distance $d_{ij} > d_{iB}$, particle i is declared the final jet and removed from the list.

3. The process is repeated until no particles remain to merge.

Jets created with corresponding clustering algorithms for $R = 0.4$ are called *AK4 PFJets*, as they are made from the PF candidates. However, applying this algorithm to the raw list of PF candidates does not consider that a certain partition of the particles in the jet does not come from the initial quark or gluon of interest but from the pileup particles.

3.7.1 Charged Hadron Subtraction

The Charged Hadron Subtraction (CHS) [107] is a method designed to reduce the impact of pileup interactions on reconstructed jets. Typically, near $\sim 65\%$ of the jet components in CMS are charged hadrons. This approach aims to reduce pileup by identifying and removing charged particles linked to pileup vertices while keeping neutral particles and charged particles originating from the PV.

The process begins by reconstructing charged hadron tracks. The PV is selected based on the sum of the squared transverse momenta of associated tracks ($\sum |p_{\mathrm{T}}^{\mathrm{TRK}}|^2$), while additional vertices are classified as pileup. Track-to-vertex associations are determined using a $\chi^2/\mathrm{d.o.f.}$ criterion, where tracks with a good fit ($\chi^2/\mathrm{d.o.f.} < 20$) are linked to their corresponding vertex. Any tracks assigned to pileup vertices are excluded from further analysis in the CHS procedure. All other tracks are kept, including those not associated with any PV. Neutral particles also stay untouched, and their contribution must also be considered. This ensures that pileup effects are significantly mitigated, allowing for a cleaner reconstruction of jets originating from the primary hard-scatter event. Such jets are named *AK4 CHS PFJets* and are essential components of the analysis described in this thesis.

3.7.2 Pileup per particle identification

The pileup per particle identification (PUPPI) algorithm [77, 108] mitigates pileup effects at the particle level by assigning weights to individual particles based on local shape information, event pileup properties, and tracking data. A local shape variable distinguishes between collimated distributions, typical of particles from the hard scatter, and diffuse distributions, associated with pileup. Each particle is assigned a "pileup weight", which indicates the probability of the particle being associated with a pileup. This weight might be particularly important for jet identification information. Therefore, it is actively used in the study, which is described in further chapters. To perform clustering based on the PUPPI algorithm, charged particles from pileup vertices are removed. In contrast, neutral particle momenta are rescaled based on their probability of originating from the PV, calculated using nearby charged particles within the tracker acceptance ($|\eta| < 2.5$) and both charged and neutral particles in forward regions. Unlike CHS, which only removes charged pileup particles, PUPPI addresses both charged and neutral pileup contributions, improving the reconstruction of physics objects like jets and missing transverse energy in

high-pileup conditions [77]. Jets clustered based on the PUPPI algorithm are called *AK4 PUPPIJets.*

3.7.3 Jet Energy Correction

The reconstructed four-momentum of a jet is calculated by summing the momenta of its PF constituents. However, corrections must account for systematic and statistical uncertainties, such as pileup effects and detector response [109, 110]. Pileup corrections used the PUPPI method, where the offset energy is subtracted based on the jet area multiplied by the pileup energy density (ρ). Further corrections, collectively called Jet Energy Scale (JES) corrections, address the calorimeter's nonlinear response, detector nonuniformities, and discrepancies between data and simulation.

Finally, simulated jets are adjusted with Jet Energy Resolution (JER) corrections to match the resolution observed in the data. These steps ensure consistent jet energy reconstruction for precision physics analyses.

3.7.4 Jet identification

The purpose of jet identification is to discriminate genuine jets, originating from quarks, gluons, or tau leptons in the primary hard-scatter interaction, from spurious jets resulting from non-collision backgrounds, pileup events, or detector-related artifacts Additional, optional criteria are required to avoid electrons or muons being misidentified as jets, called *lepton veto.*

For AK4 CHS PFJets, the efficiency of jet identification is more than 98-99% for all η regions, whereas the background rejection is more than 98% for $|\eta| < 3$. The tight identification criteria for *AK4 CHS PFJets* for the jets $|\eta| \leq 2.6$ are as follows:

- Neutral hadron fraction: the fraction of the energy absorbed in the HCAL with respect to the total energy is < 0.90.

- Neutral EM fraction: the fraction of the energy absorbed in the ECAL with respect to the total energy is < 0.90.

- Number of constituents: required to be > 1.

- Muon fraction: the fraction of the energy absorbed in the muon detector with respect to the total energy is required to be < 0.8. This criterion is part of the *Lepton Veto* and applies optionally.

- Charged hadron fraction: the fraction of the energy carried by charged hadrons with respect to the total energy is required to be > 0.

- Charged multiplicity: the number of reconstructed charged particles is required to be > 0.

- Charged EM fraction: the fraction of the energy absorbed in ECAL by charged particles with respect to the total energy is required to be < 0.8. This criterion is part of the *Lepton Veto* and applies optionally.

3.8 Missing transverse momentum

In pp collisions at the LHC, the colliding protons are highly boosted along the beam axis, with their momenta being almost entirely longitudinal, with no net momentum expected in the transverse plane at the parton level. The missing transverse momentum ($\vec{p}_\mathrm{T}^{\mathrm{miss}}$), is an observable that indicates the momentum imbalance of the collision products in the transverse plane. It is defined as the negative vector sum of the transverse momenta of all PF candidates in an event:

$$\vec{p}_\mathrm{T}^{\mathrm{miss}} = -\sum_i \vec{p}_{\mathrm{T},i}\,,$$

where $\vec{p}_{\mathrm{T},i}$ represents the transverse momentum of the i-th PF candidate. $p_\mathrm{T}^{\mathrm{miss}}$, which is calculated based on all PF candidates, is called *raw* p_T^{miss}. A nonzero $p_\mathrm{T}^{\mathrm{miss}}$ indicates the presence of undetected particles, such as neutrinos or potential new particles BSM. The variable plays a significant role in dark matter searches or R-Parity conserved SUSY when the LSPs cease a significant amount of $p_\mathrm{T}^{\mathrm{miss}}$.

Due to its sensitivity to various detector effects and additional soft activity, the measured raw $p_\mathrm{T}^{\mathrm{miss}}$ systematically deviates from the genuine $p_\mathrm{T}^{\mathrm{miss}}$ of the process. Among various reasons are the non-compensating nature of the calorimeters, detector misalignment and the pileup effects. Corrections are applied to make measured $p_\mathrm{T}^{\mathrm{miss}}$ a better estimate of genuine $p_\mathrm{T}^{\mathrm{miss}}$.

Pileup interactions usually have few non-detectable particles, e.g. neutrinos from Kaon decay, therefore small $p_\mathrm{T}^{\mathrm{miss}}$. If we could measure all visible particles accurately and precisely, pileup interactions would not significantly affect the reconstruction of $p_\mathrm{T}^{\mathrm{miss}}$. However, in reality, our measurements of visible particles are imperfect, and as the number of pileup interactions increases, the quality of $p_\mathrm{T}^{\mathrm{miss}}$ reconstruction deteriorates. The Type-0 correction mitigates pileup effects on the $p_\mathrm{T}^{\mathrm{miss}}$ by removing contributions charged and neutral particles associated with pileup interactions defined by the CHS method. Since CHS defines only charge hadrons associated with pileup, the contribution from the neutral component is calculated under the assumption of negligible genuine $p_\mathrm{T}^{\mathrm{miss}}$ in pileup interactions.

The Type-1 correction propagates jet energy correction (JEC) to $p_\mathrm{T}^{\mathrm{miss}}$ to account for miscalibrations in jet momenta. It replaces the raw jet momentum ($\vec{p}_T^{\mathrm{jet,\ raw}}$) with the corrected jet momentum ($\vec{p}_T^{\mathrm{jet,\ JEC}}$):

$$\vec{p}_\mathrm{T}^{\mathrm{miss,Type\text{-}1}} = \vec{p}_\mathrm{T}^{\mathrm{miss,raw}} + \sum_{\mathrm{jets}}\left(\vec{p}_T^{\mathrm{jet,\ raw}} - \vec{p}_T^{\mathrm{jet,\ JEC}}\right)\,.$$

In the CMS data, special noise filters are used to avoid using data with various pathological detector and reconstruction conditions [111]. These noise effects significantly impact the $p_\mathrm{T}^{\mathrm{miss}}$ estimation and can lead to overestimation. In the analysis data presented in this thesis, the following filters are used [112]:

- *PV Filter*: Requires at least one well-reconstructed PV.
- *Beam Halo Filter*: Identifies events that are contaminated by beam halo (where stray particles graze the detector).

- *HBHE Noise Filter*: Rejects events with anomalous noise in the HCAL barrel or endcap (HB/HE) regions, typically arising from electronics or photodetector issues and can mimic real energy.

- *HBHE Iso Noise Filter*: Rejects isolated noise patterns in the HB/HE. It uses isolation-based criteria to remove spurious calorimeter signals that would otherwise degrade the $p_{\mathrm{T}}^{\mathrm{miss}}$.

- *ECAL Dead Cell Trigger Primitive Filter*: Identifies events with problematic ECAL cells that can lead to large misreconstructions of energy and bias the $p_{\mathrm{T}}^{\mathrm{miss}}$.

- *Bad PF Muon Filter*: Removes events containing misreconstructed PF muons, which can create large fake $p_{\mathrm{T}}^{\mathrm{miss}}$.

- *Bad PF Muon Dz Filter*: An additional check for problematic PF muons, focusing on suspicious track z positions.

- *HF Noisy Hits Filter*: Targets spurious signals in the forward hadron calorimeter (HF), removing fake energy deposits in the forward region that would skew the $p_{\mathrm{T}}^{\mathrm{miss}}$.

- *ee Bad SC Filter*: Removes events with problematic superclusters in the ECAL endcap region.

- *ECAL Bad Calibration Filter*: Removes events affected by ECAL miscalibrations. Prevents large fake energy deposits originating from specific problematic crystals.

These filters allow the selection of only events with reliable $p_{\mathrm{T}}^{\mathrm{miss}}$ calculations.

Chapter 4

Prompt tau reconstruction and identification at CMS

The tau lepton (τ) is one of the fundamental particles in the SM that plays a crucial role in various phenomena critical to our understanding of the Universe's fundamental constituents. As the heaviest of the leptons, the τ has unique interactions and decay mechanisms, making it an excellent probe for testing the SM and exploring physics BSM. Various BSM theories, such as Supersymmetry [6], Extra Dimensions [113], Little Higgs Models [114], and others [115, 116], posit the existence of new particles and interactions that could manifest through decays to τ leptons. The ability to accurately reconstruct and identify τ leptons is crucial for high-energy physics experiments, particularly in environments with high-intensity particle collisions such as those produced by the LHC.

This chapter explores the advanced techniques for reconstructing and identifying τ leptons at CMS. Detecting and analysing the decay products of τ leptons is challenging due to the τ's short lifetime and the various ways it can decay, including both leptonic and hadronic channels. These challenges are intensified by the necessity to distinguish genuine τ leptons from fakes in a crowded particle environment. Furthermore, the chapter outlines my contribution to the state-of-the-art machine learning-based identification of hadronically decaying τ leptons (τ_{h}) in the CMS experiment, called the DeepTau algorithm [8]. It will detail the sophisticated data pre-processing, training techniques and domain adaptation methods, which have substantially enhanced the classification efficiency and minimised the discrepancies in predicted score distributions between data and simulation.

4.1 Tau lepton properties

On August 24, 1975, the first evidence for an anomalous lepton production in e^+e^- annihilation experiments at the Stanford Linear Accelerator Center (SLAC) was reported by Martin L. Perl et al. [117]. At the first four π detector, MARK I, covering nearly all directions around the collision point, many two-prong events were observed. This included events with e^+e^-, $\mu^+\mu^-$, two-prong hadrons, and eventually the $\mu^\pm e^\mp$ final state. A detailed kinematic study of the coplanarity angle, as well as kinematic selection of the muons and electrons, resulted in the suppression of events with genuine e^+e^-, $\mu^+\mu^-$ in the final state, as well as reduction of the contribution of fake electrons and muons.

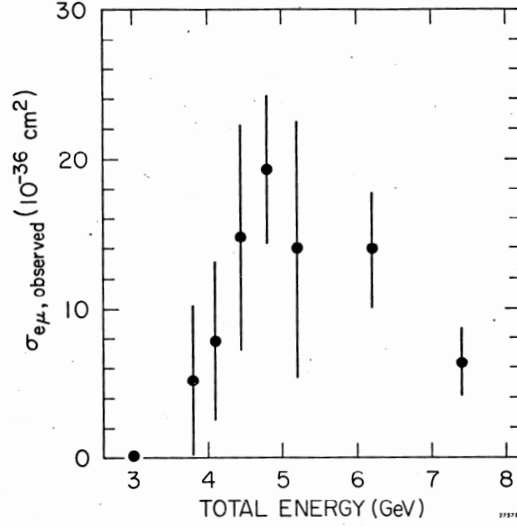The cross-section measurement of the $e^+e^- \rightarrow \mu^+ + e^- + \geq 2$ "undetectable particles"

Figure 4.1: The observed cross-section for the signature of $e\mu$ events [117]. The first observation of τ lepton.

is shown in Fig. 4.1. A further study of background sources, which consisted of lepton backgrounds and dominantly hadrons misidentified or decaying into leptons, demonstrated that the significance of the observation is beyond the scope "that can be explained either by the production and decay of any presently known particles or as coming from any of the well-understood interactions" [117]. The total number of observed events was 86, with 22 events expected from the background contribution. After observing these phenomena, it was inferred that the possible explanation was the production and decay of a pair of new particles, each with a mass in the range of 1.6 to 2.0 GeV. These particles were called *tau*.

Today, the τ lepton is known as a third-generation charged lepton in the SM of particle physics [118]. Its discovery confirmed the existence of a third lepton generation. The primary characteristics of the τ lepton are outlined below:

- **Mass**: Approximately 1776.86 ± 0.12 MeV [118], making it significantly heavier than the electron (0.511 MeV) and the muon (105.7 MeV).

- **Charge**: ± 1 elementary charge, similar to the electron and muon.

- **Lepton number**: The tau lepton (τ^-) has a tau lepton number (L_τ) of $+1$, while the tau antilepton (τ^+) has a tau lepton number of -1.

- **Lifetime**: The tau lepton has a proper lifetime of $\tau_0 = (290.3 \pm 0.5) \times 10^{-15}$ s. No significant difference has been observed in the lifetimes of τ^- and τ^+. For the typical value of $p_{\mathrm{T}} \approx 35$ GeV the travel distance can be estimated as $\lambda_\tau = \beta \cdot \gamma \cdot c \cdot \tau_0 \approx 19.72 \cdot 0.087$ mm ≈ 1.7 mm.

- **Spin**: $1/2$, classifying it as a fermion.

The τ lepton is unique among leptons due to its relatively high mass, allowing it to decay to both hadrons and other leptons via electroweak interaction. The decays are mediated by a W boson, which pairs with a $q\bar{q}$ or a $\ell\nu_\ell$ pair with equal probability for each quark

colour or lepton flavour. Due to this, the hadronic branching fraction of the tau lepton is significantly larger than the leptonic one. Table 4.1 shows the possible final states of τ decay and intermediate resonances. In this thesis, tau leptons decaying into hadrons are referred to as *hadronic* (τ_h), while decays into leptons are referred to as *leptonic* (τ_l).

Decay mode	Resonance	$\mathcal{B}$ (%)
Leptonic decays		35.2
$\tau^- \to e^- \overline{\nu}_e \nu_\tau$		17.8
$\tau^- \to \mu^- \overline{\nu}_\mu \nu_\tau$		17.4
Hadronic decays		64.8
$\tau^- \to h^- \nu_\tau$		11.5
$\tau^- \to h^- \pi^0 \nu_\tau$	$\rho(770)$	25.9
$\tau^- \to h^- \pi^0 \pi^0 \nu_\tau$	$a_1(1260)$	9.5
$\tau^- \to h^- h^+ h^- \nu_\tau$	$a_1(1260)$	9.8
$\tau^- \to h^- h^+ h^- \pi^0 \nu_\tau$		4.8
Other		3.3

Table 4.1: Decays of the τ lepton and its branching fractions are shown. The symbol $h^\pm$ represents charged hadrons, known as prongs.

When a τ lepton decays to a single charged lepton (τ_l), the final-state signature typically includes an isolated electron or muon. In the CMS detector, the reconstruction of such leptons follows the same procedures as for prompt electrons and muons (see Sections 3.6 and 3.5). Although each leptonic τ decay produces two neutrinos that are not detected, the resulting reduction in reconstructed energy alone does not suffice to distinguish τ_l from prompt electrons or muons when only one lepton is present.

However, in cases where a pair of leptons originates from decaying τ leptons (e.g. di-lepton events), the p_T^{miss} becomes a crucial observable. The undetected neutrinos can cause a substantial transverse momentum imbalance, which can serve as a clear signature of τ decay.

Tau leptons also have the potential to travel a short distance, on the order of less than a millimetre, before decaying. Unfortunately, this macroscopic displacement is too small for the CMS detector to reliably separate leptons from the PV and those from nearby secondary vertices. Consequently, the same reconstruction techniques employed for prompt muons and electrons are used for leptonically decaying τ.

4.2 Hadronic taus reconstruction

The τ_h reconstruction at the CMS is performed by hadrons-plus-strips (HPS) algorithm [119, 120]. The main steps of the reconstruction are described below.

The algorithm is seeded by an AK4 jet. The details of the jet reconstruction algorithm are given in Section 3.7. For the following steps, all particles within the distance of $R = \sqrt{\Delta\eta^2 + \Delta\phi^2} \leq 0.5$ with respect to the reconstructed jet axis are considered. The HPS algorithm aims to reconstruct τ_h properties while minimising the loss in the efficiency of reconstruction. This approach ensures that potential tau candidates are not overlooked. The algorithm explicitly targets τ_h decay modes separately. Conventionally, the decays
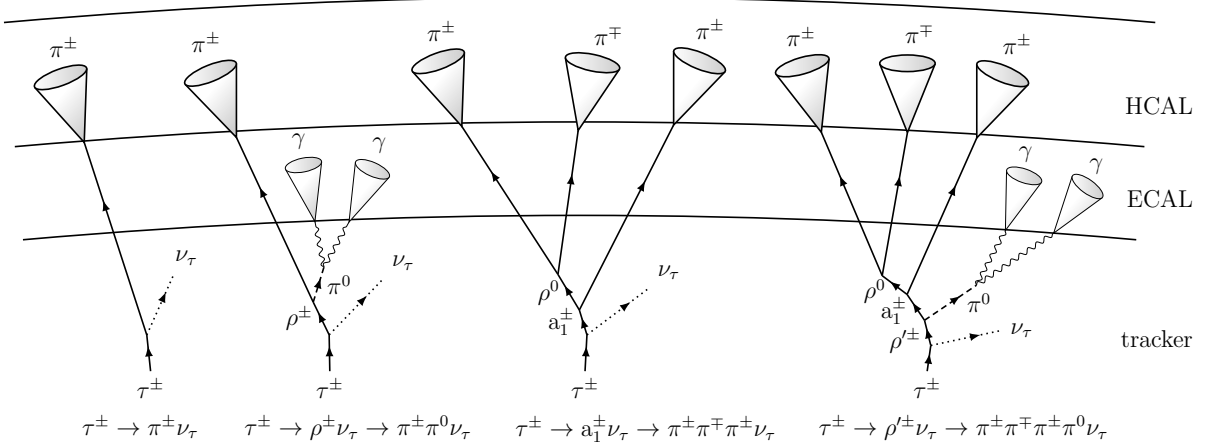
Figure 4.2: Schematic representation of tau lepton decay modes as reconstructed in CMS [121]. The figure is made using the TikZ package [122]. The diagram displays hadronic tau decay processes, highlighting the decay products and their interactions with the CMS detector components such as the ECAL, HCAL, and the tracking system.

are subdivided by the number of charged hadrons in the final state, named *prongs*. Their detection requires a combination of the information from detector parts, including trackers and calorimeters. The schematic representation of the τ_h decays and expected detector signature is shown in Fig. 4.2. The one-prong decay reconstruction targets $\tau^\pm \to h^\pm \nu_\tau$, $\tau^\pm \to h^\pm \pi^0 \nu_\tau$ and $\tau^\pm \to h^\pm \pi^0 \pi^0 \nu_\tau$ decay modes, corresponding to the detector signature $h^\pm$, $h^\pm \pi^0$ and $h^\pm \pi^0 \pi^0$. The three-prong decays $\tau^\pm \to h^\pm h^\mp h^\pm \nu_\tau$ and $\tau^\pm \to h^\pm h^\mp h^\pm \pi^0 \nu_\tau$ rely on signature of $h^\pm h^\mp h^\pm$ and $h^\pm h^\mp h^\pm \pi^0$. In cases where one of the charged hadrons has particularly low p_T, it might not leave a detectable deposit in the hadronic calorimeter. To handle three-prong decays under this condition, detector signatures such as $h^\pm h^{\pm/\mp}$ and $h^\pm h^{\pm/\mp} \pi^0$ are considered, addressing the decay modes where one of the charged pions is missing.

The critical aspect of reconstructing the τ_h lepton is capturing the signature of the π^0 meson, which typically decays into a pair of photons that often further decay to $e^+ e^-$ pairs. The produced electron and photon candidates in a particular $\Delta\eta \times \Delta\phi$ are clustered together and referred to as a "strip".

The further process for reconstructing τ_h involves the following steps:

1. **Dynamic strip reconstruction.** Photon and electron constituents of the seeding jet are clustered into $\Delta\eta \times \Delta\phi$ strips. These signatures indicate the decay of neutral pions and are used to estimate the total energy deposition in the ECAL caused by neutral pions. The process starts with the jet's leading photon or electron (e/γ). Then, an iterative process starts to cluster additional objects to the strip when they lie within the dynamic strip window. Its size is defined as $\Delta\eta = f(p_\mathrm{T}^{\mathrm{e}/\gamma}) + f(p_\mathrm{T}^{\mathrm{strip}})$ and $\Delta\phi = g(p_\mathrm{T}^{\mathrm{e}/\gamma}) + g(p_\mathrm{T}^{\mathrm{strip}})$ where $p_\mathrm{T}^{\mathrm{e}/\gamma}$ is the p_T of the electron or photon to be merged and $p_\mathrm{T}^{\mathrm{strip}}$ is the p_T of the already merged cluster. The iterative process continues until no more e/γ are found in the strip window. The dimensionless functions f and g are determined from MC so that 95% of all electrons and photons from π^0 are contained within one strip, resulting in: $f(p_\mathrm{T}) = 0.20\, p_\mathrm{T}^{-0.66}$ and $g(p_\mathrm{T}) = 0.35\, p_\mathrm{T}^{-0.71}$

where $\Delta\phi$ is limited to the range of 0.05-0.3 and $\Delta\eta$ to the 0.05-0.15.

2. **Mass constraints on decay modes.** All potential combinations of charged hadrons and strips are evaluated with respect to the various τ_{h} decay modes. The four-momentum of the τ_{h} is then calculated by summing the four-momenta of these charged hadrons and strips, corresponding to the specific decay mode of the τ_{h} candidate. The mass of the resulting τ_{h} candidate is then required to be loosely compatible with the mass of the mesons acting as intermediate resonances mentioned in Table 4.1.

3. **Charge constrains.** The τ_{h} candidates with charge other than ±1 are not considered for one-prong and three-prong decays. When one of the charged hadrons is missing, the τ_{h} candidate is labelled "two-prong", and their charge is assigned based on the p_{T}-leading charged hadron.

4. **Signal cone.** If charged particles or strips are located outside the signal cone, defined by $R_{\mathrm{sig}} = (3.0\,\mathrm{GeV})/p_{\mathrm{T}}$ with respect to the reconstructed τ_{h}, the τ_{h} candidate is rejected. The cone size is limited to the range of 0.05–0.10.

If several τ_{h} candidates pass the selection, the one with the highest transverse p_{T} is selected. In Fig. 4.3, the confusion matrix of the algorithm is shown. It demonstrates the ratio of the reconstructed decay modes with respect to the generator level τ_{h} decay mode. Overall, the algorithm successfully reconstructs approximately 90% of τ_{h} leptons, including cases where the decay mode is misassigned. For three-prong decays where a charged pion is lost, up to 13% to 19% of the cases are recovered, considering two-prong decays. In contrast, the charge assignment accuracy for all other decay modes is around 99%, based on measurements from the $Z \to \tau\tau \to \mu\tau_{\mathrm{h}}$ decays used for the estimation.

4.3 Hadronic taus identification (DeepTau)

The HPS algorithm used in the CMS experiment for reconstructing hadronically decaying tau leptons is a sophisticated and physically motivated approach. However, while being well-suited for capturing genuine τ_{h} signatures, the algorithm is not immune to challenges associated with misidentification. This primarily occurs when other objects in the detector mimic signatures the HPS algorithm associates with τ_{h} candidates. Below, a few examples of potential faking mechanisms that may arise within the detector are listed; the schematic diagram for illustrating detector response is shown in Fig. 4.4:

- **Jets** originated from quarks or gluons, the most common misreconstruction source. Highly collimated jets can practically fake any τ_{h} decay mode. Such jets are typically characterised by their extensive hadronic activity and being more widely spread than the original τ_{h}. Normally, isolation [119] provides a strong handle for reducing the $jet \to \tau_{\mathrm{h}}$ misidentification probability.

- **Electrons** might be misreconstructed as charged pions. While crossing the tracker material, electrons often emit bremsstrahlung photons, mimicking a signature similar to a π^0 in the decay mode reconstruction. In such a case, electrons are misconstrued as one prong or one prong plus π^0s decays. The

Figure 4.3: The table shows the fraction of generated decay modes being reconstructed for particular decay modes. Both generated and reconstructed τ_h candidates are required to satisfy $p_T > 20\,\text{GeV}$ and $|\eta| < 2.3$, and are selected from a MC sample of $Z \to \tau\tau$ events with invariant mass $m_{\tau\tau} > 50\,\text{GeV}$. The label *None* marks the cases where no τ_h candidate was reconstructed by HPS [123].

    electromagnetic shower pattern in the ECAL is extensively used to separate such electrons from τ_h.

- **Muons** are less likely than jets or electrons but can be misidentified as τ_h. Although muons typically create minimal energy deposits in the ECAL, unusual interactions or overlapping energy deposits from unrelated particles can create misleading signals. In such cases, matched hits in the muon chambers can be used to minimise such fakes.

To suppress the following sources of fakes, various techniques are used:

- Jet misidentification is addressed using isolation-sum or alternatively multivariate analysis (MVA)-based discriminators [119].

- Electron contributions are suppressed using a dedicated BDT [120].

- A cut-based discriminator that relies on hits in the muon chamber close to τ_h is used to suppress the contribution from a muon [120].

To address the identification more broadly, the deep neural network DeepTau v2.1 was developed [123]. Its design is based on the following three main principles:

- **Developing a multiclass algorithm** that incorporates jet, electron, muon, and tau classes is more beneficial than using separate classifiers for each class. Firstly, multiclass classifiers can leverage shared information among classes, improving the overall performance [124]. Secondly, managing one multiclass model can be simpler than handling multiple binary models, reducing complexity in implementation and maintenance.

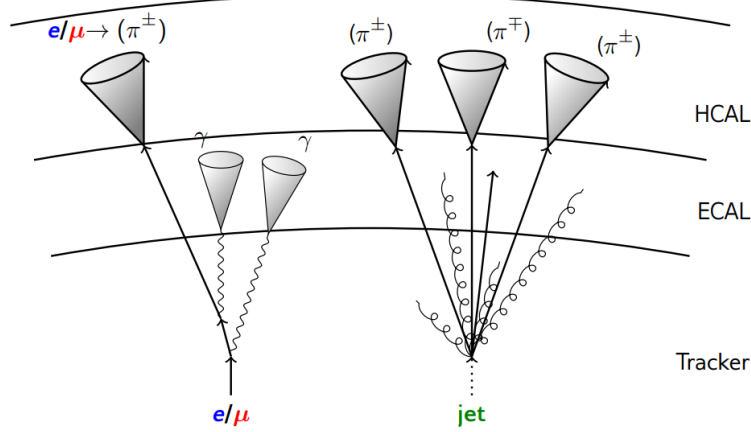- **Incorporation of Lower-Level Information:** The previously developed

Figure 4.4: Diagram of typical faking mechanisms in CMS. The figure is made using the TikZ package [122]. It highlights how electrons ($e^\pm$) or muons (μ) can be misidentified as pions ($\pi^\pm$) within the detector environment, as well as how jets are often mistaken due to their similar signatures in the HCAL and ECAL.

> MVA discriminator was based on high-level information. However, jet hadronisation and fragmentation have a complex nature that generates intricate detector signatures alongside particles from concurrent interactions. A machine learning algorithm, trained on an extensive dataset and capable of leveraging lower-level information, is anticipated to exhibit superior performance. Consequently, information related to all reconstructed particles proximate to the τ_h candidate is directly utilised as inputs in the algorithm.

- **Domain knowledge**: Adding high-level τ_h domain features that showed good discrimination potential while training previous MVA discriminators to the low-level particle information can speed up the training. This can be a good compromise since the training dataset and resources are limited.

Being the first multi-class classifier that combines the classes for all the typical reconstructed τ_h sources of background into a single training, DeepTau, in particular version 2.1, demonstrated a significant step forward in τ_h identification [123] with respect to its predecessors. The new algorithm, DeepTau v2.5, is built upon the foundation of DeepTau v2.1, incorporating numerous updates to enhance its efficiency for Run 2 and Run 3 analyses within the CMS experiment. Its training consists of two key steps:

1. **Initial Training on a Large MC Sample**: The model is first trained on a substantial MC simulation dataset. This step allows the model to learn the fundamental patterns and relationships to separate τ_h from electrons, muons, and jets.

2. **Fine-Tuning with a Combined Data+MC Sample Using an Adversarial Approach**: After the initial training, the model undergoes fine-tuning using a smaller dataset that combines both real experimental data and additional MC samples. An adversarial approach is used during this fine-tuning to further enhance the model's robustness by training it with data samples.

A detailed description of DeepTau v2.5 and the fundamental principles inherited from

DeepTau v2.1 are provided below.

4.3.1   Data pre-processing

In the context of training machine learning models for object tagging in particle physics, a critical process known as labeling is employed. The definition of the genuine source of the jet involves using MC simulations, where generator-level particles - the actual particles generated in the simulation - are well-defined. In this case, the particle can be accurately matched to the reconstructed object observed in the detector. After this, the tagger is trained to separate these particles in the simulation, ensuring it will distinguish a concrete particle of interest in the real data based on the same specific criteria. To define training classes for DeepTau v2.5, the following labeling procedure is employed:

- τ_μ (prompt muon or muon from $\tau \to \mu\nu_\mu\nu_\tau$): The reconstructed tau candidate is required to match the generator-level prompt muon with $\Delta R < 0.2$.

- τ_e (prompt electron or electron from $\tau \to e\nu_e\nu_\tau$): The reconstructed tau candidate is required to match the generator-level prompt electron with $\Delta R < 0.2$.

- τ_h (genuine hadronic tau): The reconstructed tau candidate is required to match the visible component of a generator-level hadronic tau with $\Delta R < 0.2$.

- τ_j (quark or gluon jet): The tau candidates that do not satisfy the previous requirements and match to a generator-level quark or gluon with $\Delta R < 0.5$ are considered for this class.

These four classes are sampled from various MC samples. It is assumed that the tagger should be able to discriminate background in various physics processes; therefore, combining the physics processes in one training is required. The processes that are considered for the training are listed in Table 4.2.

Table 4.2: List of the physics processes with the corresponding genuine tau types taken from them. Each of the processes consists of several available MC samples.

Process naming	τ_j	τ_e	τ_μ	τ_h
Drell-Yan	✓	✓	✓	✓
$t\bar{t}$ production	✓	✓	✓	✓
W+Jets production	✓	✓	✓	✓
Multijet production (QCD)	✓	✗	✗	✗
Higgs boson production ($\to \tau\tau$)	✗	✗	✗	✓
$Z' \to ee$	✗	✓	✗	✗
Tau gun	✗	✗	✗	✓

The original datasets in the standard CMS format, MiniAOD, contain extensive event information. However, several pre-processing steps are implemented to ensure efficient data access during training. This includes generating large *root-tuples* in which each *Tree* entry contains the requisite information for computing input variables associated with an individual τ_h candidate. As a result, combining the available MC sources of τ_h candidates, it was possible to sample up to 381 million of τ_e, 395 million of τ_μ, 167 million of τ_h and 1.463 billion of τ_j candidates. To ensure the dataset is suitable for training a general-purpose tagger applicable to a wide range of analyses, the following requirements

were imposed:

1. **Homogeneity**: For any sufficiently large, consecutive interval of entries in the training dataset, the probability of having a tau candidate with given p_T, η, tau type and physics process should always be the same, i.e. the empirical distributions are statistically compatible.

2. **Uniformity:** Reduce imbalance over different tau types (τ_e, τ_μ, τ_h, τ_j) as well as regions of kinematic phase space p_T and η. In other words, the aim is to maximise **uniformity** over the mentioned distributions.

Given the dataset size of several terabytes, which cannot fit into RAM, a customer procedure called the Shuffle and Merge (S&M) algorithm has been developed to shuffle the dataset.

Implementing the aforementioned requirements involves addressing the extreme imbalance in the available datasets, which disproportionately represent certain tau types (τ_e, τ_μ, τ_h, τ_j) and kinematic regions in p_T and η. The available combination of datasets has an extreme imbalance of tau types, p_T and η spectra, with ample statistics at low p_T and central η regions, while high p_T and forward η regions are much less populated. A three-step procedure allowed us to mitigate this imbalance: (1) since MC data, in particular, QCD and $t\bar{t}$ are highly overpopulated with low p_T jets faking tau, jets with p_T of less than 80 GeV are randomly excluded with a probability of $p = 1 - \exp\{-0.05 \cdot (80 - p_T)\}$. (2) The new S&M algorithm aims to reduce the imbalance over τ types and different kinematic regions. (3) The training weights reduce the residual discrepancy between classes within fixed (p_T, η) bins. The dataset imbalance is so extreme that using weights without steps (1)-(2) would result in some weights being too large to be represented within the limits of the dynamic range of 32-bit floating-point precision (approximately 10^7). These excessive weights could effectively be rounded to zero, causing the model to ignore underrepresented events entirely, leading to biased training.

The S&M algorithm is an approach for selecting data from the dataset to construct training sets that satisfy the aforementioned criteria. In contrast to the sampling procedure used for DeepTau v2.1, the new method involves a stochastic sampling of objects. The S&M algorithm assigns a probability to each bin based on the desired target distribution and then samples τ candidates from these bins according to their calculated probabilities. This process ensures that the final dataset is balanced across different τ types and kinematic regions, effectively matching the target spectrum while maintaining homogeneity across the data groups.

The dataset is first divided into groups $\{G_1, G_2, \ldots, G_i\}$, each representing different physics processes following the decision shown in Table 4.2. Every group contains several datasets. Sampling is performed simultaneously from each group to guarantee an equal contribution of physics processes in the final dataset. Within each group G_i, tau candidate are binned according to their p_T and η values:

- p_T intervals (GeV): (20, 30), (30, 40), (40, 50), (60, 70), (70, 100), (100, 1000).
- η intervals: (0.0, 0.5), (0.5, 1.0), (1.0, 1.5), (1.5, 2.5).

The goal is to adjust the sampling of τ_{h} candidates such that the resulting spectrum matches a predefined target spectrum, $T_{\tau_i}^{G_i}(p_{\mathrm{T}}, \eta)$. For DeepTau v2.5, an equal contribution from the bins mentioned above and an equal number of tau types τ_i are required. To achieve this, each τ_i needs to be sampled with a certain probability:

1. **The initial spectra** are estimated before interaction for each of the data groups - $I_{\tau_i}^{G_i}(p_{\mathrm{T}}, \eta)$.

2. **The probability** to accept a tau is estimated as:

$$P \approx \frac{T_{\tau_i}^{G_i}(p_{\mathrm{T}}, \eta)}{I_{\tau_i}^{G_i}(p_{\mathrm{T}}, \eta)} \, .$$

3. **Normalisation:** The ratios are normalised such that the bin with the highest ratio has a 100% selection probability. This ensures that the maximum possible number of taus is sampled from the available statistics.

Finally, the algorithm ensures homogeneity across data groups by statistically selecting which data group to process next using a weighted random selection. The probability of a sample from each group is proportional to the number of taus in the group.

This selection process is repeated until the desired number of entries is reached, ensuring that the final dataset is more uniform and balanced across all tau types and kinematic regions. The S&M algorithm ensures uniformity in the training dataset spectra with the cost of significantly reducing the dataset size to approximately ≈ 100 million tau candidates. In Figure 4.5, a comparison of the p_{T} and η distributions of the initial and pre-processed dataset is shown. The training set is split in a proportion of 80% assigned for the training and 20% for validation.

A Kolmogorov-Smirnov (KS) test is performed to ensure homogeneity across the input datasets. This test is applied by dividing the datasets into sub-intervals, allowing for a detailed comparison of distributions within each segment. The KS test is used to verify that key variables, such as p_{T}, η, tau types $(\tau_e, \tau_\mu, \tau_j, \tau_{\mathrm{h}})$, and the underlying physics processes source, are homogeneously distributed in the training dataset, practically that their distributions remain constant.

After the S&M procedure is performed, the dataset is additionally refined by applying training weights to account for more detailed differences within finer binning. During training, these weights are integrated into the loss function to adjust the model's focus equally over the tau types for all phase space regions. More details about the loss function are given in Section 4.3.3.

4.3.2   Input objects

The mid-2010s marked a pivotal era in adopting Convolutional Neural Networks (CNN) [125, 126, 127]. The successful application of AlexNet in the 2012 ImageNet competition demonstrated the immense potential of CNNs, catalysing their widespread use in various tasks. Among various problems, Computer Vision [128, 129], Healthcare [130,
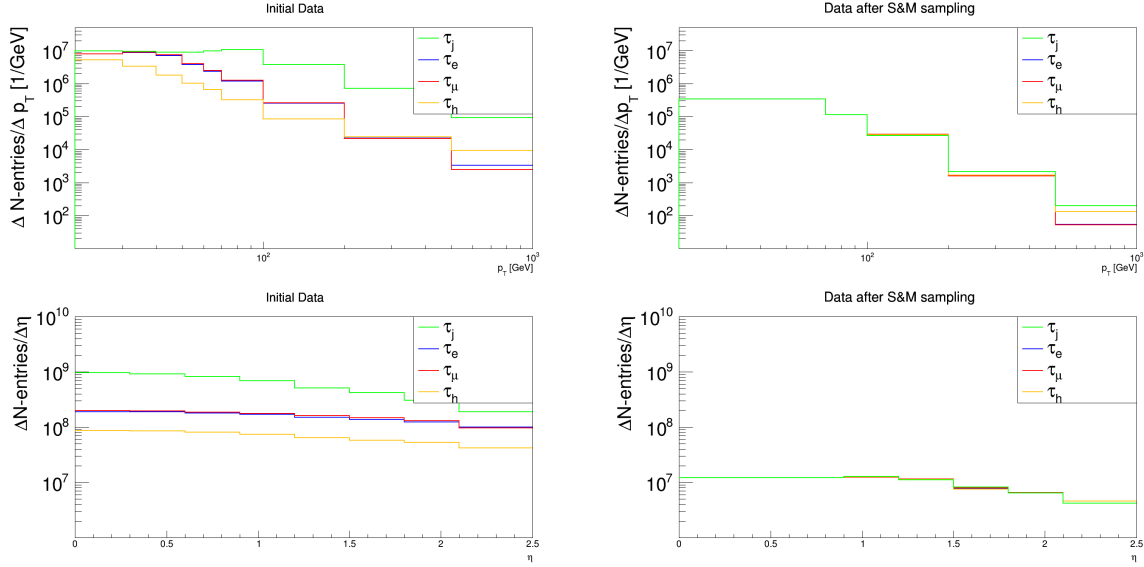
Figure 4.5: Upper row shows the p_T spectra, and lower row shows the η spectra of tau candidates from the original combined MC dataset on the left and after applying the S&M sampling method on the right.

131, 132], Automotive Industry [133, 134] and Natural Language Processing [135] can be highlighted. The high efficiency of CNNs is an empirical phenomenon attributed to several aspects of the CNN. The most significant ones are: local connections between adjacent neurons, reducing the number of parameters by sharing weights across different parts of the input, which makes learning efficient even for sparse representation; the hierarchical structure, which allows them to capture low-level features like edges and textures in the initial layers and high-level features such as shapes and objects in deeper layers; additionally, CNNs are translation invariant, making them suitable for tasks where feature positions can vary significantly, like image and speech recognition.

The use of CNNs is also advantageous in the field of high-energy physics and, in particular, jet classification [136] for several reasons. Firstly, CNNs are good at capturing complex spatial patterns, making them well-suited for the complex nature of jet fragmentation, which involves intricate energy deposits in detectors [137]. Additionally, the high-dimensional data produced in particle collisions, such as calorimeter images, can be efficiently processed by CNNs due to their ability to handle such data effectively through local connectivity and hierarchical feature extraction. Moreover, CNNs demonstrate robustness to noise and variability, making them ideal for accurately classifying and identifying jets even with overlapping and noisy signals commonly encountered in detectors.

Based on the abovementioned factors, a CNN was chosen for identifying τ_h. By organising the low-level inputs into two 2D grids, the CNN can first analyse local patterns from the tau or jet structure and then gradually combine the information to cover larger $\Delta\eta \times \Delta\phi$ regions, taking advantage of the hierarchical approach and capturing the entire τ_h signal or isolation cones.

To enhance the DeepTau training, both high-level and low-level information were combined. This approach allows the algorithm to efficiently classify tau leptons while ac-
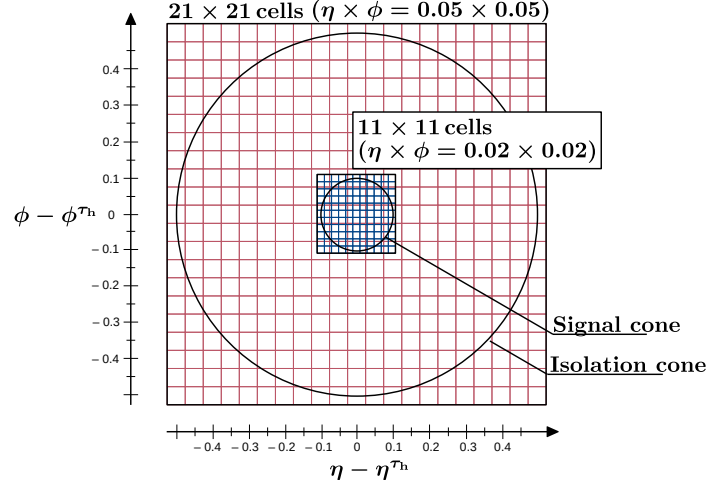
Figure 4.6: Diagram of the input grids in η-ϕ plane around the reconstructed τ_h axis used for processing the particle-level inputs [123].

celerating the learning process. High-level tau domain features, known for their good discrimination potential, are integrated with detailed lower-level particle information, ensuring comprehensive and effective training.

Particle-level inputs

Low-level input is organised in the form of the particles placed in two $\Delta\eta \times \Delta\phi$ grids, inner and outer, as shown in Fig. 4.6. The inner grid has 11×11 cells of size 0.02×0.02 covering the signal region of the radius $\Delta R < 0.1$ and the outer has 21×21 cells and grid size of 0.05×0.05 covering the outer isolation region of the radius $\Delta R < 0.5$. Every particle is assigned to a concrete cell with respect to the axis of reconstructed HPS τ_h; this results in a sparse representation with 1.7% of the inner grid cells and 7.1% of the outer grid cells being occupied on average; in case of overlap, the particle with the biggest p_T is taken. The use of two different grids is primarily supported by the fact that the products of τ_h lie within the signal cone of a radius of $\Delta R < 0.1$ [119, 123]. Furthermore, high p_T quark or gluon jets are highly collimated, necessitating a higher resolution in the central region to avoid losing information due to overlapping particles. Therefore, implementing a signal grid enables more precise coverage of the central area.

A few different types of reconstructed particles are used as input on the particle level. Firstly, objects that are reconstructed by the PF algorithm described in Section 3.4, in particular muons, electrons, photons, and charged and neutral hadrons. Additionally, muons and electrons are reconstructed using a standalone reconstruction algorithm, which adds additional particle-specific information. These particles are provided to the input as separate objects. In total, seven kinds of objects are used.

The input to the algorithm is constructed from various parameters (features) associated with each object. These parameters include:

- **Kinematic properties**: Relative p_T, differences in pseudorapidity ($\Delta\eta$), and azimuthal angle ($\Delta\phi$), calculated with respect to the reconstructed τ_h.
- **Charge**: Reconstructed charge of all charged particles.

- **Pileup information**: Estimated probability for each particle to originate from pileup interactions, determined using the PUPPI algorithm.
- **Track compatibility**: Compatibility indicators for tracks with respect to the PV and potential SV associated with τ_h reconstruction, labeled as Track PV and Track SV.
- **Track details**: Basic track information.

A detailed overview of the variables used for each particle type is provided below:

- **PF charged hadrons (27 features)**: Track quality (PV, SV, general quality), PUPPI weight, HCAL energy fraction, basic kinematic properties, reconstructed charge.
- **PF neutral hadrons (7 features)**: PUPPI weight, HCAL energy fraction, basic kinematic properties.
- **Electrons (RECO electron, 37 features)**: Electron track quality, track-cluster matching, cluster shape parameters, basic kinematic properties, and reconstructed charge.
- **PF electrons (22 features)**: Track quality (PV, SV, general quality), PUPPI weight, basic kinematic properties, reconstructed charge.
- **PF photons (22 features)**: Track quality (PV, SV, general quality), PUPPI weight, and basic kinematic properties.
- **Muons (RECO muon, 37 features)**: Track quality, muon station hits, ECAL energy deposits, basic kinematic properties, reconstructed charge.
- **PF muons (23 features)**: Track quality (PV, SV, general quality), PUPPI weight, basic kinematic properties, reconstructed charge.

In DeepTau input, after each particle is assigned to an associated pixel on the η-ϕ outer or inner grid, the variables are placed in the depth of the tensor. One can imagine this as a 3D tensor.

In a typical image, the data is usually represented as a 3D tensor with two spatial dimensions (width and height, denoted as x and y) and a depth dimension (usually representing colour channels such as RGB). Each pixel in the image is defined by three values corresponding to the red, green, and blue colour intensities. Analogously, in our case, the spatial dimensions are η and ϕ, which correspond to the pseudorapidity and azimuthal angle in the particle detector. The depth dimension, instead of colour channels, contains the features of the particles. These features include track quality, energy fractions, and other relevant parameters described above.

Thus, the η-ϕ grid serves as the spatial plane, and the depth dimension captures the multiple features associated with each particle in the grid. This structure allows the CNN to effectively learn and identify patterns in the τ_h tagging task, similar to how it processes visual information in traditional image recognition tasks.

High-level inputs

The primary high-level input variables are derived from those proven effective for the τ_h reconstruction and identification domain. These variables encompass:

- The four-momentum and charge of the τ_h.
- The number of charged and neutral constituents of the τ_h candidate.
- Variables indicating isolation, such as the energy of charged and neutral particles in the proximity of the τ_h candidate.
- The match of the leading τ_h track to the primary vertex (PV).
- Secondary vertex properties, particularly for multiprong τ_h decays.
- Variables related to the η and ϕ energy distributions in the strips.
- Variables assessing the likelihood of the τ_h candidate being an electron.
- The estimated pileup and energy density within the event.

Overall, there are 47 high-level input variables. These input variables that encapsulate domain-specific knowledge can potentially improve convergence speed.

Features standardisation

Standardisation and outlier removal are used for every individual variable. This ensures that each feature contributes equally to the model, preventing bias towards larger numerical scale features. It also improves the convergence speed of algorithms, particularly gradient-based methods, by providing a smooth optimisation on the landscape. Removing outliers reduces numerical instabilities and makes the algorithm robust against misconstructed variables. The following procedure is applied for standardisation:

1. Integers and significantly asymmetrical distributions are linearly mapped to the interval [-1,1].

2. Other input variables are transformed using $x \rightarrow \frac{(x-\mu)}{\sigma}$, where μ represents the mean and σ represents the standard deviation of the distribution of x.

3. Linear features with expected outliers are cropped outside the range of [-1,1], while the remaining features are cropped to fit within the range of [-5,5], ensuring that the majority of the distribution falls within the range of [-1,1].

4.3.3   Network architecture

The complete DeepTau architecture schematic diagram is shown in Fig. 4.7. The input is divided into three groups: *Inner* and *outer* grids and *high-level variables*, as was described in Section 4.3.2. The hyperparameter tuning is performed as described in Appendix A.2. The total number of trainable parameters for an optimal model selected as a baseline is 1.1 million. The architecture includes the following key elements:

Projection layers

One cell in the *inner* and *outer* grid contains 188 features. To reduce the dimensionality of the data, a 1×1 CNN is applied. This reduction allows the network to compress information before using 2D CNN layers, making the model more computationally efficient and less prone to overfitting.

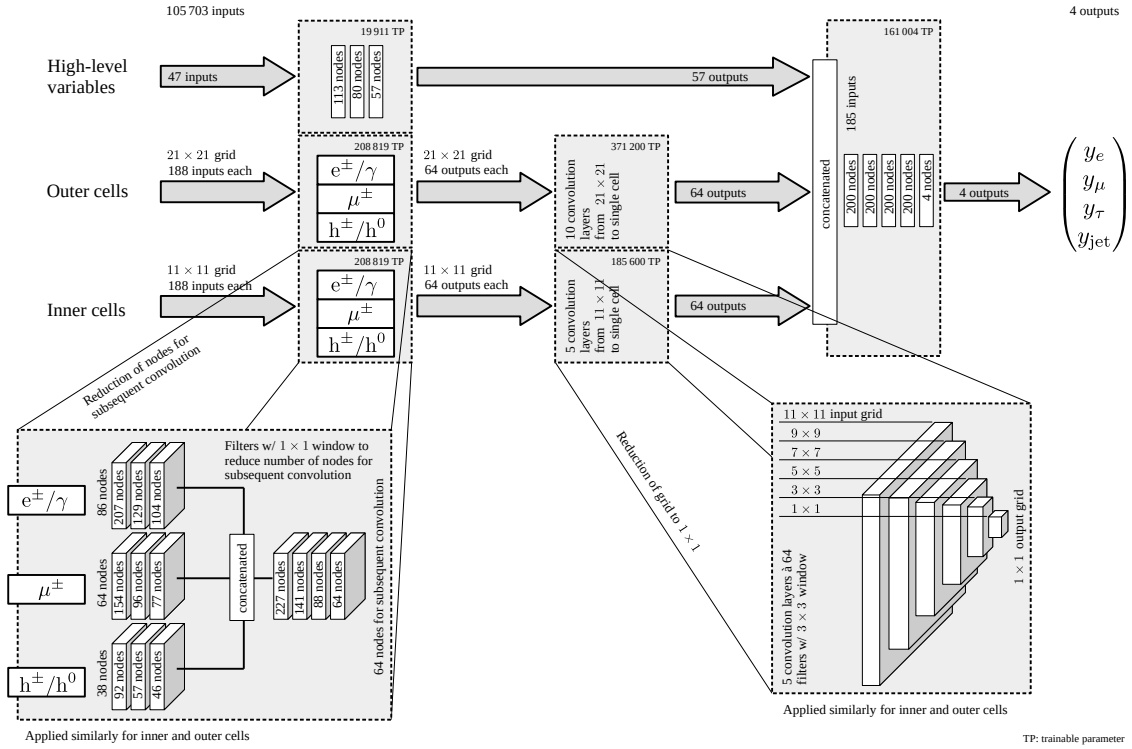Particle-level input is divided into three categories:

Figure 4.7: The schema of the DNN architecture [123]: Three input sets (inner cells, outer cells, and high-level features) are processed through subnetworks, concatenated, and passed through five fully connected layers to calculate classification probabilities. High-level features use three fully connected layers, while inner and outer cell features pass through dedicated networks with fully connected and convolutional layers, progressively reducing grid sizes. Trainable parameters for each subnetwork are also provided in the schema.

- **EGamma**: contains PF electrons, PF photons, RECO electrons.
- **Muons**: contains PF muons and RECO muons.
- **Hadrons**: PF charged hadrons and PF neutral hadrons.

Each particle category has distinct characteristics and patterns in the detector data. Firstly, each category is pre-processed separately by three layers of 1×1 convolution. One can think of a 1×1 convolutional layer as being similar to a dense (fully connected) layer, but instead of applying the dense layer to the entire input at once, the 1×1 convolution applies it independently to every grid cell/particle in the spatial dimensions of the input to construct refined features for further processing.

After separate pre-processing, all three categories are concatenated together, preserving the dimensionality of $(\Delta \eta, \Delta \phi)$ grid. Further, this output is processed with three additional 1×1 convolutional layers before 2D convolutional layers.

Before being fed into the last layers of the neural network, high-level inputs analogously undergo pre-processing using dense layers.

Convolutional layers

The pre-processing step produces two grids: $11 \times 11 \times 64$ for the *inner* grid and $21 \times 21 \times 64$ for the *outer* grid. Since the input grids are small and already undergo pre-processing, these grids are processed through multiple 3×3 convolutional layers without padding or max pooling. This reduces the grid size by a factor of 2 in each spatial dimension with each layer. The final layer reduces the grid to $1 \times 1 \times 64$, effectively transforming the input into a flattened array of 576 inputs. The inner grid passes through 5 convolutional layers, while the outer grid passes through 10 layers, where each layer uses 64 filters.

Merging part

In the next step, the outputs from the *inner*, *outer*, and *high-level* blocks are concatenated, yielding 185 inputs in total. These are processed through four fully connected dense layers with 200 nodes each. After each layer, batch normalisation and dropout (with $r_{drop} = 0.2$) are applied for regularisation. Non-linearity is introduced through the parametric rectified linear unit (PReLU) activation, with weight initialisation performed using the He uniform variance scaling method [138].

Output

The final dense layers convert 200 features into four output probabilities y_i, which estimate the likelihood that the reconstructed tau candidate is either τ_e, τ_μ, τ_j, or a genuine τ_h. These outputs are normalised using the softmax activation function:

$$y_i = \text{softmax}(x)_i = \frac{\exp(x_i)}{\sum_j \exp(x_j)} \, .$$

The discriminator can be written as:

$$D_\alpha(y) = \frac{y_\tau}{y_\tau + y_\alpha} \, ,$$

where $D_\alpha(y)$ is the discriminator for the particle type $\alpha \in \{e, \mu, \text{jet}\}$, y_τ represents the predicted probability that the candidate is τ_h, y_α is the predicted probability for a candidate being an electron, muon or jet, depending on the type of particle being discriminated against. This variable represents the likelihood that a given candidate is a tau in comparison to another particle type.

Loss function

The custom loss function is built to classify the tau in DeepTau. Categorical cross-entropy [139] is the basis of the custom loss function, as it is proven effective for general classification tasks to quantify the difference between the true distribution $p(x)$ and the predicted distribution $q(x)$. The cross-entropy loss can be computed for a dataset X containing N samples using the following formula:

$$H(y^\text{true}, y^\text{pred}; w) = - \sum_{\alpha \in \{e, \mu, \tau, j\}} \frac{1}{\sum_{x \in X} w_{x,\alpha}} \sum_{x \in X} w_{x,\alpha} \cdot y_{x,\alpha}^\text{true} \log y_{x,\alpha}^\text{pred} \, ,$$

where $w_{x,\alpha}$ represents the weight assigned to each tau candidate x and class α, $y_{x,\alpha}^\text{true}$ is the ground truth label (which is 1 for the true class and 0 otherwise), and $y_{x,\alpha}^\text{pred}$ is the predicted probability for class α. This formulation generalises the cross-entropy calculation across all classes. As mentioned in the previous Section 4.3.1, the re-weighting on the loss function level is used to correct the residual discrepancy between $\{e, \mu, \tau, j\}$ classes. The re-weighting is done by producing each class's (η, p_T) distribution and then correcting each of the $\{e, \mu, j\}$ class to the ratio with respect to the spectrum of the τ.

Furthermore, the construction of the loss function aims to improve the following key aspects:

- While cross-entropy is a frequent choice for general classification tasks, it tends to concentrate more on the low-purity ($\epsilon_\tau < 20\%$) and high-efficiency ($\epsilon_\tau > 95\%$) while most of the analyses with taus at the final state achieve the best sensitivity with true tau identification efficiency, ϵ_τ around 50% to 80%.

- The categorical cross-entropy does not consider the uniqueness of tau identification, in particular, that the τ_h class holds a distinct importance compared to the other three classes. For low-efficiency regimes, where the probability of a candidate being a genuine τ_h is low, a binary classification between τ_h and non-τ_h is more important than distinction among $\{e, \mu, j\}$ classes. In this way, unnecessary computation can be reduced, and the model can focus on more relevant areas of the parameter space.

Based on the abovementioned consideration, a custom loss function was constructed; its full form is given in Appendix A.1. It is based on modifying the cross-entropy with a focal-loss term [140], which helped to prioritise efficiency regions relevant for physics analyses, which include taus in the final state. The second modification aims to introduce a step function that prioritises classification between τ_h and non-τ_h when the τ_h probability for genuine tau is small.

4.3.4 Adversarial attack

As mentioned in Section 4.3.1, MC simulation is used extensively in the training of Deep-Tau for tau identification because a genuine source of reconstructed taus can be defined in this case. However, these simulations are imperfect replicas of actual detector data due to several inherent limitations. MC simulations usually rely on simplified models, approximations, and input parameters that carry uncertainties. At the same time, detectors always have imperfections, leading to discrepancies with actual experimental observations. As a result, while MC simulations are crucial for training, they cannot fully capture the complexities of actual data.

This effect of MC mismodelling becomes particularly critical in the region around the tight working points region, where the neural network might be sensitive to small discrepancies because it is trying to make fine distinctions. As a result, any difference between MC and real data can lead to the network making incorrect decisions when applying NN on the domain of the actual detector data. Usually, this discrepancy is mitigated with the calibration [123, 120], so-called scale factors that are measured by fitting data to MC in control regions for fixed working points. However, within this approach, the raw DeepTau score remains uncorrected, and its direct use as an input in analysis results in more considerable uncertainties. Additionally, the mismodelling of the variables in the training MC data may contribute to suboptimal performance because the neural network learns numerical values that may have been miscalculated quantitatively.

To address this, a domain adaptation technique is employed [141, 142, 143]. Domain adaptation during the training phase focuses on making the neural network less sensitive to the specific features of MC simulations that do not align with real data. The general concept involves introducing penalties to the neural network training process to discourage overfitting when the network learns to differentiate between MC simulated data and real detector data. The scale factors to correct residual differences are still to be extracted. However, the method has the advantage of bringing them closer to unity with smaller uncertainties.

In the case of DeepTau v2.5, this method is implemented as an additional fine-tuning training step after the initial training on a large MC sample is performed. During this step, an additional part of the neural network is added with the purpose of separating MC and real detector data, as shown in Fig. 4.8. The quality of this separation is measured by the binary cross-entropy loss function L_{adv}.

During the gradient update process in the training, two types of gradients are computed: classification gradients and adversarial gradients. In the shared part of the neural network architecture, the adversarial gradient is sign-reversed to prevent the model from distinguishing between data and MC events in the shared layers. In this part, the combined gradient update is proportional to the difference between the two components:

$$k_1 \cdot \frac{\partial L_{\mathrm{class}}}{\partial w} - k_2 \cdot \frac{\partial L_{\mathrm{adv}}}{\partial w} \, ,$$

where $k_1 > 0$ and $k_2 > 0$ can be seen as hyperparameters controlling the importance of tau classification and minimising data/MC discrimination, respectively, $k_1 = 1$ and
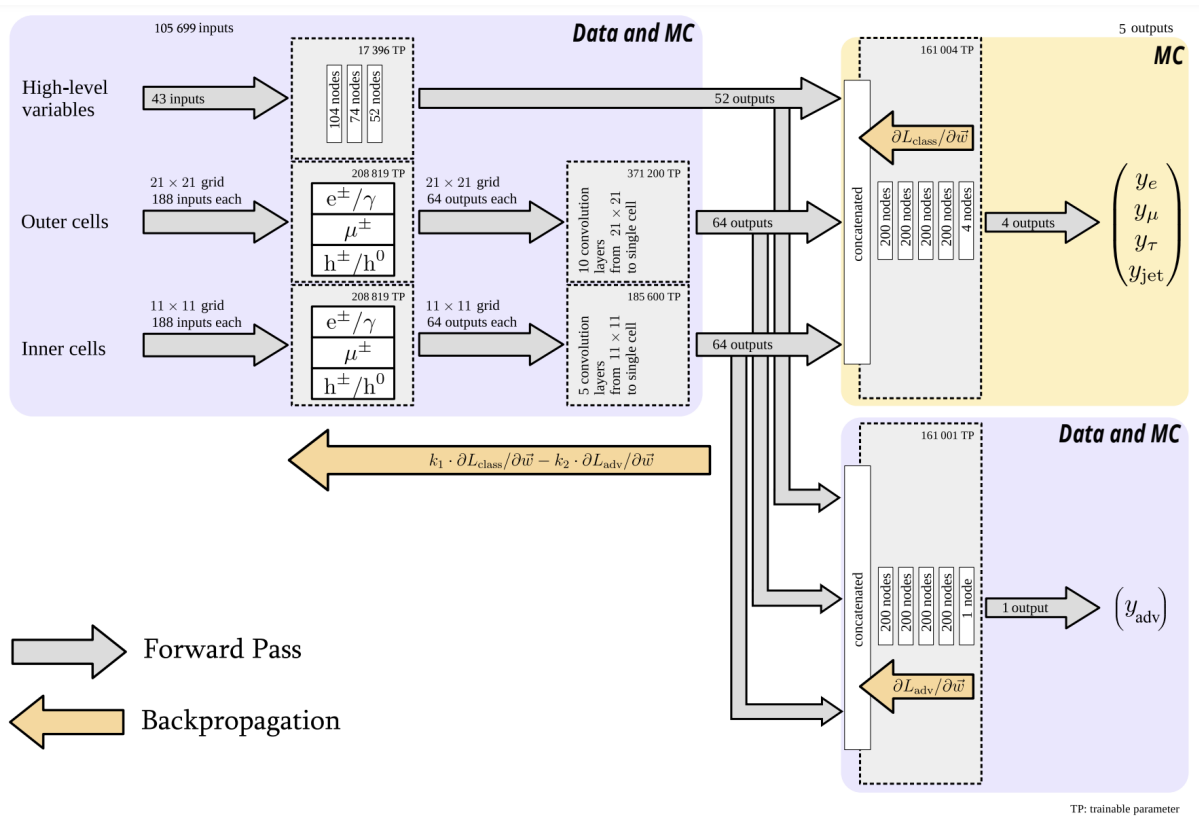
Figure 4.8: Diagram of the DeepTau v2.5 architecture - Adversarial Configuration [144, 8].

$k_2 = 10$ are chosen as optimal values [144].

For the domain adaptation step, tau candidates from MC were additionally sampled from various processes, including Drell-Yan, $t\bar{t}$, W+jets, and QCD multijet samples. The selection of taus from MC and data was based on the $H \to \tau\tau \to \mu\tau_{\mathrm{h}}$ region definition, which guarantees relatively high purity of the τ_{h} candidates in data. To target the regions most likely affected by mismodeling, the following selection criteria were applied: τ_{h} candidates with transverse momentum $p_{\mathrm{T}} > 30\,\mathrm{GeV}$, and a DeepTau v2p1 versus jet score $D_{\mathrm{jet}}^{\mathrm{v2p1}} > 0.90$ were selected to ensure focus on areas with the highest potential discrepancies. Additionally, candidates passing the DeepTau v2p1 very loose working point for electrons $D_{\mathrm{e}}^{\mathrm{v2p1}} > 0.168$ and the tight working point for muons $D_{\mu}^{\mathrm{v2p1}} > 0.875$ were included. The tau decay modes were required to be either 0, 1, 10, or 11, corresponding to 1- or 3-prong decays, with or without a π^0.

The adversarial training process for DeepTau utilises batches containing 100 taus, evenly split between 50 real data events and 50 MC simulated events shared proportionally among MC mentioned above. This mixture ensures balanced input from both real events and simulated data. In total, around 187500 tau candidates are used for the adversarial training.
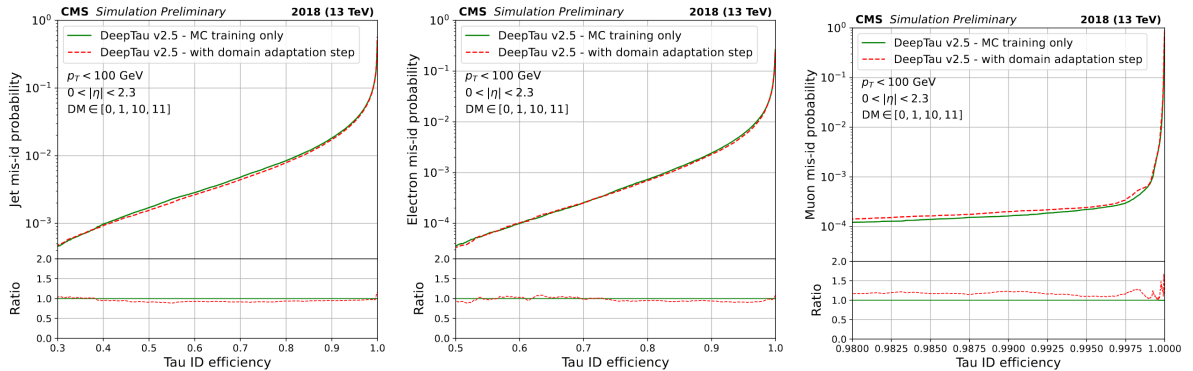

Figure 4.9: The receiver operating characteristic curves display the performance comparison between base MC-based training (green solid line) and additional adversarial training (dashed red line), showing tau identification efficiency versus the misidentification probability for jets (left), electrons (middle), and muons (right). The receiver operating characteristic curves are plotted for the phase space $p_{\mathrm{T}} < 100\,\mathrm{GeV}$, $|\eta| < 2.3$, and decay mode $\in \{0, 1, 10, 11\}$. The lower ratio plots indicate the relative comparison between training w/o and w/ adversarial step.

The potential effect of adversarial training on classification efficiency was studied. The change in the classification performance after the adversarial step is shown in Fig. 4.9. It shows no significant performance degradation in terms of classification efficiency, except for a slight drop in the muon efficiency. However, this reduction is considered an acceptable trade-off, as the model achieves a much better alignment between MC simulations and data, a topic that is elaborated on in Section 4.3.7. The improvement in the MC/data agreement outweighs the minor efficiency loss in muon classification. Additionally, a more detailed discussion of the training workflow and results is given in the section. In summary, adversarial training significantly improved the data/MC agreement in critical regions, particularly in tight regions, while maintaining satisfactory classification performance.

4.3.5 Training pipeline

Technical improvement of the training framework

Developing the machine learning framework for τ_h identification, called *TauMLTools* [145] required significant efforts to build a robust machine learning-based τ_h identification algorithm.

Working with large datasets for the generalised τ_h lepton tagger has significant I/O challenges. The main bottlenecks identified through testing were related to the time taken to fill grid-like tensors with particle-level inputs and the conversion of serialised data from the saved format back into numerical tensors when passing it to the training step.

To address these issues, a heterogeneous architecture was implemented. In this setup, C++ handles tensor filling for efficient data loading from ".root" files, and then the processed data is passed to Python for further handling. This division significantly reduces the time spent on tensor filling. Unlike DeepTau v2.1, in this approach, the conversion step from ".root" to training operations was conducted on the fly, without using an intermediate format. This provides additional flexibility regarding changes in the training data input configuration.

Additionally, the use of the PyTorch [146] `multiprocessing` queue was introduced, which allows for faster deserialisation compared to the default Python `multiprocessing.Queue`. This effectively improved data transmission from the queue to the model, reducing the bottlenecks during backpropagation.

As a result of the framework optimisation, the time required for the training was significantly reduced. The training of DeepTau v2.1 was performed on a GeForce RTX 2080 with 142.8 million tau candidates, resulting in a training speed of 3 days/epoch. In contrast, after optimising the DeepTau v2.5 training infrastructure, the training on GeForce GTX 1080 Ti with around 110 million τ_h candidates resulted in around 1.5 days on average, which is found to be an optimal balance between training time and flexibility. However, fully factoring in the impact of framework optimisation on training time presents significant challenges.

Training steps

The final version of the DeepTau v2.5 training process was split into 3 steps:

1. A baseline model was trained with simulation data using the NAdam optimiser [147] with a learning rate of 10^{-3} for three complete epochs.

2. Since it was observed that the model could potentially undergo further significant improvement, especially in discrimination against electrons with optimisers with a lower learning rate, models were trained with two additional epochs with a lower learning rate of 10^{-4} using NAdam. Multiple choices of optimisers, such as SGD, Adam and NAdam, were tested.

3. The final phase of the training incorporates an adversarial approach, building on the model from step 2. This phase specifically targets discrepancies between data and MC, focusing on improving performance in the tight working point region.
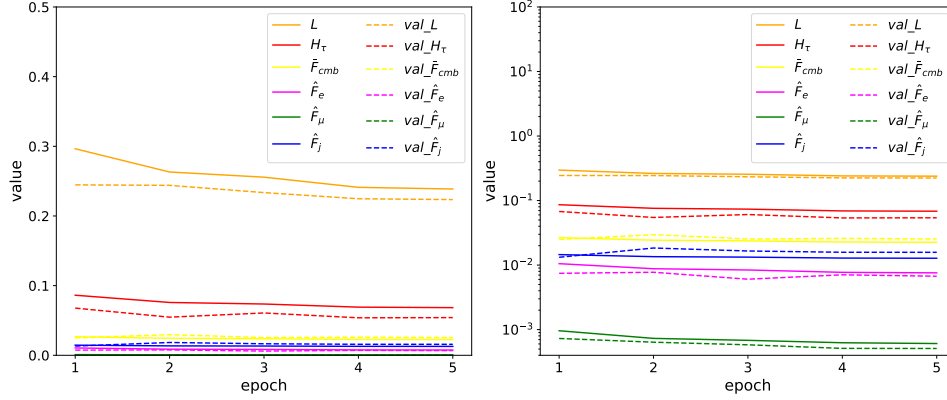
Figure 4.10: Evolution of the loss function components during the training of DeepTau v2.5, shown with a linear axis scale on the left and a logarithmic axis scale on the right.

The evolution of the loss function during the training of DeepTau v2.5 is shown in Fig. 4.10. A detailed description of the components of the loss function can be found in Appendix A.1.

4.3.6 Definition of the working points

To evaluate the performance and make the tagger usable for physics analyses, working points (WPs) are defined. They represent specific values of the discriminator outputs, setting the target efficiency for genuine taus from the $H \to \tau\tau$. To handle correlations between the threshold for VSe, VSmu, and VSjet discriminator outputs, the WPs are defined iteratively, refining thresholds to ensure convergence. When the threshold for one type is determined, the two other working points are fixed to the minimal thresholds: for electron VVVLoose for muon VLoose and jet to VVVLoose. The condition defines the convergence criterion: $\max_{i \in \{e, \mu, \text{jet}\}} \left(\left| thr_i^k - thr_i^{k-1} \right| \right) < 10^{-5}$ where thr_i^k denotes the threshold of the loosest WP of the discriminator against background i at iteration k. The various working points are established to enhance flexibility in balancing signal efficiency and background rejection across different physics analyses, enabling analysts to select the appropriate threshold based on the specific requirements of their study.

The target efficiencies for various WPs are as follows:

- **VVVLoose**: VSe: 99.5%, VSjet: 98%
- **VVLoose**: VSe: 99%, VSjet: 95%
- **VLoose**: VSe: 98%, VSmu: 99.95%, VSjet: 90%
- **Loose**: VSe: 95%, VSmu: 99.9%, VSjet: 80%
- **Medium**: VSe: 90%, VSmu: 99.8%, VSjet: 70%
- **Tight**: VSe: 80%, VSmu: 99.5%, VSjet: 60%
- **VTight**: VSe: 70%, VSjet: 50%
- **VVTight**: VSe: 60%, VSjet: 40%

4.3.7 Performance of DeepTau v2.5

The performance is estimated based on MC simulation. None of the MC processes used in the evaluation below are included in the training sample, ensuring that the results are unbiased and not influenced by overlap with the training data. Tau objects are selected within the kinematic range of $20 < p_T < 1000\,\text{GeV}$, $|\eta| < 2.3$ and longitudinal impact parameter of the τ_h with respect to the primary vertex lying within the region of $|d_z| < 0.2$ cm. In Figs. 4.11 and 4.12, the performance of DeepTau v2.5 in comparison to the previous version (DeepTau v2.1) is shown in low-p_T ($p_T < 100\,\text{GeV}$) and high-p_T ($p_T > 100\,\text{GeV}$) regions correspondingly.

The identification efficiency is estimated from a $H \to \tau\tau$ sample using τ_h leptons labelled as genuine τ_h based on the definition in Section 4.3.1. The jet misidentification rate is determined from semi-leptonic $t\bar{t}$ MC event by using reconstructed τ_h candidates that do not match prompt electrons, muons, or τ_h decay products at the generator level. The electron and muon misidentification rates are estimated from Drell-Yan MC samples, focusing on reconstructed τ_h candidates that correspond to electrons or muons at the generator level.
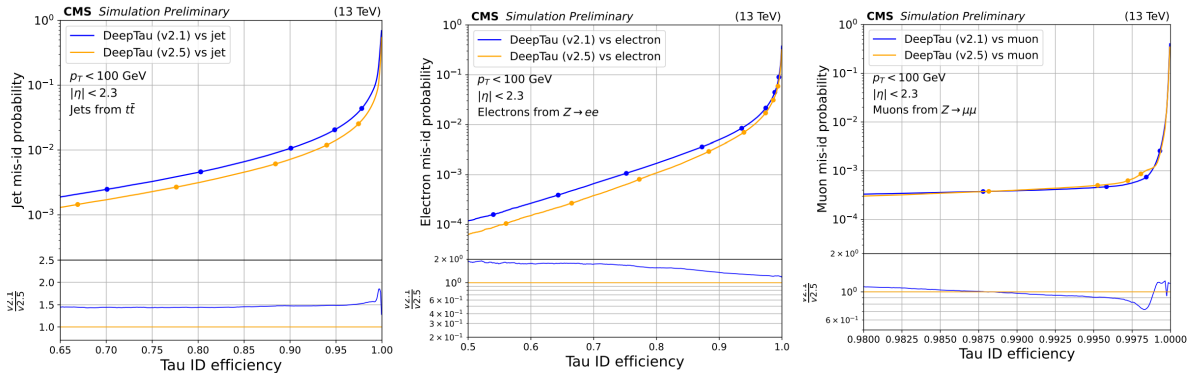

Figure 4.11: Receiver operating characteristic [8] is shown for classification vs jet (left), vs electron (central) and vs muon (right). The misidentification rate is shown as a function of signal efficiency. Jets are samples from $t\bar{t}$ and τ, electrons from $Z \to ee$, muons from $Z \to \mu\mu$ and genuine τ_h from $H \to \tau\tau$ MC samples. Plots are shown for a low-pt region with $p_T < 100\,\text{GeV}$.

For the same Tau ID efficiency, DeepTau v2.5 demonstrates a near 50% reduction of the jet misidentification rate with respect to v2.1. A reduction of up to two times is observed for the electron misidentification rate. The rate of misidentified muons is generally consistent with the previous version (v2.1), with minor divergences in the plots. The limited statistics cause these divergences since the misidentification rate for muons is already relatively high, making statistical uncertainties more noticeable in this area.

One of the critical ingredients of DeepTau v2.5 is the adversarial technique, which helps the model be trained, ignoring systematic differences between the two domains and reducing the gap between simulation and real-world performance. To study the effect of the aforementioned technique, the performance measured in the real data has to be compared with the MC-based performance. In the context of τ_h identification, a discrepancy of the efficiency between data and MC is characterised by *scale factors*, defined as the ratio of efficiency in data to efficiency in MC. This scale factor is a multiplicative factor for MC
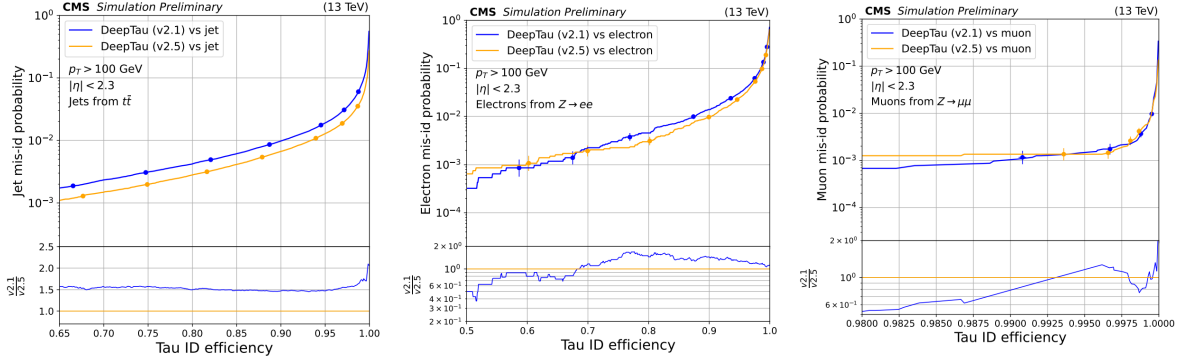
Figure 4.12: Receiver operating characteristic is shown for classification vs jet (left), electron (central) and muon (right). The misidentification rate is shown as a function of signal efficiency. Jets are samples from $t\bar{t}$ and τ, electrons from $Z \to ee$, muons from $Z \to \mu\mu$ and genuine τ_h from $H \to \tau\tau$ MC samples. Plots are shown for a high-pt region with $p_T > 100\,\text{GeV}$.

and is essential to model the behaviour of the τ_h in the real data. The τ_h identification efficiency scale factors are measured to quantify the improvement of the tagger modelling in actual data for the DeepTau v2.5.

The method followed to measure the τ_h identification efficiency for DeepTau v2.5 is the same as the one described in [120, 123] for DeepTau v2.1. The procedure is performed using a $\mu\tau_h$ events sample. Events are selected with the single-muon trigger, requiring the muon to have a nominal transverse momentum of $p_T > 25\,\text{GeV}$, $|\eta| < 2.4$, and a longitudinal impact parameter of $d_z < 0.2\,\text{cm}$. The τ_h is required to have $p_T > 20\,\text{GeV}$, $|\eta| < 2.3$, and $d_z < 0.2\,\text{cm}$. The selected muon and tau candidates must form a pair with opposite charges and a $\Delta R(\mu, \tau) > 0.5$ separation. The DeepTau working points selected for the measurement are Tight against jets, VVLoose against electrons, and Tight against muons. The efficiencies are determined through a maximum likelihood fit applied to the distribution of the reconstructed visible invariant mass of the $\mu\tau_h$ system. Within this fit, the ratio of the observed to the expected efficiency for a genuine τ_h to pass the selection criteria is treated as a free parameter, allowing the fit to yield a scale factor relative to the simulated efficiency.

The comparison of the corresponding scale factors for DeepTau v2.5 against DeepTau v2.1 as a function of $p_T(\tau_h)$ is shown in Fig. 4.13. These corrections are measured separately for each decay mode of τ_h since, in the general case, the scale factors vary significantly depending on the decay mode [8]. However, to demonstrate the effect of the adversarial technique comprehensively, weighted scale factors are calculated with respect to the τ_h branching ratios and HPS algorithm efficiencies per decay mode [119, 8]. The DeepTau v2.5 correction factors are significantly closer to unity (1.0) than the DeepTau v2.1 correction factors. The effect is more pronounced for low $p_T(\tau_h)$ values. This observation suggests that the new DeepTau version shows a decrease in mismodelling between data and MC.

The observed improvements in both data-to-MC agreement and overall performance in DeepTau v2.5 can be attributed to a combination of enhancements made in the algorithm. These include integrating domain adaptation techniques, specifically targeting data and
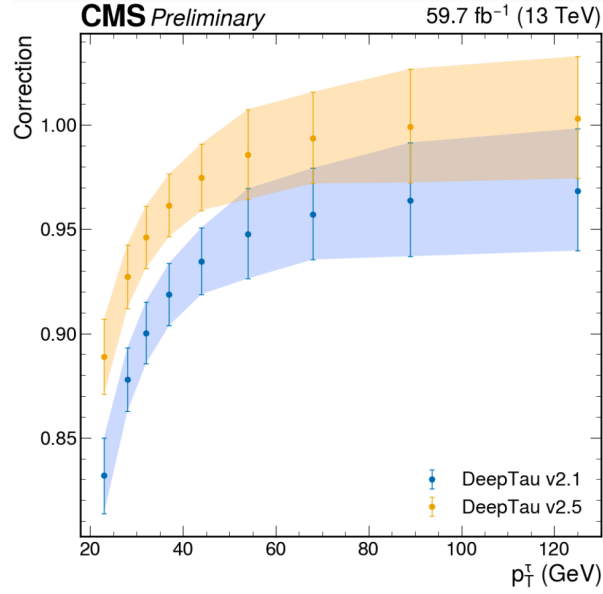
Figure 4.13: Measured correction factors for τ_h efficiency for Tight WP against jets, VVLoose WP against electrons and Tight WP against muons, which are weighted with respect to the τ_h decay branching ratios and hadron-plus-strip (HPS) algorithm efficiencies per decay mode [119, 8, 123].

simulation discrepancies, using more up-to-date datasets, rigorous feature standardisation, careful hyperparameter optimisation, and balanced data sampling. Rather than relying on a single modification, the collective impact of these advancements has led to a significant reduction in discrepancies between data and simulation and the general performance of the τ_h identification.

Chapter 5

Displaced tau reconstruction at CMS

Displaced τ could be an important signature for BSM searches in CMS detector. This signature is characterised by τ being produced at a significant distance from the IP. Corresponding is a suitable method of study and searches for various BSM scenarios, as detailed in Chapter 1. Direct searches for the process $\widetilde{\tau}^{\pm} \to \tau^{\pm} + \widetilde{G}$, where $\widetilde{G}$ is the LSP, are limited by the reconstruction efficiency of displaced τ leptons at CMS. These τ leptons can be produced at distances exceeding tens of centimetres from the interaction point (IP). As discussed in Section 4, the reconstruction of hadronic decays of τ is essential to study the physics processes with the involvement of τ lepton. However, CMS's current τ_{h} reconstruction algorithm is not designed for the displaced τ_{h} signature. This study focuses on improving the reconstruction of the displaced τ_{h} leptons in CMS.

The reconstruction of the displaced τ_{h} with the default HPS algorithm [119, 123] is discussed in Section 5.2. This default approach is less effective in such scenarios, leading to limited reconstruction efficiency performance. The efficiency of reconstructing displaced τ_{h} with the jet clustering algorithm is discussed in Section 5.3.3. The possibility of adapting ParticleNet [9] for identifying displaced τ_{h} is studied in Section 5.4. Adopting a ParticleNet-like architecture enables exploiting its powerful feature learning capabilities, facilitating robust and efficient displaced τ_{h} reconstruction.

As demonstrated in Section 5.5, the neural network successfully captures the internal characteristics of the signal, demonstrating its ability to separate the specific features of the τ_{h} from the other SM jets. Even though the model's training dataset was initially limited to jets sampled from a QCD MC sample, it demonstrated the capacity to effectively separate the signal from jets sampled from other MC processes, indicating its robust generalisation abilities across different jet types.

5.1 Displaced tau production mechanism

This study focuses on the τ leptons produced in the decay of long-lived $\widetilde{\tau}$ pairs. An illustration of a simulated event of di-$\widetilde{\tau}$ pairs, each decaying to τ_{h} and the LSP, is shown in Fig. 5.1.

The long-lived $\widetilde{\tau}$ simulation used in this study is detailed in Section 1.3, using the CMS simulation framework, which incorporates a full GEANT4-based simulation of the CMS detector, including realistic detector responses and reconstruction algorithms. This study uses a few representative mass points, specifically $m(\widetilde{\tau}) = 100$, 250, and 400 GeV, with a

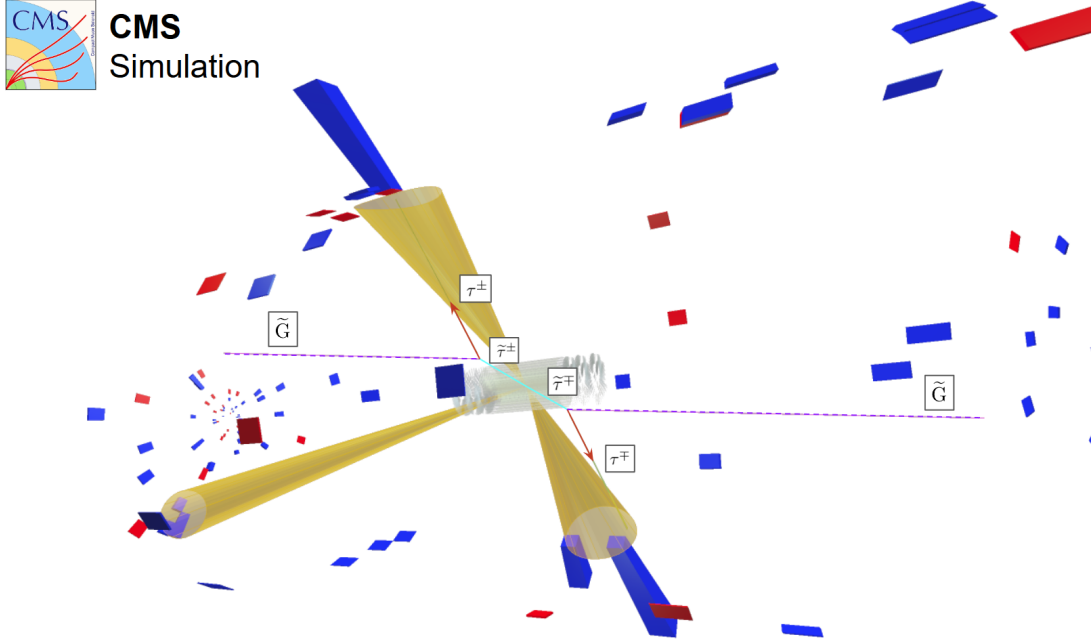Figure 5.1: The figure shows a simulated event scenario involving displaced di-τ_h in a long-lived stau model, where sleptons are the hypothetical supersymmetric partners of the τ lepton. In this event, the mass and proper decay length of the $\widetilde{\tau}$ are assumed to be 100 GeV and 10 cm, respectively. The paths of the long-lived $\widetilde{\tau}$ particles are illustrated by cyan lines, indicating their extended travel before decay. The direction of hadronic showers resulting from the decay of the τ_h leptons is shown in red arrows, highlighting the directionality of the hadronic decay products. The products of τ_h decays (charged and neutral pions) are shown with light green lines. Purple dotted lines represent the LSP. Yellow cones indicate AK4 jets. The red and blue towers represent the magnitude of the energy observed in the ECAL and the HCAL calorimeters, respectively.

proper decay length of 10 cm and 100 cm. Notably, these training events are not included in the analysis described in Chapter 6.

In Fig. 5.2, the kinematic properties of the τ_h are shown. Detectable final state children of τ_h are summed up to represent the visible component of the τ_h four-momentum, which is measurable experimentally. The distribution of the visible mass of the τ_h provides crucial validation of the simulated decay dynamics. The visible mass, $m_{\tau_\mathrm{h}}^{vis}$, is computed from the invariant mass of the decay products, including charged hadrons and neutral pions. The mass distribution exhibits a characteristic peak, corresponding to the resonance structures of intermediate states, such as the $\rho(770)$ and $a_1(1260)$ mesons. Its accurate representation indicates that the decay dynamics of the τ_h are modelled correctly. This simulation is used to study the τ_h reconstruction in the following sections.
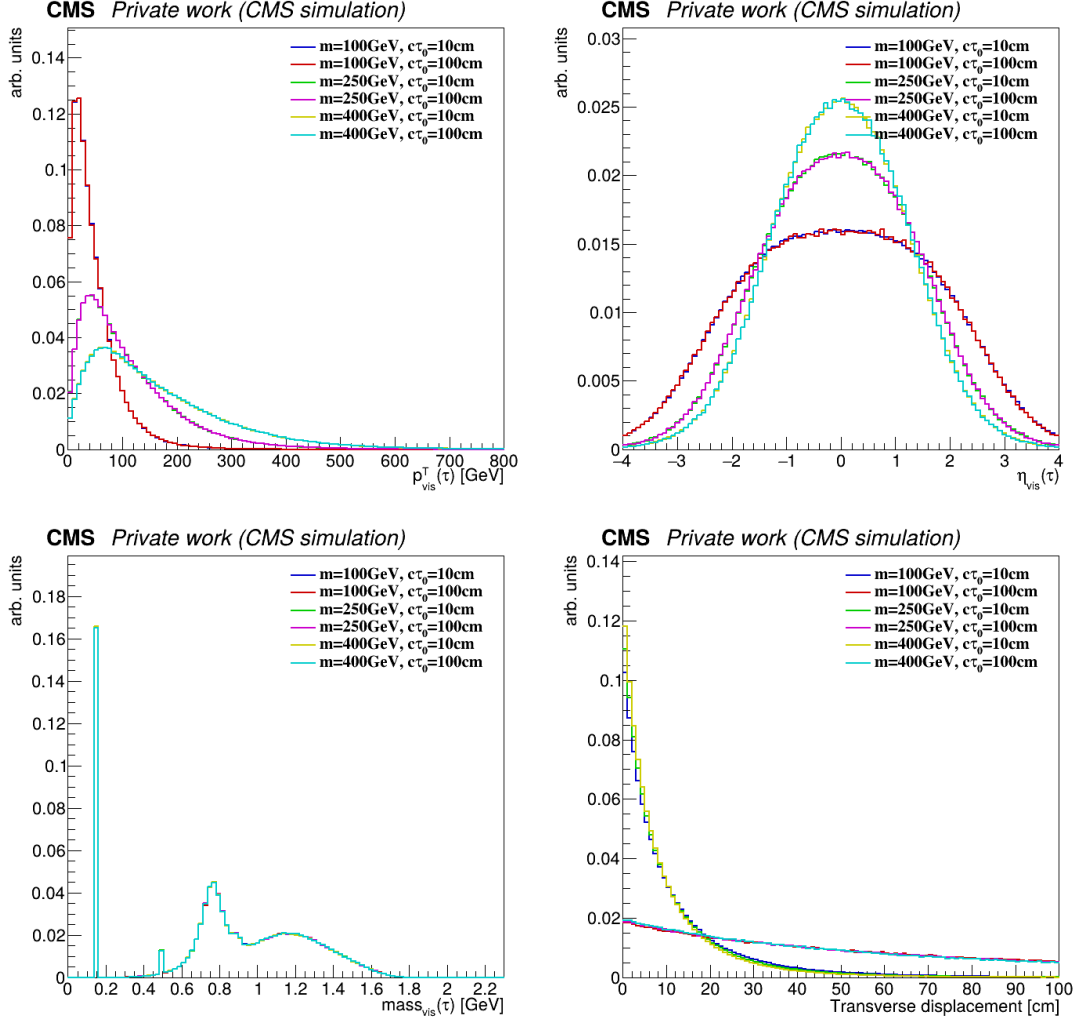
Figure 5.2: Generator-level kinematic properties of the τ_h lepton produced in long-lived $\widetilde{\tau}$ sleptons model for various lifetime scenarios. Visible transverse momentum, pseudorapidity, mass of τ and transverse displacement of the τ_h decay vertex in the detector coordinates are shown.

5.2 Displaced tau reconstruction with HPS

Section 4.2 discusses the fundamentals of the HPS algorithm. The limitation of the applicability of this algorithm for the reconstruction of displaced τ_h signature is shown in this section.

To study the τ_h reconstruction efficiency, τ_h decays reconstructed with the HPS algorithm are selected. On the generator level, τ_h are selected with visible $p_T > 20\,\text{GeV}$ and $|\eta| < 2.4$. The same kinematic selections are applied on the reconstruction level, only τ leptons that decay to hadrons are considered. In addition to reconstructed HPS τ_h, jets are investigated to see if they can serve as an object to *seed* the reconstruction of τ_h. For the following study, *AK4 CHS PFJets* are used [107], the reconstruction method of which is described in detail in Section 3.7. Jets are selected with consistent kinematic selections of $p_T > 20\,\text{GeV}$ and $|\eta| < 2.4$. A generator-level τ_h is considered successfully reconstructed if a jet or τ_h is reconstructed within a cone of radius $\Delta R < 0.4$ around it. The efficiency,

which is defined as $N^{matched}_{\tau_h}/N^{gen}_{\tau_h}$ for HPS τ_h and $N^{matched}_{jets}/N^{gen}_{\tau_h}$ for jets, is studied as a function of the transverse displacement between the PV and the τ_h production vertex $L_{xy} = \sqrt{(vtx_x(\tau) - vtx_x(PV))^2 + (vtx_y(\tau) - vtx_y(PV))^2}$. The resulting efficiency is shown in Fig. 5.3. Plots are displayed for $\widetilde{\tau}$ mass of $300\,\text{GeV}$ and proper decay length $c\tau_0 = 100\,\text{cm}$. The $\widetilde{\tau}$ decays to a τ lepton and a gravitino of mass $1\,\text{GeV}$, which is weakly interacting and escapes detection.
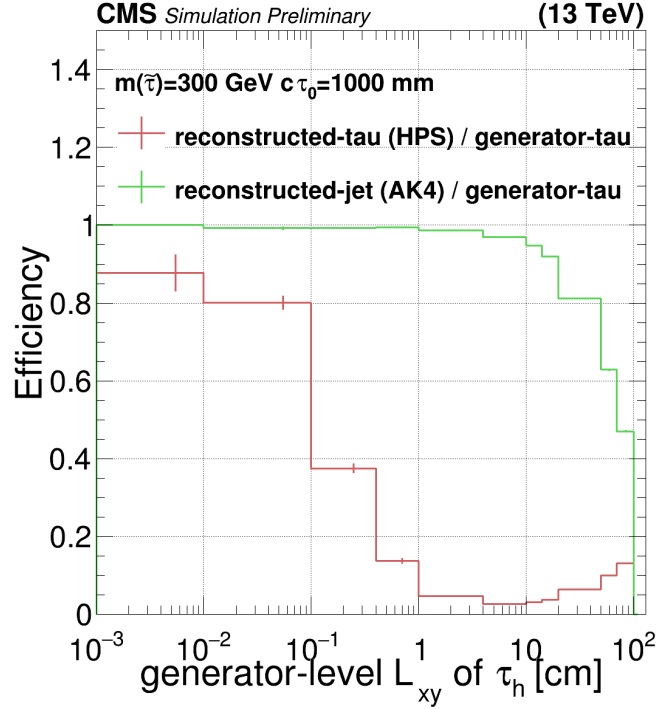
Figure 5.3: The fraction of displaced τ_h candidates that are reconstructed by the traditional HPS algorithm (red) and as *AK4 CHS PFJets* (green), as a function of the transverse displacement between the PV and the τ_h lepton production vertex (L_{xy}).

The efficiency of reconstructing τ_h leptons using the standard reconstruction algorithm decreases significantly for transverse displacements greater than $L_{xy} > 0.1 - 1.0\,\text{cm}$. This reduction in performance can be attributed to several factors. Among the primary contributors are the stringent quality cuts on the association of constituents with the PV enforced by the HPS algorithm, as well as the challenges in reconstructing tracks for significantly displaced charged hadrons, which are vital to the algorithm's overall performance. While these quality cuts are essential to filter out noise and fake signals, ensuring that only genuine particle signatures are considered, they can inadvertently reject displaced τ_h leptons. It should be emphasised that these factors represent only a subset of the potential limitations, and other mechanisms may also play a role in the observed performance loss. The standard reconstruction HPS algorithm was explicitly designed for prompt τ_h signatures and is not well-suited to handle the unique kinematic and spatial features of displaced τ_h leptons.

A small enhancement in efficiency is observed for significant displacements around $100\,\text{cm}$, where the $\widetilde{\tau}$ track, accompanied by calorimeter deposits, is misreconstructed as a charged hadron. The HPS algorithm might identify the $\widetilde{\tau}$ as a prompt τ_h. However, the reconstructed tau exhibits incorrect properties and can be suppressed by requiring consistent

p_T of the generator-level object with respect to the reconstructed object. It's worth noting that this phenomenon aligns with the regime where $\widetilde{\tau}$ is reconstructed as a final state particle. Such a signature is studied in Heavy Stable Charged Particle (HSCP) searches, which is not the primary focus of this study.
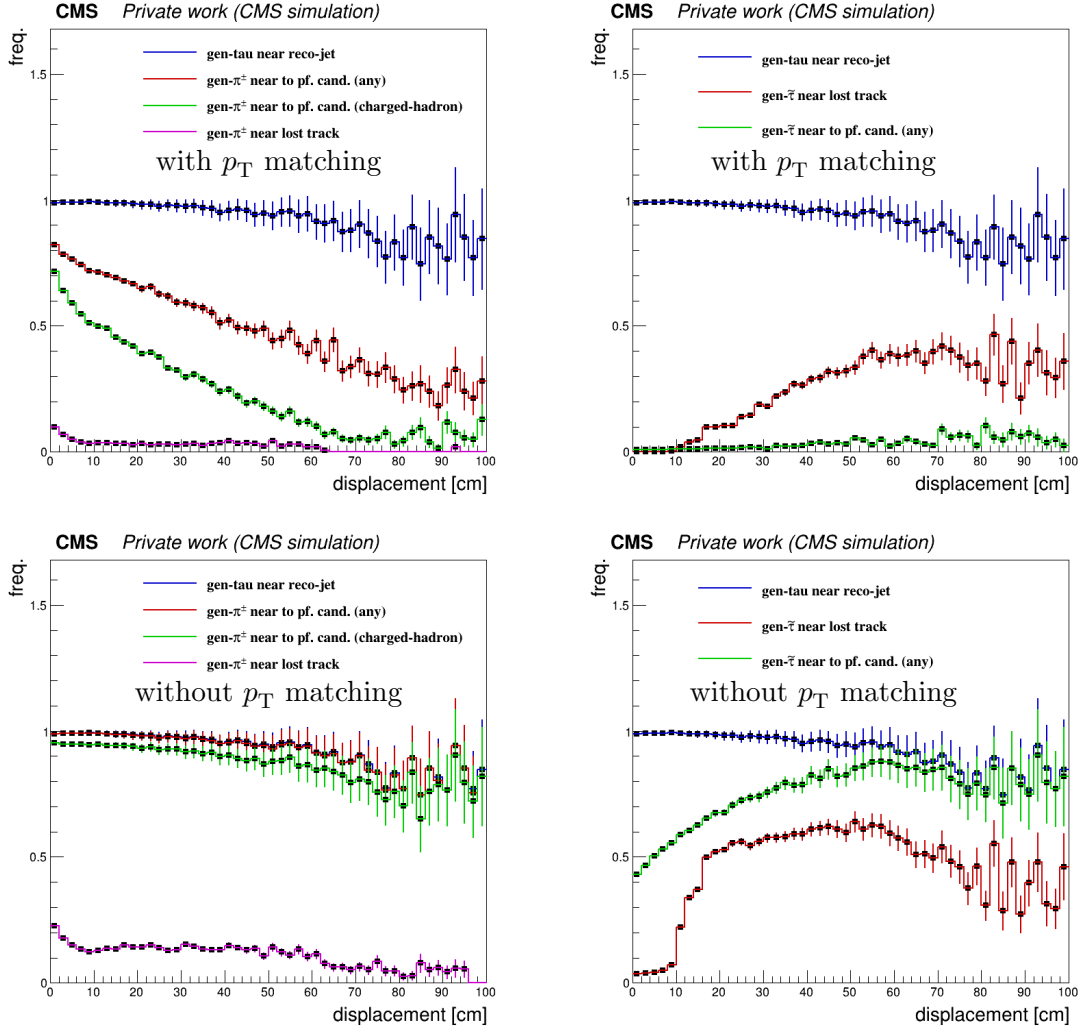

Figure 5.4: Efficiency of generator level τ_h matching to the reconstucted jets and HPS τ_h, shown together with $\pi^\pm$ matching to PF objects (left) and $\widetilde{\tau}$ matching to PF objects (right). The LSP mass equals $1\,\text{GeV}$, the $\widetilde{\tau}$ mass equals $400\,\text{GeV}$, and the $\widetilde{\tau}$ proper decay length is $c\tau_0 = 100\,\text{cm}$. The upper plots are shown, including the requirement that p_T of the generator-level $\pi^\pm$ or $\widetilde{\tau}$ matches the reconstructed object's p_T within a 20% (30%) margin, while this requirement is excluded in the bottom plots. A charged hadron is considered successfully matched if at least one of the charged hadrons originating from the τ_h decay is matched to a PF candidate.

The efficiency of reconstructing the charged component - predominantly $\pi^\pm$ from τ_h decays - is studied to understand how well τ_h is reconstructed at the level of its constituent particles. Figure 5.4 presents the frequency at which charged hadrons from τ_h are reconstructed as charged hadrons using the PF algorithm, misreconstructed as other PF objects, or identified as lost tracks. The matching criterion requires the reconstructed

object to be within a distance of $\Delta R < 0.2$ from the generator-level charged hadron.

The upper plots in Fig. 5.4 include the requirement that the relative p_T difference, defined as $p_T^{rel} = (p_T^{reco} - p_T^{gen})/p_T^{gen}$, remains within 20%. Conversely, the bottom plots illustrate the efficiency without this p_T matching requirement. A charged PF candidate match is successfully reconstructed if at least one generator-level charged hadron from τ_h is matched. The left-hand side of the plots displays the matching efficiency for charged hadrons from τ_h, while the right-hand side focuses on the $\widetilde{\tau}$ reconstruction, highlighting their reconstruction behaviours. The $\widetilde{\tau}$ can produce a detectable track in the detector, particularly at high displacements, which might interfere with the reconstructed jet structure. To assess the impact of the $\widetilde{\tau}$ track on jet reconstruction, its proximity to reconstructed objects within the jet is examined. The right-hand side of Fig. 5.4 specifically illustrates the frequency of the $\widetilde{\tau}$ being reconstructed as either a lost track or a PF candidate, including cases with relative p_T matching. The $\widetilde{\tau}$ is considered matched if the reconstructed object is within $\Delta R < 0.2$, and the relative transverse momentum difference (p_T^{rel}) is within 30%.

The results demonstrate that the efficiency of reconstructing charged hadrons as PF candidates or lost tracks declines sharply with increasing displacement. This trend is particularly pronounced at large displacements ($> 50\,\mathrm{cm}$), where the charged hadron reconstruction efficiency approaches zero. However, the plots without the p_T matching requirement reveal an important observation: while highly displaced constituents from τ_h may not always be reconstructed with accurate p_T, the generator-level $\pi^\pm$ or $\widetilde{\tau}$ is still frequently close to the reconstructed objects. This suggests that even when these displaced objects are not fully reconstructed, they can leave a significant footprint at the reconstruction level, potentially influencing the reconstructed object's properties.

The findings indicate that the $\widetilde{\tau}$ track significantly influences jet reconstruction, especially at large displacements where charged track reconstruction efficiency declines considerably. In addition to the τ_h constituents, the $\widetilde{\tau}$ track contributes to the residual efficiency of jet reconstruction. This contribution helps compensate for missing charged hadrons or π^0-related products that do not satisfy the matching criteria, thereby maintaining a degree of reconstruction efficiency even under challenging conditions.

In summary, the investigation highlights the importance of incorporating PF candidates and lost tracks to enhance the reconstruction of τ_h leptons. Including both is critical for improving efficiency and accurately identifying displaced τ_h signatures. However, including lost tracks may introduce a particular bias of the reconstruction to cases of τ_h production from $\widetilde{\tau}$ and limit robustness across different physics cases of τ_h production.

5.3 Object selection

This section describes the selection of objects used in the development of displaced τ_h tagging. The aforementioned observation of a displaced τ_h signature in the detector suggests that *AK4 CHS PFJets* and its particle flow constituents, as well as lost tracks, play crucial roles in the reconstruction of such τ_h. The proper selection of these objects is essential for ensuring the reliability and integrity of the displaced τ_h signature reconstruction.

5.3.1 Particle-flow objects

Particle-flow objects are essential for the displaced τ_h reconstruction. The detailed reconstruction mechanism of these objects is discussed in Section 3.4. These objects are photons, electrons, muons, charged hadrons and neutral hadrons that form jets as described in Section 3.7. In this study, two methods of PF object selection are used:

1. **Jet PF constituents collection**: After *AK4 CHS PFJets* are clustered, jet constituents are provided as an object of consideration to the reconstruction algorithm.

2. **All PF objects close to the jet**: It was shown that using all the PF candidates around *AK4 CHS PFJets* is particularly efficient for prompt τ_h identification [123, 119, 8]. In this study, the alternative is to consider all PF candidates within a distance of $\Delta R < 0.5$ to *AK4 CHS PFJets*, as it provides particularly useful information about the isolation of the object.

5.3.2 Lost track objects

Lost track objects refer to charged particles, such as electrons, muons, or hadrons, that are not associated with any PF candidate. Such charged particles might not be successfully reconstructed as PF candidates for various reasons, such as low momentum or inefficient reconstruction. Even though these particles leave hits in the tracker, they might fail to have a corresponding energy deposition signature in the calorimetric system and do not form PF candidates. To retain information about these particles, CMS stores them in a dedicated collection called *lost tracks*. These *lost tracks* are essentially high-purity charged tracks reconstructed by the tracking system but not matched to PF candidates. They are essential for capturing low-momentum particles, which might be crucial in specific physics analyses, such as those involving displaced decays or low-energy particles. Lost tracks are selected within a distance of $\Delta R < 0.5$ to *AK4 CHS PFJets*.

As demonstrated in Section 5.2, in the case of highly long-lived $\widetilde{\tau}$, it can be reconstructed as a lost track. In the case of GMSB models, considering lost tracks might increase the performance. However, it is essential to mention that relying on the lost tracks reconstruction might make τ_h valid only for specific scenarios of the GMSB topology and not generally for displaced $\widetilde{\tau}$ reconstruction.

5.3.3 Seeding jets

As discussed in Section 5.2, *AK4 CHS PFJets* can be used to *seed* the reconstruction of the displaced τ_h. Section 3.7 gives a detailed overview of the jet reconstruction algorithm. To investigate the efficiency of τ_h reconstruction with such jets, central jets are selected with a requirement of $p_T > 20\,\text{GeV}$ and $|\eta| < 2.4$. These selection criteria are sufficient to select the majority of signal jets. The generator-level τ_h are chosen with a consistent requirement of $p_T > 20\,\text{GeV}$ and $|\eta| < 2.4$.

A matching between the generator-level visible components of τ_h and reconstructed jets is performed, assuming the matching criteria $\Delta R(jet, \tau_h) < 0.4$. The efficiency is defined as the ratio of the generator-level τ_h that has a jet associated with it and the number of

all generator-level τ_{h} leptons ($eff. = N_{jets}^{matched}/N_{\tau}^{gen}$). It is shown as a function of L_{xy} in Fig. 5.5 and as a function of the visible τ_{h} transverse momentum in Fig. 5.6.
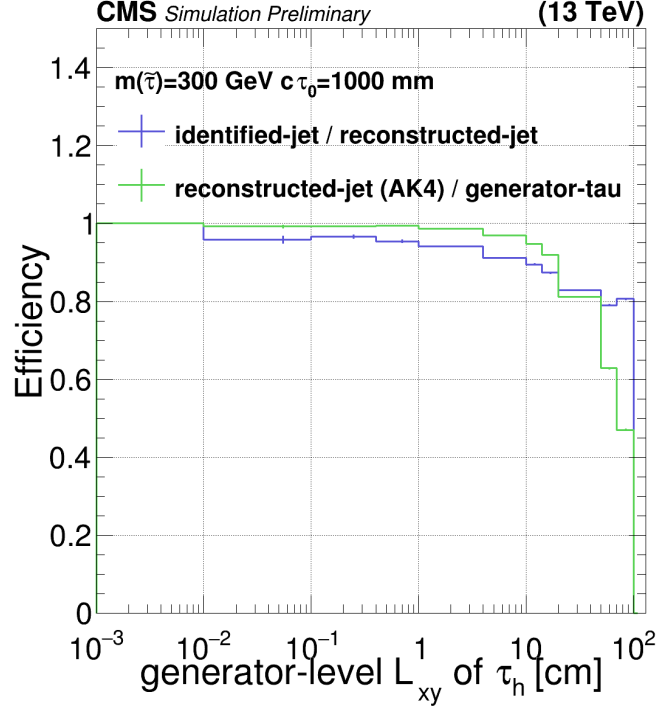

Figure 5.5: Reconstruction efficiency of the displaced τ_{h} with the AK4 CHS jet (green) and identification efficiency of the corresponding jet with tight jet id (blue), for different bins of generator level transverse displacement L_{xy}. These events are generated with a $\tilde{\tau}$ mass of 300 GeV, an LSP mass of 1 GeV and a proper decay length of $c\tau_0 = 1$ m.

Additionally, the efficiency of the corresponding jet to pass the tight jet identification criteria is studied. However, it is essential to note that for training the neural network-based tagger, the application of jet identification is not a prerequisite.

The reconstruction efficiency for τ_{h} leptons with jets drops when L_{xy} approaches $\sim$ 70-100 cm. However, it does not drop to zero due to the matching with noise and the presence of the initial $\tilde{\tau}$ track. The reconstruction efficiency for different hypothetical $c\tau_0$ of the $\tilde{\tau}$ is shown in Fig 5.6 as a function of p_{T}. The reconstruction efficiency is significantly worse at low p_{T}, as low-p_{T} displaced objects are generally more difficult to reconstruct due to their smaller energy deposition and the limited sensitivity of the tracking and calorimeter systems for low-energy particles. As p_{T} increases, the reconstruction efficiency improves significantly. This behaviour is attributed to the fact that high-p_{T} particles leave more prominent signals in the detector. The jet identification efficiency stays at $\sim$ 80% for $p_{\text{T}} > 300$ GeV.

In Fig. 5.7, the resolution of the reconstructed jet p_{T} is shown. For highly displaced τ_{h}, the matched reconstructed jet has lower momentum compared to the generator-level τ_{h}. A detailed investigation has shown that, for a proper decay length of $c\tau_0 = 10$ m, a considerable fraction of τ_{h} at the generator level matches with jets originating from pileup and detector noise. Additionally, the presence of a track from a $\tilde{\tau}$ decay further complicates the reconstruction process, as these tracks can be associated with PF candidates and
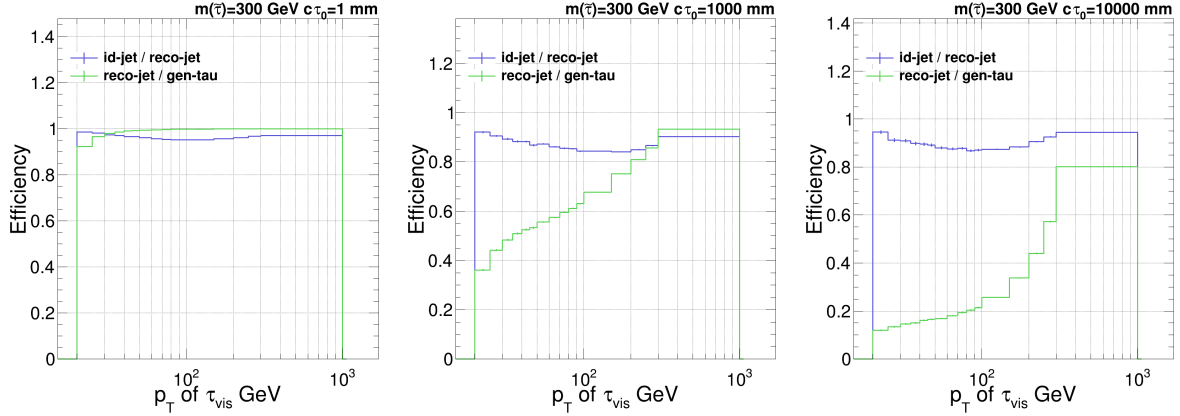
Figure 5.6: Reconstruction efficiency of displaced τ_h with the AK4 CHS jet (green) and identification efficiency of the corresponding jet with tight jet id (blue), for different bins of generator-level transverse visible momentum of τ_h. The left plot corresponds to a proper $\widetilde{\tau}$ decay length of 1 mm, the central plot to 1000 mm, and the right plot to 10000 mm.

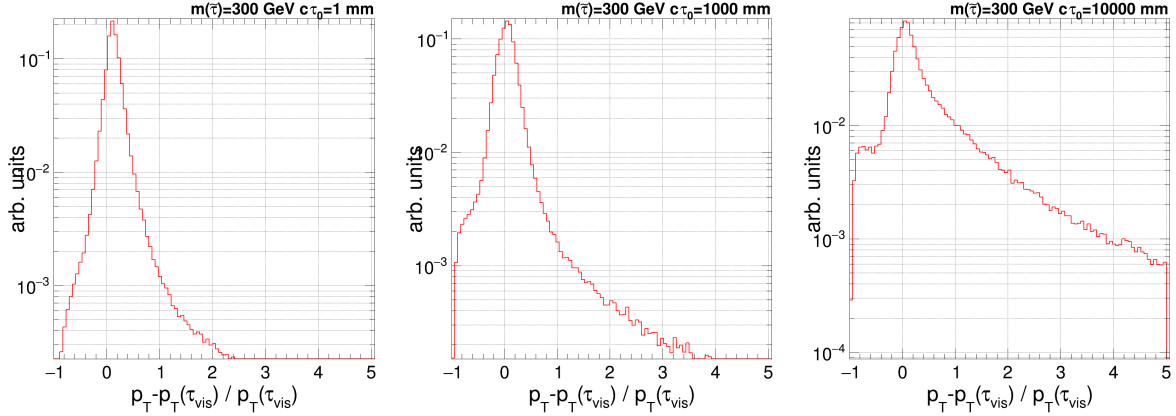Figure 5.7: Momentum resolution of the displaced τ_h with respect to the AK4 CHS jet momentum. The p_T represents the transverse momentum of the reconstructed jet $p_T(\tau_{vis})$ is the visible component of the transverse momentum of the τ_h. The left plot corresponds to a proper $\widetilde{\tau}$ decay length of 1 mm, the central plot to 1000 mm, and the right plot to 10000 mm.

considered during jet clustering.

To mitigate the impact of these effects on the reconstruction and ensure a cleaner signal, the generator-level $\widetilde{\tau}$ decay vertex was limited to 1 m in the z-direction and 50 cm in the transverse plane. Imposing these spatial constraints helps to leave events with displacements of the order of tens of centimetres. This ensures that the objects in the training dataset have relatively clean detector signatures as *AK4 CHS PFJets* without $\widetilde{\tau}$ tracks.

5.4 Neural-network-based displaced tau tagger

The following describes a new DisTau tagger algorithm based on Graph Neural Networks (GNN) for identifying displaced τ_h signatures, utilising an architecture similar to ParticleNet [9]. The algorithm is designed to distinguish displaced τ_h jets from those primarily originating from light quarks and gluons. In the following section, the choice of the neural

network architecture, as well as the specific input pre-processing, is discussed.

The training of the displaced τ_h tagger background is based solely on the τ_h leptons from the SUSY MC signal and the jets from QCD MC samples due to several considerations. QCD MC provides diverse jet types, including gluon jets, light-quark jets, and heavy-flavour jets, representing the dominant backgrounds in the current analyses. Firstly, this ensures sufficient coverage of relevant jet topologies and kinematics while avoiding the need for additional MC samples, such as $t\bar{t}$ or W+jets, which typically do not introduce significant new information. Secondly, considering only QCD MC minimises the overlap with the potential background simulation used further in the analysis in the control and validation regions. Furthermore, it ensures computational efficiency by limiting the training to the essential background dataset since the number of MC events for the signal process is highly limited, and a low amount of background events is required. While additional MC samples may be used for validation, their inclusion in the training will unlikely provide substantial improvements, given the robust generalisation achieved with QCD jets alone.

5.4.1 Labeling procedure

Following the approach mentioned in Section 4.3.1, the ground-truth labels for training the displaced τ_h tagger are defined based on generator-level information and then sampled from signal and QCD MC. Specifically, generator-level τ_h leptons are sampled from signal MC, while jets are taken using generator-level jets from QCD MC.

Reconstructed jets are selected with transverse momentum $p_T > 20\,\text{GeV}$ and pseudorapidity $|\eta| < 2.4$, to ensure they fall within the detector's sensitive region.

In this study, τ_h leptons are specifically considered, excluding leptonically decaying τ_h leptons and prompt electrons and muons from the training. Generator-level τ_h leptons are selected with $p_T > 20\,\text{GeV}$ and $|\eta| < 2.4$ and are required to have a displacement with respect to the PV within the ranges $|z| < 100\,\text{cm}$ and $\rho < 50\,\text{cm}$ for the reasons of tagger generalisation described above.

If τ_h or lepton is found within $\Delta R < 0.4$ to the reconstructed jet, the jet is matched to the generator-level jet within $\Delta R < 0.4$. If the matching criteria are satisfied, the jet is labelled as a genuine jet (τ_j).

The DisTau tagger is trained to separate the τ_h class from τ_j as its objective, with the possibility of vetoing leptons in the later stages of the analysis. However, a more extensive range of classification categories might be adopted in future developments.

The dataset is limited to 5.3 million τ_h objects. The τ_j objects are sampled from QCD MC to correspond to the available signal sample. This sums up to 11.6 million jets for the training.

5.4.2 Input preprocessing

Two types of objects described in Section 5.2 are provided to the deep neural network (DNN) input: particle flow candidates (26 features) and lost tracks (21 features). Using the jet properties is intentionally avoided to enforce the NN to learn intricate patterns

and relationships directly from the raw data and not depend on the jet reconstruction algorithm.

The particle flow candidates serve as the core input to the model. Their features can be categorised into three groups: object kinematics, track information, and calorimeter information. A detailed description of each feature and its role is provided in Table 5.2.

Lost tracks serve as valuable input to the model, as they might help to aid in the reconstruction of charged tau constituents (charged pions) when the calorimeter does not capture the energy of such charged pions. The primary features of lost tracks include track kinematics and track information. A detailed description of each feature and its role is shown in Table 5.1.

The particle cloud-based architecture [9] allows for a flexible input structure, handling a variable number of objects of each input type. Due to technical constraints, the number of objects provided to the NN is limited to 50 particle flow candidates and five lost tracks, selecting p_T-leading objects. This approach ensures computational feasibility while preserving the robustness of data interpretation. The input point cloud features are provided together with the object's coordinates, pseudorapidity ($\Delta\eta$) and azimuthal angle ($\Delta\phi$) with respect to the jet momentum direction. It is essential to mention that three configurations of input are studied:

1. Providing particle flow constituents of *AK4 CHS PFJets*.

2. Providing all particle flow candidates within a distance of $\Delta R < 0.5$ to *AK4 CHS PFJets*.

3. Providing all particle flow candidates and lost tracks within a distance of $\Delta R < 0.5$ to *AK4 CHS PFJets*.

All input features undergo a pre-processing step to ensure data consistency and maintain neural network stability. Non-defined values (e.g., NaNs) and infinities are identified and removed to prevent disruptions during training. Features that are inherently integer-based or exhibit a significantly non-Gaussian distribution within a finite range are normalised using linear transformations, scaling their values to lie within predefined intervals, such as $[-1, 1]$ or $[0, 1]$. Additionally, inputs are truncated to ensure they remain within their respective valid ranges, thereby mitigating the impact of outliers.

This pre-processing step is critical for optimising the neural network's performance, as it ensures that all features contribute equally during training and avoids biases caused by disparate value ranges or extreme outliers. Furthermore, normalisation enhances the efficiency of the learning process by enabling faster convergence and reducing the likelihood of numerical instability.

For features with narrow distribution peaks, standardisation is applied:

$$x \to \frac{x - \mu}{\sigma},$$

where μ and σ represent the mean and standard deviation of the feature, estimated from the training set. This standardisation ensures equal contribution from all features during training and enhances model accuracy. Standardised inputs are truncated to the range $[-5, 5]$ to protect the training from outliers. These pre-processing steps optimise the neural network's ability to learn and discern patterns effectively.

Table 5.1: Parameters of the lost track constituents. Corresponding parameters are used as an input to NN.

Vars.	Std. Tr.		Linear Tr.	Variable Description
	σ	μ	$[a, b]$	
η	-	-	$[-3, 3]$	Pseudorapidity
ϕ	-	-	$[-3.15, 3.15]$	Azimuthal angle
$ln(p_{\mathrm{T}})$	-	-	$[-4.0, 7.0]$	Logarithm of the transverse momentum
$ln(E)$	-	-	$[-4.0, 7.0]$	Logarithm of the energy
charge	-	-	-	Electric charge
nPixelHits	-	-	$[0, 10]$	Number of valid hits in the pixel tracker
nHits	-	-	$[0, 30]$	Total number of valid hits
hasTrackDetails	-	-	-	Boolean to define if object has tracker information
dxy	6.138	-0.06467	-	Signed transverse impact parameter with respect to the the PV
$dxy/\sigma(dxy)$	132.8	-1.321	-	Significance of the transverse impact parameter
dz	18.66	-0.09124	-	Impact parameter in $z - axis$ with respect to PV
$dz/\sigma(dz)$	789.8	-1.303	-	Significance of the dz
χ^2/ndf	2.141	0.8883	-	Chi-square per degree of freedom of the pseudo track
ndof	5.217	8.5	-	Number of degrees of freedom of the pseudo track
particleType	-	-	$[0, 9]$	Encoded type of reconstructed object
pvAssociationQuality	-	-	$[0, 9]$	Quality of the association of the Lost Track to the PV
fromPV	-	-	$[0, 5]$	Encoded value that defines the association of PV
$\Delta\eta$	-	-	-	Difference in pseudorapidity between the lost track and reconstructed jet
$\Delta\phi$	-	-	-	Difference in azimuthal angle between the lost track and reconstructed jet

Table 5.2: Parameters of the PF constituents. Corresponding parameters are used as an input to NN.

Variable name	Normal transformation		Linear transformation	Variable Description
	σ	μ	$[a, b]$	
η	-	-	$[-3, 3]$	Pseudorapidity
ϕ	-	-	$[-3.15, 3.15]$	Azimuthal angle
$ln(p_\mathrm{T})$	-	-	$[-4.0, 7.0]$	Logarithm of the transverse momentum
$ln(E)$	-	-	$[-4.0, 7.0]$	Logarithm of the energy
charge	-	-	-	Electric charge
puppiWeight	-	-	-	Weight from full PUPPI algorithm
puppiWeightNoLep	-	-	-	Weight from PUPPI algorithm removing leptons
lostInnerHits	-	-	$[-1, 5]$	Number of lost inner hits
nPixelHits	-	-	$[0, 10]$	Number of valid pixel hits
nHits	-	-	$[0, 30]$	Total number of valid hits
hasTrackDetails	-	-	-	Boolean that define whether the PF candidate has track information
dxy	2.37	-0.0160	-	Signed transverse impact parameter with respect to PV
$dxy/\sigma(dxy)$	135.4	-0.5032	-	Significance of the transverse impact parameter
dz	7.466	-0.0159	-	Impact parameter in $z - axis$ with respect to PV
$dz/\sigma(dz)$	588.0	-2.178	-	Significance of the dz
χ^2/ndf	3.681	0.7833	-	Chi-square per degree of freedom of the pseudo track associated to the PF candidate
ndof	6.494	13.61	-	Number of degrees of freedom of the pseudo track associated to the PF candidate
caloFraction	-	-	$[0, 2]$	Fraction of ECAL for HF tower, neutral hadrons and isolated charged hadrons
hcalFraction	-	-	$[0, 1]$	Fraction of HCAL for HF tower, neutral hadrons and isolated charged hadrons
rawCaloFraction	-	-	$[0, 2.6]$	Raw ECAL energy over candidate energy for isolated charged hadrons
rawHcalFraction	-	-	$[0, 1]$	Raw HCAL energy over candidate energy for isolated charged hadrons
particleType	-	-	$[0, 9]$	Encoded type of the reconstructed PF candidate
pvAssociationQuality	-	-	$[0, 9]$	Quality of the association of the PF candidate to the PV
fromPV	-	-	$[0, 5]$	Encoded value type of association of the PF candidate to PV
$\Delta\eta$	-	-	-	Difference in pseudorapidity between the PF candidate and reconstucted jet
$\Delta\phi$	-	-	-	Difference in azimuthal angle between the PF candidate and reconstructed jet

5.4.3   Network architecture

The architecture of the DisTau tagger is designed to efficiently capture relevant information while maintaining computational performance suitable for practical use in physics analyses. Recent developments in jet tagging have demonstrated the increasing adoption of GNNs, which are particularly well-suited for representing jets as sets of constituents with relational structure. Graph-based models have emerged as a state-of-the-art solution in this domain due to their ability to exploit the underlying geometry of jets.

Multiple factors underlie the effectiveness of GNNs in jet tagging tasks:

- **Hierarchical Representations:** GNNs excel in learning hierarchical representations by combining information from multiple levels, such as the features of individual particles and the overall structure of the jet. This ability enables the model to capture local and global patterns, essential for distinguishing subtle differences between displaced τ_{h} leptons and other background jets.

- **Variable Input Size:** Unlike traditional architectures requiring fixed inputs, GNNs are inherently flexible and can process a changing number of particles within each jet. This adaptability is crucial for jet tagging, where the number of constituent particles varies between the different jets.

- **Robustness to Noise and Missing Data:** GNNs have shown resilience in handling noisy or incomplete data, a common occurrence in experimental environments. This robustness ensures that the model can maintain performance even when detector inefficiencies or artefacts introduce inconsistencies in the input features.

- **Empirical Success in Jet Classification:** GNNs have been empirically proven to perform efficiently in jet classification tasks, demonstrating superior accuracy and generalisation compared to traditional feedforward networks or convolutional architectures.

Given these advantages, the ParticleNet architecture, a specialised GNN variation, was chosen as the backbone of the DisTau tagger. ParticleNet's dynamic edge convolutional layers are particularly effective in capturing relational features between particles within a jet, enabling the tagger to extract high-level representations directly from low-level detector information. Moreover, its scalability and computational efficiency make it feasible for large-scale analyses. In our case, the particles are represented as nodes in the graph. The central component of this architecture is the edge convolution (EdgeConv) operation. The EdgeConv operation helps to process point cloud-like data effectively and is central to information aggregation from neighbouring nodes. A more detailed description of the architecture is given below.

5.4.3.1   Node features padding

To combine particle flow candidates and lost track objects for the classification of the jet, attention has to be paid to the following: Firstly, the information about the object type needs to be encoded to inform the neural network about differences in the object's properties. Secondly, it would be beneficial to process objects of both types together to be sensitive to the relative position of neighbouring nodes across all the objects. For this

purpose, padding is applied as illustrated in Fig 5.8; the first 26 positions in each node's feature are preserved for particle flow objects and the next 21 for lost tracks. Then, each node is pre-processed with two hidden layers of the dense neural network, with a rectified linear unit activation function (23 neurons each), to produce 30 output features for each node. Then these 30 features, together with $\Delta\eta$ and $\Delta\phi$, are used as an input directly to edge convolution layers. After experimentation, it was empirically decided that this approach yielded the best results in terms of classification performance.
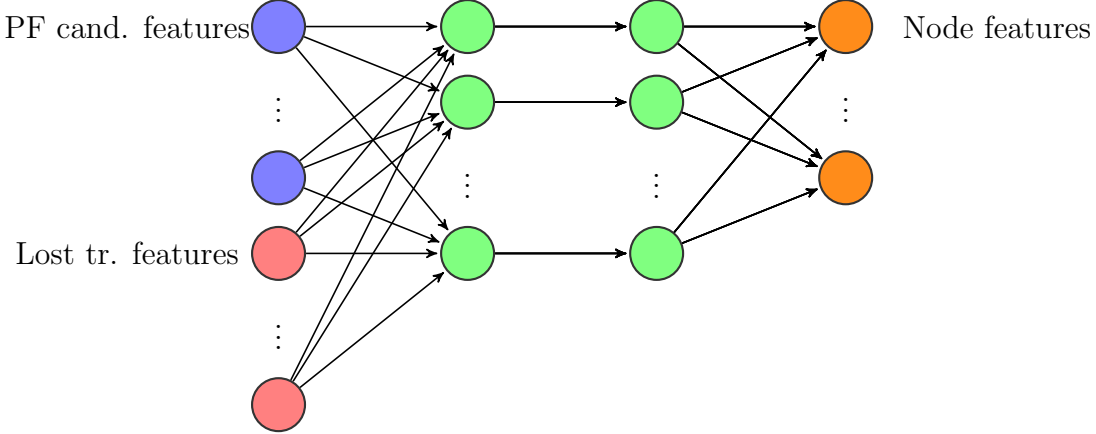
Figure 5.8: Illustrative diagram of node feature pre-processing.

5.4.3.2 EdgeConv operation

Constructing the k-nearest neighbour (k-NN) graph is the first step in applying the Edge-Conv operation. The graph is built using the relative coordinates of the particles with respect to the jet axis, specifically $\Delta\eta$ and $\Delta\phi$. These coordinates facilitate the computation of distances necessary to determine the graph's connected neighbours.

Let $\mathbf{X} = \{\mathbf{x}_1, \mathbf{x}_2, ..., \mathbf{x}_n\}$ represent the set of nodes (particle-flow candidates or lost tracks) features in the graph, where $\mathbf{x}_i$ is the feature vector of node i. The EdgeConv operation in ParticleNet transforms these features as follows:

$$\mathbf{x}'_i = \bigoplus_{j \in \mathcal{N}(i)} h_{\Theta}(\mathbf{x}_i, \mathbf{x}_j - \mathbf{x}_i), \tag{5.1}$$

where $\mathbf{x}'_i$ is the updated feature vector of a node i, $\mathcal{N}(i)$ denotes the set of neighbouring nodes of i, and h_{Θ} is a learnable function parameterized by Θ that aggregates the features of node i and its neighbors. The operator $\bigoplus$ represents an aggregation operation over the neighbours, such as summation, mean or maximal value. In the following architecture, the mean value is used as the aggregator, which was proven to have the best performance for the ParticleNet case [9]. To construct the corresponding graph, the first EdgeConv block uses the spatial coordinates of the particles with respect to the jet axis $\Delta\eta$, $\Delta\phi$ to compute the distances. In contrast, the subsequent blocks use the learned feature vectors as coordinates.

The subtraction $\mathbf{x}_j - \mathbf{x}_i$ ensures that the aggregation is sensitive to the relative position of neighbouring nodes in the feature space. The illustration of EdgeConv block is shown in

Fig. 5.9. The input to h_Θ consists of a concatenation of the node features and the pairwise differences between each node and its neighboring nodes, represented as $\{f_1^i, f_2^i, ..., f_n^i, f_1^i - f_1^j, f_2^i - f_2^j, ..., f_n^i - f_n^j\}$, where f_k^n denotes the k-th feature of the n-th node. This combined representation is referred to as the set of *edge features*.
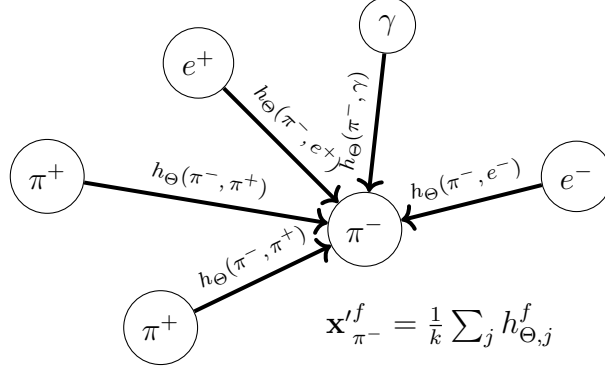

Figure 5.9: Illustrative diagram of the EdgeConv operation in ParticleNet. Each node represents a particle flow or lost track object.

To process the edge features, three layers of a multi-layer perceptron (MLP) network are used as an h_Θ function. Each layer involves a sequential process starting with a linear transformation, then applying batch normalisation, and rectified linear unit (ReLU). Each block also incorporates a shortcut connection parallel to the EdgeConv operation, enabling direct passage of input features, following an idea first used for ResNet [148].

One of the advantages of EdgeConv is that this operation is stackable, which is achieved by keeping the number of nodes constant and changing only the dimension of the feature vector. Because of this advantage, one can build an effective deep neural network utilising high-level and low-level information in the data.

5.4.3.3   Baseline architecture design

In the design of the DisTau tagger, the complexity of ParticleNet is simplified to make it computationally less expensive with a larger number of input features than the original ParticleNet. As mentioned above, three input types are used, which results in 3 different architectures: based on jet constituents, particle flow candidates in $\Delta R < 0.5$ and a combined model containing particle flow candidates together with lost tracks in $\Delta R < 0.5$. The detailed hyperparameter tuning was performed, and the results are described in Appendix. A.3. Here, the best model chosen as a baseline for analysis purposes with $\approx 104 \times 10^3$ trainable parameters that utilise PF objects and lost tracks is described.

The network architecture, shown in Fig. 5.10, begins by pre-processing the features of every particle flow candidate and lost track with the dense neural network to unify the dimensionality of the feature vector to 30 features as described above. Each node's 30 features together with $(\Delta\eta, \Delta\phi)$ coordinates are provided in the input of the first Edge Convolution layer.

As already described, the k-nearest neighbours are derived based on the coordinate features on the first layers of ParticleNet. After this, all subsequent EdgeConv blocks use all derived features for corresponding purposes while preserving the number of nodes. The

EdgeConv1 graph is built with k=9 nearest neighbours, containing three layers with 32 neurons each. The number of neighbours k=9 was sufficient for the displaced τ_h, while it allows for the computational complexity to be low enough. In ParticleNet, when the number of nodes is smaller than k=9, padding introduces artificial interactions due to empty nodes, potentially distorting the feature representation and negatively impacting model performance. A smaller k helps minimise these adverse effects in graphs with fewer nodes, which is sufficient for the τ_h case.
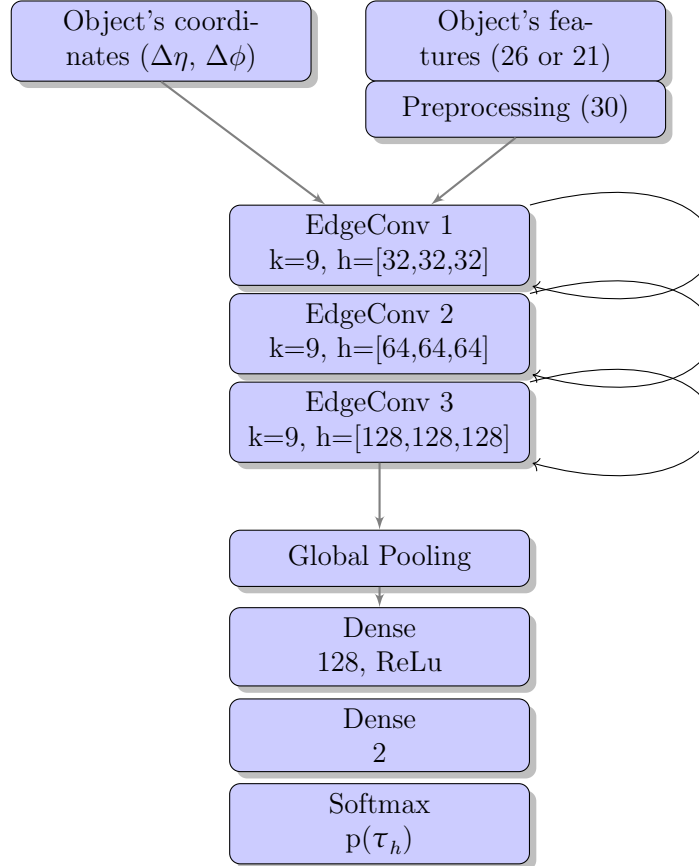
Figure 5.10: Architecture of DisTauTag tagger.

The second and third layers are constructed with k=9 neighbours but with a more complex hidden layer configuration of 3 layers with 64 neurons and three layers with 128 neurons correspondingly.

As a global pooling, the mean ($f'_{i-ftr.} = \frac{1}{n}\sum_j f^{j-node}_{i-ftr}$) is used over all the nodes. This approach scales relatively well with the number of nodes. At the same time, it helps to reduce overfitting because the mean does not overemphasise minor variations in the data due to an increase or decrease in the values of a single node feature, leading to a model that generalises better. After aggregating features, ParticleNet employs a dense neural network layer with 128 neurons. This layer is further connected to a dense layer with two neurons, followed by a softmax activation that computes the probabilities $p(\tau_h)$ or $p(\text{jet}) = 1 - p(\tau_h)$.

In the binary classification of jets and hadronically decaying taus (τ_h), the cross-entropy loss function is utilised, which is defined as:

$$L = -\frac{1}{N} \sum_{i=1}^{N} w_i \left[y_i \log(p(\tau_{h,i})) + (1 - y_i) \log(1 - p(\tau_{h,i})) \right] , \qquad (5.2)$$

where y_i is the true label (1 for τ_h and 0 for jet), $p(\tau_{h,i})$ is the predicted probability of the object being a τ_h, and $1 - p(\tau_{h,i})$ is the predicted probability of the instance being a jet, w_i is the weight for the i-th object. In the DisTau tagger, class balancing is not just conducted to equalise the number of τ_h and τ_j, but to refine balance in each kinematic region of reconstructed jet η and p_T. This approach to reweighting ensures an unbiased classifier across the different kinematic regions, aligning the jet object distribution using the weight w_i with that of the τ_h objects. The weight values are shown in Fig. 5.11.
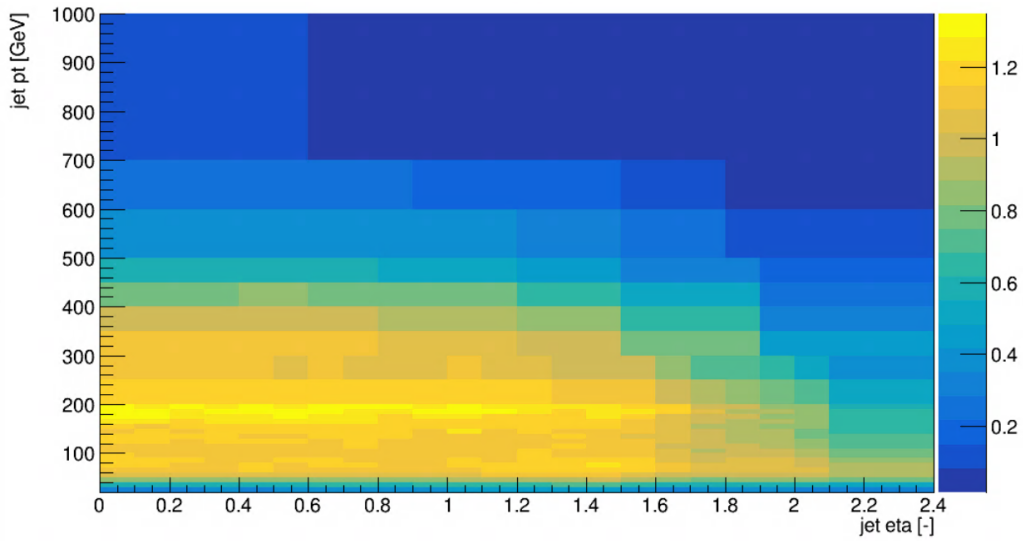
Figure 5.11: Weights that are applied to each τ_j to emulate the η and p_T distribution of τ_h dataset. Each cell in the heatmap corresponds to a bin. The x-axis corresponds to the jet η bins; the y-axis shows the jet p_T, and the colour demonstrates the magnitude of the weight applied to the τ_j dataset.

5.5   Tagger efficiency

The model was trained on NVIDIA Tesla P100 for 10 epochs. This section demonstrates the study of DisTau tagger performance in MC and the validation of its behaviour in collision data. Signal MC events in datasets that are used for performance study are not used during training. The background jets are sampled from the $t\bar{t}$ sample, as the model is trained on QCD jets that differ in jet flavour composition; the performance measured in $t\bar{t}$ demonstrates how robust the model is across different background jet flavours. Due to limited signal statistics, the tagger performance study uses the same $\tilde{\tau}$ mass point as in training, relying on events not included during the training process. No overtraining effects are observed between the training data and events reserved for the performance study.

Evaluating the score distribution of the tagger across the four data-taking periods is crucial for assessing its generalisation performance over different years. As the tagger was solely
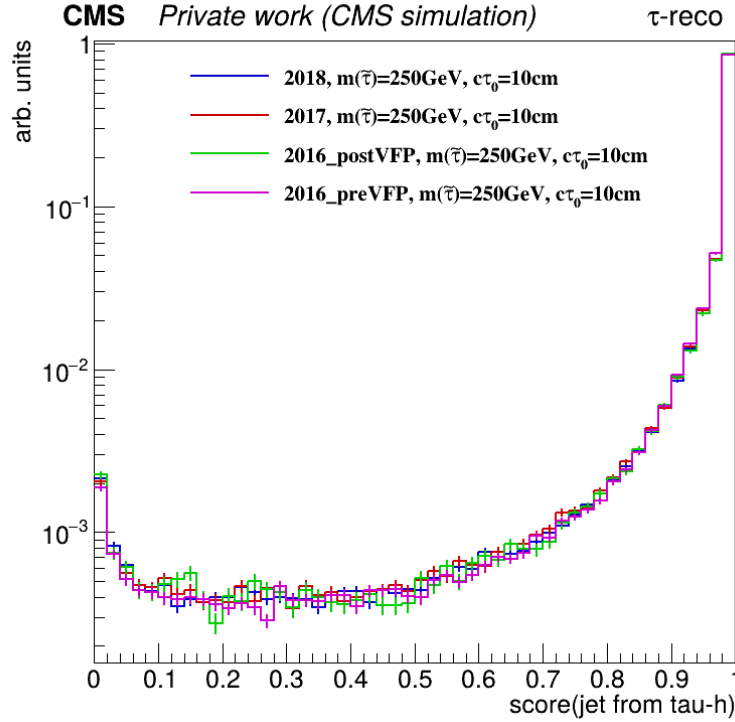
Figure 5.12: Comparison of the tagger score distributions for generator-level τ_h across four data-taking periods for $\widetilde{\tau}$ with masses 250 GeV and proper decay length of $c\tau_0 = 10$ cm. The distributions are shown separately for each year to evaluate the generalisation performance of the tagger trained on 2018 data. Consistency in the score distributions across years demonstrates the robustness of the tagger to year-to-year variations in detector conditions and calibrations.

trained on 2018 data, any variations in detector conditions, calibrations, and operational stability from year to year might lead to shifts in the data distributions. The comparison of score distributions for $\widetilde{\tau}$ masses of 100 GeV, 250 GeV, and 400 GeV across these periods show overall compatible behaviour, as illustrated in Fig. 5.12. The distributions remain primarily in agreement, suggesting that the tagger developed with 2018 data effectively generalises to other years.

5.5.1 Comprehensive performance

The ROC curves shown in Fig. 5.13 illustrate the inclusive tagger performance for the GMSB SUSY scenario with a $\widetilde{\tau}$ mass equal to 400 GeV and a proper decay length of 10 cm for three main baseline models.

The tagging efficiency of the developed τ_h tagger is evaluated for different input configurations and feature sets, as shown in Fig. 5.13. The first version, named **v1 pf-candidates**, relies solely on the *AK4 CHS PFJet* constituents as input features. In the second configuration named **v2 pf-candidates**, the input is expanded to include Particle Flow (PF) candidates matched within a radius of $\Delta R < 0.5$ to the *AK4 CHS PFJet* axis. This version incorporates additional features such as $\log(E)$ and $\log(p_T)$, which enhance the encoding of input information. Further improvements are introduced through optimised
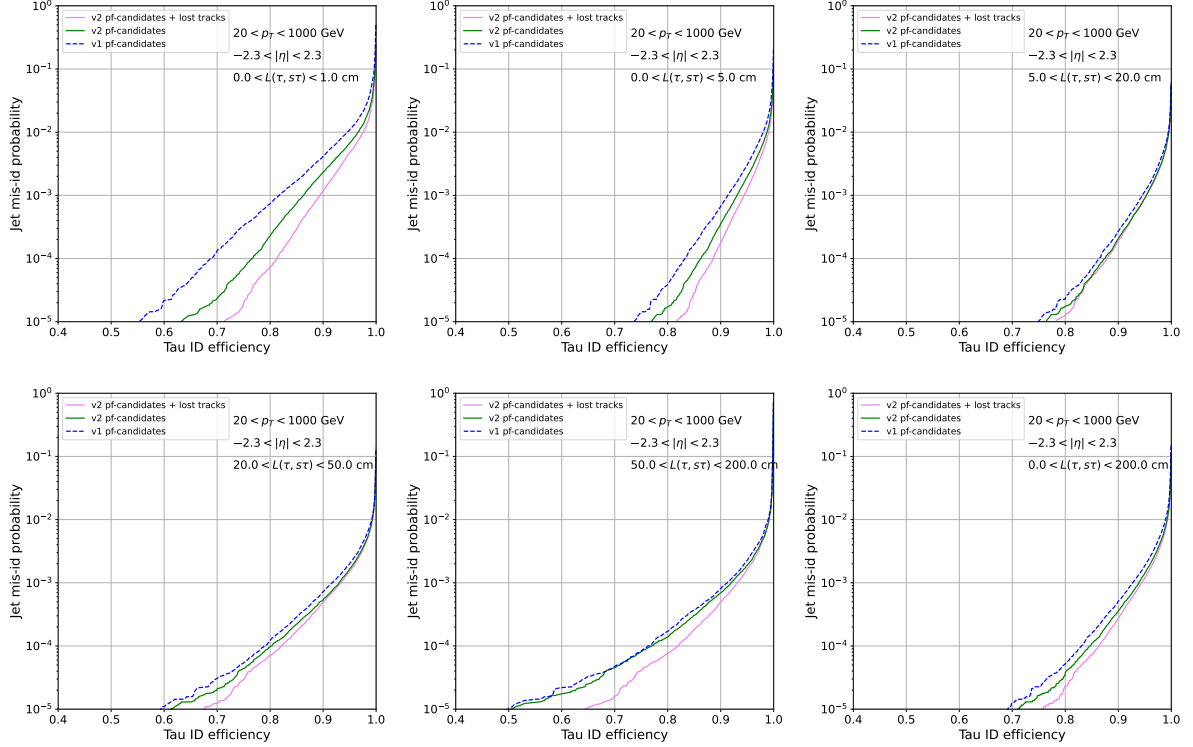
Figure 5.13: Receiver operating characteristic for different versions of the tagger. Background jet objects are taken from semileptonic $t\bar{t}$ events. Signal τ_h leptons are taken from a $\widetilde{\tau}$ sample for $\widetilde{\tau}$ mass $400\,\mathrm{GeV}$ and proper decay length equals $c\tau_0$ =10cm. The performance is shown in intervals of τ displacement relative to the $\widetilde{\tau}$ vertex, ranging from small displacements (less than $1\,\mathrm{cm}$, top left) to larger displacements (up to $200\,\mathrm{cm}$, bottom right).

scaling and clamping ranges and a more granular re-weighting procedure with refined p_T and η bins to better capture the feature distributions. In the final configuration, which is named **v2 pf-candidates + lost tracks**, the input includes both PF candidates and lost tracks matched within $\Delta R < 0.5$ to the *AK4 CHS PFJet* direction. Including lost tracks is particularly advantageous for identifying highly displaced τ_h with $L_{xy} > 50\,\mathrm{cm}$ and for the low displacement of $L_{xy} < 5\,\mathrm{cm}$. While this approach significantly boosts the tagger's ability to capture displaced tau signatures, it is tailored specifically for such scenarios. It may require additional validation for applicability in other models beyond the standard model. The hyperparameter tuning is described in Appendix A.3.

Considering the advantages and trade-offs of each configuration, Version 1 is chosen as the baseline model. This configuration is computationally more efficient, relying solely on AK4 CHS jet constituents, reducing the input pre-processing complexity. Additionally, excluding lost tracks ensures that the tagger remains robust across various scenarios. Incorporating lost tracks, while beneficial for capturing τ_h in GMSB models, introduces a potential bias toward these specific signatures and may reduce the general applicability of the model to other BSM scenarios.

5.5.2 Working points

Working points are defined to study performance with respect to kinematic properties and to use a tagger in analysis. They are defined similarly as described in Section 4.3.6 but for binary classification discrimination of τ_h versus jet. Table 5.3 summarises the signal efficiency and misidentification rate for different WPs of the tagger. The efficiencies are calculated for τ_h produced by $\widetilde{\tau}$ particles with two proper decay length $c\tau_0 = 10\,\text{cm}$ and $c\tau_0 = 100\,\text{cm}$ and three mass points $100\,\text{GeV}$, $250\,\text{GeV}$, and $400\,\text{GeV}$. These efficiency estimates do not take into account the limited jet reconstruction efficiency. The misidentification rate is calculated using $t\bar{t}$ MC events.

Table 5.3: Signal efficiency and misidentification (mis-ID) rate for different working points (WP) of the tagger. The efficiencies are shown for $\widetilde{\tau}$ with $c\tau_0 = 10$ cm and $c\tau_0 = 100$ cm, across different $\widetilde{\tau}$ mass points (100 GeV, 250 GeV, and 400 GeV). The mis-ID rate is calculated using $t\bar{t}$ MC events.

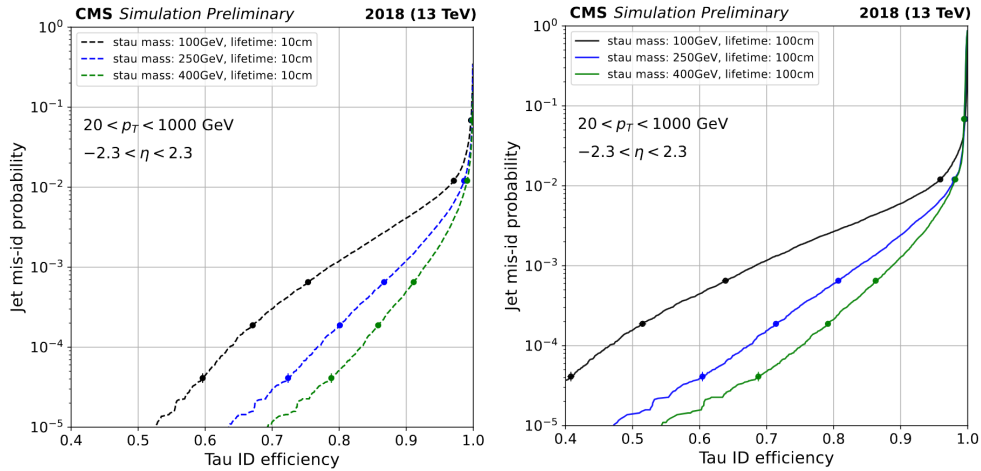| WP (threshold)	Efficiency ($c\tau_0 = 10\,\text{cm}$)			Efficiency ($c\tau_0 = 100\,\text{cm}$)			Mis-ID rate
	100 GeV	250 GeV	400 GeV	100 GeV	250 GeV	400 GeV	
Loose (>0.05)	99.6%	99.8%	99.9%	99.6%	99.5%	99.4%	6.8×10^{-2}
Medium (>0.7)	97.1%	98.6%	99.1%	95.9%	98.0%	98.2%	1.2×10^{-2}
Tight (>0.99)	75.4%	86.7%	91.1%	63.9%	80.7%	86.2%	6.4×10^{-4}
VTight (>0.997)	67.1%	80.1%	85.8%	51.5%	71.4%	79.1%	1.8×10^{-4}
VVTight (>0.9992)	59.6%	72.4%	78.8%	40.8%	60.4%	68.8%	4.1×10^{-5}

Figure 5.14: Receiver operating characteristic for different mass points. Background jet objects are taken from the $t\bar{t}$ MC sample, and signal displaced taus are taken from $\widetilde{\tau}$ sample for $\widetilde{\tau}$ ranging in mass from $100\,\text{GeV}$ to $400\,\text{GeV}$, LSP mass is $1\,\text{GeV}$ and proper decay length equals $c\tau_0 = 10\,\text{cm}$ (right) and $c\tau_0 = 100\,\text{cm}$ (left).

In Fig. 5.14, the performance for various $\widetilde{\tau}$ masses and lifetimes is demonstrated together with the aforementioned WPs. The τ_h ID efficiency is estimated from $\widetilde{\tau}$ MC using reconstructed jet candidates that match τ_h at the generator level. Comparisons are shown for three $\widetilde{\tau}$ mass values of 100, 250 and 400 GeV, the LSP mass of $1\,\text{GeV}$, and a proper decay length of $100\,\text{cm}$. The plots show the DisTau performance in 2018 MC. The tagger performance demonstrates a promising rejection efficiency of signal versus background. The larger masses of the hypothetical $\widetilde{\tau}$ are characterised by a harder p_T spectrum for the resulting τ_h. Because higher momentum efficiency in the DisTau tagger enhances classification performance, the higher $\widetilde{\tau}$ mass points demonstrate better efficiency.

The signal efficiency as the function of the transverse displacement L_{xy} of τ_{h} leptons and p_{T} of the jet together with misidentification rate as a function of the jet p_{T} is shown in Fig. 5.15 for various working points (Loose, Medium, Tight, VTight, and VVTight). The figures highlight performance differences between the detector's barrel region ($|\eta| < 1.5$) and endcap region ($|\eta| > 1.5$). The signal efficiency as a function of L_{xy} shows the peak signal efficiency at small displacements (a few centimetres), after which it gradually decreases as L_{xy} increases. At higher displacements, the efficiency drops significantly, attributed to the reduced tracking efficiency for highly displaced signatures. The signal efficiency increases with jet p_{T}, increasing at lower p_{T} before levelling off around $\sim 100\,\mathrm{GeV}$ at higher p_{T}. This trend stays consistent across all working points and aligns with the behaviour observed for prompt τ_{h} identification. Looser working points show significantly higher misidentification rates, particularly at low p_{T}, due to their focus on maximising signal efficiency.
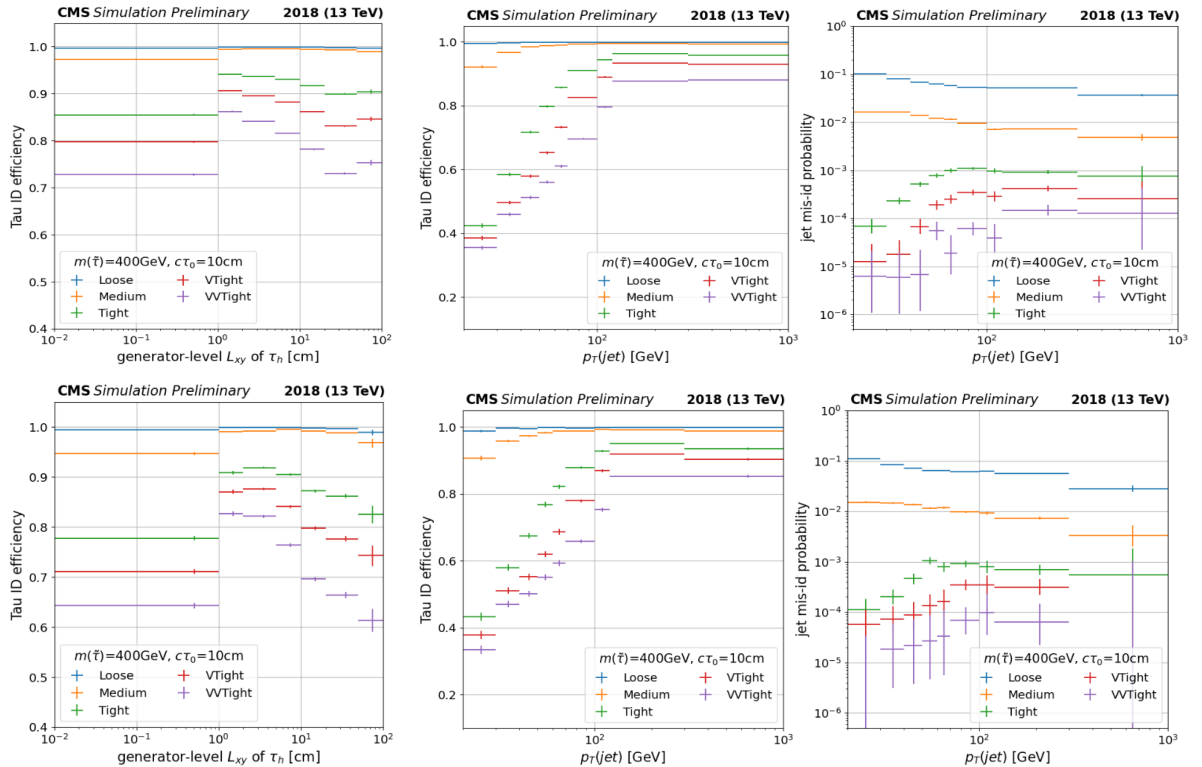
Figure 5.15: The efficiency and misidentification rate of the DisTau algorithm for the different working points. The signal efficiency (left and middle columns) is shown as a function of transverse displacement (L_{xy}) and jet p_{T}, using jet candidates from a $\widetilde{\tau}$ sample that match τ_{h} at the generator level. The right column illustrates the misidentification rate versus jet p_{T} from $t\bar{t}$ MC simulations, explicitly noting the rates for jets that do not match prompt electrons, muons, or products of τ_{h} decays at the generator level. The Figures highlight the performance differences between the detector's barrel (upper row) and endcap regions (bottom row).

5.5.3 Validation of the tagger in data

Validating the tagger in data is essential to ensure its reliability in real data analysis. The tagger is trained using simulated samples, and there can be differences between

simulation and actual data due to imperfections in detector modelling or the underlying event conditions. Validation in data allows for identifying these differences, correcting potential mismodeling through scale factors, and confirming the tagger's performance in realistic environments. This step is crucial for ensuring the robustness and accuracy of the tagger in physics analyses, particularly for rare signals or displaced signatures. Below, the study of the tagger performance in two validation regions is described.

1. The tagger behaviour for the SM background jets is studied in a control region enriched with Drell-Yan(DY)+jets events in the di-muon final state ($Z \rightarrow \mu\mu + $jets) region. The jets in this region originate from the QCD process. This region ensures a purity of the DY process of approximately 96% while not overlapping with the hypothetical signal, ensuring a negligible overlap with jets coming from potential $\widetilde{\tau}$ signal. The following selection requirements increase the purity of the DY+jets process:

   - Requiring two opposite sign, well-identified and isolated muons with $|\eta| <$ 2.4, $p_\mathrm{T} > 28\,\mathrm{GeV}$, $|d_{xy}| < 0.045\,\mathrm{cm}$, $|d_z| < 0.2\,\mathrm{cm}$, and total mass being consistent with Z-boson mass $70 < m(\mu, \mu) < 120\,\mathrm{GeV}$.
   - Requiring no additional leptons or b-tagged jets in the events.
   - At least two AK4 CHS jets with $p_\mathrm{T} > 30\,\mathrm{GeV}$, $|\eta| < 2.3$, and being separated from muons with $\Delta R > 0.4$. The leading two jets must also be separated from each other with $|\Delta\phi| > 0.5$. In addition, the leading PF candidate in the jet must be associated with the PV.

   The closure between data and MC is shown in Fig. 5.16. Overall, closure within 10% is observed over wide ranges of kinematic parameters. The plots are shown with statistical uncertainty only. Figure 5.17 shows the NN output for the p_T-leading and p_T-subleading jets. The tests, overall, demonstrate reasonable closure.

   Given that events from SM processes do not exhibit signal-like highly displaced τ_h leptons, there is no direct method to validate the performance of the DisTau tagger on displaced τ_h within data. In the SM, τ_h are primarily produced in processes such as Z-boson decays and other electroweak interactions. These τ_h leptons are produced promptly, with an average transverse displacement of approximately $\mathcal{O}(100\,\mu\mathrm{m})$, far smaller than the macroscopic displacements expected from long-lived particles in BSM scenarios.

2. Validation of the tagger on data is performed using well-identified hadronic τ_h leptons originating from Z-boson decays in DY+jets events, specifically in the final state with a τ_h and a muon ($Z \rightarrow \tau\tau \rightarrow \tau_\mathrm{h}\mu + $jets). While these prompt τ_h leptons are not an ideal approximation of highly displaced τ leptons, they serve as the most suitable proxy for signal-like behaviour currently available in data.

   The purity of the DY+jets process is increased by applying the following selection requirements:

   - Requiring opposite-sign muon and τ_h pairs with a total mass consistent with the visible Z-boson mass, $60 < m(\mu, \tau_\mathrm{h}) < 80\,\mathrm{GeV}$.
     - The muon is required to be well-identified and isolated, with $|\eta| < 2.4$, $p_\mathrm{T} > 25\,\mathrm{GeV}$, $|d_{xy}| < 0.045\,\mathrm{cm}$, and $|d_z| < 0.2\,\mathrm{cm}$.
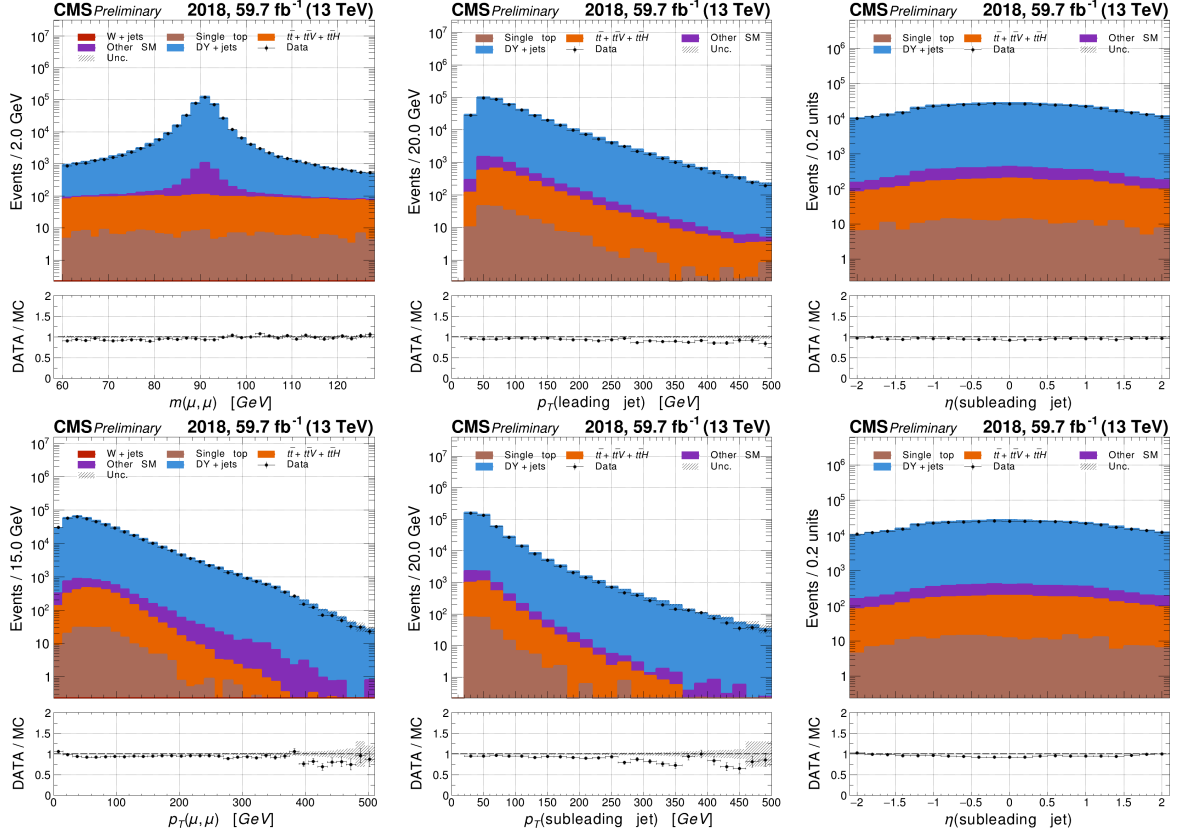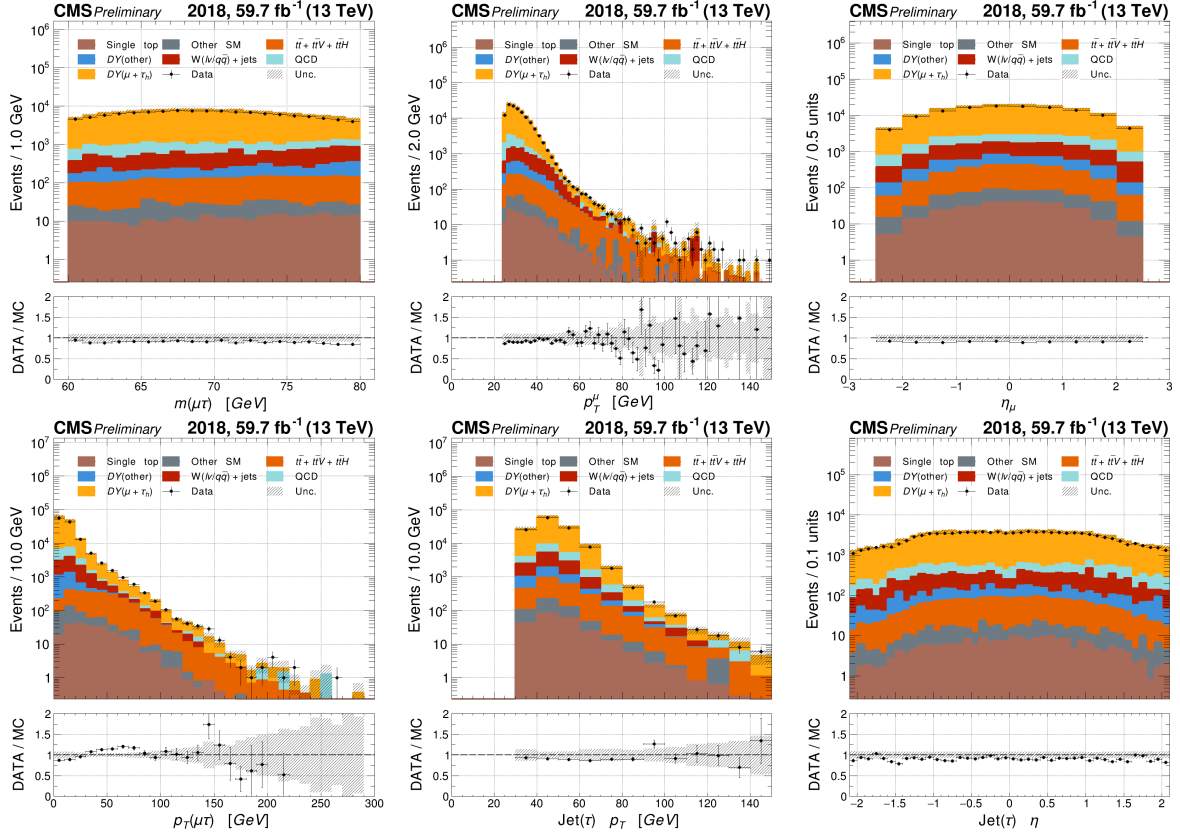
Figure 5.16: The figures illustrate the data-to-MC agreement on the general event properties for the 13 TeV 2018 data in the DY + jets enriched region, which includes two muons in the final state and an additional requirement of at least two jets, showing (from left to right, top to bottom) the invariant mass of the di-muon system ($m(\mu, \mu)$), the transverse momentum of the leading jet ($p_{\mathrm{T}}(\text{leading jet})$), the pseudorapidity of the subleading jet ($\eta(\text{subleading jet})$), the transverse momentum of the di-muon system ($p_{\mathrm{T}}(\mu, \mu)$), the transverse momentum of the subleading jet ($p_{\mathrm{T}}(\text{subleading jet})$), and the pseudorapidity of the subleading jet ($\eta(\text{subleading jet})$), with the lower panel in each plot displaying the ratio of the data to the summed MC yield.

- The τ_{h} is required to pass tight identification, with $p_{\mathrm{T}} > 30\,\text{GeV}$, $|\eta| < 2.3$, $|d_z| < 0.2\,\text{cm}$, and to be separated from the muon by $\Delta R > 0.5$.

- The transverse mass of the muon and missing transverse energy is required to be less than $60\,\text{GeV}$.

- At least one jet must be matched to the reconstructed τ_{h} within $\Delta R < 0.3$, with $p_{\mathrm{T}} > 30\,\text{GeV}$ and $|\eta| < 2.3$.

The purity of the DY+jets process with a muon and genuine τ_{h} in the final state is measured to be greater than 86%. The closure between data and MC is shown in Fig. 5.18 for general kinematic properties. The agreement for tagger output is evaluated for the jet matched to the reconstructed τ_{h}. This validation ensures that the tagger performs reliably on real data, even though the prompt τ_{h} from SM processes differs from the displaced τ_{h} expected in BSM scenarios. Using the Z-boson decays as a control sample provides a robust benchmark for understanding the
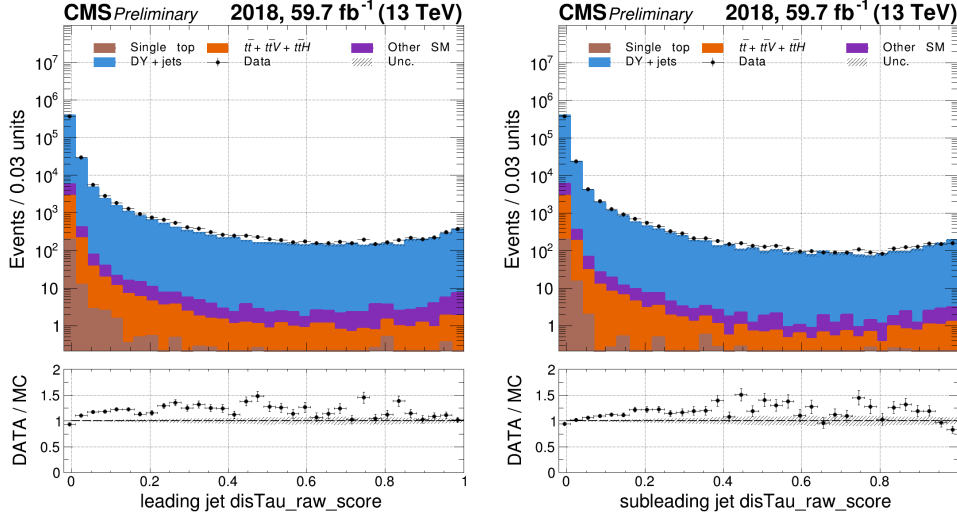
Figure 5.17: The figures demonstrate the data-to-MC agreement of the tagger output score for p_T-leading (left) and p_T-subleading (right) jets from the 13 TeV 2018 data within the DY+jets enriched region, featuring two muons in the final state and an additional requirement of at least two jets. The lower panel displays the ratio of the data to the summed MC yield.

tagger's behaviour and identifying any potential mis-modelling in the simulation.

The tagger's performance is validated using 2018 data, with samples primarily consisting of events from the DY+jets process. The tagger score distribution in the simulation shows good agreement with real data for both background and signal-like jets. Details of this study are provided in Appendix A.5. Since the methodology focuses on identifying displaced τ_h leptons with minimal reliance on process-specific kinematic properties, the tagger is expected to be versatile and applicable to a wide range of searches involving displaced τ signatures. Furthermore, this tagger can enable a more precise study of GMSB models with long-lived $\tilde{\tau}$, as demonstrated in the following chapters.

Figure 5.18: The figures illustrate the data-to-MC agreement of the general event properties for the 13 TeV 2018 data in the DY+jets enriched region, which includes a muon and τ_{h} in the final state, showing (from left to right, top to bottom) the invariant mass of the muon and τ_{h} system ($m(\mu, \tau_{\mathrm{h}})$), the transverse momentum of the τ_{h} ($p_{\mathrm{T}}(\tau_{\mathrm{h}})$), the pseudorapidity of the muon (η_{μ}), the transverse momentum of the muon ($p_{\mathrm{T}}(\mu)$), the transverse momentum of the jet associated with τ_{h} ($p_{\mathrm{T}}(\mathrm{Jet}(\tau_{\mathrm{h}}))$), and the pseudorapidity of the jet associated with τ_{h} ($\eta(\mathrm{Jet}(\tau_{\mathrm{h}}))$), with the lower panel in each plot displaying the ratio of the data to the summed MC yield.
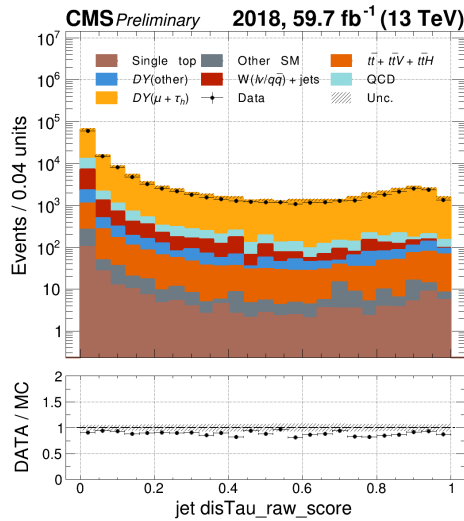
Figure 5.19: The figure displays the data-to-MC agreement of the tagger score for the jet matched to the reconstructed τ_h within $\Delta R < 0.3$ for the 13 TeV 2018 data in the DY+jets enriched region, in the final state with a τ_h and a muon. The lower panel shows the ratio of the data to the summed MC yield.

Chapter 6

Search for the direct pair production of long-lived $\widetilde{\tau}$ in Run 2

The core of this thesis is the search for pair production of long-lived $\widetilde{\tau}$ in proton-proton collisions at a centre-of-mass energy of $\sqrt{s} = 13\,\mathrm{TeV}$ using data collected with the CMS detector. The data corresponds to an integrated luminosity of 138 fb^{-1} recorded over the 2016-2018 data-taking period. In a scenario where $\widetilde{\tau}_{\mathrm{L}}$ and $\widetilde{\tau}_{\mathrm{R}}$ are maximally mixed, a previous search for long-lived $\widetilde{\tau}$ production [10] excluded masses between 150 and 220 GeV for a proper $\widetilde{\tau}$ decay length ($c\tau_0$) of 0.01 mm. This search was performed in a final state with two hadronically decaying τ leptons. Sensitivity to higher lifetimes was limited because standard τ_{h} reconstruction and identification techniques are sub-optimal for displaced τ_{h}, which produce non-conventional signatures in the detector. Based on the new reconstruction algorithm described in Chapter 5, the search for GMSB scenarios, where the supersymmetric partners of the τ lepton have a macroscopic decay length of the order $\mathcal{O}(\mathrm{cm}-\mathrm{m})$, are targeted in this thesis.

This chapter presents the full analysis performed to search for $\widetilde{\tau}$ decays, including all key components of the study. It covers the trigger strategy used to record events containing $\widetilde{\tau}$ decays, as well as the event selection criteria designed to isolate events in which both τ leptons from the $\widetilde{\tau}$ decay hadronically. A data-driven method is employed for background estimation, relying on control regions that are kinematically similar to the signal region to extrapolate background contributions. Systematic uncertainties arising from instrumental effects and methodological assumptions are evaluated and incorporated into the final results.

The results were interpreted by setting stringent upper limits on the production cross section of $\widetilde{\tau}$ pairs, improving previous results significantly.

6.1   Overview of the analysis strategy

This analysis addresses the limitations of previous searches, which could not effectively explore displaced τ_{h} signatures with new reconstruction techniques described in Chapter 5. The signal region is defined based on the presence of large $p_{\mathrm{T}}^{\mathrm{miss}}$ and the characteristic signature of two displaced jets arising from pair production of long-lived $\widetilde{\tau}$.

A significant challenge in this analysis is associated with the limitations of the simu-

lation of the background processes in the signal region. As described in Section 6.6.1, the background contribution, primarily from QCD multijet events, is not modelled with sufficient precision, especially in regions characterised by large $p_{\mathrm{T}}^{\mathrm{miss}}$ and displaced signatures. To address this issue, a data-driven background estimation method was developed to model the expected fake background yield in the signal region. This method, described in Section 6.7, is validated across multiple control regions.

The background prediction methodology is built and validated based on jets from two control regions with W($\mu\nu$)+jets and DY($\mu\mu$)+jets enriched events. The W($\mu\nu$)+jets control region serves as the baseline due to its event statistics and kinematic closeness to the signal region by the presence of $p_{\mathrm{T}}^{\mathrm{miss}}$, while the DY($\mu\mu$)+jets control region provides additional validation. Sections 6.6.2 and 6.6.3 give a detailed description of these control regions.

Selecting a control region containing signal-like objects presents a challenge, as the SM does not produce highly displaced τ_{h}. The prompt τ_{h} from DY($\mu\tau_h$)+jets enriched events is used as a proxy to validate the reconstruction algorithm as described in Section 6.6.4. While not genuine signal-like objects, they provide the closest available approximation within the data to measure the difference between the data and the simulation. The background prediction itself and the closure tests are given in Section 6.7.

Section 6.8 describes the evaluation of uncertainties and necessary corrections, covering both data-driven and simulation-based signal prediction. The results from the full Run 2 dataset are combined to enable the exclusion of supersymmetry scenarios across a range of cross-section hypotheses. The exclusion limits, derived using statistical techniques described in Section 6.9, provide critical constraints on the production of long-lived supersymmetric particles.

6.2   Collision data and simulation

The data sets and triggers used in this analysis are listed in Tables 6.1, 6.2, 6.3, and 6.4. The $p_{\mathrm{T}}^{\mathrm{miss}}$ triggers, such as `HLT_PFMET100_PFMHT100_IDTight`, `HLT_PFMET110_PFMHT110_IDTight`, and `HLT_PFMET120_PFMHT120_IDTight`, play a core role because of the large $p_{\mathrm{T}}^{\mathrm{miss}}$ caused by non-interacting LSPs.

Table 6.1: Data sets and corresponding HLT paths in data-taking period 2016-preVFP.

Data sets	HLT paths
`/SingleMuon/Run2016*UL2016_HIPM*/MINIAOD`	`HLT_IsoMu24` or
	`HLT_IsoMu27` or
	`HLT_IsoTkMu24` or
	`HLT_IsoTkMu27`
`/MET/Run2016*UL2016_HIPM*/MINIAOD`	`HLT_PFMET120_PFMHT120_IDTight` or
	`HLT_PFMET130_PFMHT130_IDTight` or
	`HLT_PFMET140_PFMHT140_IDTight`

The following simulated processes are used in various control regions of the analysis:

- Drell-Yan (DY) production $Z/\gamma^* \to \ell^+\ell^-/q\bar{q}/\nu\bar{\nu}$.
- W+Jets production.

Table 6.2: Data sets and corresponding HLT paths in the data-taking period 2016-postVFP.

Data sets	HLT paths
/SingleMuon/Run2016*UL2016*/MINIAOD	HLT_IsoMu24 or
	HLT_IsoMu27 or
	HLT_IsoTkMu24 or
	HLT_IsoTkMu27
/MET/Run2016*UL2016*/MINIAOD	HLT_PFMET120_PFMHT120_IDTight or
	HLT_PFMET130_PFMHT130_IDTight or
	HLT_PFMET140_PFMHT140_IDTight

Table 6.3: Data sets and corresponding HLT paths in the data-taking period 2017.

Data sets	HLT paths
/SingleMuon/Run2017*UL2017*/MINIAOD	HLT_IsoMu24 or
	HLT_IsoMu27
/MET/Run2017*UL2017*/MINIAOD	HLT_PFMET120_PFMHT120_IDTight or
	HLT_PFMET130_PFMHT130_IDTight or
	HLT_PFMET140_PFMHT140_IDTight

Table 6.4: Data sets and corresponding HLT paths in the data-taking period 2018.

Data sets	HLT paths
/SingleMuon/Run2018*UL2018*/MINIAOD	HLT_IsoMu24 OR
	HLT_IsoMu24_eta2p1 OR
	HLT_IsoMu27
/MET/Run2018*UL2018*/MINIAOD	HLT_PFMET120_PFMHT120_IDTight or
	HLT_PFMET130_PFMHT130_IDTight or
	HLT_PFMET140_PFMHT140_IDTight

- Single top quark production $t + X$.
- Top quark pair production $t\bar{t}$.
- Diboson production VV ($V = W, Z$).
- Triboson production VVV ($V = W, Z$).
- QCD multijet production.

The SM MC samples and their cross sections, used for various control regions in the analysis, are listed in Appendix A.6. To account for the NNLO to LO cross-section correction ratio, k-factors of 1.37 and 1.22 are applied to DY+Jets and W+Jets, respectively. Some MC samples have been produced separately for an individual number of additional jets in the matrix element. A stitching procedure is applied to combine these, as described in Appendix A.7. The analysis is carried out in four distinct data-taking periods to account for changes in detector conditions and calibration procedures, ensuring consistency and accuracy across the dataset. The data periods are categorised as follows:

- **2016 pre-VFP**, corresponding to early data from 2016, processed with the campaign tag: `RunIISummer20UL16MiniAODAPVv2-106X_mcRun2_asymptotic_preVFP_v11*`.
- **2016 post-VFP**, covering the later phase of 2016 data-taking

with updated tracker setup, processed with the campaign tag: `RunIISummer20UL16MiniAODv2-106X_mcRun2_asymptotic_v17*`.

- **2017**, processed under the campaign tag: `RunIISummer20UL17MiniAODv2-106X_mc2017_realistic_v9*`.

- **2018**, representing the final Run 2 data-taking year, processed under the campaign tag: `RunIISummer20UL18MiniAODv2-106X_upgrade2018_realistic_v16_L1v1*`.

6.3   Signal triggering

During the LHC Run 2, no dedicated trigger was explicitly configured to record the long-lived $\widetilde{\tau}$ signature. Standard triggers aimed at selecting events with two hadronically decaying τ_h proved ineffective due to the challenges associated with accurately reconstructing displaced τ_h using the HPS algorithm. Instead, it was determined that triggers based on high p_T^{miss} were notably more effective for identifying events involving long-lived $\widetilde{\tau}$, with their efficiency improving as the mass of the $\widetilde{\tau}$ increased. More significant values of the $\widetilde{\tau}$ mass are characterised by harder p_T^{miss} spectra; therefore, they are more probable to be captured by the trigger; this behaviour is demonstrated in Fig 6.1.
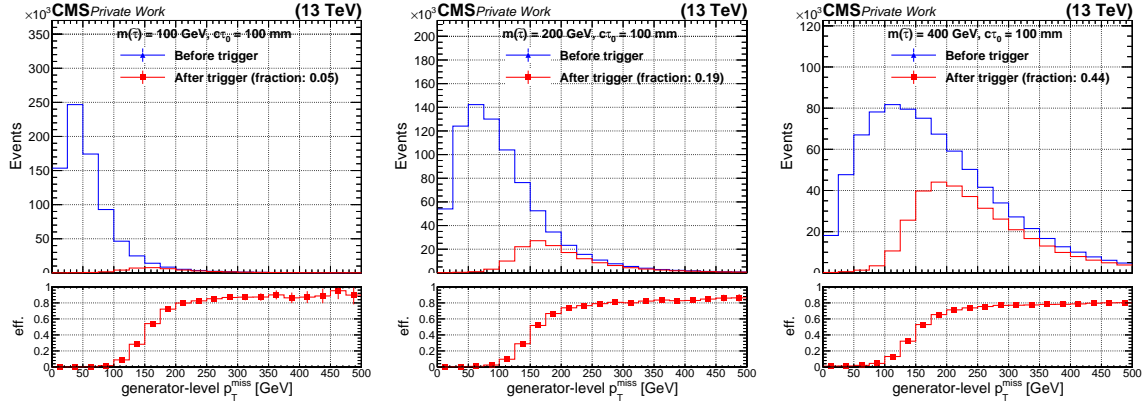
Figure 6.1: Efficiency of the p_T^{miss} triggers in 2018 as a function of generator level p_T^{miss}, for 2018 signal MC corresponding to various $\widetilde{\tau}$ masses and proper decay length of $c\tau_0 = 10$ cm.

The detailed trigger efficiency rate for various $\widetilde{\tau}$ mass points and $c\tau_0$ is calculated and shown in Table 6.5. As mentioned above, the trigger efficiency significantly increases with the $\widetilde{\tau}$ mass. For instance, at a $c\tau_0$ of 0.01 mm, the efficiency for a $\widetilde{\tau}$ mass equal to 90 GeV is only 4.9%, whereas for a 600 GeV $\widetilde{\tau}$, it reaches 66.65%. This suggests that such a trigger is more sensitive or effective at detecting particles with higher masses. Efficiency declines as $c\tau_0$ extends, indicating detection limitations with longer decay lengths. A notable efficiency decrease is observed for $c\tau_0$ values exceeding 1 m across all masses because of the limited reconstruction efficiency for displaced jets as demonstrated in Section 5.3.3.

6.4   Object selection

This analysis uses four distinct signal and control regions. These regions are designed to handle different background compositions and signal characteristics: The baseline region,

Table 6.5: Efficiency percentages for different values of $c\tau_0$ and masses of $\widetilde{\tau}$. The table displays how the efficiency varies with changes in the $c\tau_0$ across different mass scenarios for $\widetilde{\tau}$ ranging from 90 GeV to 600 GeV. Each entry represents the efficiency of the trigger. Values are presented in percentage units (%).

$c\tau_0$ \ $m(\widetilde{\tau})$	90 GeV	100 GeV	200 GeV	300 GeV	400 GeV	500 GeV	600 GeV
0.01 mm	4.90	6.12	23.78	40.92	52.89	60.95	66.65
0.05 mm	4.88	6.09	23.73	41.06	53.01	60.95	66.52
0.1 mm	4.91	6.07	23.81	40.90	52.96	60.94	66.69
0.5 mm	4.87	6.07	23.43	40.63	52.48	60.57	66.21
1.0 mm	4.88	6.07	23.14	39.85	51.78	59.76	65.35
5.0 mm	4.71	5.77	21.65	37.29	48.64	56.58	62.26
1 cm	4.58	5.68	20.89	36.34	47.62	55.41	61.10
5 cm	4.36	5.40	19.59	34.48	45.49	53.51	59.21
10 cm	4.34	5.30	18.69	33.00	43.81	51.69	57.37
1 m	3.34	4.21	14.32	23.84	31.37	37.47	42.61
10 m	1.91	2.23	5.92	10.23	14.35	17.72	20.38

characterized by events with high $p_{\mathrm{T}}^{\mathrm{miss}}$; the DY($\mu\mu$)+jets, DY($\mu\tau_h$)+jets regions, which are enriched in events from Drell-Yan processes accompanied by jets; the W($\mu\nu$)+jets region is utilized to assess and model backgrounds from W boson decays. The specific criteria applied for object selections to construct and isolate study regions are described in the following section.

6.4.1 Primary vertex

The following criteria are applied to select good vertices in an event

- The reconstructed tracks used for the vertex fit must have $\chi^2 > 0$.
- The vertex fit must have at least 5 degrees of freedom.
- The longitudinal distance between the vertex and the centre of the detector must be less than 24 cm.
- The transverse displacement of the vertex from the beam line must be less than 2 cm.

Events are required to have at least one good vertex. The primary vertex, which corresponds to the hardest scattering in the event, is evaluated using tracking information alone.

6.4.2 Lepton selection and veto

Muons are used to define control regions in this search. They are required to satisfy the following criteria:

- $p_{\mathrm{T}} > 28$ GeV.
- $|\eta| < 2.4$.
- Tight muon identification criteria described in Section 3.6.

- Tight PF based, $\Delta\beta$-corrected relative isolation $I_{\mathrm{PF}}^\mu < 15\%$, with:

$$I_{\mathrm{PF}}^\mu = \frac{I^{\mathrm{ch}} + \max[(I^\gamma + I^{\mathrm{nh}} - 0.5 I^{\mathrm{PU}}), 0]}{p_{\mathrm{T}}{}^\mu} \,. \tag{6.1}$$

.

- Transverse impact parameter w.r.t. the PV (d_{xy}) less than 0.2 cm.
- Longitudinal impact parameter w.r.t. the PV (d_z) less than 0.5 cm.

Here I^{ch}, I^γ, and I^{nh} are the sum of the transverse momenta of charged hadrons, photons, and neutral hadrons, respectively, in a cone size of $\Delta R = \sqrt{(\Delta\eta)^2 + (\Delta\phi)^2} = 0.4$ around the muon direction. I^{PU} is the $\sum p_{\mathrm{T}}{}^{\mathrm{PU}}$ of charged hadrons associated with the vertices other than the primary vertex. It estimates the contribution of neutral particles from pileup vertices, where the factor 0.5 considers the neutral-to-charged particle ratio.

To ensure the purity of the signal region and maintain orthogonality with other similar signal processes containing leptons, it is crucial to exclude events that contain prompt muons and electrons not associated with the targeted decay signatures. This is achieved by vetoing any additional muons or electrons in the event, using the loose selection criteria described below.

For a muon veto:

- $p_{\mathrm{T}} > 20\,\mathrm{GeV}$.
- $|\eta| < 2.4$.
- A loose identification criterion based on the identification criteria described in Section 3.6.
- Loose PF-based isolation, $\Delta\beta$-corrected, with a relative isolation threshold of less than 25%, to discriminate against muons embedded in jet activity or arising from pile-up interactions.

For an electron veto, the following criteria are required:

- $p_{\mathrm{T}} > 20\,\mathrm{GeV}$.
- $|\eta| < 2.4$.
- A conversion veto to reject electrons originating from photon conversions, reducing the background from electromagnetic processes.
- Loose working point of the *Fall17V2* MVA isolation-based identification, described in Section 3.5.

Implementing these vetoes decreases the chances of confusing background events with actual signals and helps to lower contribution from other background processes with leptons in the final state.

6.4.3   Jet selection

Jets are reconstructed by clustering PF candidates using the anti-k_{T} algorithm with a distance parameter of 0.4 (AK4), as described in Section 3.7. CHS jets are employed, which exclude charged particles associated with pileup vertices before clustering. Selected
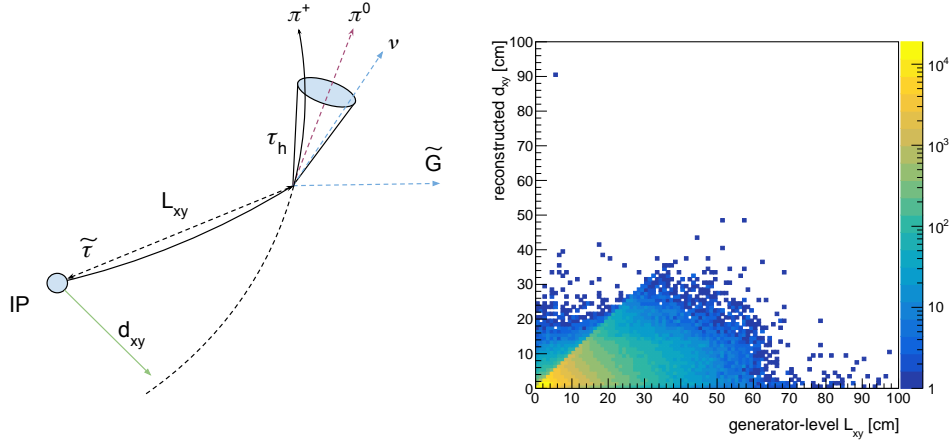
Figure 6.2: Schematic view of the $\widetilde{\tau}$ decaying to τ_{h} (left). Dependence of the leading PF candidate reconstructed d_{xy} from the generator-level $\widetilde{\tau}$ decay length for $\widetilde{\tau}$ mass of 300 GeV and a proper decay length of 1 m.

jets must have transverse momentum $p_{\mathrm{T}} > 30$ GeV and pseudorapidity $|\eta| < 2.1$. Jets are required to satisfy Tight ID criteria.

The jets within the HEM veto region are dropped to eliminate jets originating from regions affected by adverse calorimeter effects. This ensures that spurious jet contributions from instrumental effects are mitigated. The HEM veto is detailed in Section 6.5.2.

6.4.4 Displaced tau lepton identification

The displaced τ_{h} is selected based on the AK4 jet that passes the aforementioned criteria in Section 6.4.3. It is essential to mention that the lifetime of the $\widetilde{\tau}$ cannot be measured directly. However, the impact parameter of the leading charged PF candidate within a τ_{h} jet is a vital proxy to infer its displacement. This candidate's transverse impact parameter (d_{xy}) represents the shortest distance between the particle's trajectory and the primary vertex in the transverse plane. This quantity is closely related to the true transverse displacement of the τ_{h} (L_{xy}), which corresponds to the generator-level distance between the primary and secondary vertices, as shown in Fig. 6.2. At the generator level, d_{xy} does not exceed L_{xy}; however, at the reconstruction level, detector effects can smear the measured value of d_{xy}.

While L_{xy} directly characterises the τ_{h} decay vertex, d_{xy} offers a practical and measurable proxy, making it a crucial tool for this analysis. Despite potential detector resolution and tracking uncertainties, studying d_{xy} allows for effective background suppression as discussed in Sections 6.6.

Finally, each selected jet undergoes a scoring process using the neural network described in Chapter 5, this score is referred to as the `DisTau` tagger score. This scoring is crucial for both the selection and categorisation of jets into signal and background classes. Two thresholds are used in the analysis: a *loose* and a *tight* working point referred to as WPL and WPT, correspondingly, based on the definition provided in Chapter 5. The WPL and WPT correspond to the tagger threshold of 0.05 and 0.99 with an estimated misidentification rate of 10^{-2} and 10^{-4} measured in $t\bar{t}$ events.

6.4.5   Missing energy

A significant missing transverse momentum is expected in signal events because weakly interacting gravitinos ($\widetilde{\text{G}}$) and neutrinos from τ_h decay escape the detector undetected.

The $\vec{p}_\text{T}^{\,\text{miss}}$ is computed as the negative vector $\vec{p}_\text{T}$ sum of all the PF objects in an event, and its magnitude is denoted as p_T^miss. The $\vec{p}_\text{T}^{\,\text{miss}}$ is modified to account for the energy calibration of all the PF candidates in an event clustered into jets. The "Type-1" corrected p_T^miss is used, where the jet energy corrections are applied as described in Section 3.8.

The following recommended noise filters are applied to all events to minimise the impact of detector noise in reconstructing objects and hence p_T^miss:

- primary vertex filter (`Flag_goodVertices`);
- beam halo filter (`Flag_globalSuperTightHalo2016Filter`);
- HBHE noise filter (`Flag_HBHENoiseFilter`);
- HBHEiso noise filter (`Flag_HBHENoiseIsoFilter`);
- ECAL TP filter (`Flag_EcalDeadCellTriggerPrimitiveFilter`);
- Bad PF Muon Filter (`Flag_BadPFMuonFilter`);
- Bad PF Muon Dz Filter (`Flag_BadPFMuonDzFilter`);
- ee badSC noise filter (`Flag_eeBadScFilter`);
- ECAL bad calibration filter update (`Flag_ecalBadCalibFilter`).

6.5   Period-specific factors impacting data

6.5.1   ECAL Endcap Noise in 2017

In 2017, forward ECAL readout issues introduced noise, causing discrepancies in p_T^miss distributions between data and simulation. To address this, forward jets with uncorrected $p_\text{T} < 50$ GeV in the pseudorapidity range $2.65 < |\eta| < 3.139$ were excluded from the p_T^miss calculation, improving agreement at the cost of performance.

To account for the resulting background increase, a variable $H_\text{T}(\text{Soft},\text{Forward})$ was introduced, representing the scalar sum of transverse momenta of excluded jets. Large values of $H_T(\text{Soft},\text{Forward})$ may indicate genuine soft activity not included in p_T^miss, increasing backgrounds from Drell–Yan and misidentified τ_h. A veto of $H_\text{T}(\text{Soft},\text{Forward}) < 50$ GeV is applied to mitigate this effect.

6.5.2   HEM veto in 2018

In the 2018 data-taking period, the HCAL endcap (HE) sectors HEM15 and HEM16 became unresponsive and remained inoperable for the rest of the 2018 run. These sectors cover the region $\eta \in (-3.0, -1.3)$ and $\phi \in (-1.57, -0.87)$. The loss of HCAL data from these sectors affects the reconstruction of leptons, photons and jets in this area and, consequently, the missing transverse momentum in the event. To minimise the impact of the HEM failure, a veto is applied to the events in 2018 data from Run 319077 onward (when the issue occurred), containing any of the following objects.

- An electron candidate with $p_T > 20$ GeV, $\eta \in (-3.0, -1.3)$ and $\phi \in (-1.57, -0.87)$.
- A jet or a τ_h candidate with $p_T > 20$ GeV, $\eta \in (-3.2, -1.3)$ and $\phi \in (-1.77, -0.67)$.

Simulated events corresponding to 2018 (both background and signal) containing any of the above objects are weighted by 0.33, corresponding to the fraction of the data not affected by the 2018 HEM issue.

6.5.3 Level-1 prefiring inefficiency

During 2016 and 2017, a gradual timing shift in the ECAL was not correctly propagated to the L1 trigger primitives. This misalignment caused a significant fraction of trigger primitives at high pseudorapidity (η) to be incorrectly associated with the previous bunch crossing. Since the L1 trigger rules prevent two consecutive bunch crossings from triggering the event, this led to an inefficiency for events with substantial ECAL energy in the region $2 < |\eta| < 3$. This inefficiency is not modelled in the simulated samples. To account for this, event weights are applied to simulation samples based on a calculation of the prefiring probability per event.

6.6 Definition of signal and control regions

6.6.1 Baseline signal region

Significant p_T^{miss} typically characterises the long-lived $\widetilde{\tau}$ pair production signature due to the LSPs that escapes detection. An offline $p_T^{miss} > 120$ GeV pre-selection threshold is applied to select such events.

The vetos mentioned in Section 6.5 are applied to avoid detector-specific problems. A requirement for at least one good primary vertex is imposed, and events containing an electron or muon veto are excluded. In Fig. 6.3, the contribution of the signal and background processes in the inclusive region is shown after requiring more than two jets in the event, with the selection consistent with the one described in Section 6.4.3. This high-p_T^{miss} regime's predominant backgrounds stem from $W(\mu\nu)$+jets, $t\bar{t}$ pair production, and $Z \to \nu\bar{\nu}$+jets, where neutrinos contribute to high p_T^{miss}. Additionally, a residual background from QCD multijet events naturally does not contain neutrinos but frequently contains fake p_T^{miss} due to inaccuracies in measuring jet energies.

Further, to reduce background associated with prompt τ leptons, the presence of exactly two jets is required, both with $d_{xy} > 0.2$ cm and passing the loose working point limit for the `DisTau` tagger score, which is described in Section 5. The significance of the measured d_{xy} must be $d_{xy}/\sigma_{d_{xy}} > 5$ to avoid tracks with enormous uncertainty on d_{xy}. To additionally reduce the contribution from QCD multijet events and to mitigate potential contributions from beam halo interactions as detailed in Appendix A.8, the two jets, referred to as j_1 and j_2 and ranked by their p_T, are required to have an angular separation greater than 0.5 radians in $\Delta\phi$. These selections define the baseline region (BR), a high-p_T^{miss} region that contains the signal region (SR).
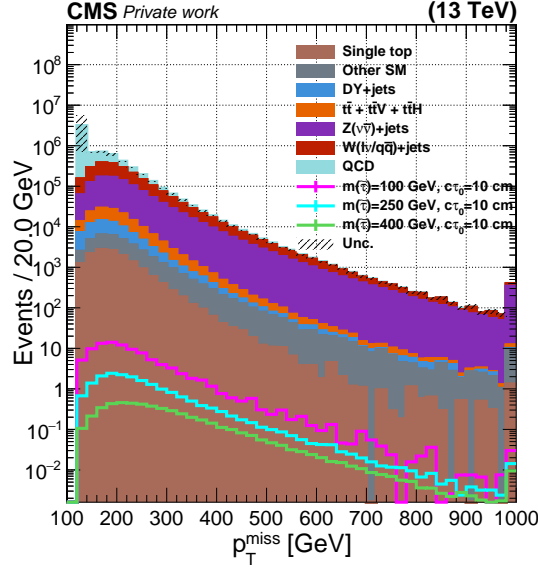
Figure 6.3: Distribution of p_T^{miss} is shown after the requiring $p_T^{miss} > 120\,\text{GeV}$ (2018 MC).

The phase space is divided into three distinct regions, each serving a particular purpose in the analysis. Events are initially categorized into three regions: **RT0**, **RT1**, and **RT2**, depending on how they meet the selection criteria of the tight `DisTau` working point threshold: **RT0** indicates neither jet meets the tight `DisTau` working point threshold, **RT1** denotes that one jet satisfies the tight `DisTau` working point threshold, and **RT2**, designated as the search region (SR), is defined when both jets meet the tight threshold. This classification is essential for the background prediction method described in Section 6.7.

In addition to the baseline region, two control regions are defined, enriched with specific event types for background prediction purposes as described later: W($\mu\nu$)+jets enriched events (WCR), which are primarily used for understanding backgrounds associated with W+jets processes, this detailed in Section 6.6.2, and DY($\mu\mu$)+jets enriched events (DYC) focusing on events related to Drell-Yan di-muon + jets processes, discussed in Section 6.6.3. Each analysis region (BR, DYC, WCR) is divided according to the classification mentioned above. The detailed classification scheme is shown in Fig. 6.4.

To exploit the signal's unique kinematic signature associated with the undetectable LSP, the transverse mass m_T is constructed as follows:

$$m_T^2(\vec{p}_T^{\,\text{vis}}, \vec{p}_T^{\,\text{inv}}) = m_{\text{vis}}^2 + m_{\text{inv}}^2 + 2(E_T^{\text{vis}} E_T^{\text{inv}} - \vec{p}_T^{\,\text{vis}} \cdot \vec{p}_T^{\,\text{inv}}), \qquad (6.2)$$

where $E_T^2 = m^2 + p_T^2$ for either visible or invisible particles.

In this context, the masses of the particles that are visible (m_{vis}) and those that are invisible (m_{inv}) in the detector are represented, respectively. The m_T is kinematically bound by the mass of the parent particle of both the visible and invisible particles, providing a single source of missing momentum within the system.

To account for pair-produced particles where both have visible and invisible decay prod-
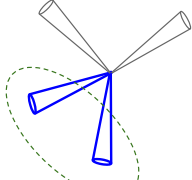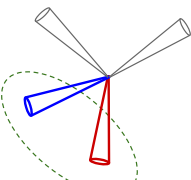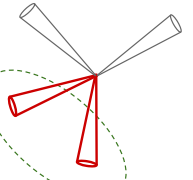
	RT0	RT1	RT2
	Exactly 2 jets passing L but not T	Exactly 1 jet passing T 1 jet passing L but not T	Exactly 2 jets passing T
Baseline region	BRT0	**BRT1**	**BRT2 (SR)**
W+jets CR	WCRT0	WCRT1	WCRT2
DY+jets CR	DYCRT0	DYCRT1	DYCRT2

Figure 6.4: A schematic illustration of the different region definitions.

ucts, the "stransverse mass" (m_{T2}) [149, 150, 151, 152] is defined as:

$$m_{T2}^2(\text{vis1}, \text{vis2}, p_T^{\text{miss}}) = \min_{\vec{p}_T^{\text{inv1}} + \vec{p}_T^{\text{inv2}} = \vec{p}_T^{\text{miss}}} \left[\max\{ m_T^2(\vec{p}_T^{\text{vis1}}, \vec{p}_T^{\text{inv1}}), m_T^2(\vec{p}_T^{\text{vis2}}, \vec{p}_T^{\text{inv2}}) \} \right].$$

(6.3)

Since the momenta of the individual invisible particles in Eq. (6.3) are unknown, $\vec{p}_T^{\text{miss}}$ is divided into two components ($\vec{p}_T^{\text{inv1}}$ and $\vec{p}_T^{\text{inv2}}$) in such a way that the value of m_{T2} is minimized. If m_{T2} is computed using the two displaced τ_h candidates as the visible objects, "vis1" and "vis2", then its upper limit in the signal will be at the $\widetilde{\tau}$ mass. This is different from the SM background processes. For example, in the case of $t\bar{t}$ enriched events, the upper limit is at the W boson mass.

In an earlier analysis of the $\widetilde{\tau}$ pair production with both $\widetilde{\tau}$ leptons decaying into τ_h [153], the p_T of the subleading τ_h has been identified as an effective discriminative variable. Similarly, in the current analysis of displaced τ_h pairs, the subleading jet p_T, named p_T^{j2} enhances discrimination.
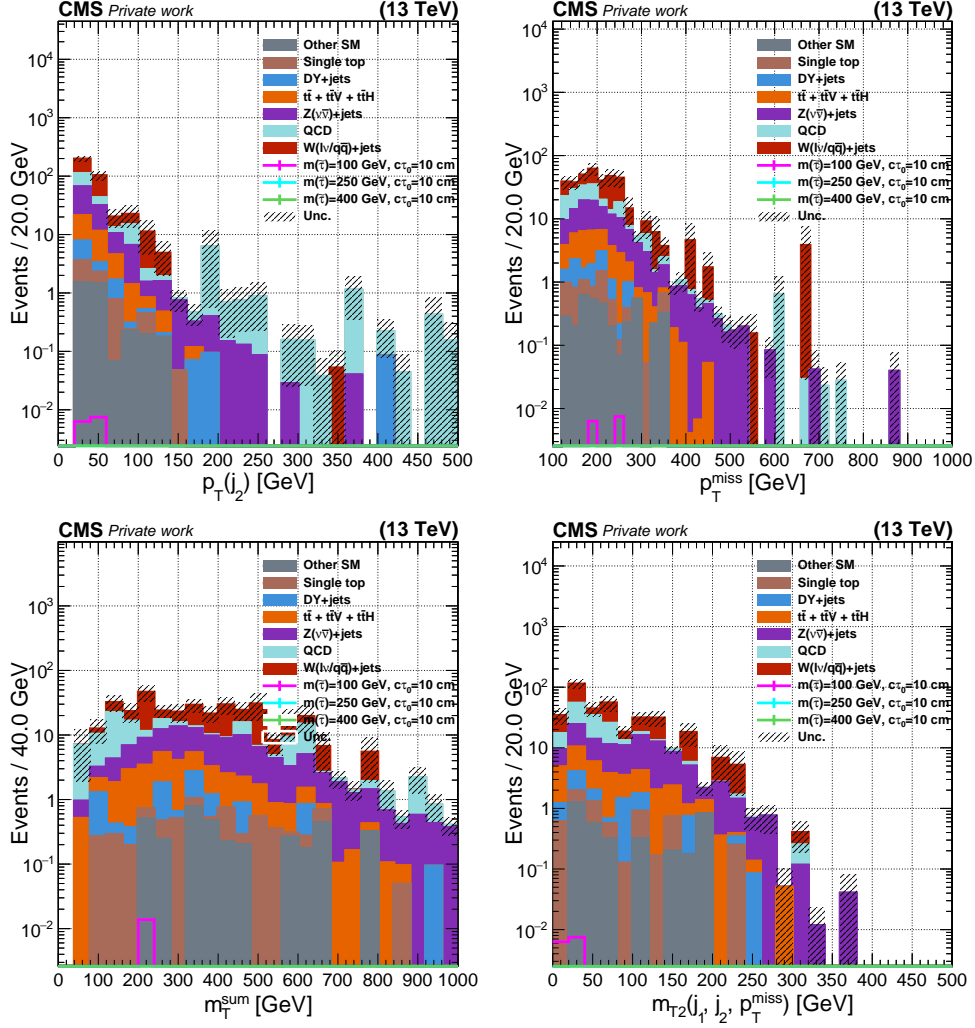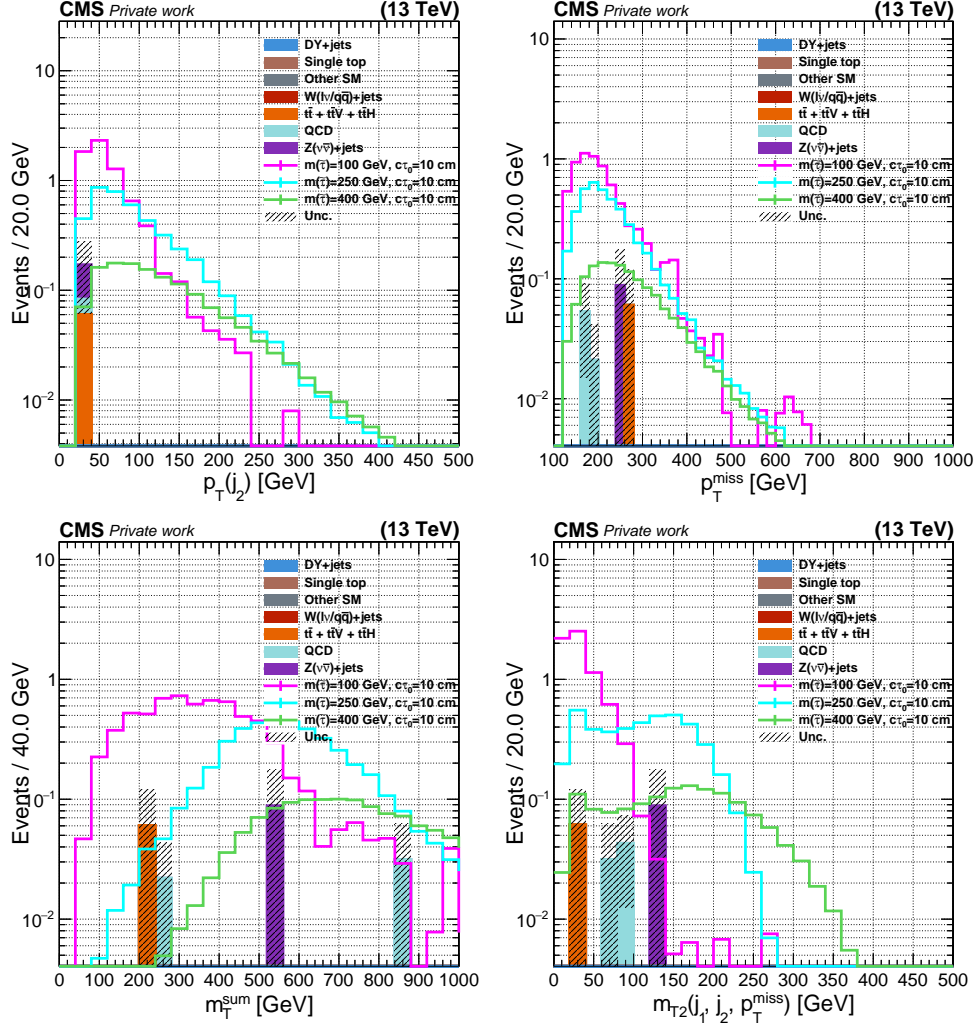
Figure 6.5: Distributions of p_T^{j2}, p_T^{miss}, Σm_T and m_{T2} in BRT0, showing the contributions from different SM processes.

The signal region is divided into five bins of p_T^{j2}, p_T^{miss}, and m_{T2}, as they show a good separation between signal and background events. These bins are listed in Table 6.6. To perform closure tests, the same binning scheme is applied to other control regions (WCRs described in Section 6.6.2, DYCRs described in Section 6.6.3, and BRT1).

Table 6.6: The SR bins in terms of p_T^{j2}, p_T^{miss}, and m_{T2}.

Bin number	p_T^{j2}	p_T^{miss}	m_{T2}
1	$[0, 50)$	$[0, 250)$	$[0, 100)$
2	$[0, 50)$	$[0, 250)$	≥ 100
3	$[0, 50)$	≥ 250	
4	$[50, 100)$	$[0, 250)$	$[0, 100)$
5	$[50, 100)$	$[0, 250)$	≥ 100
6	$[50, 100)$	≥ 250	
7	≥ 100		$[0, 100)$
8	≥ 100		≥ 100
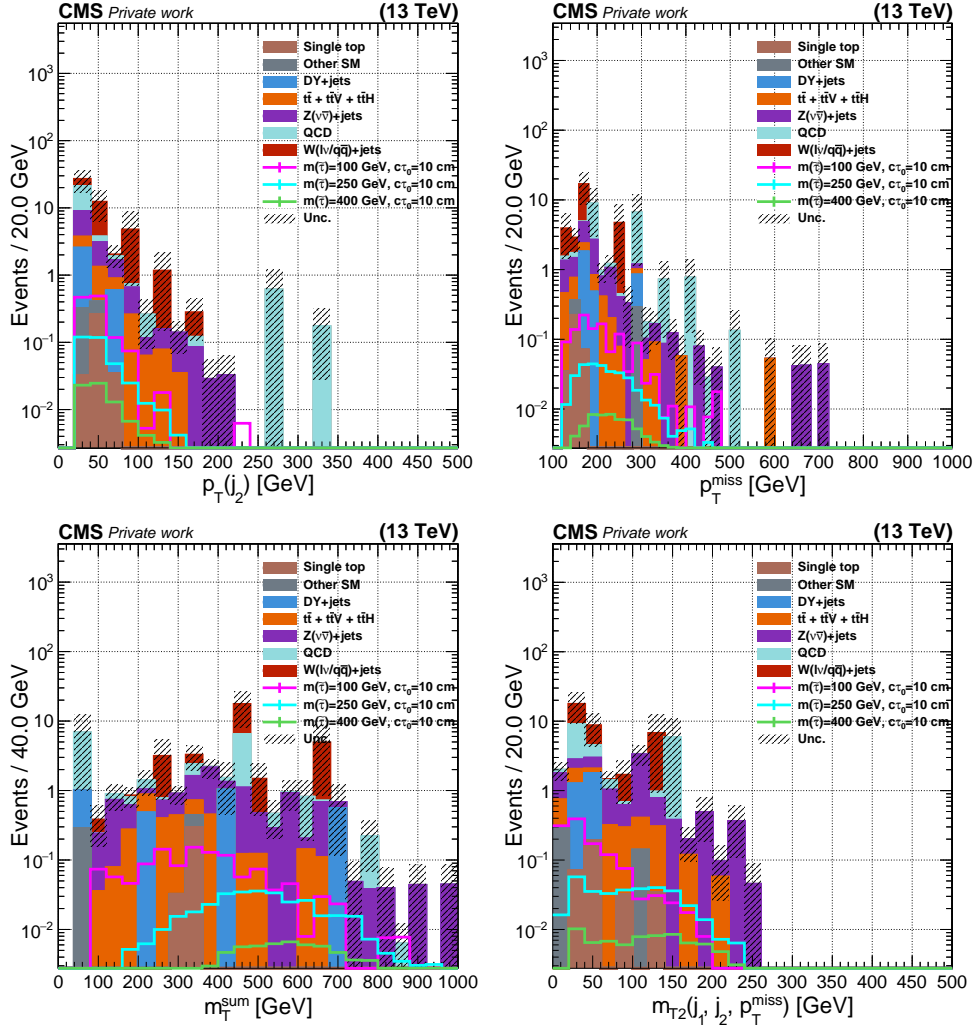
Figure 6.6: Distributions of p_T^{j2}, p_T^{miss}, Σm_T and m_{T2} in BRT1, showing the contributions from different SM processes.

Figures 6.5, 6.6, and 6.7 show the contribution from simulated SM processes and a few signal models in BRT0, BRT1, and BRT2, respectively. A generator-level study shows that all regions are mainly dominated by jets originating from light quarks and gluons. The gluon-based jets are attributed to 30%, 20%, and 40% of the background jets in BRT0, BRT1 and BRT2. The light quarks constitute to the 40%, 60%, 30% of the background jets in BRT0, BRT1 and BRT2, while the rest of the jets are associated with the heavy charm, bottom quarks or remaining leptons.

The BRT0 and BRT1 are dominated by the background and are, hence, well-suited for use as control/validation regions. On the other hand, BRT2, assigned as the search region, is mainly populated by the signal. Within BRT1, the signal contamination is notably evident in the distribution tails. Nevertheless, simulations in such tight regimes often struggle to accurately describe background contributions in such regions, particularly at the tails of distributions, where the signal-to-background ratio might seem disproportionately high due to modelling limitations. A comprehensive data-driven approach for background yield estimation in the baseline regions is implemented to address the poor MC modelling in

Figure 6.7: Distributions of p_T^{j2}, p_T^{miss}, Σm_T and m_{T2} in BRT2, showing the contributions from different SM processes.

such regions, described in Section 6.7.

6.6.2 W+jets enriched region

The $W(\mu\nu)$+jets control region (WCR) is designed to measure the fake rates in a region dominated by jets misidentified as τ_h. More details on the background estimation method are given in Section 6.7. This control region is selected explicitly for its closeness to the signal region kinematics, primarily due to significant p_T^{miss}, which aligns it closer to the conditions encountered in the signal region.

The control region utilises the `SingleMuon` datasets along with the corresponding HLT paths detailed in Table 6.4. The recommended p_T^{miss} filters described in Section 3.8 are applied to ensure good data quality. Additionally, the vetos mentioned in Section 6.5 are used to address detector-specific effects.

Each event in the $W(\mu\nu)$+jets region must contain at least one good primary vertex, ensuring a well-reconstructed interaction point. Furthermore, the event must include

exactly one muon that complies with the tight criteria specified in Section 6.4.2, and events containing any additional veto electron or veto muon are excluded. The missing transverse momentum is required to exceed 50 GeV, and the missing transverse mass, $m_\text{T}(\mu, p_\text{T}^\text{miss})$, is constrained within the range of 60 to 120 GeV to be consistent with the visible W boson mass. Figure 6.8 illustrates the muon p_T and $m_\text{T}(\mu, p_\text{T}^\text{miss})$ kinematic variables within the WCR at this selection stage. The resulting events maintain approximately 84% purity of W($\mu\nu$)+jets events.
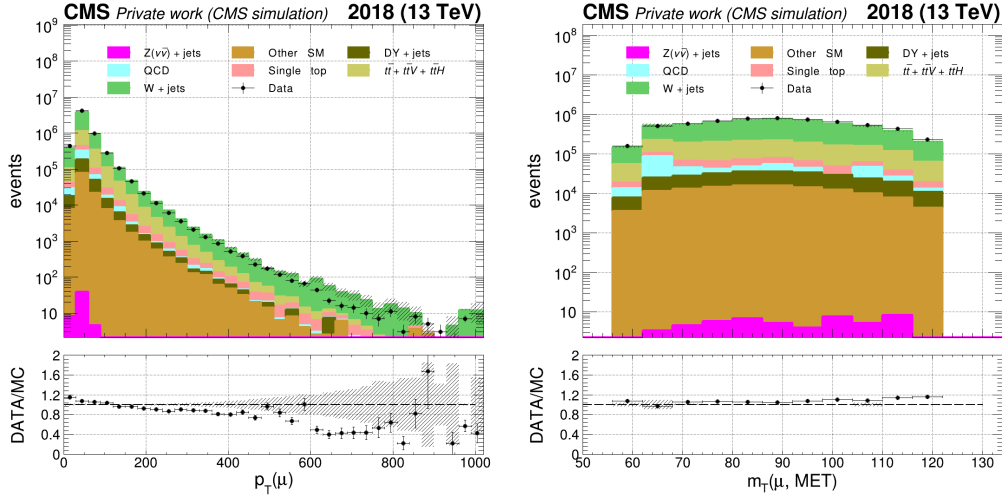
Figure 6.8: The distributions of the muon p_T (left) and $m_\text{T}(\mu, p_\text{T}^\text{miss})$ (right) in the WCR, corresponding to data and simulation in 2018. Only statistical uncertainties are shown.

Each event must contain two jets that satisfy the jet selection criteria specified in Section 6.4.3. Specifically, each jet must meet the loose `DisTau` working point requirement, with $d_{xy} > 0.2$ cm and $d_{xy}/\sigma_{d_{xy}} > 5$, ensuring a jet composition that better aligns with the expected signal kinematic region. The angular separation between the jets labelled j_1 and j_2 in order of their p_T, must be greater than 0.5 radians in $\Delta\phi$.

This selection strategy forms a robust foundation for measuring the fake rate in the WCR events, which closely mirrors the conditions anticipated in the search region. At the same time, requiring two loose jets and a muon ensures that the WCR is orthogonal to the search region (SR). Events in the WCR are further categorised based on how many of the two jets pass the tight `DisTau` working point threshold, classified into WCRT0, WCRT1, or WCRT2, as illustrated in Figure 6.4. These categories help to understand and measure fake rates within this control region.

6.6.3 DY enriched region

A DY($\mu\mu$)+jets control region (DYCR) is established to provide an additional region to measure the fake rate and study the tagger behaviour on the jets from the Drell-Yan processes. This control region uses the `SingleMuon` datasets and the corresponding HLT paths as specified in Table 6.4. The recommended p_T^miss filters given in Section 6.4.5 and the vetos mentioned in Section 6.5 are applied. Each event in the DYCR must include at least one good primary vertex.

Two oppositely charged muons are required to satisfy the selection criteria outlined in Section 6.4.2, further ensuring that no additional veto electron or veto muon is present in

the event. The dimuon invariant mass for these events is constrained to be within 70 and 120 GeV to be consistent with the Z boson mass. This region is orthogonal to the SR. It maintains a high purity of approximately 96% of DY+jets events, as shown in Fig. 6.9.
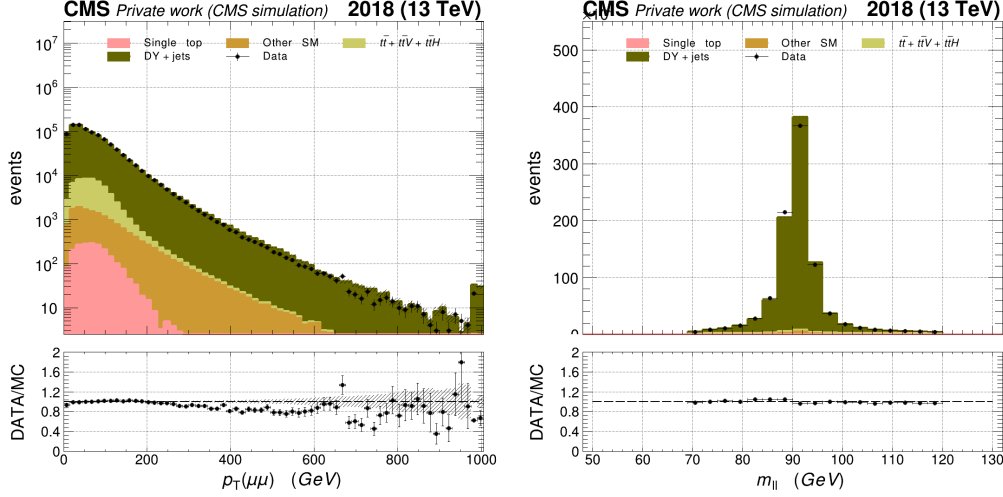

Figure 6.9: The distributions of the leading (upper left) and subleading (upper right) muon p_T, $p_T(\mu, \mu)$ (lower left) and $m(\mu, \mu)$ (lower right) in the DYCR, corresponding to data and simulation in 2018. Only statistical uncertainties are shown.

Each event must include at least two jets that meet the specific jet selection criteria discussed in Section 6.4.3. Additional criteria are imposed further to align this control region with the baseline region classification to measure the `DisTau` fake rates. These include exactly two jets satisfying the displacement requirement with $d_{xy} > 0.2$ cm, $d_{xy}/\sigma_{d_{xy}} > 5$ and passing the `DisTau` WPL. The angular separation between these two jets must be more than 0.5 radians in $\Delta\phi$.

Events in the DYCR are classified into DYCRT0, DYCRT1, or DYCRT2, as outlined in Figure 6.4. Compared to W($\mu\nu$)+jets events, the DY($\mu\mu$)+jets region faces low statistics after requiring two additional jets as described above. Therefore, this region is used as a fake rate validation and testing region rather than a region for measuring the actual fake rate.

6.6.4   Tau enriched region

Given that no highly displaced τ leptons are produced within SM processes, direct validation of the `DisTau` tagger on the genuine displaced τ objects within the detector data is not possible. Instead, well-identified hadronic τ leptons from Z boson decays in the DY($\mu\tau_h$)+jets process are utilized to validate the tagger's performance. While these τ_h leptons are not an ideal proxy for signal-like behaviour, they represent the most suitable approximation available in the data.

The region enriched with $Z \to \tau\tau \to \mu\tau_h$ events is established to access genuine τ_h leptons. This region is used for extracting scale factors for the `DisTau` tagger. The procedure is described in Section 6.8.2. The selection criteria involve using the `SingleMuon` data sets and corresponding HLT paths as outlined in Table 6.4, along with the recommended MET filters as described in Section 6.4.5 and the vetos mentioned in 6.5.
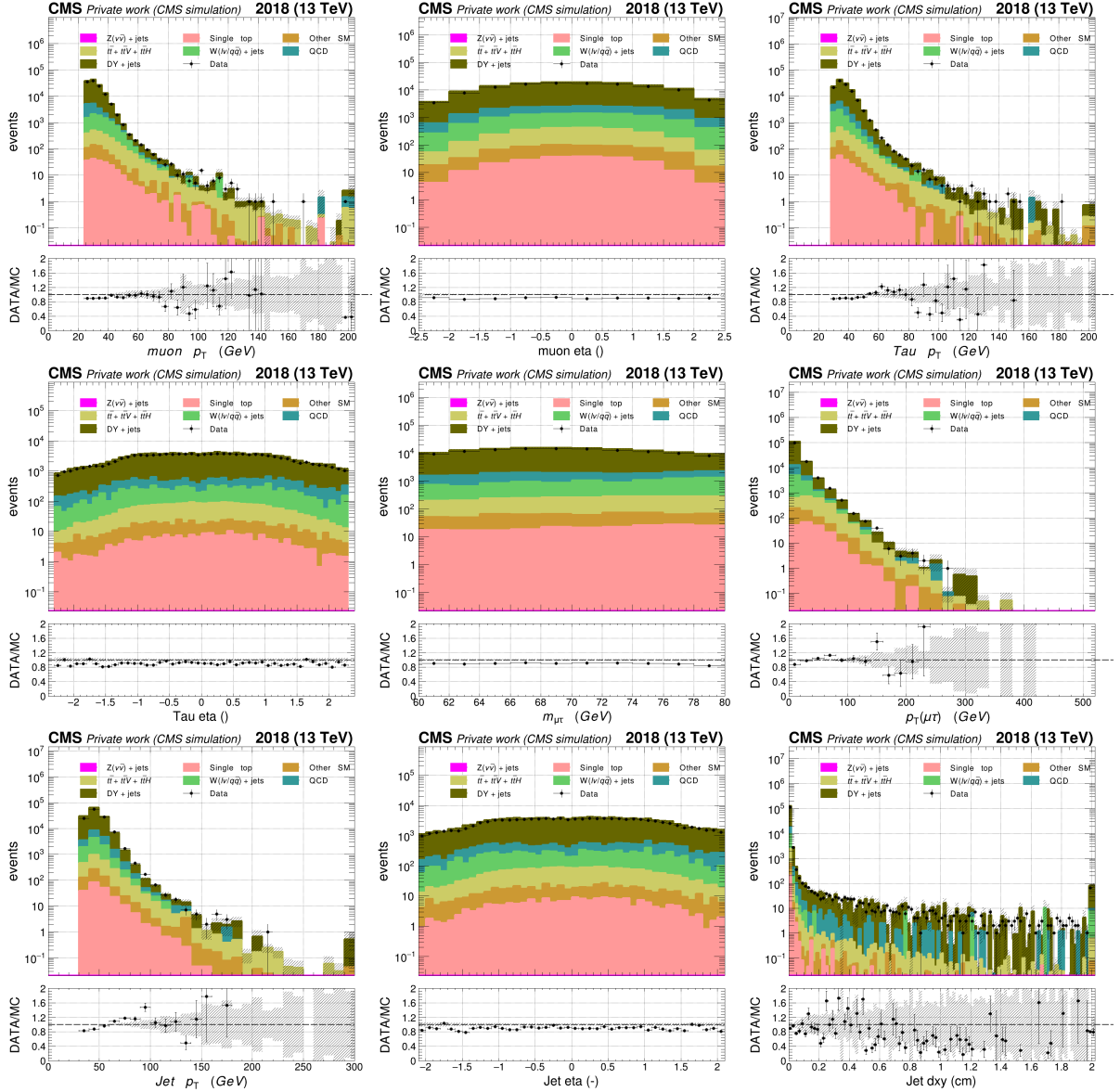
Figure 6.10: From top to bottom, left to right: distributions of p_T and η of the muon, p_T and η of the τ_h, $m(\mu, \tau_h)$, $p_T(\mu, \tau_h)$, and p_T, η, and d_{xy} of the jet matched to the τ_h, in the τ-enriched region as described in Section 6.6.4. The plots correspond to data and simulation in the 2018 data-taking period, and only statistical uncertainties are shown.

Each event must have at least one good primary vertex and exactly one muon with $p_T > 25$ GeV, $|\eta| < 2.4$, medium muon ID, and tight relative PF isolation ($I_{PF}^\mu < 15\%$) within a cone of $\Delta R < 0.4$ as described in Section 6.4.2. The muon must also have $d_{xy} < 0.045$ cm and $d_z < 0.2$ cm. Oppositely charged τ_h candidates are required to meet the medium WP of the `DeepTau v2.5` identification versus jets, very loose WP versus electrons, and tight WP versus muons, with $d_z < 0.2$ cm. Events containing any additional veto electrons or veto muons are excluded, and a spatial separation between the muon and τ_h of $\Delta R > 0.5$ is required.

To minimize contamination from top quark and W($\mu\nu$)+jets events, $D_\zeta > -25$ GeV is required, where D_ζ [154] is defined as the projection difference of visible and missing

momentum along the ζ-axis, the bisector of the muon and τ_{h} transverse momentum vectors. The transverse mass $m_{\mathrm{T}}(\mu, p_{\mathrm{T}}^{\mathrm{miss}})$ has to be less than 60 GeV, and the invariant mass $m(\mu, \tau_{\mathrm{h}})$ must fall within 60 to 80 GeV to be consistent with a visible component of Z boson mass.

The QCD background is calculated using a data-driven method as shown in Equation 6.4. Simulated non-multijet SM contributions are subtracted from the data. The QCD-multijet contributions in the opposite-sign (OS) dilepton region are derived by extrapolating yields from a same-sign (SS) dilepton region where the muon is isolated. The extrapolation factor (F), calculated as the ratio of OS to SS events in a side band defined by inverting the muon isolation criteria, is measured to be 1.10, 1.04, 1.0 for 2018, 2017, and 2016 pre/postVFP data-taking periods correspondingly.

$$N_{\mathrm{OS}}^{\mathrm{QCD}} = F \times (N_{\mathrm{SS,\ iso}}^{\mathrm{Data}} - N_{\mathrm{SS,\ iso}}^{\mathrm{non\text{-}QCD\ MC}}),$$
$$\text{where, } F = \frac{N_{\mathrm{OS,\ anti\text{-}iso}}^{\mathrm{Data}} - N_{\mathrm{OS,\ anti\text{-}iso}}^{\mathrm{non\text{-}QCD\ MC}}}{N_{\mathrm{SS,\ anti\text{-}iso}}^{\mathrm{Data}} - N_{\mathrm{SS,\ anti\text{-}iso}}^{\mathrm{non\text{-}QCD\ MC}}}. \tag{6.4}$$

Figure 6.10 displays the distributions of several kinematic variables within this τ-enriched region.

6.7 Background prediction

It has been shown that SM simulations do not accurately describe the search region, necessitating a data-driven approach for the background prediction. The primary background in this analysis consists of prompt jets misidentified as displaced τ_{h}, which meet the criteria of a specific `DisTau` working point. After the pre-selection, the most prevalent backgrounds include top quark pair production, QCD multijet production, and W($\mu\nu$)+jets and $Z(\nu\bar{\nu})$ + jets processes. There are no long-lived particles in these scenarios, and all observed tagged jets are mis-tagged. These mis-tagged jets typically arise from tracking inefficiencies, creating jets that seem to have displaced tracks. While these jets primarily originate from SM processes during proton-proton collisions, they may infrequently arise from non-collision interactions, which are expected to be negligible after requiring events to pass the baseline selection. Due to the low statistical power and limited reliability of the simulated SM samples, particularly in the tails of distributions, a data-driven technique is used to estimate the background yields in the signal region.

6.7.1 Data-driven method

As described previously, prompt jets mistakenly identified as displaced τ_{h} are the main source of background. To estimate the contribution of such a background, a data-driven method which combines the methods outlined in Refs. [10, 155] is developed. To explain the method, the following quantities must be defined:

- Misidentification probability f: the probability of a jet passing the tight WP, provided it has passed the loose WP:

$$f = n_{\mathrm{jet}}(T)/n_{\mathrm{jet}}(L). \tag{6.5}$$

- f_1 and f_2 correspond to the probability of the leading-p_{T} and subleading-p_{T} jets, respectively.
- The probability of a jet passing the loose WP but failing the tight WP can be expressed as $p = 1 - f$.
- N is the total number of events where exactly two jets pass the loose WP.
- N_{RT0} is a number of events in RT0 (i.e. two jets pass the loose WP but not the tight WP).
- N_{RT1} is a number of events in RT1 (i.e. one jet passes the tight WP; the other passes the loose WP but not tight WP).
- N_{RT2} is a number of events in RT2 (i.e. two jets pass the tight WP).

Then, the following equations can be established:

$$
\begin{aligned}
N_{\mathrm{RT0}} &= (1 - f_1)(1 - f_2)N \,, \\
N_{\mathrm{RT1}} &= [f_1(1 - f_2) + (1 - f_1)f_2]N \,, \\
N_{\mathrm{RT2}} &= f_1 f_2 N \,.
\end{aligned} \tag{6.6}
$$

Eliminating N from Eq. 6.6 reduction to the following form can be established:

- Prediction of the yield in RT1 from RT0 (RT1f0):

$$
N_{\mathrm{RT1f0}} \equiv N_{\mathrm{RT1}}^{\mathrm{pred}} = \frac{f_1(1 - f_2) + (1 - f_1)f_2}{(1 - f_1)(1 - f_2)} N_{\mathrm{RT0}} \,. \tag{6.7}
$$

- Prediction of the yield RT2 from RT0 (RT2f0):

$$
N_{\mathrm{RT2f0}} \equiv N_{\mathrm{RT2}}^{\mathrm{pred}} = \frac{f_1 f_2}{(1 - f_1)(1 - f_2)} N_{\mathrm{RT1}} \,. \tag{6.8}
$$

- Prediction of the yield in RT2 from RT1 (RT2f1):

$$
N_{\mathrm{RT2f1}} \equiv N_{\mathrm{RT2}}^{\mathrm{pred}} = \frac{f_1 f_2}{[f_1(1 - f_2) + (1 - f_1)f_2]} N_{\mathrm{RT1}} \,. \tag{6.9}
$$

The formulas provide the weight factors that, when applied on an event-by-event basis, transform the observed yield in one region into a predicted yield in another. This is a common technique in analyses (such as those involving fake rate methods) where it's necessary to estimate background contributions from misidentified objects.

As illustrated in Fig. 6.4, this prediction method can also be applied to the $W(\mu\nu)$+jets and $DY(\mu\mu)$+jets enriched events, providing the regions for testing the background prediction methodology. The prediction of BRTm/DYCRTm/WCRTm from BRTn/DYCRTn/WCRTn is referred to as BRTmfn/DYCRTmfn/WCRTmfn henceforth. As the signal contamination in BRT1 is very low, as shown in Fig.6.6, BRT1 can be used as a validation region. The residual non-closure can be propagated as an uncertainty in the SR. For the SR, there are two alternative predictions:

- BRT2f1: using Eq. 6.9. This is the primary prediction as it is performed from a region close to the SR (i.e. BRT1).

- BRT2f0: using Eq. 6.8. This alternate prediction is performed from a more signal-depleted region (i.e. BRT0). Hence, it is useful to check against potential signal contamination in BRT1, which can affect the prediction for BRT2f1. However, this prediction method is more sensitive to uncertainties that affect f_1 and f_2 .

The fake rates are measured in two regions, each enriched with QCD-like jets, but under different conditions: the W($\mu\nu$)+jets enriched region described in Section 6.6.2 and the DY($\mu\mu$)+jets dominated region described in Section 6.6.3. Measuring these two distinct regions serves as a cross-check and demonstrates consistency under different conditions.

The f specified in Eq. 6.5 measured in the W($\mu\nu$)+jets enriched region is referred to as f_{W}. An alternate measurement of f in DY($\mu\mu$)+jets region is referred as f_{DY}. For the main measurement, f_{W} is parametrised in terms of jet p_{T} and d_{xy} and represented as $f_{\text{W}}(p_{\text{T}}, d_{xy})$. Because of the lower statistics, only a 1D parameterisation in terms of either jet p_{T} or d_{xy} is used. These parameterizations are represented as $f_{\text{DY}}(p_{\text{T}})$ and $f_{\text{DY}}(d_{xy})$, respectively.

The measured fake rates f_{W} and f_{DY} are shown in Fig. 6.11 over various data collection periods (2016 preVFP, 2016 postVFP, 2017, and 2018). The fake rates are shown as functions of d_{xy}. The fake rates generally increase with larger d_{xy} values, with this trend consistent across data-taking periods. The increase in fake rates in the 2016 preVFP era appears more pronounced for d_{xy} of a few centimetres, suggesting a possible variation in detector conditions between these periods. Consistent behaviour is observed between the f_{W} and f_{DY} measurements, demonstrating the reliability of background modelling.

The displayed plots in Figs. 6.12 provide the final measurements of the fake rate for W($\mu\nu$)+jets across the data-taking periods from 2016 to 2018, parametrised over p_{T} and d_{xy}. These measurements are utilised to predict yields in the signal region. The fake rate generally increases with both higher d_{xy} and lower p_{T}, with a particularly noticeable peak at high transverse impact parameter. This trend suggests that background jets with greater d_{xy} and lower momentum are more prone to misidentification as displaced τ_{h}. The consistency observed over the years highlights the reliability of this measurement. However, to accommodate varying detector conditions, background estimation for the signal region is conducted separately for each data-taking period. A slightly higher background fake rate is observed for the 2016 preVFP data-taking period, which can be attributed to the older pixel tracker detector used.

6.7.2 Validation of the method

6.7.2.1 Closure in simulation

The limited amount of simulated events, especially in the SR, as shown in Fig. 6.7, makes the validation of the background prediction method in simulation highly problematic. The available simulation is not well suited to describe the background contribution in such a region, especially in the distribution's tails.

The dependence of the fake background jet's composition in the signal region was studied to test the validity of the aforementioned background prediction method for background processes in the SR. The absolute and relative jet flavour composition as a function
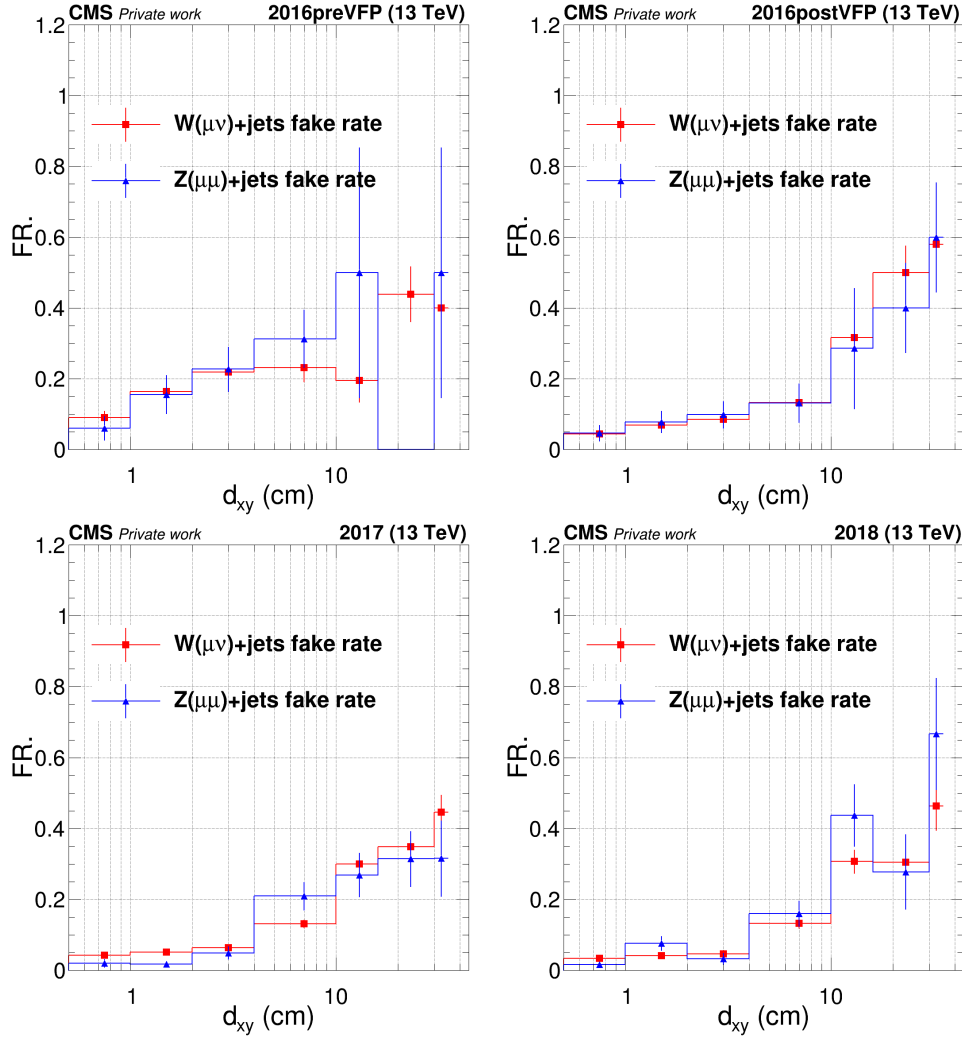
Figure 6.11: The values of f_{W} and f_{DY} measured in 2016 pre-VFP, 2016 post-VFP, 2017 and 2018 data-taking periods, as a function of jet d_{xy}.

of different `DisTau` score thresholds is shown in Fig. 6.13. At higher score thresholds, most misidentified jets are primarily from light quarks (up, down, or strange) or gluons. Notably, the flavour composition remained relatively stable across various score thresholds in the RT2 region. This stability in flavour contribution implies that the background prediction method's sensitivity to flavour might not be significant.

Based on this observation, the method can be tested at a medium working point, referred to as WPM (`DisTau` score threshold > 0.70), alternatively to a tight working point (`DisTau` score threshold > 0.99). Testing at the medium threshold is particularly justified because it offers a similar flavour composition to the tighter thresholds, allowing for validation of whether the method can accurately predict yields in simulated events under different operational conditions.

Before validation of the background estimation in the data, it is initially evaluated in simulation. To do so, f is measured and applied in simulation to estimate the yields in BRT1 (BRT1f0) and BRT2 (BRT2f1 and BRT2f0) and compared against the respective yields predicted directly from simulation. The results using WPM are presented in Figs. 6.14
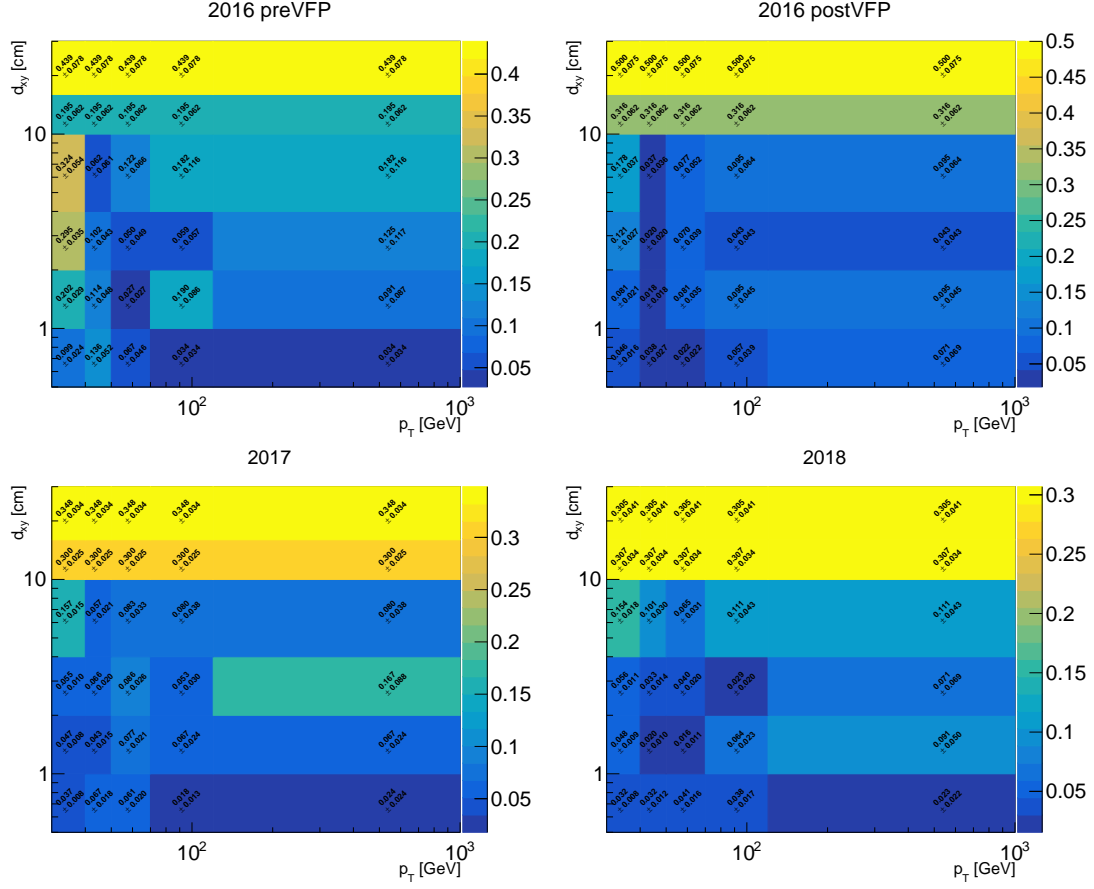
Figure 6.12: The values of f_{W} as a function of jet p_{T} and d_{xy}. The plots correspond to the 2016 pre-VFP, 2016 post-VFP, 2017 and 2018 data-taking periods.

and 6.15. The consistency demonstrated in these plots validates the internal coherence of the background prediction method. The closure in BRT2 suggests that this approach is appropriately designed for background estimation in the SR, an aspect that cannot be directly assessed using data. However, it is important to note that while the statistical coverage in the simulations is generally limited, even in the BRT0 region, the modelling in the most statistically significant bins remains robust. As shown in Fig. 6.13, WPM and WPT have a similar flavour composition; hence, the conclusion drawn using the former is expected to be valid for the latter.

6.7.2.2 Closure in data control regions

One of the aforementioned possibilities is to measure the fake rate in the DY($\mu\mu$)+jets enriched events and apply it for the background prediction in the W($\mu\nu$)+jets enriched events. After selecting two loose jets as described in Sections 6.6.2 and 6.6.3, both control regions do not contain contributions from hypothetical signal processes and, consequently, are used for background method testing.

Figure 6.16 demonstrates closure in the W($\mu\nu$)+jets events with one loose and one tight jet with the prediction that is extracted using the fake rate measured in DY($\mu\mu$)+jets events in data. Overall, the observed number of events in the actual yield coincides with the predicted yield.
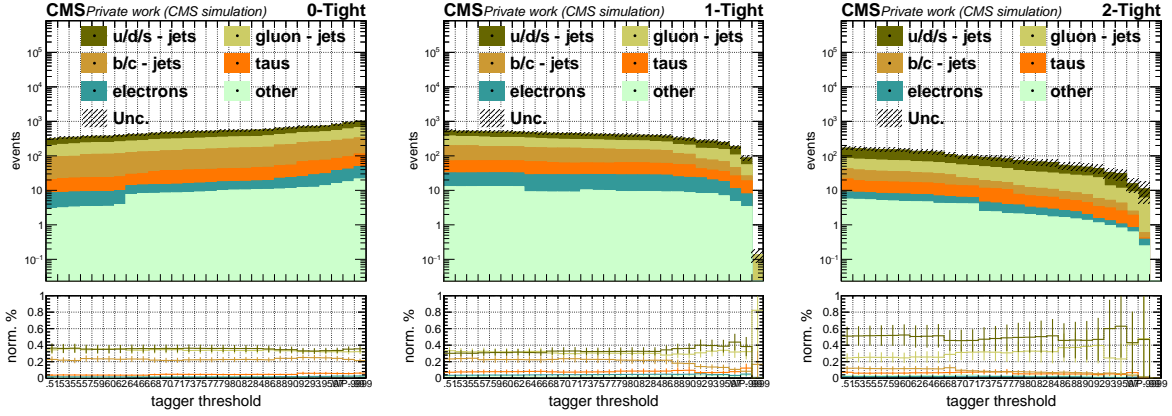
Figure 6.13: Absolute and relative contribution from jets of different flavours as a function of the `DisTau` score threshold starting from 0.5 and up to 0.999, in BRT0 (left), BRT1 (central), and BRT2 (right).
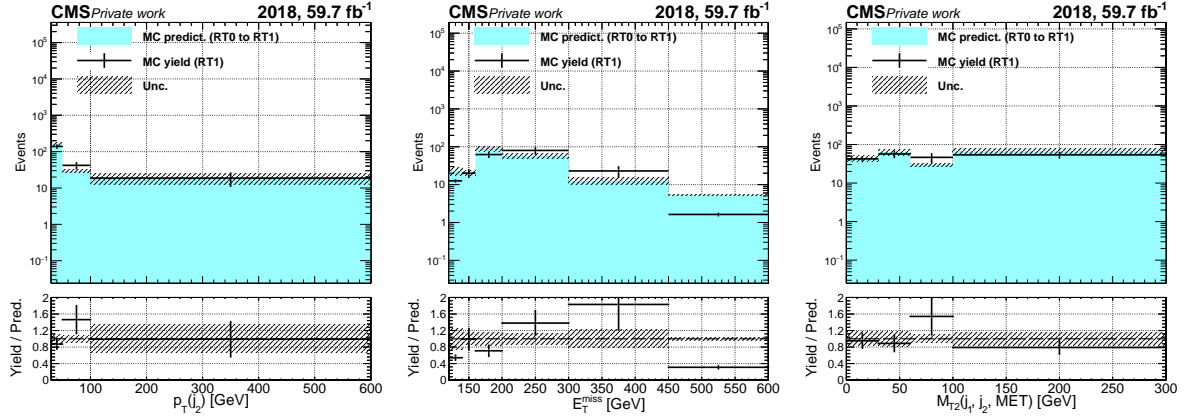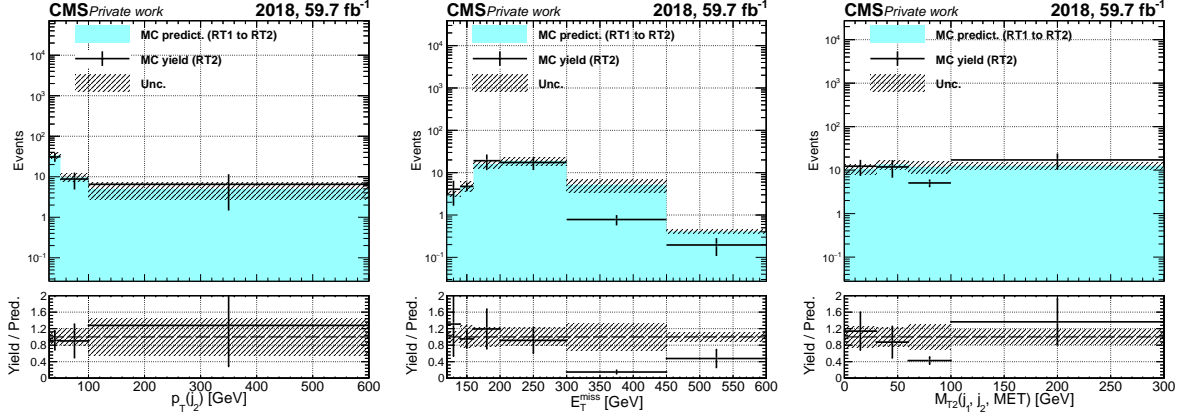

Figure 6.14: Distributions of p_T^{j2}, p_T^{miss}, m_{T2}, showing the comparison between BRT1 and BRT1f0 in simulation, using WPM. The plots are shown with statistical uncertainty and 2018 simulation.

Figure 6.17 contains similar tests but in the region with two tight jets. Due to the limited number of events in the $W(\mu\nu)$+jets region after requiring two tight jets, such a closure is problematic. Another important aspect is that the closure is not ideal due to the fact that the fake rate measured in the $DY(\mu\mu)$+jets region was parameterised only as a function of d_{xy}. This simplification was necessary due to the limited statistics available for more detailed parameterisation. However, the general trend demonstrates that the predictions in both WCRT1 and WCRT2 are compatible with the corresponding observed yield in the data. Additionally, the closure was tested within $DY(\mu\mu)$+jets events to validate the method further. The results demonstrate a similar level of agreement, indicating that the approach is reasonably robust. Furthermore, a consistent closure behaviour is observed across all data-taking periods, reinforcing the reliability of the background estimation method.

Figure 6.15: Distributions of $p_{\mathrm{T}}^{\mathrm{j2}}$, $p_{\mathrm{T}}^{\mathrm{miss}}$, m_{T2}, showing the comparison between BRT2 and BRT2f1 in simulation, using WPM. The plots are shown with statistical uncertainty and 2018 simulation.
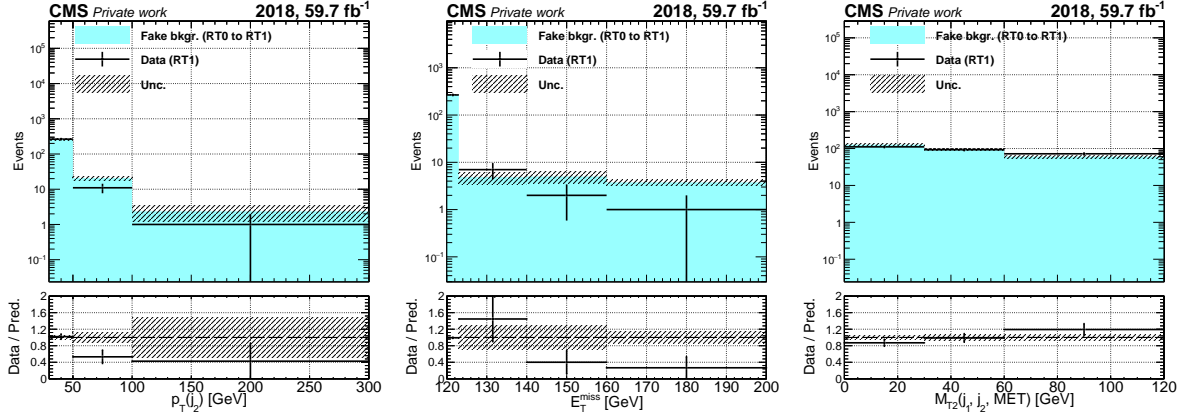
Figure 6.16: Distributions of $p_{\mathrm{T}}^{\mathrm{j2}}$, $p_{\mathrm{T}}^{\mathrm{miss}}$, m_{T2}, showing the comparison between WCRT1 and WCRT1f0 prediction in W$(\mu\nu)$+jets enriched events, using fake rate measured in DY$(\mu\mu)$+jets enriched events. The plots are shown with statistical uncertainty and 2018 simulation.

6.8 Uncertainties and corrections

The uncertainties and corrections incorporated for this analysis are reviewed in the corresponding section.

6.8.1 The $p_{\mathrm{T}}^{\mathrm{miss}}$ trigger efficiency corrections

The $p_{\mathrm{T}}^{\mathrm{miss}}$ trigger efficiency is determined using auxiliary triggers. For this purpose, the `SingleMuon` triggers listed in Section 6.2 are utilised. Events are required to satisfy these triggers and contain a muon that meets the selection criteria outlined in Section 6.4.2. The muon must be matched to the trigger object that activated the trigger within a distance of $\Delta R < 0.1$. To ensure similarity with the baseline region, events must also include at least two jets that fulfil the criteria described in Section 6.4.3, excluding any selection based on impact parameters. These criteria are collectively referred to as auxiliary selections. The $p_{\mathrm{T}}^{\mathrm{miss}}$ trigger efficiency is evaluated in both simulation and `SingleMuon` data sets as the ratio of event counts.
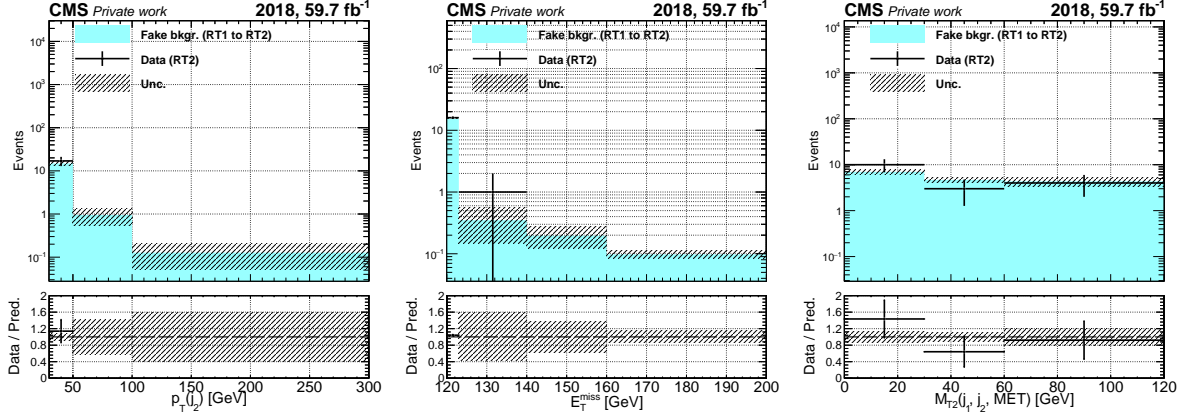
Figure 6.17: Distributions of p_T^{j2}, p_T^{miss}, m_{T2}, showing the comparison between WCRT2 and WCRT2f1 prediction in W($\mu\nu$)+jets enriched events, using fake rate measured in DY($\mu\mu$)+jets enriched events. The plots are shown with statistical uncertainty and 2018 simulation.

$$\epsilon = \frac{N(\text{passing auxiliary selections and } p_T^{miss} \text{ triggers})}{N(\text{passing auxiliary selections})} \,. \tag{6.10}$$

The correction factor is defined as the ratio $\epsilon^{\text{Data}}/\epsilon^{\text{MC}}$. This is presented, along with the efficiencies in data and simulation, in Figs. 6.18. The error on the corrections is extracted as binomial and propagated as systematic uncertainty in the final yield prediction.

6.8.2 The displaced tau tagger efficiency corrections

Considering potential disagreement between tagger responses in the data and simulation is essential. The `DisTau` tagger efficiency scale factors study uses well-identified τ_h with a relatively high impact parameter from DY($\mu\tau_h$)+jets enriched events. These serve as the best possible proxy for displaced τ_h, since the latter do not exist in the SM. To select the region enriched with DY($\mu\tau_h$)+jets events, the requirements described in Section 6.6.4 are applied. The SF measurement follows a tag-and-probe procedure similar to that used for the standard τ_h identification [119, 120].

The muon serves as the tag object, and the AK4 jet that is matched to the τ_h is used as the probe. Events from the DY($\mu\tau_h$)+jets simulation are split into two groups. The events where the probe is matched to a generator level τ_h are considered signals in this measurement procedure, and all other events are background. The method estimates the scale factors that affect the efficiency of the signal. For a chosen WP, events can be divided into two categories: one where the probe passes the WP, and the other where it fails the WP, N_{pass} and N_{fail} respectively. The efficiency ϵ for that WP then can be expressed as follows.

$$\epsilon = \frac{N_{pass}}{N_{tot}} = \frac{N_{pass}}{N_{pass} + N_{fail}}, \tag{6.11}$$

where N_{tot} is the total number of signal events. The SF is obtained by a simultaneous fit of the $m(\mu, \tau_h)$ distribution in the pass and fail categories. In this fit model, the SF is defined as a parameter of the fit such that it scales N_{pass} as $\text{SF} \times N_{pass}$. The model
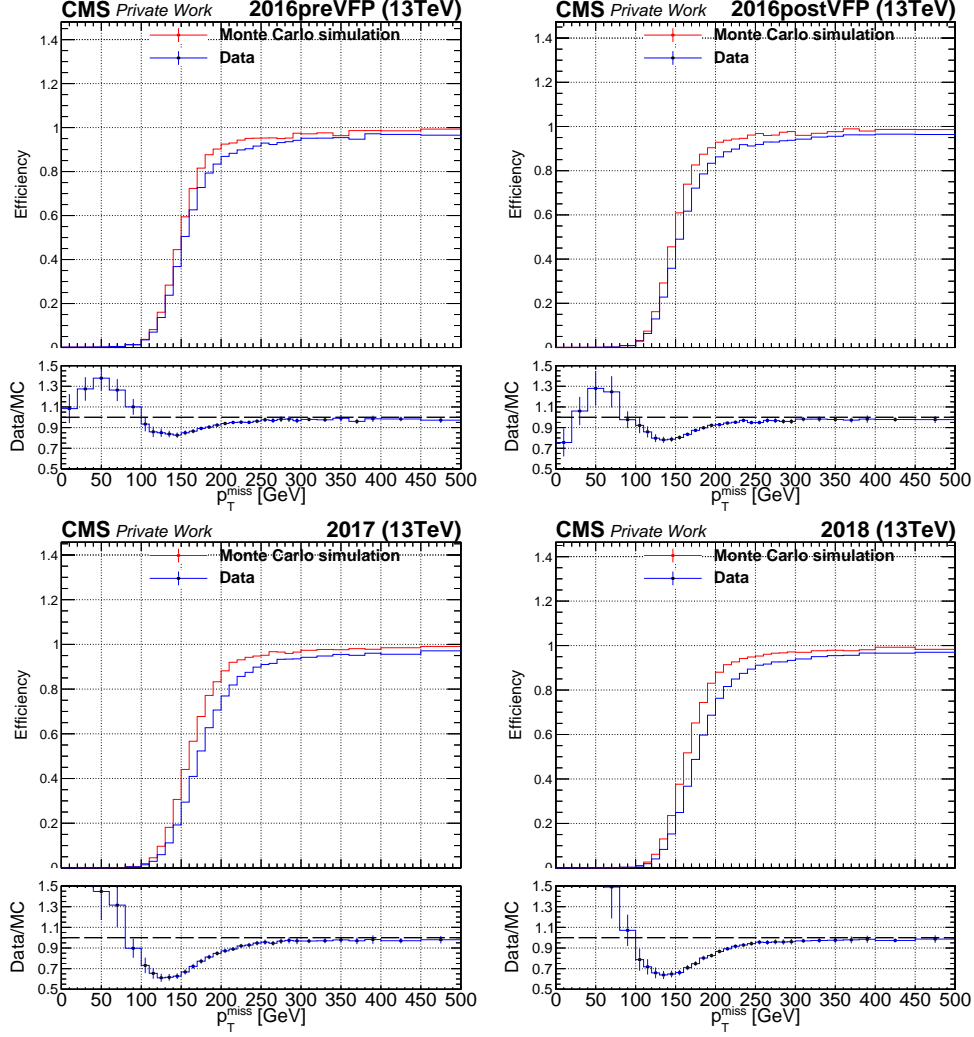
Figure 6.18: Efficiency of the $p_{\mathrm{T}}^{\mathrm{miss}}$ triggers measured in 2016 pre-VFP (upper left), 2016 post-VFP (upper right), 2017 (lower left), and 2018 (lower right) data sets and simulation.

also includes a parameter of interest $\mathrm{SF}_{\mathrm{fail}}$ that scales $\mathrm{SF}_{\mathrm{fail}} \times N_{\mathrm{fail}}$. However, $\mathrm{SF}_{\mathrm{fail}}$ is a dependent quantity obtained from the constraint, $\mathrm{SF} \times N_{\mathrm{pass}} + \mathrm{SF}_{\mathrm{fail}} \times N_{\mathrm{fail}} = N_{\mathrm{pass}} + N_{\mathrm{fail}}$. This ensures that SF and $\mathrm{SF}_{\mathrm{fail}}$ scale their respective regions in an anticorrelated way, such that the total number of signal events remains the same. In such an approach, the SF only controls the migration of events between the pass and fail categories and not the total number of signal events.

The scale factors are measured for d_{xy} thresholds of 0, 0.01, 0.02, 0.03, 0.04, 0.05, 0.07, and 0.09 cm, and for `DisTau` score thresholds of 0.7, 0.8, 0.9, 0.95, 0.97, 0.98, and 0.99. The d_{xy} threshold is capped at 0.09 cm because of the HPS algorithm's impact parameter internal constraints, resulting in no τ_{h} being reconstructed for larger d_{xy}. This setup allows the study of how the SFs evolve with increasing displacement of the jets.

Fits are stable at lower thresholds but become asymmetric at high d_{xy} and `DisTau` thresholds due to limited yields in the pass category, which leads to large, asymmetric uncertainties. High `DisTau` thresholds (e.g., 0.99, WPT) are stringent and result in highly limited statistics, making the SFs less reliable and prone to large uncertainties. Interme-
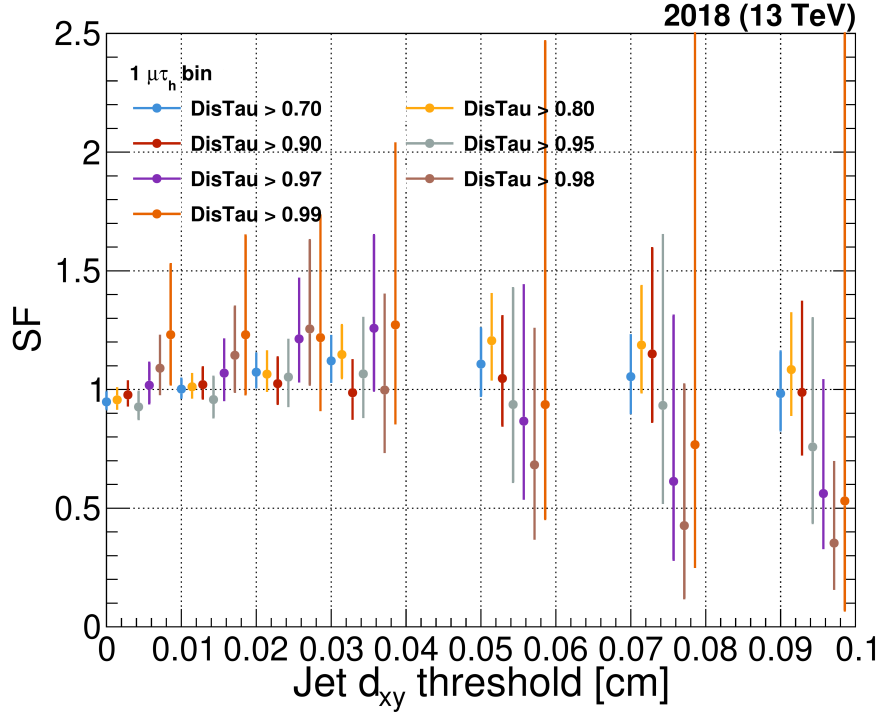
Figure 6.19: Scale factors measured for different jet d_{xy} and `DisTau` score thresholds. There are seven groups of points, each group for a particular d_{xy} threshold. For example, the group of points in the range $d_{xy} \in [0.01, 0.02)$ all correspond to $d_{xy} > 0.01$ cm. Within each group, the different colours correspond to different `DisTau` score thresholds.

diate `DisTau` thresholds, such as 0.7 (WPM), provide stable SFs across the range of d_{xy} thresholds, with uncertainties saturating at ± 0.15. This stability suggests WPM is robust for capturing signal-like jet properties while avoiding the limitations of WPT. Increasing d_{xy} thresholds align probe jets more closely with signal-like jets, and the SF for WPM remains consistent with unity in these cases, indicating reliable performance.

As a result of the study, the SF of 1 ± 0.15 per jet is applied for jets passing WPT in the signal region, resulting in a conservative 30% uncertainty on yields from tagger efficiency. This ensures robustness in capturing variations in tagger performance for true signal jets. The chosen thresholds balance sensitivity to signal-like jets and statistical reliability. This uncertainty ensures robustness in capturing variations in tagger performance for true signal jets.

6.8.3 Uncertainties

Systematic uncertainties are imposed on the data-driven background prediction and the expected yield of the signal MC simulation.

The following sources of systematic uncertainties are considered for the misidentified displaced τ_h background.

- Since the prediction in the BR is obtained using f_W measured with $W(\mu\nu)$+jets enriched events, one needs to account for the fact that differences (such as jet flavour and kinematics) between the $W(\mu\nu)$+jets enriched and baseline regions

can lead to f_W being different from f in the BR (f_{BR}). As the SR is a part of the BR, f_{BR} measured in data cannot be used to predict the background in the BR. Therefore, the relative difference between f_W and f_{BR} is estimated from the background simulation as follows:

$$\Delta f_{\text{region}}^{\text{rel}} = \frac{|f_W^{\text{MC}} - f_{\text{BR}}^{\text{MC}}|}{f_W^{\text{MC}}} .$$
      (6.12)

When predicting BR yields with f_W, the corresponding difference is included as an uncertainty in f_W as, $f_W(1 \pm \Delta f_{\text{region}}^{\text{rel}})$. This amounts to $\approx 10\%$ in the BRT2f1 (primary prediction) search bins.

- Due to the limited amount of events available in W($\mu\nu$)+jets enriched events, the misidentification probability f measurement is associated with non-negligible statistical uncertainty. This is the dominant source of uncertainty (up to 50% in the BRT2f1 search bins and depends on p_T and d_{xy} because of the f_W parameterisation).

The generation of the hypothetical signal process is associated with systematic uncertainties due to imperfections in modelling the physics process and measurement of physics objects. Below is the list of the uncertainties used for the simulation processes:

- *The hard process uncertainty* arises from variations in the renormalization μ_R and factorization scales μ_F in the matrix element calculation. These two scales are independently scaled up or down by a factor of two, providing two uncertainties viewed as an estimate for potential higher-order corrections to the ME.

- *Parton distribution functions uncertainties*: The simulated samples use PDFs from NNPDF3.1, and the uncertainty associated with the PDF choice is propagated. The PDF set includes 100 variations generated using either the eigenvector or Hessian methods [156, 157]. The uncertainty on α_s is additionally propagated to the PDFs. These variations create a 68% confidence interval envelope around the nominal PDF and are proportional to the predicted yield in signal simulation.

- *The p_T^{miss} trigger efficiency correction uncertainties* is estimated from measuring the scale factors as described in Section 6.8.3. The 68% confidence interval envelope is propagated and used to vary the p_T^{miss} trigger efficiency. If $p_T^{\text{miss}} < 250\,\text{GeV}$, the envelope is multiplied by a factor of two.

- *The `DisTau` tagger efficiency uncertainty* is discussed in Section 6.8.2. The 15% uncertainty is placed on one jet passing WPT, resulting in $\sim 30\%$ uncertainty in the yield with two jets passing WPT.

- *Jet energy scale corrections* systematic uncertainties arise from 27 sources, including parton shower modelling and pileup estimation. Section 3.7 details the jet energy correction procedure. These uncertainties impact jet energy measurements, affecting the selection process as jets shift in and out of acceptance. This, in turn, influences derived quantities, particularly p_T^{miss}.

- *Jet energy resolution* systematic uncertainties affect the measurement of jet energies and propagate to derived quantities such as p_T^{miss}. The selection of

properties dependent on jet kinematics is re-evaluated with jet energy smearing to account for resolution uncertainties.

- *Unclustered p_T^{miss} uncertainties:* The primary source of uncertainty in the p_T^{miss} measurement comes from jet energy measurement uncertainties. However, additional contributions arise from tracks and calorimeter deposits not associated with jets but included in the p_T^{miss} calculation. The selection is repeated with variations in unclustered energy within its uncertainties to account for it.

- *Luminosity:* This uncertainty is associated with the measurement of luminosity, 1.2% in 2016, 2.3% in 2017 and 2.5% in 2018.

- *Pre-firing* weights uncertainties are estimated based on MC simulation [88].

- *Pileup:* The uncertainty of the pileup reweighting factors associated with total pp collision cross section.

The summary of the systematic uncertainty values is shown in Table 6.7. The uncertainty demonstrates the yield scale effect after the signal region binning shown in Table 6.6. The effect is shown after a combination of the yield for four data-taking periods. Systematic uncertainties, including the fake rate region dependence, PDF uncertainties, hard process renormalization (μ_R) and factorization scales (μ_F), as well as the correlated component of the measured integrated luminosity, are treated as correlated across the different years. All other systematic uncertainties are considered uncorrelated.

Table 6.7: Relative systematic uncertainties in the SR from various sources in signal and background yields. The three values correspond to the minimum, median, and maximum values across the 8 SR bins, as defined in Tab. 6.6. For cases where the minimum and maximum differ by less than 1%, only the median is shown. In the header row, $\widetilde{\tau}$ and $c\tau_0$ are in units of GeV and mm, respectively. The uncertainty values shown here are prior to the maximum likelihood fit described in Sec. 6.9.

Uncertainty source	Misid. jets	$m_{\widetilde{\tau}} = 100\,\text{GeV}$		$m_{\widetilde{\tau}} = 200\,\text{GeV}$	
		$c\tau_0 = 50\,\text{cm}$	$c\tau_0 = 100\,\text{cm}$	$c\tau_0 = 50\,\text{cm}$	$c\tau_0 = 100\,\text{cm}$
	Values are shown as [min, median, max] in percentage units (%).				
μ_R scale	–	0.1, 0.3, 1.4	0.1, 0.5, 1.3	0.1	0.1
μ_F scale	–	0.5, 4.5, 7.1	1.2, 5.1, 7.1	0.6, 1.0, 2.9	0.6, 0.9, 2.8
pdf	–	3.5, 3.8, 6.0	2.8, 4.2, 6.0	4.0, 4.6, 5.9	3.9, 4.4, 5.1
p_T^{miss} trigger	–	1.6, 3.4, 3.8	1.6, 3.2, 4.1	1.7, 3.1, 3.4	1.6, 3.1, 3.4
DisTau ID	–	16.5, 17.3, 18.4	16.3, 17.2, 19.1	16.7	16.9
JER	–	0.2, 0.5, 8.0	0.1, 0.8, 4.6	0.2	0.2
JES	–	0.9, 2.2, 8.0	0.7, 3.0, 10.9	0.4, 1.3, 2.4	0.4, 1.0, 2.4
p_T^{miss} unclustered energy	–	0.3, 0.9, 8.0	0.3, 1.1, 8.5	0.3	0.3
Luminosity	–	1.6	1.6	1.6	1.6
Pre-firing	–	0.1	0.2	0.1	0.1
Pileup	–	0.7, 1.1, 4.0	0.6, 1.0, 5.2	0.6	0.6
Fake rate region	10.8, 11.1, 12.8	–	–	–	–
Fake rate statistics	14.6, 30.4, 56.2	–	–	–	–

6.9 Results and interpretation

This section is dedicated to hypothesis testing, validation of the established analysis workflow and statistical inference.

6.9.1 Validation region

As described in Section 6.7, the BRT1 region with exactly one loose and one tight jet is used to validate the background prediction. In Fig. 6.20, the predicted yield in comparison with the actual yield in the four data-taking periods is shown. The definition of the bins follows Table 6.6. The uncertainties include the statistical errors as well as those described in Section 6.8.3.
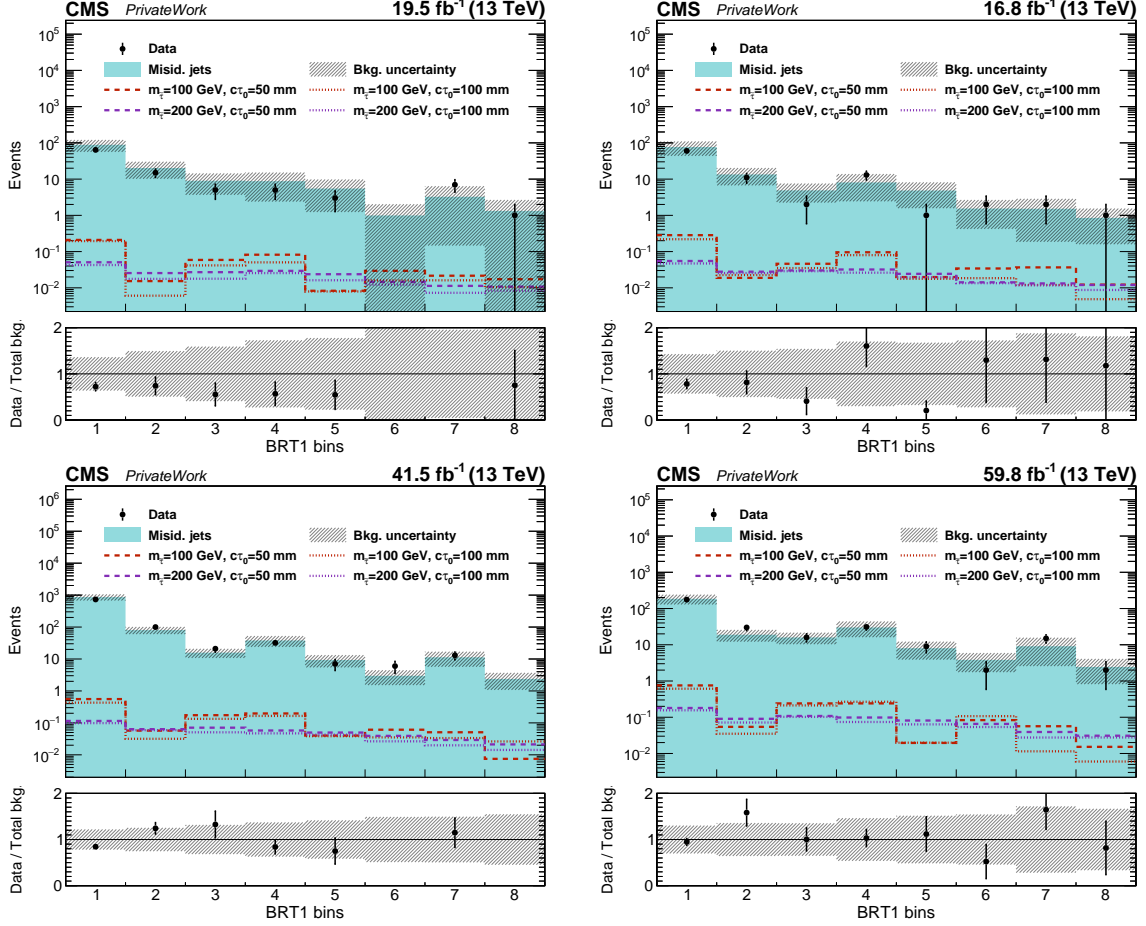

Figure 6.20: Observed and predicted event yields in the baseline region with one loose and one tight jet. A blue-filled histogram shows the predicted fake background. The black points show the number of events observed in the data. The coloured marker illustrates the expected yield for benchmark scenarios of the signal hypothesis with the $\widetilde{\tau}$ mass equal to 100 or 200 GeV and the proper decay length $c\tau_0$ of 5 and 10 cm. Each plot corresponds to a specific data-taking period: 2016 pre-VFP (top left), 2016 post-VFP (top right), 2017 (bottom left), and 2018 (bottom right). The lower panel displays the ratio of the data to the predicted event yields. The shown uncertainty includes both statistical error and systematic uncertainty.

Overall, good closure is achieved throughout the entire kinematic range of the validation region, and the data-to-MC normalisations are close to unity. Minor fluctuations are observed in bins with limited data statistics. However, these disagreements are typically within one standard deviation of the systematic uncertainty of the predicted yield. A more detailed validation of various kinematic properties in this region is shown in the

Appendix A.10.

6.9.2 Signal region

Figure 6.21 shows the comparison of the data-driven prediction with the observed data in the signal region and the expected signal yield in the corresponding region. Only two reference signal hypotheses are displayed, but effective signal-to-background separation is evident across a wide range of $\widetilde{\tau}$ mass hypotheses.
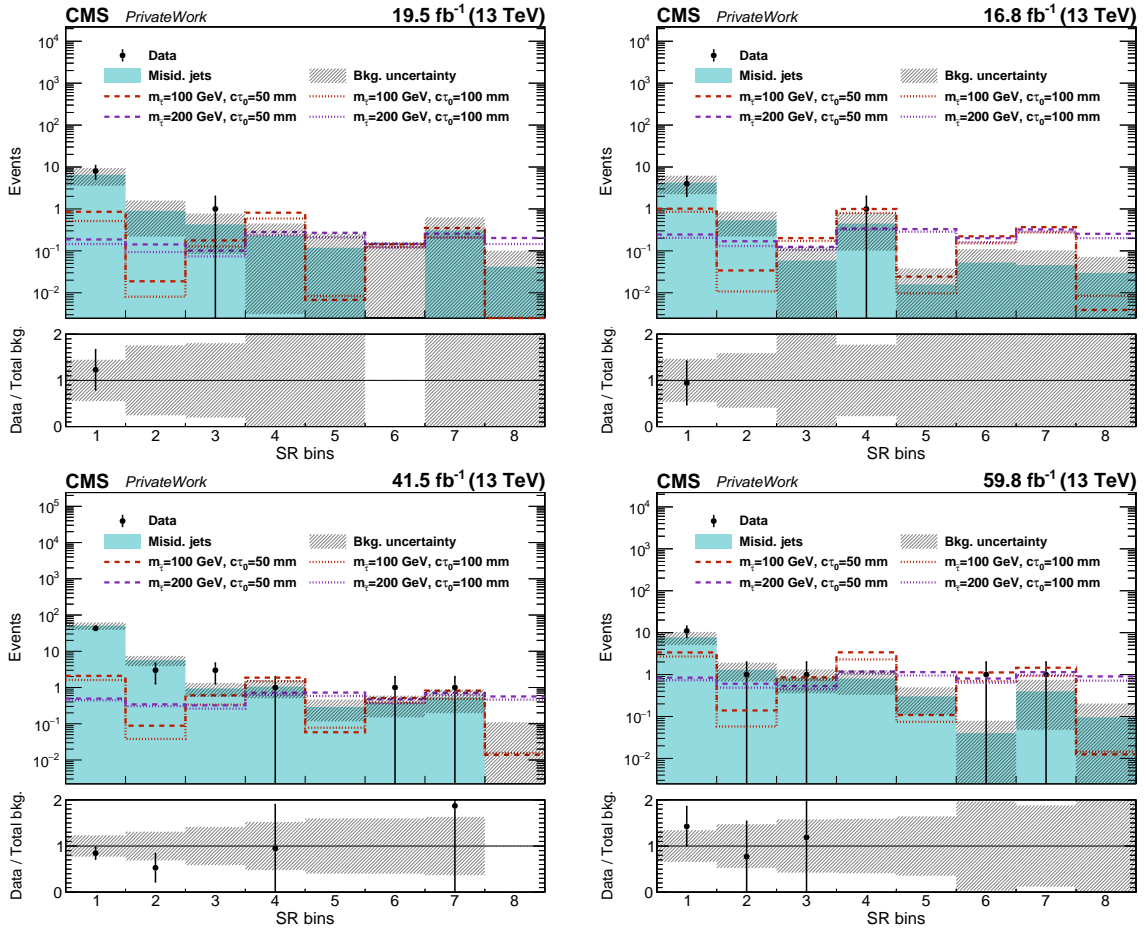
Figure 6.21: Observed and predicted event yield in the baseline region with two tight jets. A blue-filled histogram shows the predicted fake background. The black points show the number of events observed in the data. The coloured marker illustrates the expected yield for benchmark scenarios of the signal hypothesis with the $\widetilde{\tau}$ mass equal to 100 or 200 GeV and the proper decay length $c\tau_0$ of 5 and 10 cm. Each plot corresponds to a specific data-taking period: 2016 pre-VFP (top left), 2016 post-VFP (top right), 2017 (bottom left), and 2018 (bottom right). The lower panel displays the ratio of the data to the predicted event yields. The shown uncertainty includes both statistical error and systematic uncertainty.

The observed, predicted number of events and signal is given in Table 6.8. The expected signal yield is computed assuming a maximally mixed scenario. Bins 1-3, which have subleading jet $p_T^{j2} < 50$ GeV, are mostly background dominated; however, for larger $p_T^{j2} > 50$ GeV, mainly in bins 5,6 and 8 with $m_{T2} > 100$ GeV, the expected signal yield is mostly

dominant over the background.

Table 6.8: Predicted background and signal yields along with uncertainties in the 8 SR bins, as defined in Tab. 6.6. In the header row, $\widetilde{\tau}$ mass and $c\tau_0$ are shown. The number of events observed in the recorded data is also shown. The first uncertainty value listed is statistical, and the second is systematic. The yields and uncertainties shown here are prior to the maximum likelihood fit described in Sec. 6.9.3. The results correspond to an integrated luminosity of 138 fb^{-1} recorded over the Run2 period.

SR bins	Data	Misid. jets	$m_{\widetilde{\tau}} = 100\,\text{GeV}$		$m_{\widetilde{\tau}} = 200\,\text{GeV}$	
			$c\tau_0 = 50\,\text{cm}$	$c\tau_0 = 100\,\text{cm}$	$c\tau_0 = 50\,\text{cm}$	$c\tau_0 = 100\,\text{cm}$
1	66	69.3±3.1±13	7.3±0.19±1.4	5.7±0.17±1.1	1.8±0.027±0.33	1.5±0.025±0.28
2	4	8.4±0.9±1.9	0.3±0.04±0.06	0.1±0.024±0.027	1.3±0.023±0.23	1.0±0.021±0.19
3	5	2.3±0.5±0.5	1.8±0.10±0.4	1.4±0.09±0.28	1.1±0.024±0.20	0.9±0.022±0.17
4	2	2.5±0.32±0.8	7.1±0.18±1.3	5.2±0.16±0.9	2.5±0.032±0.5	2.2±0.031±0.4
5	0	0.7±0.18±0.24	0.2±0.032±0.04	0.2±0.029±0.04	2.5±0.032±0.4	2.0±0.029±0.4
6	2	0.5±0.17±0.17	2.0±0.11±0.4	1.4±0.09±0.28	1.6±0.029±0.31	1.3±0.026±0.25
7	2	1.3±0.23±0.5	3.0±0.12±0.6	1.9±0.10±0.4	2.4±0.033±0.5	2.1±0.030±0.4
8	0	0.2±0.09±0.10	0.0±0.012±0.007	0.0±0.014±0.009	1.9±0.029±0.4	1.5±0.026±0.28
Total	81	85.1±3.3±17	21.8±0.33±4	15.8±0.28±3.0	15.1±0.08±2.8	12.6±0.07±2.3

Figure 6.22 presents the observed and predicted event yields in the signal region, combining all four data-taking periods of Run 2.

6.9.3 Limit setting methodology

The special procedure for the hypothesis testing [158] developed by the LHC Higgs Combination group, referred to as CL$_\text{s}$ method, is used in this analysis. It aims to exclude new physics hypotheses under the observed experimental outcome. The procedure for computing exclusion limits is based on the modified frequentist method.

The prediction of the signal yield s and the background yield b are subject to multiple uncertainties that are introduced through nuisance parameters θ. The expected yield is expressed as $\mu \cdot s(\theta) + b(\theta)$, where μ is a signal strength modifier. The goal is to derive an upper limit on μ.

Uncertainties are treated as fully correlated or uncorrelated for a clean likelihood factorisation. The systematic error PDFs $\rho(\theta|\hat{\theta})$ represent belief in θ. Here, θ denotes the nuisance parameters that encode systematic uncertainties in the model, and $\hat{\theta}$ is the "best fit" estimate of the nuisance parameter θ. Using Bayes' theorem, these PDFs can be reinterpreted as posteriors from hypothetical measurements:

$$\rho(\theta|\hat{\theta}) \sim p(\hat{\theta}|\theta) \cdot \pi_\theta(\theta)\,, \tag{6.13}$$

where $\pi_\theta(\theta)$ is the prior PDF. This reformulation integrates systematic uncertainties into a frequentist framework via auxiliary measurements, adding likelihood constraints and test statistic distributions.

To distinguish between the background-only hypothesis and the signal+background hypothesis, the profile likelihood ratio test statistic is used. The Poisson probability of observing n_i events in bin i is given by:

$$\mathcal{P}(n_i) = \frac{(\mu s_i(\theta) + b_i(\theta))^{n_i}}{n_i!} e^{-(\mu s_i + b_i)}\,. \tag{6.14}$$
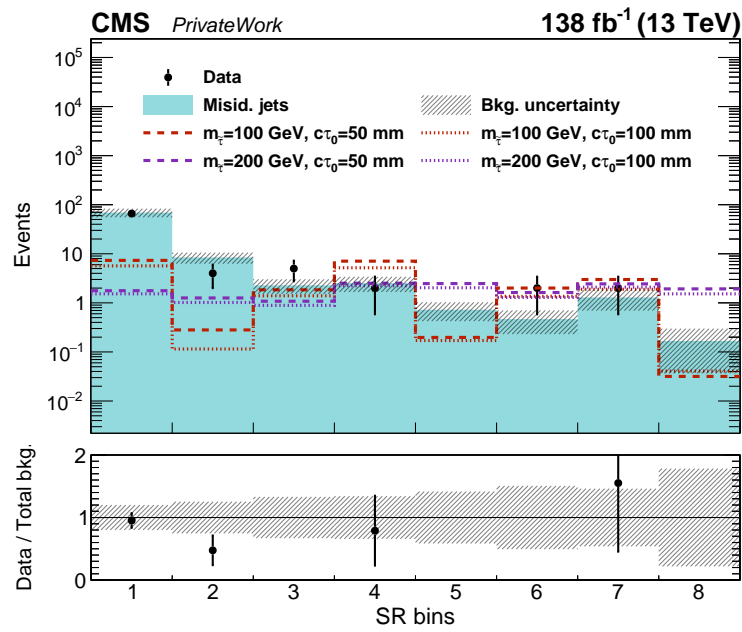
Figure 6.22: Observed and predicted event yield in the baseline region with two tight jets, combining all three years. A blue-filled histogram shows the predicted fake background. The black points show the number of events observed in the data. The coloured marker illustrates the expected yield for benchmark scenarios of the signal hypothesis with the $\widetilde{\tau}$ mass equal to 100 or 200 GeV and the proper decay length $c\tau_0$ of 5 and 10 cm. The lower panel displays the ratio of the data to the predicted event yields. The shown uncertainty includes both statistical error and systematic uncertainty.

The **likelihood function** is then constructed as:

$$\mathcal{L}(\text{data}|\mu,\theta) = \text{Poisson}(\text{data}|\mu s(\theta) + b(\theta)) \cdot \rho(\theta|\tilde{\theta}) \,. \tag{6.15}$$

The **test statistic** $\tilde{q}_\mu$ is defined using the profile likelihood ratio:

$$\tilde{q}_\mu = -2\ln\frac{\mathcal{L}(\text{data}|\mu,\tilde{\theta}_\mu)}{\mathcal{L}(\text{data}|\hat{\mu},\hat{\theta})}, \quad \text{with constraint } 0 \le \hat{\mu} \le \mu \,. \tag{6.16}$$

Here, $\tilde{\theta}_\mu$ represents the conditional estimate of the nuisance parameters θ under the assumption of a specific signal strength μ and $\hat{\theta}$ is global maximum likelihood estimate of the signal strength, effectively giving the "best fit" signal strength to the observed data.

Using the test statistic, the probability distributions $f(\tilde{q}_\mu|\mu,\tilde{\theta}_\mu^{\text{obs}})$ are constructed via pseudo-experiments. The p-values for the signal+background and background-only hypotheses are given by:

$$p_\mu = P(\tilde{q}_\mu \ge \tilde{q}_\mu^{\text{obs}}|\text{signal} + \text{background}) = \int_{\tilde{q}_\mu^{\text{obs}}}^{\infty} f(\tilde{q}_\mu|\mu,\tilde{\theta}_\mu^{\text{obs}})d\tilde{q}_\mu \,, \tag{6.17}$$

$$1 - p_b = P(\tilde{q}_\mu \ge \tilde{q}_\mu^{\text{obs}}|\text{background only}) = \int_{\tilde{q}_\mu^{\text{obs}}}^{\infty} f(\tilde{q}_\mu|0,\tilde{\theta}_0^{\text{obs}})d\tilde{q}_\mu \,. \tag{6.18}$$

The **confidence level** CL_s is then calculated as:

$$CL_s(\mu) = \frac{p_\mu}{1 - p_b} \,. \tag{6.19}$$

A model is excluded at 95% CL if $CL_s \le 0.05$.

The **expected limit** is determined by generating pseudo-data under the background-only hypothesis and computing the median 95% CL_s limit. The $\pm 1\sigma$ and $\pm 2\sigma$ bands are defined by crossing points at 16% and 84%, as well as 2.5% and 97.5%, respectively.

An asymptotic formula is used for large sample sizes, reducing computational costs. The pdf of q_μ follows:

$$f(q_\mu|\mu') = \frac{1}{2}\delta(q_\mu) + \frac{1}{2\sqrt{2\pi q_\mu}}e^{-q_\mu/2} \,. \tag{6.20}$$

The CLs value can then be approximated using Gaussian cumulative distributions; this method is called asymptotic approximation:

$$CL_s = \frac{1 - \Phi(\sqrt{q_\mu})}{\Phi(\sqrt{q_\mu^A} - \sqrt{q_\mu})} \,, \tag{6.21}$$

where Φ is the cumulative standard Gaussian function and q_μ^A approximates the test statistic on the signal + background Asimov data set.

This approximation is widely used in LHC experiments for rapid limit setting in large-scale searches. The hypothesis test of the Supersymmetry model is performed using the CL_s method with profile likelihood ratio tests. This procedure ensures a robust statistical treatment of uncertainties and allows precise determination of 95% CL limits.

6.9.4 Upper limits and fit profiling

The systematic uncertainties are modelled as log-normal nuisance parameters; to profile the fit procedure, they are varied around their nominal values after being constrained by the maximum likelihood fit to determine the pulls. The nuisance pulls quantify the deviation of the post-fit values of nuisance parameters $\hat{\theta}$ with respect to pre-fit expectations θ_I, normalized to their respective standard deviations (σ_I). This can be expressed as $\frac{\hat{\theta}-\theta_I}{\sigma_I}$. The pulls are an important insight into the likelihood fit dynamic.

The impact of a nuisance parameter θ on the signal strength r (also referred to as μ in Section 6.9.3) is assessed by determining the shift in r when θ is fixed at its $+1\sigma$ and -1σ post-fit values. During this evaluation, all other nuisance parameters are simultaneously profiled as log-normal. This approach quantifies the influence of individual systematic uncertainties on the extracted signal strength.
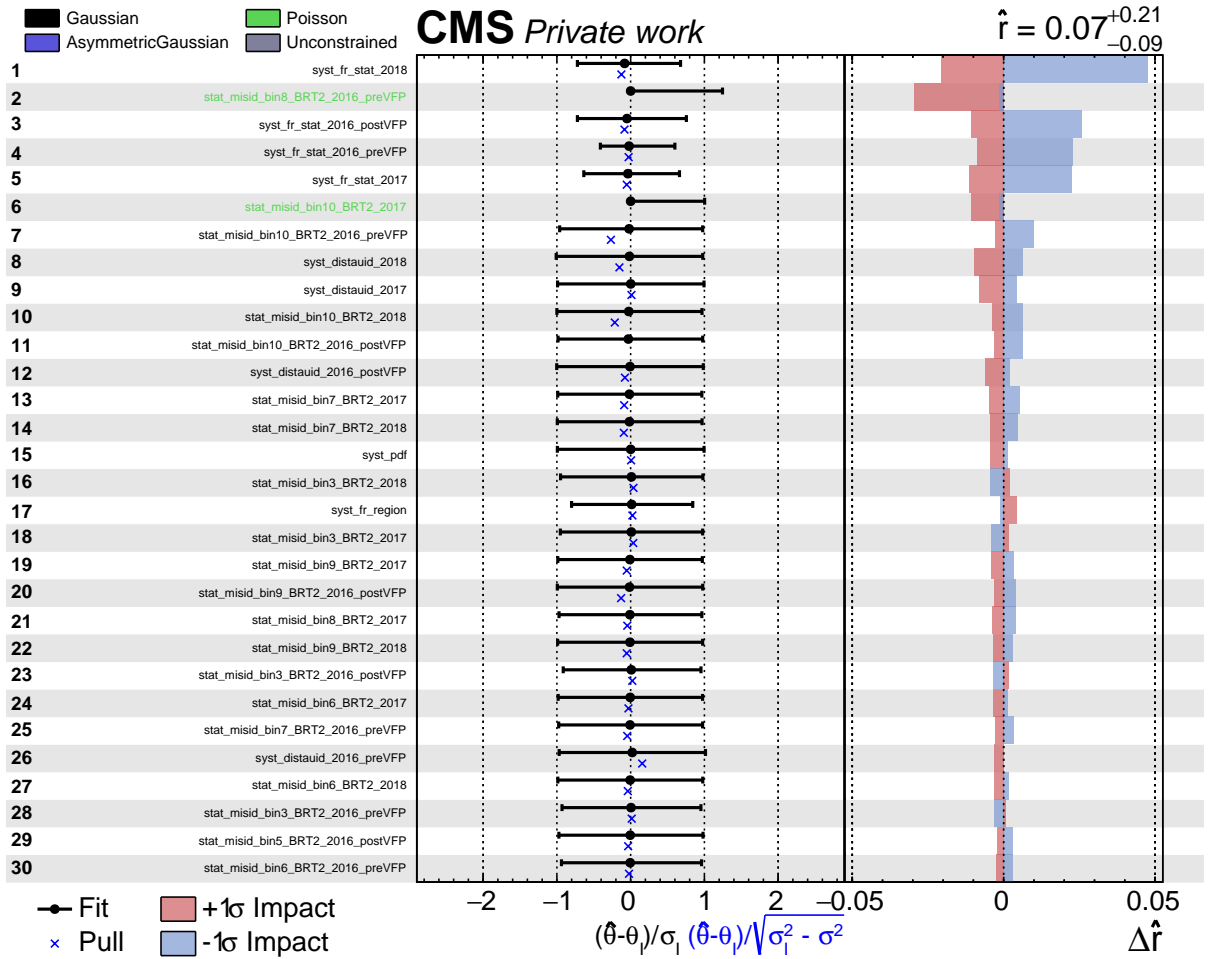
Figure 6.23: The most relevant 30 uncertainties, sorted by the impact and associated pulls for the $\widetilde{\tau}$ mass equal to $200\,\mathrm{GeV}$ and $c\tau_0 = 100\,\mathrm{mm}$, derived from a background Asimov dataset. The middle panel illustrates the pulls, while the right panel depicts the impact on the signal strength when scaling the uncertainty by 1σ upward (red band) and downward (blue band).

Following the aforementioned metrics definition, the likelihood fit is profiled for a bench-
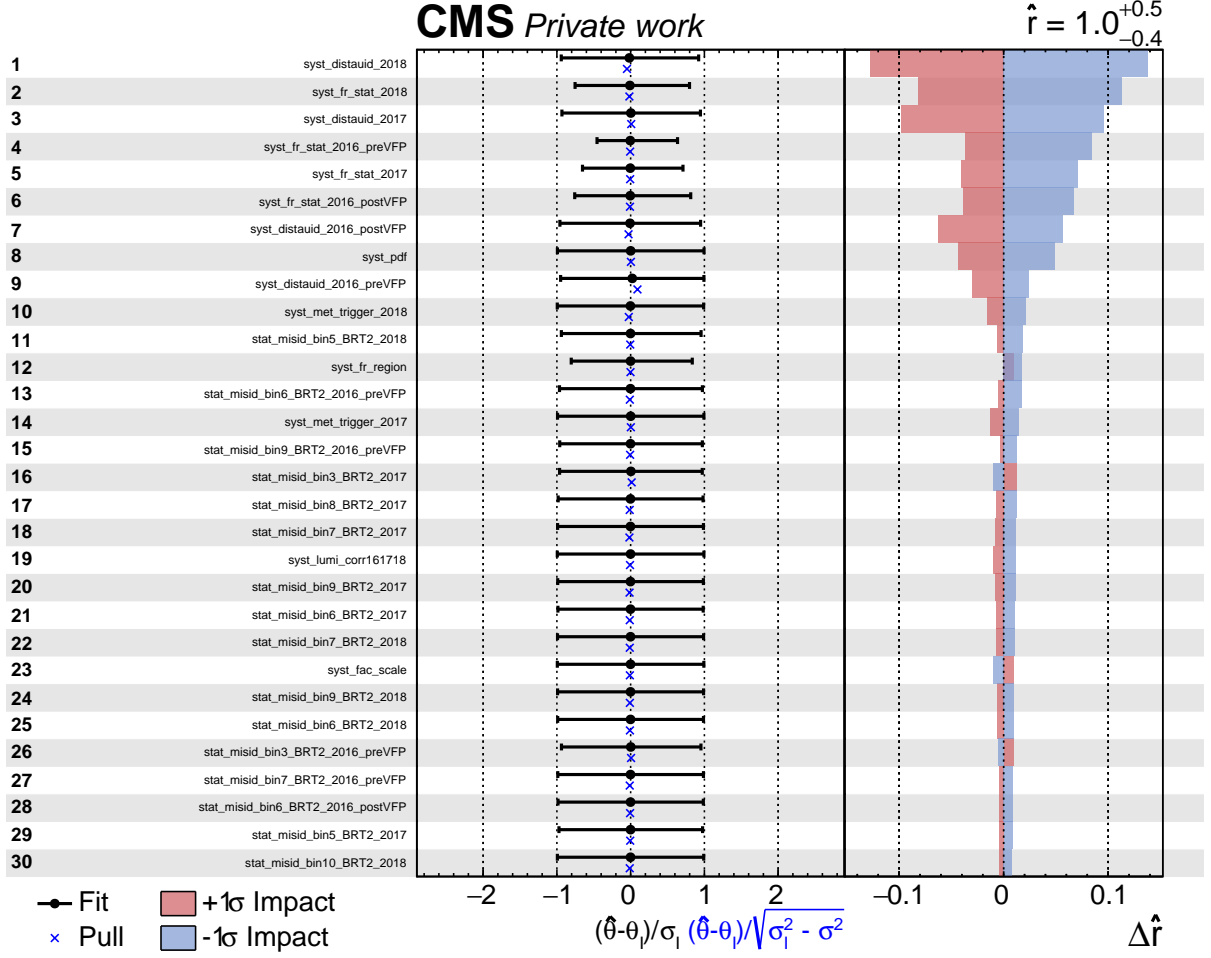
Figure 6.24: The most relevant 30 uncertainties, sorted by the impact and associated pulls for the $\widetilde{\tau}$ mass equal to $200\,\mathrm{GeV}$ and $c\tau_0 = 100\,\mathrm{mm}$, derived from a signal plus background Asimov dataset. The middle panel illustrates the pulls, while the right panel depicts the impact on the signal strength when scaling the uncertainty by 1σ upward (red band) and downward (blue band).

mark signal model with the $\widetilde{\tau}$ mass equal to $200\,\mathrm{GeV}$ and $c\tau_0 = 100\,\mathrm{mm}$. The profiling derived from a background Asimov dataset and from a signal plus background Asimov dataset is shown in Fig. 6.23 and Fig. 6.24, respectively. The fit performed on the background Asimov dataset results in the $r = 0.07^{+0.21}_{-0.09}$, demonstrating compatibility with the null hypothesis. The fit on the background plus signal Asimov dataset results in the $r = 1.0^{+0.5}_{-0.4}$, showing the sensitivity to the hypothetical signal process.

The results are represented as constraints on the production of $\widetilde{\tau}$ pairs cross-section within the framework of simplified models [159], which presuppose that $\widetilde{\tau}$ decays into a τ lepton and a gravitino. The 95% CL exclusion limits have been calculated for the GMSB model. The fit is performed on the combination of four data-taking periods described before. Figure 6.25 shows the 95% CL expected limit for a scenario with maximal mixing between the right- and left-handed ($\widetilde{\tau}_\mathrm{L}$ and $\widetilde{\tau}_\mathrm{R}$) eigenstates. The plots are shown for a few benchmark scenarios of a proper decay length ranging from $5\,\mathrm{mm}$ to $1\,\mathrm{m}$ and $\widetilde{\tau}$ mass ranging from 100 to $600\,\mathrm{GeV}$. The gravitino mass is set to $1\,\mathrm{GeV}$.

While the limit is set in the scenario of maximal mixing between the right- and left-handed eigenstates, alternative interpretations can be adopted. The observed count in each bin of the signal region can be expressed as $\mu \cdot s(\theta) + b(\theta)$ where $s(\theta)$ is derived as $\sigma \cdot \mathcal{L} \cdot \frac{n_i}{N}$, where $\frac{n_i}{N}$ is acceptance ratio that depends on the initial number of generated invents (N) and number of events passing selection (n_i), $\mathcal{L}$ is the integrated luminosity and σ is the signal cross section. The acceptance ratio remains the same numerically in case two hypotheses are kinematically identical. In this case, results can be evaluated by simply scaling the cross-section to the other scenario. As shown in Appendix A.11, the mass-degenerate production scenario—where the two $\widetilde{\tau}$ mass eigenstates have nearly identical masses and exhibit similar behaviour at the level of jet reconstruction—is found to be kinematically close to the maximal mixing scenario. Based on this observation, the results can be interpreted for the mass degenerate scenario. The exclusion limit for this interpretation is shown in Fig 6.26.
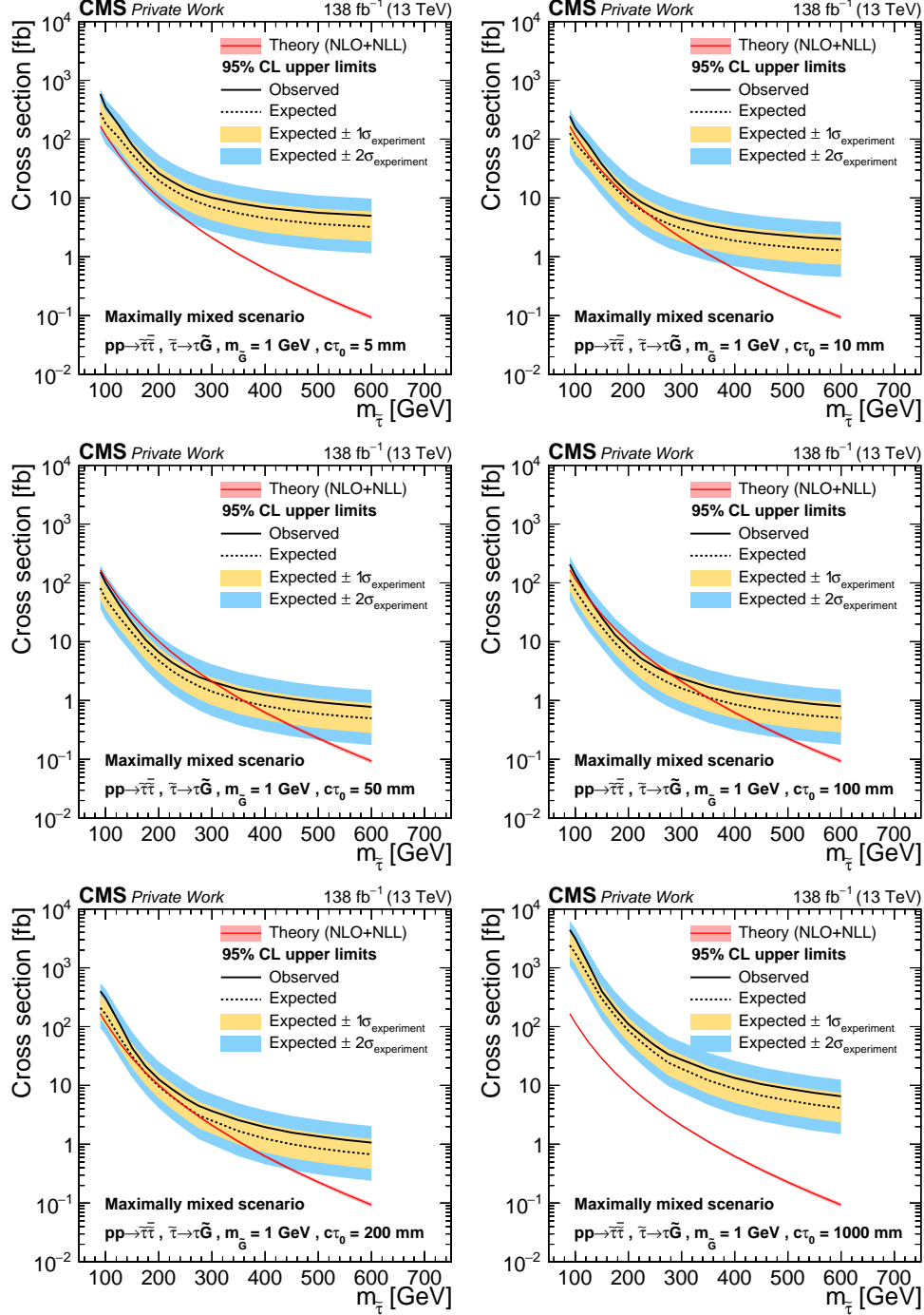
Figure 6.25: The expected and observed 95% CL upper limit on the production cross section of $\widetilde{\tau}$ pairs in the maximally mixed scenario. The limit is shown as a function of different $\widetilde{\tau}$ masses in the range of 100-600 GeV. Each figure corresponds to a certain proper decay length $c\tau_0$ of the $\widetilde{\tau}$, ranging from 5 mm to 1000 mm.
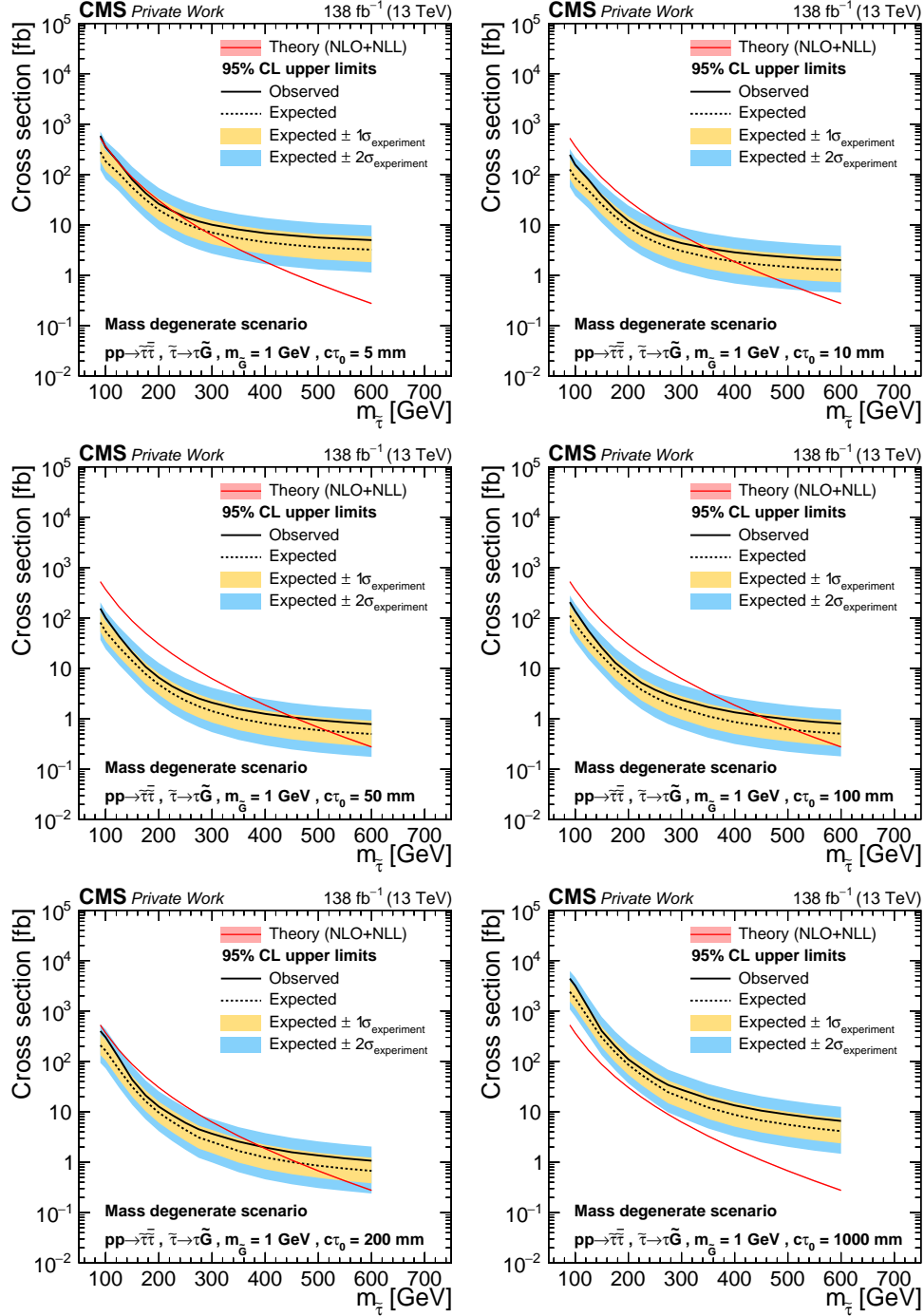
Figure 6.26: The expected and observed 95% CL upper limit on the production cross section of $\widetilde{\tau}$ pairs in the mass degenerate scenario. The limit is shown as a function of different $\widetilde{\tau}$ masses in the range of 100-600 GeV. Each figure corresponds to a certain proper decay length $c\tau_0$ of the $\widetilde{\tau}$, ranging from 5 mm to 1000 mm.

6.9.5   Exclusion region

Exclusion limits as a function of the $\widetilde{\tau}$ mass and decay length $c\tau_0$ are shown in Fig. 6.27. Only a discrete number of LLP lifetimes are generated due to computational constraints. To cover the continuous exclusion plane, a lifetime reweighting procedure is used as described in Appendix A.9. Overall, the plot demonstrates the exclusion limit for long-lived $\widetilde{\tau}$ pair production in the maximally mixed scenario with a gravitino mass of $m_{\widetilde{G}} = 1\,\text{GeV}$, with the most stringent exclusion observed at lower masses (up to $300\,\text{GeV}$) and intermediate decay lengths from $20\,\text{mm}$ up to $15\,\text{cm}$. The solid black line, representing the observed exclusion limit, closely follows the solid red line, which denotes the expected exclusion limit under the background-only hypothesis. Moreover, the observed limit remains within the $\pm 1\sigma$ experimental uncertainties (dashed red lines) throughout the entire parameter space. This suggests that the observed data aligns with the expected background prediction within statistical and systematic uncertainties. No significant excess over the expected background implies the absence of a strong signal indicative of new physics within the analysed parameter space.
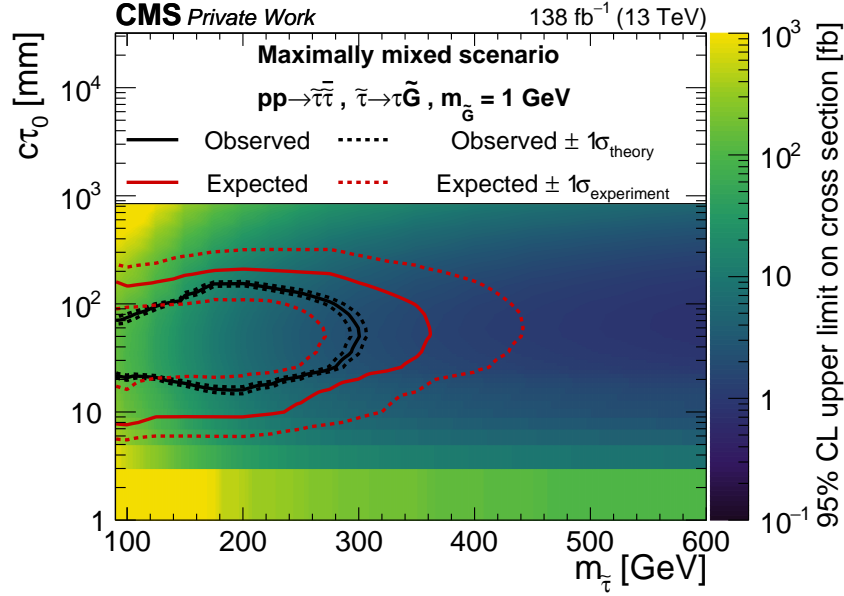
Figure 6.27: The expected and observed 95% CL upper limit on maximally mixed $\widetilde{\tau}$ pairs production. The limit is shown at different $\widetilde{\tau}$ masses and proper decay length $c\tau_0$.

Exclusion limits for the mass degenerate scenario are shown in Fig. 6.28. Compared to the maximally mixed scenario (previous plot), the exclusion region is significantly broader, extending over a wider range of $\widetilde{\tau}$ masses and $c\tau_0$ values. This broader exclusion space arises due to the higher production cross-section in the mass degenerate scenario, enhancing the sensitivity of the analysis. For a $\widetilde{\tau}$ mass of $250\,\text{GeV}$, decay length from $5\,\text{mm}$ up to $40\,\text{cm}$. The mass exclusion limit for a moderate displacement of $10\,\text{cm}$ is up to $500\,\text{GeV}$.
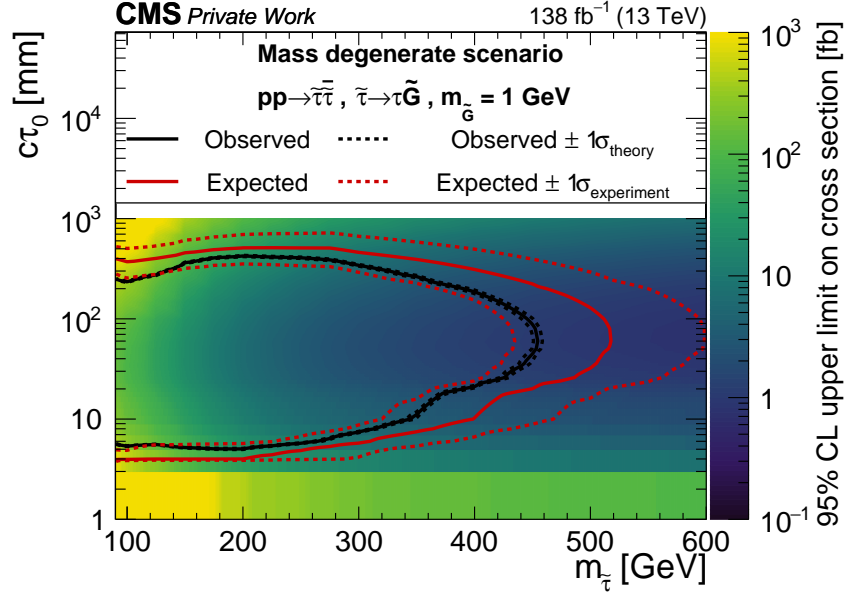
Figure 6.28: The expected and observed 95% CL upper limit on mass degenerate $\widetilde{\tau}$ pairs production. The limit is shown at different $\widetilde{\tau}$ masses and proper decay length $c\tau_0$.

6.10 Analysis summary and prospects

The sensitivity on the production cross section of $\widetilde{\tau}$ pairs in the maximally mixed scenario is significantly improved compared to previous searches. Specifically, Ref. [10] considered a fully hadronic channel and achieved an exclusion sensitivity up to a proper decay length of $c\tau_0 = 0.1\,\mathrm{mm}$, relying on the default τ_h reconstruction and identification to tag displaced τ_h decays. However, this analysis has demonstrated that a dedicated reconstruction method can significantly improve the reach in this channel, thereby excluding a previously unexplored region.

The analysis in Ref. [48] focused on a mass-degenerate scenario with a higher cross-section and considered only the fully leptonic channel. This approach excluded $c\tau_0$ values in the range of 0.02–10 cm for $m(\widetilde{\tau}) = 100\,\mathrm{GeV}$. In contrast, the results presented in this thesis extend the sensitivity by incorporating displaced hadronic tau decays, leading to the exclusion of $c\tau_0$ values in the range of 0.5–30 cm for the same $\widetilde{\tau}$ mass.

The results obtained in this analysis are consistent with the ATLAS analysis presented in Ref. [49], particularly regarding the upper 95% confidence limit on the cross section. The improved sensitivity of the displaced τ_h reconstruction allows to set comparable or even more stringent limits in specific regions of parameter space. This consistency reinforces the robustness of this approach and highlights the potential for future searches utilising dedicated displaced τ_h identification techniques.

Overall, for the maximally mixed scenario, the observed exclusion limit excludes $\widetilde{\tau}$ masses in the range of approximately 100 GeV to 300 GeV. The exclusion covers $c\tau_0$ values between 10 mm and a few hundred mm, with the strongest sensitivity in the 20–100 mm range. The observed limits stay well within the 1σ experimental uncertainty (dashed red lines), showing a good match between observed and expected results.

The observed exclusion limit for the mass degenerate scenario demonstrates a broader

mass exclusion, up to nearly 450 GeV. The exclusion extends across a wider range of proper decay length, from a few mm to approximately 30 cm, highlighting strong sensitivity to both short and long-lived particles. The mass degenerate scenario provides a significantly wider exclusion region, showcasing the effect of a higher cross-section. The contours indicate robust exclusion performance, with the observed limit consistently within the 1σ experimental uncertainty band.

In conclusion, this work demonstrates that a dedicated displaced τ_{h} reconstruction approach significantly enhances the sensitivity of long-lived particle searches, revealing new exclusion regions and strengthening the experimental constraints on long-lived $\widetilde{\tau}$ production within the GMSB scenario. This advancement paves the way for further improvements in searching BSM phenomena at the LHC.

Chapter 7

Summary and outlook

Despite its remarkable successes in describing a wide range of observed phenomena, the Standard Model (SM) of particle physics is known to be incomplete. It leaves unanswered questions, among them the origin of dark matter and dark energy and the matter–antimatter imbalance. Nevertheless, extensive searches for beyond the Standard Model (BSM) phenomena at high-energy colliders, including the Large Hadron Collider (LHC), have so far essentially confirmed the SM 's predictions, indicating little evidence of new particles or interactions.

This thesis investigates Supersymmetry (SUSY) as an extension of the SM. Its central focus is a search for the pair production of long-lived SUSY partners of the τ lepton ($\widetilde{\tau}$) in proton-proton collisions at a centre-of-mass energy of $\sqrt{s} = 13\,\text{TeV}$, using data from the Compact Muon Solenoid (CMS) detector corresponding to an integrated luminosity of $138\,\text{fb}^{-1}$ collected between 2016 and 2018. In a maximally mixed scenario, where the supersymmetric partners of the left- and right-handed τ leptons ($\widetilde{\tau}_{\text{L}}$ and $\widetilde{\tau}_{\text{R}}$) are equally mixed, a previous study [10] excluded $\widetilde{\tau}$ masses in the range of 150 to 220 GeV for a proper decay length ($c\tau_0$) of 0.01 mm. However, the suboptimal performance of standard τ_{h} reconstruction and identification algorithms for displaced signatures constrained its sensitivity to larger lifetimes. Therefore, this thesis investigated the development of both prompt and displaced τ identification algorithms.

The prompt hadronically decaying τ lepton (τ_{h}) identification algorithm, DeepTau v2.5, has been notably improved in both data-to-MC agreement and overall performance. This is achieved thanks to a combination of domain adaptation techniques, updated training datasets, thorough feature standardisation, careful hyperparameter tuning, and balanced data sampling. A key achievement of this release is the comprehensive redevelopment of the framework for τ_{h} identification, covering data format design, refinement of the data-sampling algorithm, updates to the training machinery, and accurate neural network architecture tuning - all culminating in a model that is readily deployable in the CMS data pipeline and recommended for Run 2 and Run 3 analyses. This algorithm has already shown a $\approx 30\%$ reduction in background contributions and yields efficiency correction factors closer to unity—on average $\approx 5\%$ better—thereby reinforcing the model's robustness and reliability for future CMS physics studies.

Since the hadrons-plus-strips (HPS) algorithm [119, 120] is not designed to accommodate significantly displaced τ_{h} topologies, a novel neural-network-based displaced τ_{h} tagger (DisTauTag) has been developed, building upon the ParticleNet [9] architecture to iden-

147

tify displaced τ_h decays that originate significantly away from the primary vertex, where traditional algorithms fall short. The tagger performance is estimated for displaced τ_h using simulated long-lived $\widetilde{\tau}$ sleptons, hypothesised in GMSB [38, 39, 40, 41] scenarios. Demonstrating promising rejection of quark- and gluon-initiated backgrounds while retaining signal, the tagger's behaviour on real collision data was validated with 13 TeV data in a region dominated by jets from DY + jets. The tagger score distribution in the simulation aligns well with real data for both background and signal-like jets, showcasing good data-to-MC agreement. Furthermore, because the tagger minimally relies on process-specific kinematic selections, it broadly applies to other searches involving displaced τ_h signatures. Certain dark matter models, vectorlike leptons, leptoquarks, and hidden sector scenarios can produce long-lived particles decaying into displaced τ leptons, making this signature a common probe for diverse BSM phenomena. Appendix A.5 provides the proceedings describing this implementation. Building on the new identification algorithm, the work presented here achieved sensitivity in GMSB scenarios in which the supersymmetric partners of the τ lepton exhibit macroscopic lifetimes on the order of $\mathcal{O}(\text{cm} - \text{m})$.

The search for pair production of long-lived $\widetilde{\tau}$ extends previous efforts to search for long-lived supersymmetric particles by incorporating a dedicated displaced τ_h reconstruction algorithm that addresses the limitations of the standard τ_h reconstruction. The signal region is characterised by large p_T^{miss} and two jets with substantial displacement, compatible with pair-produced, long-lived $\tilde{\tau}$ sleptons. Because simulated backgrounds in this phase space are subject to significant uncertainties, a data-driven method is developed and validated in multiple control regions (notably $W(\mu\nu)$ + jets and $DY(\mu\mu)$ + jets) to accurately estimate the dominant Quantum chromodynamics (QCD) multijet background contributions. Furthermore, prompt τ_h objects from $DY(\mu\tau)$ + jets processes serve as a proxy for displaced τ_h in validating the reconstruction performance. A full suite of systematic uncertainties is evaluated before combining the Run 2 dataset to set exclusion limits.

Compared to previous searches using conventional τ_h reconstruction algorithms, this dedicated technique substantially enhances the sensitivity to long-lived $\tilde{\tau}$ production. In particular, it surpasses the reach in Ref. [10] in a fully hadronic channel by enabling the exclusion of proper decay lengths beyond $c\tau_0 = 0.1\,\text{mm}$. In scenarios where $\widetilde{\tau}$ masses are degenerate or low, this method extends the exclusion range for $c\tau_0$ by incorporating displaced hadronic decays (up to 0.5-30 cm for $m(\tilde{\tau}) = 100$ GeV), improving upon Ref. [48], which only considered fully leptonic decays. The results also exhibit good consistency with the ATLAS measurement in Ref. [49], indicating that comparable or more stringent constraints can be set in some areas of the parameter space.

In the maximally mixed scenario, masses between 100 and 300 GeV are excluded for $c\tau_0$ spanning from 10 mm to a few hundred millimetres, with the strongest sensitivity between 20 and 100 mm. The observed and expected limits are in good agreement within the 1σ uncertainty bands. For the mass-degenerate scenario, exclusions reach up to nearly 450 GeV and cover lifetimes from a few millimetres to approximately 30 cm, highlighting the broad sensitivity of this analysis. Overall, these observations underscore the effectiveness of the displaced τ_h reconstruction approach in probing new regions of supersymmetric parameter space and pave the way for further advancements in searching for BSM phenomena

at the LHC.

It is important to emphasise that, while achieving a significant improvement in the sensitivity for the pair production of long-lived $\widetilde{\tau}$ and enhancing the identification performance of displaced τ_h, several aspects present opportunities for further refinement:

- A dedicated reconstruction of displaced τ_h properties, such as momentum, charge, and decay mode, could provide additional benefits, particularly in defining signal and background prediction regions. Utilising same-sign or opposite-sign lepton pair selection strategies and achieving a more precise reconstruction of kinematic variables related to τ_h momentum may further enhance the sensitivity and improve the treatment of systematic uncertainties. However, while refined τ_h property reconstruction is valuable, it does not eliminate the need for a dedicated algorithm to reject the background events.

- The analysis could benefit from further improving the displaced τ_h tagger and exploring alternative architectures, such as transformers, which may enhance efficiency. As demonstrated in this study, incorporating additional objects during training, such as lost tracks and secondary vertices, could enhance the performance. An alternative approach that leverages the full event topology rather than focusing on a single jet may also provide a promising alternative for increasing sensitivity.

- A high-precision study would benefit from exploring alternative calibration techniques for the displaced τ_h tagger. For instance, evaluating the tagger's performance on long-lived mesons that decay within the tracker volume could improve the accuracy of mismodeling effects and systematic uncertainties. Additionally, future developments could leverage domain adaptation techniques to further mitigate differences between data and simulation, ensuring improved robustness across various detector conditions.

- A specialised displaced τ_h trigger introduced in Run 3 has the potential to significantly enhance sensitivity in the low-$\widetilde{\tau}$ mass region, where $p_\mathrm{T}^\mathrm{miss}$ is relatively small.

- The combination of this search in the fully hadronic τ final state with semileptonic and fully leptonic final states has the potential to enhance exclusion limits.

This thesis significantly improves sensitivity to beyond-the-Standard-Model physics involving long-lived $\widetilde{\tau}$ at CMS by developing and optimising τ identification algorithms and analysis strategies. **The author's contributions include**:

Development of prompt τ identification (DeepTau v2.5) [8]: The author contributed to the development, refactoring, and optimisation of the τ identification algorithm training framework [145], with particular emphasis on enhancing the data processing pipeline. These contributions led to substantial performance improvements of the base model, as well as successful deployment of the optimised model within the CMS data processing software.

Development of displaced τ identification (DisTauTag) [160, 161]: The author identified the limitations of the default τ reconstruction algorithm [123] when applied to displaced τ leptons and developed a novel neural-network-based tagger from scratch using

ParticleNet, a GNN-like architecture. This tagger, validated using both simulated and collision data, is specifically tailored to displaced τ leptons and represents a significant advancement over previous methods. The author also integrated this model into the further analysis pipeline.

Analysis strategy and pipeline: The author designed the overall analysis strategy of the long-lived $\widetilde{\tau}$ search with the two displaced hadronically decaying τ leptons in the final state and implemented the corresponding analysis pipeline, including the definition of the signal region, robust background estimation methods, comprehensive systematic uncertainty evaluation, ultimately enabling accurate final result estimations.

Appendix A

Appendix

A.1 DeepTau v2.5 loss function

The final loss function has the following general form:

$$L(\mathbf{y}^{\mathrm{true}}, \mathbf{y}; \boldsymbol{\kappa}, \boldsymbol{\gamma}, \boldsymbol{\omega}) = \underbrace{\kappa_\tau\, H_\tau(\mathbf{y}^{\mathrm{true}}, \mathbf{y}; \boldsymbol{\omega})}_{\text{(a) Separation of all } \alpha} + \underbrace{\left(\kappa_{\mathrm{e}} + \kappa_\mu + \kappa_{\mathrm{jet}}\right)\overline{F}_{\mathrm{cmb}}(1 - y_\tau^{\mathrm{true}}, 1 - y_\tau; \gamma_{\mathrm{cmb}})}_{\substack{\text{(b) Focused separation of} \\ \text{e, } \mu, \text{ jet from } \tau_{\mathrm{h}}}}$$

$$+ \underbrace{\kappa_F \sum_{i \in \{\mathrm{e}, \mu, \mathrm{jet}\}} \kappa_i\, \hat{D}(y_\tau - 0.1)\, \overline{F}_i(y_i^{\mathrm{true}}, y_i; \gamma_i)}_{\substack{\text{(c) Focused separation of } \tau_{\mathrm{h}} \text{ from e, } \mu, \\ \text{jet for } y_\tau > 0.1}},$$

(A.1)

where $H(\mathbf{y}^{\mathrm{true}}, \mathbf{y}; \boldsymbol{\omega}) = -\sum_\alpha \omega_\alpha\, y_\alpha^{\mathrm{true}}\, y_\alpha$ with $\alpha \in \{\tau, \mathrm{e}, \mu, \mathrm{jet}\}$ is a categorical cross entropy component, and $\overline{F}(y^{\mathrm{true}}, y; \gamma) = \mathcal{N}\, F(y^{\mathrm{true}}, y; \gamma)$ with $F(y^{\mathrm{true}}, y; \gamma) = -y^{\mathrm{true}}\, (1 - y)^\gamma \log(y)$ is focal loss function with $\mathcal{N}$ serving as a normalisation factor, and $\hat{D}$ is a smoothened step function that turns on when y_τ has a value greater than 0.1. The focal loss terms in Eq. A.1 (b) and (c) place greater importance on regions of the parameter space where it is more challenging to distinguish τ_{h} candidates from e, μ, and jets. The step function in Eq. A.1 (c) excludes areas of the parameter space where the likelihood of a τ_{h} candidate being a genuine τ_{h} is low, as precise separation between e, μ, and jets in these scenarios is not a priority.

The parameters used in defining the loss function are as follows:

- The parameter κ_τ is set to 2.0, emphasizing the separation of τ_{h} from other classes.

- The parameters κ_{e}, κ_μ, and κ_{jet} are set to 0.4, 1.0, and 0.6 respectively. These parameters contribute to both general separation and focused separation of τ_{h} from electrons (e), muons (μ), and jets.

- The parameter κ_F is assigned a value of 5.0 to specifically enhance high τ_{h} efficiency during the focused separation process.

- The parameters γ_{e}, γ_{μ}, and γ_{jet} are assigned values of 2.0, 2.0, and 0.5 respectively. These parameters focus on the separation of τ_{h} from electrons, muons, and jets in scenarios where this separation is more challenging.

- The parameter γ_{cmb} is set to 2.0 and is used in the combined focal loss function, which applies to the separation of τ_{h} from electrons, muons, and jets.

- The parameter ω_{α} varies and is utilized for sample normalization to ensure that each sample contributes appropriately to the loss function based on its class.

These parameters are chosen to balance the different components of the loss function, with particular emphasis on discriminating against jets, which are the predominant background source.

A.2   DeepTau v2.5 hyper-parameter tuning

The DeepTau v2.5 training was conducted in three steps. First, a **baseline model** was trained on simulation data using the **NAdam optimizer** with a learning rate of 10^{-3} for three epochs. Then, to enhance electron discrimination, the model was trained for two more epochs with a lower learning rate of 10^{-4}, testing **SGD, Adam, and NAdam**. Finally, an **adversarial training phase** addressed data-MC discrepancies, focusing on improving performance in the tight working point region. Below, tuning results for the **first training steps** are shown.

The following hyperparameter tunning was performed, training 4 neural networks for each variation of architecture, and then the average value of the validation loss function was calculated as an average. The following architectures were tested:

Name	Val Loss Avg $\pm$ Std.	Trainable Parameters
v2	0.27318 ± 0.00207	1,151,378
fixed_conv_dense	0.27675 ± 0.00322	1,197,474
comp_merge_net_last_up	0.27421 ± 0.00215	3,210,581
comp_merge_net_last_down	0.28715 ± 0.00846	652,848
conv_reduction_up	0.27980 ± 0.00218	768,356
conv_reduction_down	0.28735 ± 0.01913	2,570,315
dense_reduction_up	0.27597 ± 0.00443	1,097,035
dense_reduction_down	0.32364 ± 0.07996	1,383,082

Table A.1: Validation loss statistics and trainable parameters for different models.

- **v2**: Baseline architecture with balanced reduction rates across all components. Uses a moderate number of trainable parameters.

- **fixed_conv_dense**: Increases the reduction rate in the convolutional layers to 1.8 and in the fully connected network to 2. Reduces the first-layer width of the fully connected network to half.

- **comp_merge_net_last_up**: Expands the last layer width of the component merging network from 64 to 128, increasing the contribution of convolutional feature extraction.

- **comp_merge_net_last_down**: Reduces the last layer width of the component merging network from 64 to 32, significantly lowering the number of parameters in the convolutional feature extraction branch.

- **conv_reduction_up**: Increases the reduction rate in the two-dimensional convolutional network to 2 while keeping other components unchanged.

- **conv_reduction_down**: Applies a more aggressive reduction in the two-dimensional convolutional network, lowering the number of convolutional filters.

- **dense_reduction_up**: Increases the reduction rate in the fully connected network to 3 and reduces the first-layer width to one-third for high-level features dense part.

- **dense_reduction_down**: Uses a less aggressive reduction in the fully connected network with a reduction rate of 1.5 and a first-layer width of $n/1.5$, maintaining a higher number of parameters.

A.3   DisTau tagger hyper-parameter tuning

To ensure optimal performance and mitigate potential bottlenecks within the architecture, extensive hyperparameter tuning was conducted. This process aimed to address any limitations that could hinder the performance of the model. The results are presented in Figure A.1. The following configurations were evaluated:

- **Small:** A simplified architecture with only two blocks of edge-convolution. The first block contains 32 neurons per 3 hidden layers, and the second block contains 64 neurons per 3 hidden layers (38k trainable parameters).

- **PF:** The nominal architecture using only Particle Flow candidates as input parameters (99k trainable parameters).

- **PF_Tracks:** The nominal architecture using both Particle Flow candidates and Lost Tracks as input parameters (104k trainable parameters).

- **PF_Tracks_SV:** The nominal architecture using Particle Flow candidates, Lost Tracks, and secondary vertices as input parameters (106k trainable parameters).

- **NoWeight/Weight:** The nominal architecture tested with and without applying re-weighting to balance the classes (nominal trainable parameters).

- **KNN-Up:** Architecture with an increased number of nearest neighbors, set to $k = 16$ (nominal trainable parameters).

- **KNN-Reduce:** Architecture with a reduced number of nearest neighbors, set to $k = 7$ (nominal trainable parameters).

- **Pad_Conv:** Padding edge features to the same dimensionality and preprocessing them with a neural network, as described in Chapter 5.4.3.1 (104k trainable parameters).

- **Type_Conv:** Preprocessing each object type with a different neural network to the same dimensionality (101k trainable parameters).
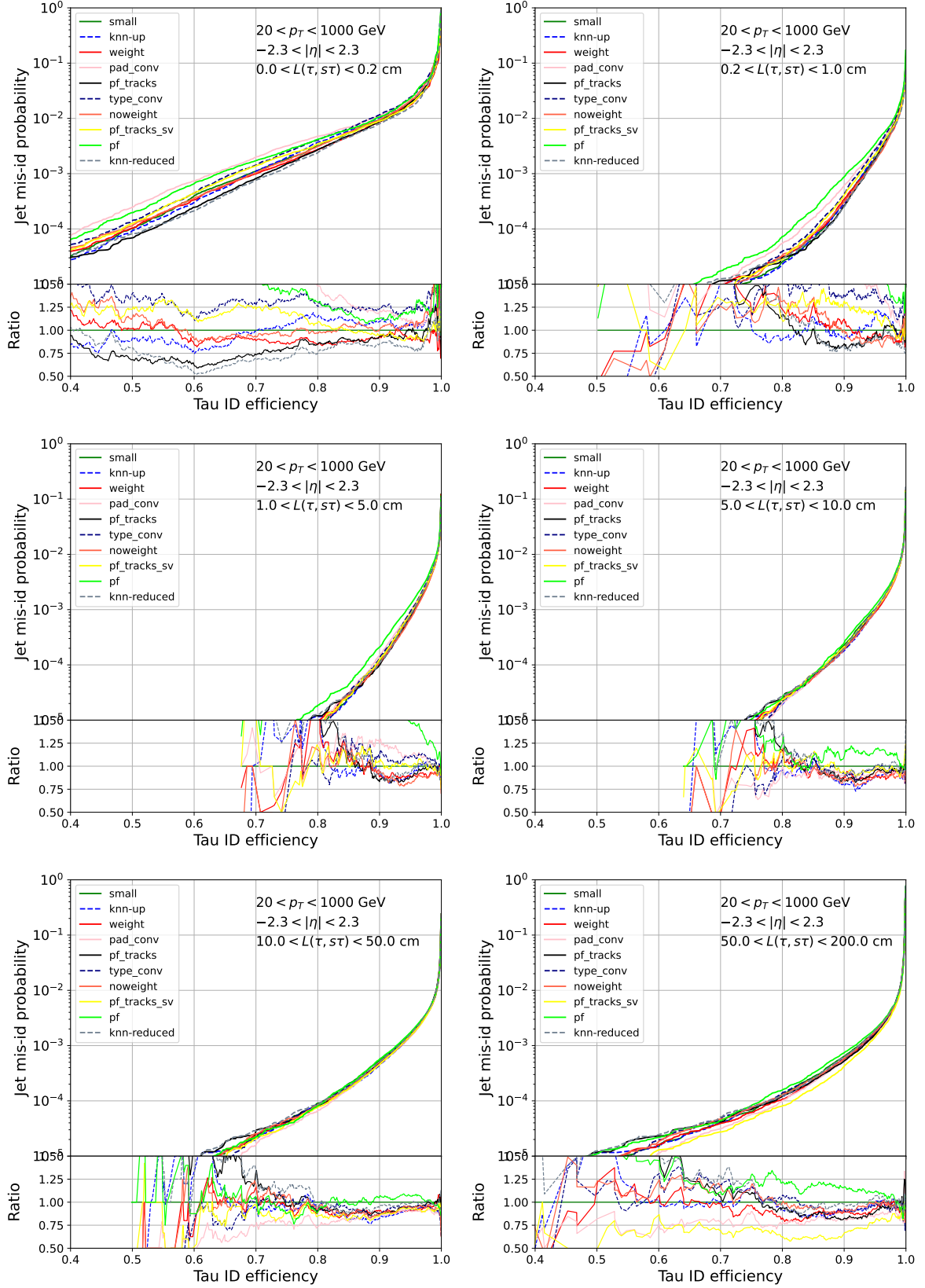
Figure A.1: Receiver operating characteristic for various architectures of NN. Background jet objects are taken from $t\bar{t}$ sample, signal displaced taus are taken from $\tilde{\tau}$ sample for $\tilde{\tau}$ mass 400 GeV and proper decay length equals $c\tau_0 =$1m. Performance is shown in the intervals of τ displacement with respect to the $\tilde{\tau}$ vertex.

A.4 Feature importance (Gradient-based)

Gradient-based feature importance is used to assess the significance of input features in predicting the output of a machine learning model. For an input tensor X and a model f, the predictions are given by $\hat{y} = f(X)$. The gradients $\frac{\partial \hat{y}}{\partial X}$, computed using TensorFlow's `GradientTape`, quantify the sensitivity of the predictions to changes in the input features. The overall importance of each feature is determined by averaging the absolute gradients across all PF candidates:

$$\text{feature\_importance} = \frac{1}{n} \sum_{i=1}^{n} \left| \frac{\partial \hat{y}_i}{\partial X} \right|,$$

where n is the number of samples. This approach provides an aggregate measure of feature influence but may be less effective for discrete features than continuous ones. Figure A.2 shows the averaged gradient for all PF candidates, offering a comprehensive view of feature importance across the dataset.
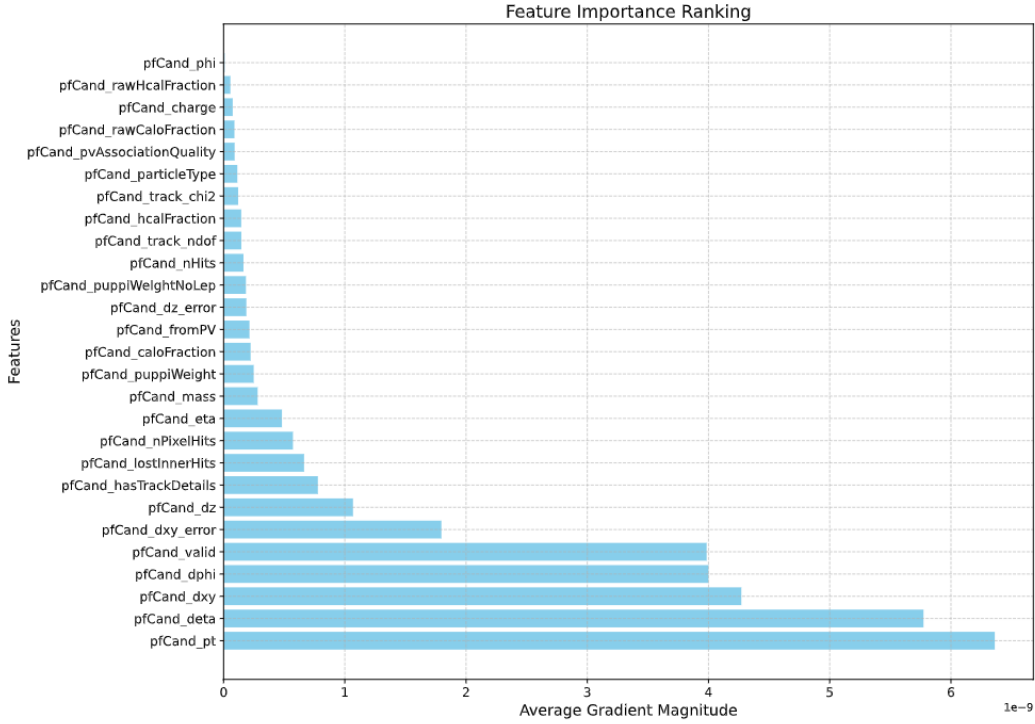
Figure A.2: Feature importance ranking based on averaged gradient magnitudes, showing the contribution of each input feature to the model's predictions.

A.5 Tau lepton identification in displaced topologies using machine learning at CMS

Tau lepton identification in displaced topologies using machine learning at CMS

Mykyta Shchedrolosiev[a] **on behalf of the CMS Collaboration**

[a]*Deutsches Elektronen-Synchrotron DESY,*
Notkestr. 85, 22607, Hamburg, Germany

E-mail: mykyta.shchedrolosiev@desy.de

Many extensions of the standard model can give rise to tau leptons produced with non-conventional signatures in the detector. Certain long-lived particles may decay into tau leptons displaced significantly from the primary proton-proton interaction vertex. Traditional tau reconstruction and identification methods are not designed for such displaced signatures, necessitating the development of specialized techniques. This note details an implementation of a machine learning approach that employs the ParticleNet architecture to tag these displaced tau leptons effectively. The newly developed tagger demonstrates strong performance in distinguishing tau leptons from quark and gluon jets, particularly in events with large displacements of 10-100 cm, where it has a typical efficiency of 70-80% at a misidentification probability of 1.8×10^{-4}. Its performance is validated with proton-proton data collected in 2018 by the CMS detector.

PoS(ICHEP2024)996

1. Introduction

Some extensions of the standard model (SM) [1, 2] provide strong motivation to search for the tau slepton ($\tilde{\tau}$), the supersymmetric partner of the tau lepton τ, with a macroscopic lifetime. This results in τ leptons displaced from the primary proton-proton interaction vertex (PV), called displaced τ. The decay of tau particles into hadrons, denoted as τ_h, accounts for 64.8% of all τ decays. The traditional hadrons-plus-strips (HPS) algorithm [3, 4] is not designed to reconstruct such displaced signatures. These proceedings introduce DisTau: a graph neural network (GNN)-based tagger of jets to improve the identification of displaced τ_hs.

2. Reconstruction of τ_h

The HPS algorithm was designed to efficiently reconstruct τ_h originating near the PV. However, its performance degrades significantly with an increasing distance between the PV and a τ production vertex ($V(\tau)$). In the Fig. 1, the efficiency of reconstructing an HPS τ_h and an anti-k_t jet with distance parameter 0.4 (AK4 jet) [5] are shown as a function of the transverse displacement between PV and $V(\tau)$ (L_{xy}). A τ_h or an AK4 jet is considered successfully reconstructed if it falls within a cone of radius $R = \sqrt{\Delta\eta^2 + \Delta\phi^2} = 0.4$ around a generator-level τ_h.
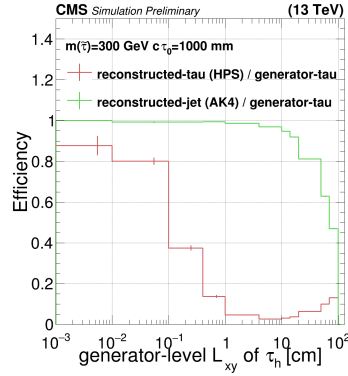
Figure 1: The fraction of displaced τ_h candidates that are reconstructed by the traditional HPS algorithm (red) and as AK4 jets (green), as a function of the transverse displacement between the PV and $V(\tau)$ (L_{xy}) on the generator level.

The displaced τ leptons are generated using simulations of long-lived $\tilde{\tau}$, which are hypothetical supersymmetric partners of the τ lepton. For the simulation, a $\tilde{\tau}$ mass of 300 GeV and a lifetime ($c\tau_0$) of 100 cm are assumed. In this scenario, each $\tilde{\tau}$ decays into a τ lepton, with an associated weakly interacting gravitino with mass of 1 GeV escaping detection. The HPS algorithm shows a sharp decline in performance after $L_{xy} > 0.1$ cm, as it is not designed for displaced decays. However, there is a small efficiency gain for $L_{xy} > 30$ cm, where the $\tilde{\tau}$ track is misidentified as an isolated charged hadron, which may mimic one of the decay modes of the τ_h. In contrast, AK4 jets maintain high efficiency across a broader L_{xy} range, demonstrating their robustness in capturing

displaced τ_h over a wide displacement range. Based on this observation, AK4 jets can effectively seed the reconstruction of displaced τ_h leptons.

3. Displaced hadronic tau tagger

The DisTau tagger is based on the ParticleNet [6] architecture. The network is trained to distinguish between displaced τ_h and background jets from quarks and gluons.

Signal jets are taken from simulated long-lived $\widetilde{\tau}$ samples, requiring $p_T > 20$ GeV, $|\eta| < 2.4$ and matching within $R = 0.4$ to generator-level τ_h. Background jets come from simulation of quantum chromodynamics (QCD) multi-jet processes. To ensure that the τ_h is still reconstructed as an AK4 jet, geometrical constraints are placed on the generator-level displacement: $|V(\tau)_z| < 100$ cm and $|V(\tau)_{xy}| < 50$ cm, where $V(\tau)_z$ and $V(\tau)_{xy}$ are respectively longitudinal and transverse coordinates of $V(\tau)$. The training uses three $\widetilde{\tau}$ masses in the range of 100-400 GeV and lifetime of 10 and 100 cm. The sample is reweighted to match p_T and η spectra between signal and background.

The input to the network is features describing particles reconstructed by the particle-flow algorithm [7] (PF candidates), limited to the first 50 (p_T-ordered) PF candidates in a jet. The features used for each PF candidate are: $\Delta\eta = \eta_{\text{jet}} - \eta_{\text{PF candidate}}$, $\Delta\phi = \phi_{\text{jet}} - \phi_{\text{PF candidate}}$, momentum and charge, probability of not being pileup candidate associated by the PUPPI algorithm [8] (PUPPI weight), number of tracker hits (total, in pixel and strip detector), impact parameter and track fit quality information, ECAL and HCAL energy deposition ratios relative to PF candidate energy, association to the PV, particle type identified by the particle-flow algorithm. Each feature is standardized to the interval [-1, 1]. No high-level jet information is used, allowing the network to learn directly from the low-level data.

The architecture employs Dynamic Edge Convolution blocks to learn both local and global relationships among PF candidates. The overall architecture is similar to the original ParticleNet, with a reduced number of neurons and neighbours in each convolution block. The model consists of approximately 100 000 trainable parameters.

4. Tagger performance

The performance of the DisTau tagger is evaluated using Monte Carlo (MC) simulations with reconstructed AK4 jets having p_T greater than 20 GeV and $|\eta|$ less than 2.3. The τ_h identification efficiency was estimated from $\widetilde{\tau}$ MC samples considering reconstructed AK4 jets that are matched to τ_h at the generator level. Comparisons were performed for three $\widetilde{\tau}$ mass values, 100, 250 and 400 GeV, a lifetime of 10 and 100 cm, and the lightest supersymmetric particle mass equals to 1 GeV. Signal efficiencies are assessed for various working points (WPs). The jet misidentification probability is estimated from $t\bar{t}$ MC samples using reconstructed jets that do not match prompt electrons, muons, or products of τ_h decays at the generator level. Figure 2 illustrates the DisTau performance with 2018 MC simulations. Data set processes used for performance evaluation are not included in the training.
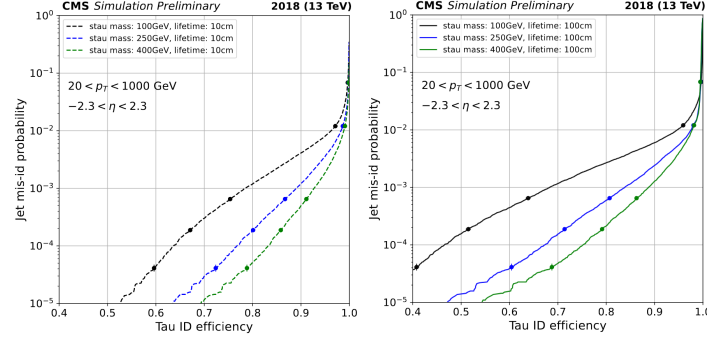
Figure 2: Receiver operating characteristic (ROC) curves illustrating the performance of the tau identification algorithm on 2018 MC simulations. The signal efficiencies, derived from $\widetilde{\tau}$ MC samples with masses of 100, 250 and 400 GeV, a lifetime of 10 cm (left) and 100 cm (right) and the lightest supersymmetric particle mass of 1 GeV, are plotted against the jet misidentification probabilities estimated from $t\bar{t}$ MC samples. Various working points (WPs) are indicated with thresholds defined as (from right to left) Loose (> 0.05), Medium (> 0.7), Tight (> 0.99), Very Tight (> 0.997), and Very Very Tight (> 0.9992).

5. Tagger validation for background jets

The tagger is validated with data using jets from a Drell-Yan(DY)+jets enriched events, targeting events with two muons in the final state.

To increase the purity of the DY($\mu\mu$)+jets process, the following selection requirements are applied. Two oppositely charged, well-identified, and isolated muons are required, each with $|\eta| < 2.4$, transverse momentum $p_T > 28$ GeV, transverse impact parameter $|d_{xy}| < 0.045$ cm, and longitudinal impact parameter $|d_z| < 0.2$ cm. The invariant mass of the muon pair must be consistent with the Z-boson mass $70 < m(\mu\mu) < 120$ GeV. Events with additional leptons or b-tagged jets are excluded. At least two AK4 jets are required, each with $p_T > 30$ GeV and $|\eta| < 2.3$, and being separated from the muons by $R > 0.4$. The leading two jets are also required to be separated from each other by $|\Delta\phi| > 0.5$. Additionally, the leading PF candidate in the jet is required to be associated with the PV.

With these selection criteria, DY($\mu\mu$)+jets purity exceeds 96%. Figure 3 illustrates the tagger output distribution for the leading and sub-leading jets in DY($\mu\mu$)+jets sample. An overall good agreement between MC and data is observed. However, fluctuations are observed due to the limited number of background events for high-score regions.

6. Tagger validation for genuine τ_h

Given that events from SM processes do not exhibit signal-like displaced τ_hs, there is no direct method to validate the performance of the DisTau tagger on displaced tau objects with real data. Consequently, the validation can be performed only with prompt τ_hs. Well-identified hadronic tau leptons from Z-boson decay in the DY+jets process are utilized. While not an ideal approximation,

Tau lepton identification in displaced topologies using machine learning at CMS
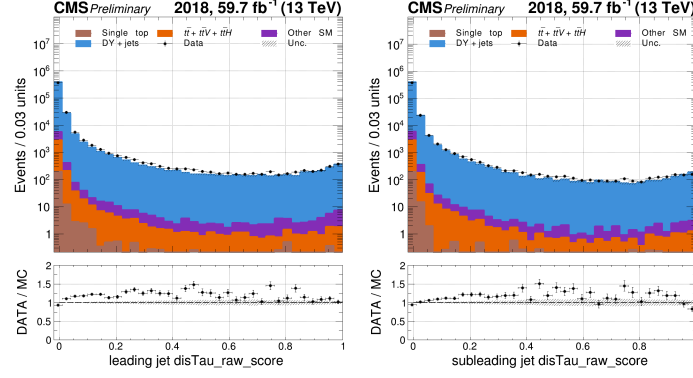
Figure 3: MC-to-data agreement of the DisTau tagger output score for p_T-leading (left) and subleading (right) jets from the 2018 data within the DY($\mu\mu$)+jets enriched sample, requiring presence of at least two additional jets. The lower panels show data-to-MC ratio.
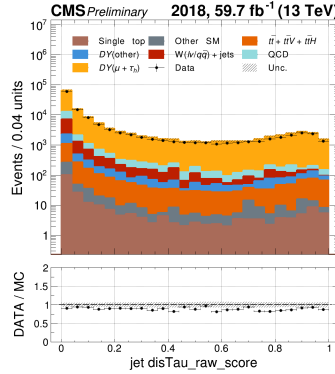
Figure 4: MC-to-data agreement of the DisTau tagger output score for the jet matched to the reconstructed τ_h for the 2018 data in the DY($\mu\tau_h$)+jets enriched sample. The lower panel shows data-to-MC ratio.

these hadronic taus serve as the most suitable proxy for signal-like behavior available in the real data.

The selection requirements are applied to increase the purity of the DY($\mu\tau_h$) + jets process. A pair of oppositely charged muon and τ_h candidate reconstructed with HPS are required, with an invariant mass consistent with the visible Z-boson mass, $60 < m(\mu\tau_h) < 80$ GeV. The muon must be well-identified and isolated, with $|\eta| < 2.4$, $p_T > 25$, GeV, $|d_{xy}| < 0.045$ cm, and $|d_z| < 0.2$ cm. The τ_h candidate is required to pass a tight identification criterion with DeepTau algorithm [4], have $p_T > 30$ GeV, $|\eta| < 2.3$, $|d_z| < 0.2$ cm, and must be separated from the muon by $R > 0.5$. The transverse mass of the muon and missing transverse energy is required to be less than 60 GeV. Additionally, there must be one AK4 jet matched to the reconstructed tau lepton within $R < 0.3$,

Tau lepton identification in displaced topologies using machine learning at CMS

with $p_T > 30\,$GeV and $|\eta| < 2.3$.

With these selection criteria, the purity of the DY($\mu\tau_h$)+jets process exceeds 86%. The agreement between data and MC simulation for the the DisTau tagger score for the AK4 jet matched the reconstructed τ_h is shown in Fig. 4. There is a good overall agreement between MC and data.

7. Summary

A novel neural-network-based displaced τ_h tagger (DisTau) has been developed. It demonstrates promising performance for discriminating τ_h against quark and gluon jets. Its behaviour was validated with 2018 data, with data samples dominated by events from DY+jets process. The tagger score distribution in simulation is found to agree well with real data for both background and signal-like jets. Since the methodology focuses on identifying displaced tau leptons with minimal use of any process-dependent kinematic properties, the tagger is expected to be applicable to various searches involving displaced τ signatures.

References

[1] J.A. Evans and J. Shelton, *Long-lived staus and displaced leptons at the LHC*, *Journal of High Energy Physics* **2016** (2016) 1–39.

[2] S. Kaneko, J. Sato, T. Shimomura, O. Vives and M. Yamanaka, *Long-lived slepton in the coannihilation region and measurement of lepton flavour violation at LHC*, *Journal of Physics: Conference Series* **171** (2009) 012092.

[3] CMS Collaboration, *Performance of reconstruction and identification of τ leptons decaying to hadrons and ν_τ in pp collisions at $\sqrt{s} = 13$ TeV*, *Journal of Instrumentation* **13** (2018) P10005.

[4] CMS Collaboration, *Identification of hadronic tau lepton decays using a deep neural network*, *Journal of Instrumentation* **17** (2022) P07023.

[5] M. Cacciari, G.P. Salam and G. Soyez, *The anti-kt jet clustering algorithm*, *Journal of High Energy Physics* **2008** (2008) 063.

[6] H. Qu and L. Gouskos, *Jet tagging via particle clouds*, *Phys. Rev. D* **101** (2020) 056019.

[7] CMS Collaboration, *Particle-flow reconstruction and global event description with the CMS detector.*, *JINST* **12** (2017) P10003.

[8] CMS Collaboration, *Pileup mitigation at CMS in 13 TeV data*, *Journal of Instrumentation* **15** (2020) P09018.

A.6　Standart Model simulation samples

Sample name	Cross section [pb]
DYJetsToLL_M-50_TuneCP5_13TeV-madgraphMLM-pythia8	5343.0
DY1JetsToLL_M-50_MatchEWPDG20_TuneCP5_13TeV-madgraphMLM-pythia8	928.3
DY2JetsToLL_M-50_MatchEWPDG20_TuneCP5_13TeV-madgraphMLM-pythia8	293.6
DY3JetsToLL_M-50_MatchEWPDG20_TuneCP5_13TeV-madgraphMLM-pythia8	86.53
DY4JetsToLL_M-50_MatchEWPDG20_TuneCP5_13TeV-madgraphMLM-pythia8	41.28
ZJetsToQQ_HT-200to400_TuneCP5_13TeV-madgraphMLM-pythia8	1244.76
ZJetsToQQ_HT-400to600_TuneCP5_13TeV-madgraphMLM-pythia8	143.172
ZJetsToQQ_HT-600to800_TuneCP5_13TeV-madgraphMLM-pythia8	31.3281
ZJetsToQQ_HT-800toInf_TuneCP5_13TeV-madgraphMLM-pythia8	16.113
ZJetsToNuNu_HT-100To200_TuneCP5_13TeV-madgraphMLM-pythia8	344.8305
ZJetsToNuNu_HT-200To400_TuneCP5_13TeV-madgraphMLM-pythia8	95.5341
ZJetsToNuNu_HT-400To600_TuneCP5_13TeV-madgraphMLM-pythia8	13.1979
ZJetsToNuNu_HT-600To800_TuneCP5_13TeV-madgraphMLM-pythia8	3.14757
ZJetsToNuNu_HT-800To1200_TuneCP5_13TeV-madgraphMLM-pythia8	1.450908
ZJetsToNuNu_HT-1200To2500_TuneCP5_13TeV-madgraphMLM-pythia8	0.3546459
ZJetsToNuNu_HT-2500ToInf_TuneCP5_13TeV-madgraphMLM-pythia8	0.00854235
WJetsToLNu_TuneCP5_13TeV-madgraphMLM-pythia8	50380
W1JetsToLNu_TuneCP5_13TeV-madgraphMLM-pythia8	9644.5
W2JetsToLNu_TuneCP5_13TeV-madgraphMLM-pythia8	3144.5
W3JetsToLNu_TuneCP5_13TeV-madgraphMLM-pythia8	954.8
W5JetsToLNu_TuneCP5_13TeV-madgraphMLM-pythia8	485.6
WJetsToQQ_HT-200to400_TuneCP5_13TeV-madgraphMLM-pythia8	3080.66
WJetsToQQ_HT-400to600_TuneCP5_13TeV-madgraphMLM-pythia8	333.234
WJetsToQQ_HT-600to800_TuneCP5_13TeV-madgraphMLM-pythia8	72.0555
WJetsToQQ_HT-800toInf_TuneCP5_13TeV-madgraphMLM-pythia8	35.211
ST_s-channel_4f_leptonDecays_TuneCP5_13TeV-madgraph-pythia8	3.36
ST_t-channel_top_4f_InclusiveDecays_TuneCP5_13TeV-powheg-madspin-pythia8	136.02
ST_t-channel_antitop_4f_InclusiveDecays_TuneCP5_13TeV-powheg-madspin-pythia8	80.95
ST_tW_top_5f_inclusiveDecays_TuneCP5_13TeV-powheg-pythia8	35.85
ST_tW_antitop_5f_inclusiveDecays_TuneCP5_13TeV-powheg-pythia8	35.85
TTToSemiLeptonic_TuneCP5_13TeV-powheg-pythia8	366.29
TTToHadronic_TuneCP5_13TeV-powheg-pythia8	378.93
TTTo2L2Nu_TuneCP5_13TeV-powheg-pythia8	88.51
TTWJetsToLNu_TuneCP5_13TeV-amcatnloFXFX-madspin-pythia8	0.2149
TTWJetsToQQ_TuneCP5_13TeV-amcatnloFXFX-madspin-pythia8	0.4316
TTZToQQ_TuneCP5_13TeV-amcatnlo-pythia8	0.5104
TTZToLLNuNu_M-10_TuneCP5_13TeV-amcatnlo-pythia8	0.2432
ttHToNonbb_M125_TuneCP5_13TeV-powheg-pythia8	0.2151
WW_TuneCP5_13TeV-pythia8	75.8
WZ_TuneCP5_13TeV-pythia8	27.6
ZZ_TuneCP5_13TeV-pythia8	12.14
WWW_4F_TuneCP5_13TeV-amcatnlo-pythia8	0.2086
WWZ_4F_TuneCP5_13TeV-amcatnlo-pythia8	0.1651
VHToNonbb_M125_TuneCP5_13TeV-amcatnloFXFX_madspin_pythia8	0.0009561
QCD_Pt_15to30_TuneCP5_13TeV_pythia8	1244000000
QCD_Pt_30to50_TuneCP5_13TeV_pythia8	106500000
QCD_Pt_50to80_TuneCP5_13TeV_pythia8	15700000
QCD_Pt_80to120_TuneCP5_13TeV_pythia8	2346000
QCD_Pt_120to170_TuneCP5_13TeV_pythia8	407700
QCD_Pt_170to300_TuneCP5_13TeV_pythia8	103700
QCD_Pt_300to470_TuneCP5_13TeV_pythia8	6826
QCD_Pt_470to600_TuneCP5_13TeV_pythia8	551.2
QCD_Pt_600to800_TuneCP5_13TeV_pythia8	156.7
QCD_Pt_800to1000_TuneCP5_13TeV_pythia8	26.25
QCD_Pt_1000to1400_TuneCP5_13TeV_pythia8	7.465
QCD_Pt_1400to1800_TuneCP5_13TeV_pythia8	0.6487
QCD_Pt_1800to2400_TuneCP5_13TeV_pythia8	0.08734
QCD_Pt_2400to3200_TuneCP5_13TeV_pythia8	0.005237
QCD_Pt_3200toInf_TuneCP5_13TeV_pythia8	0.0001352

Table A.2: Standard model MC samples and corresponding cross sections.

Sample name	SMS-TStauStau_MStau-*_ctau-*_mLSP-1_TuneCP5_13TeV-madgraphMLM
2016 pre-VFP campaign	RunIISummer20UL16MiniAODAPVv2-SUS_106X_mcRun2_asymptotic_preVFP_v11*
2016 post-VFP campaign	RunIISummer20UL16MiniAODv2-SUS_106X_mcRun2_asymptotic_v17*
2017 campaign	RunIISummer20UL17MiniAODv2-SUS_106X_mc2017_realistic_v9*
2018 campaign	RunIISummer20UL18MiniAODv2-SUS_106X_upgrade2018_realistic_v16_L1v1*
Datatier	MINIAODSIM

Table A.3: Centrally produced long-lived $\widetilde{\tau}$ samples.

$c\tau_0$ [mm]	$m(\widetilde{\tau}_1)$ [GeV]
0.01	90
0.05	100
0.1	125
0.5	150
1	175
5	200
10	225
50	250
100	275
1000	300
	350
	400
	450
	500
	550
	600
10000	90
	100
	200
	300
	400
	500
	600

Table A.4: The central samples have been simulated for the $\widetilde{\tau}_1$ lifetimes and masses listed here.

A.7   N-jet sample stitching

N-jet binned DY samples need to be added to increase the statistics of events with many jets. This process allows us to combine events from different jet multiplicity bins, ensuring that we have sufficient data across all regions of the phase space, especially for events with a high number of jets where statistics might otherwise be limited.

These samples have to be combined ("stitched") as described in Ref. [162]. To calculate the weight for each exclusive sample with n jets ($n = 1, 2, 3, 4$), where n is the number of partons generated at LHE level (called `LHE_Njets` in `nanoAOD`)

$$w_{n\text{jet}} = \frac{L\sigma_{n\text{jet}}}{N_{n\text{jet}} + \epsilon_{n\text{jet}}^{\text{incl}} N_{\text{incl}}},$$

where $N_{n\text{jet}}$ are the total number of MC events in the n-jets sample, and $\epsilon_{n\text{jet}}^{\text{incl}}$ is defined as the ratio of the $N_{n\text{-jet}}$ events to the number of all events in LO inclusive DY sample.

$$\epsilon_{n\text{jet}}^{\text{incl}} = \frac{\sigma_{n\text{jet}}}{\sigma_{\text{incl}}},$$

Figure A.3 illustrates the validation of this procedure. The discrepancy between the generator-level p_T distribution of the Z-boson before and after the stitching indicates that this procedure does not alter the resulting distribution.
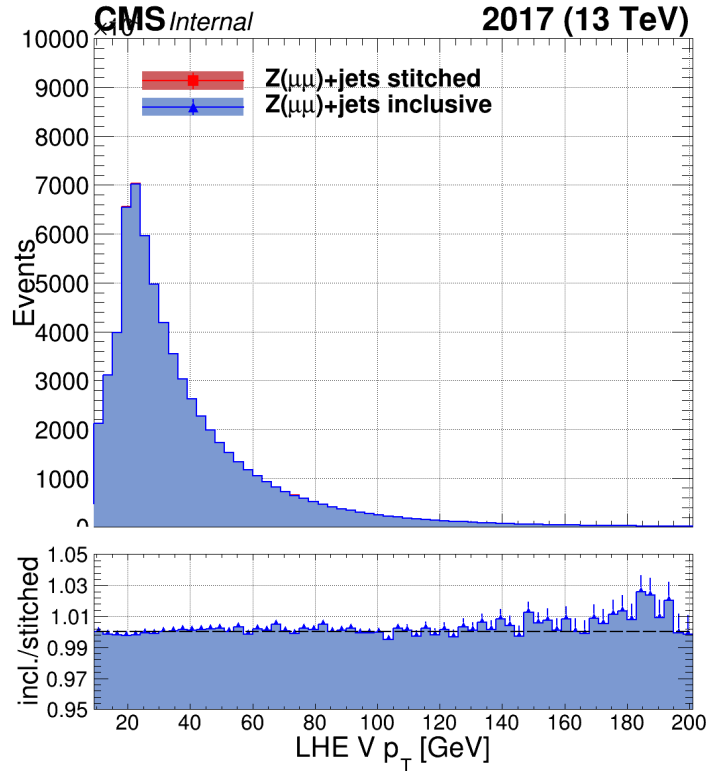
Figure A.3: The LHE V p_T distribution for the stitched vs. inclusive DY+jets sample.

A.8 Study of the beam halo effect

The specialized p_T^{miss} filter, as described in Section 3.8, is designed to suppress beam halo effects by identifying characteristic patterns in calorimeters and checking for associated deposits in the cathode strip chambers. Beam halo particles, originating from interactions with the beam pipe or surrounding material, are mainly located in the LHC plane and generate high-energy clusters in the calorimeters, which can fake p_T^{miss}. The filter specifically targets these events, leveraging their large radius of curvature and long time of flight to distinguish them from genuine physics signals.

To study the potential effect of the beam halo background for the signal region in this thesis, the p_T^{miss} filter is inverted. As a result, a negligible contribution in the two-jet region after the baseline selection described in Section 6.6.1 is observed. Figure A.4 shows that the beam halo background in the two-jet region is negligible. Additionally, the data indicate that most jets lie within the LHC plane, consistent with beam optics. This motivates applying a $\Delta\phi > 0.5$ cut to suppress residual beam halo contamination.
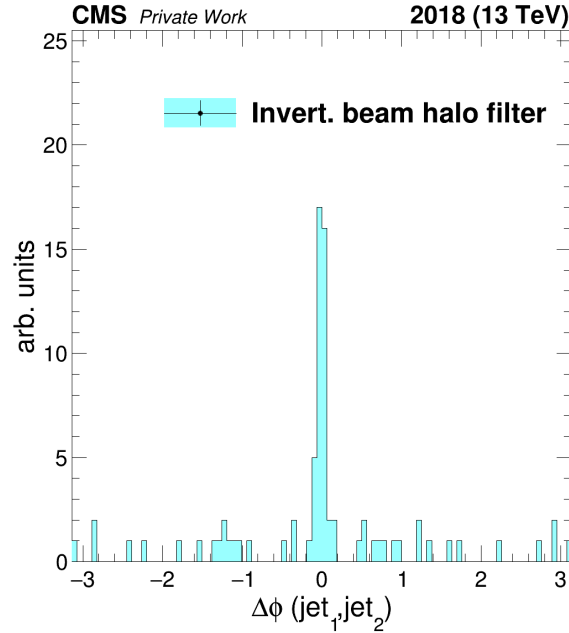
Figure A.4: Distribution of the azimuthal angle difference ($\Delta\phi$) between the two jets (jet$_1$, jet$_2$) passing the selection criteria detailed in Section 6.6.1, but with the beam halo filter inverted. Although no signal events pass this selection, the distribution clearly shows that the two jets are predominantly collinear in the ϕ plane, a hallmark feature of beam-induced background processes.

A.9   LLP lifetime reweighting

Only a limited number of $\widetilde{\tau}$ lifetimes are generated due to computational constraints. However, to study a broader range of lifetime scenarios, reweighting techniques are used to interpolate between simulated points.

For a single $\widetilde{\tau}$ particle, the decay probability follows an exponential law:

$$P(t|\tau) = \frac{1}{\tau}e^{-t/\tau} \, ,$$

where $P(t|\tau)$ represents the probability density function of the $\widetilde{\tau}$ decaying at time t given the proper lifetime τ. In the lab frame, the time variable t is related to the proper lifetime by the Lorentz factor: $t = t'\gamma$, where t' is the proper decay time, γ is the Lorentz factor given by: $\gamma = \frac{E}{m}$ with E and m being the total energy and mass of the $\widetilde{\tau}$, respectively.

We follow a reweighting procedure to obtain results for a $\widetilde{\tau}$ lifetime for which simulated samples are unavailable. When reweighting from an initial (i) to a final (f) $\widetilde{\tau}$ lifetime, the following weight needs to be applied per $\widetilde{\tau}$ in the event.

$$w = \exp\left(\frac{-x}{\beta\gamma c\tau_0^f}\right) \bigg/ \exp\left(\frac{-x}{\beta\gamma c\tau_0^i}\right) , \tag{A.2}$$

where x is the flight length of the $\widetilde{\tau}$ in the laboratory frame. It is calculated as the distance between the $\widetilde{\tau}$ production vertex and the vertex at which its daughter τ is produced; note that the latter is the same $\widetilde{\tau}$ decay vertex. Then the final sample is obtained by applying the weight $w_1 w_2$ to each event in the initial sample, where w_1 and w_2 are the weights corresponding to the two $\widetilde{\tau}$ sleptons in an event.

A.10 Background prediction validation

The validation of the data-driven prediction is shown for the RT1 region as defined in Section 6.6.1. Figures A.5, A.6, A.7 and A.8 demonstrate the validation in 2016 pre-VFP, 2016 post-VFP, 2017 and 2018 correspondingly.
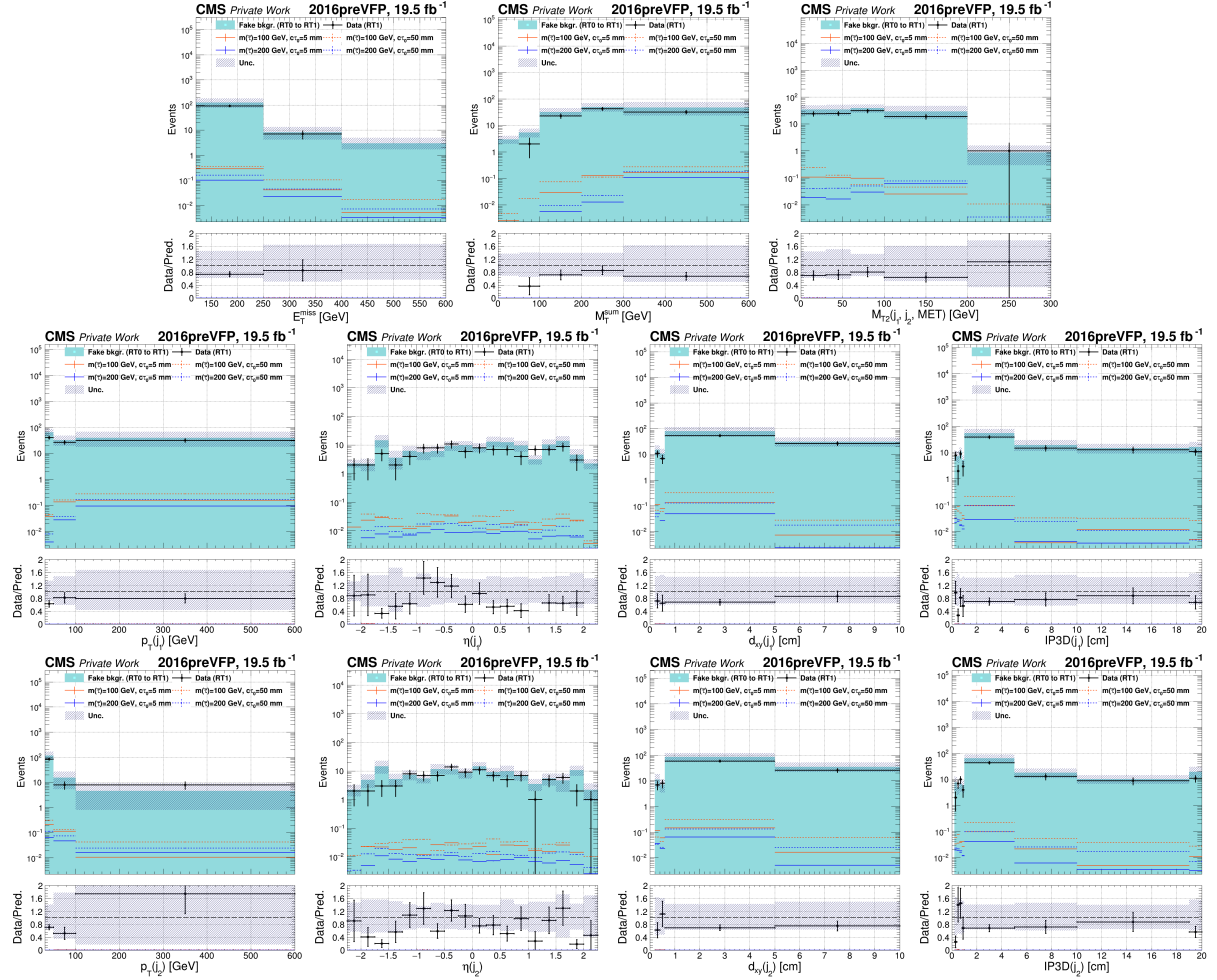
Figure A.5: From left to right and top to bottom: the distributions of p_T^{miss}, Σm_T, m_{T2}, p_T^{j1}, η^{j1}, d_{xy}^{j1}, IP_{3D}^{j1}, p_T^{j2}, η^{j2}, d_{xy}^{j2}, IP_{3D}^{j2}, showing the background prediction in BRT1 from BRT0. The prediction uses $f_W(p_T, d_{xy})$, and the plots correspond to the 2016 pre-VFP data-taking period.
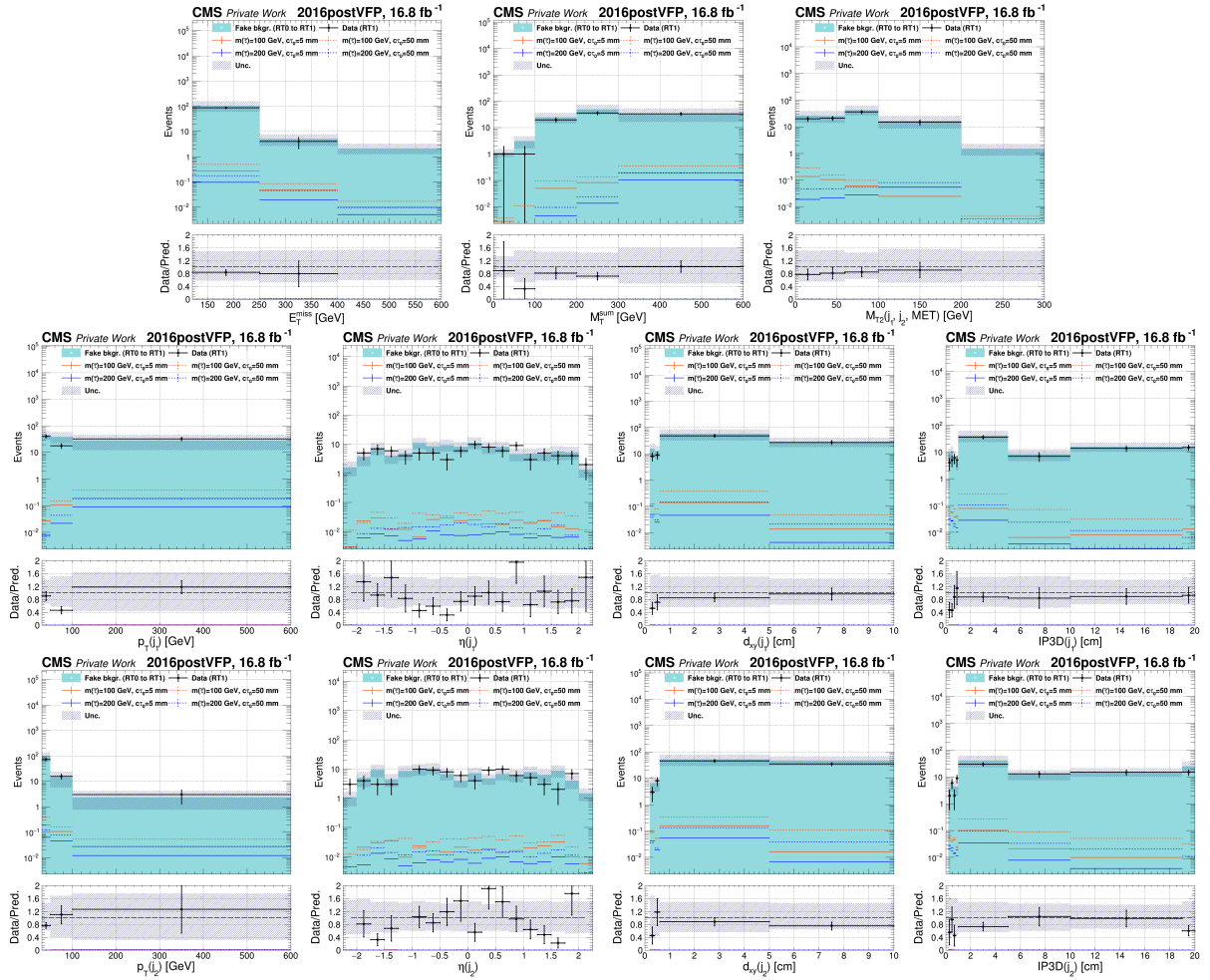
Figure A.6: From left to right and top to bottom: the distributions of p_T^{miss}, Σm_T, m_{T2}, p_T^{j1}, η^{j1}, d_{xy}^{j1}, IP_{3D}^{j1}, p_T^{j2}, η^{j2}, d_{xy}^{j2}, IP_{3D}^{j2}, showing the background prediction in BRT1 from BRT0. The prediction uses $f_W(p_T, d_{xy})$, and the plots correspond to the 2016 post-VFP data-taking period.
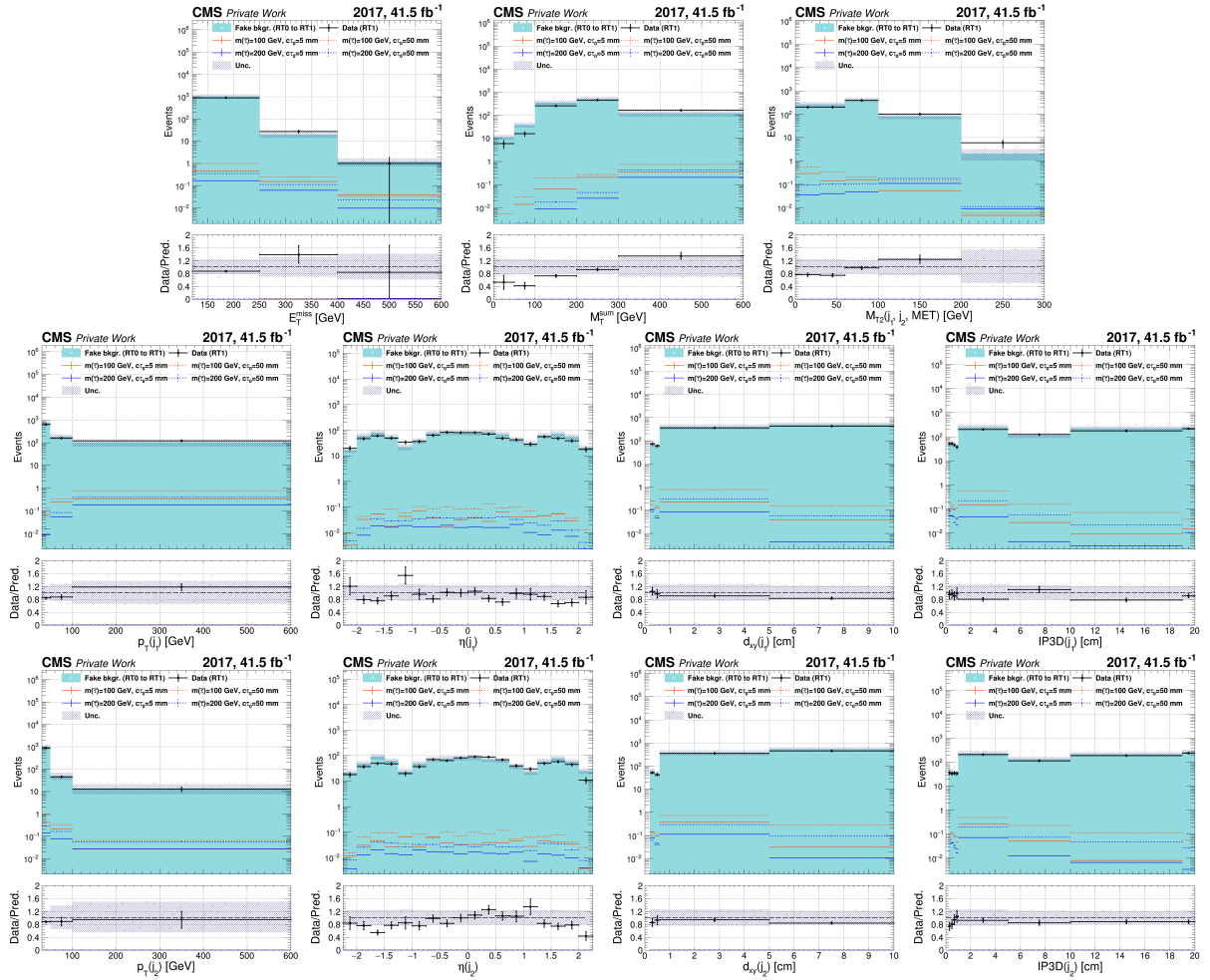
Figure A.7: From left to right and top to bottom: the distributions of $p_\mathrm{T}^\mathrm{miss}$, Σm_T, m_T2, p_T^j1, η^j1, d_{xy}^j1, $\mathrm{IP}_\mathrm{3D}^\mathrm{j1}$, p_T^j2, η^j2, d_{xy}^j2, $\mathrm{IP}_\mathrm{3D}^\mathrm{j2}$, showing the background prediction in BRT1 from BRT0. The prediction uses $f_\mathrm{W}(p_\mathrm{T}, d_{xy})$, and the plots correspond to the 2017 data-taking period.
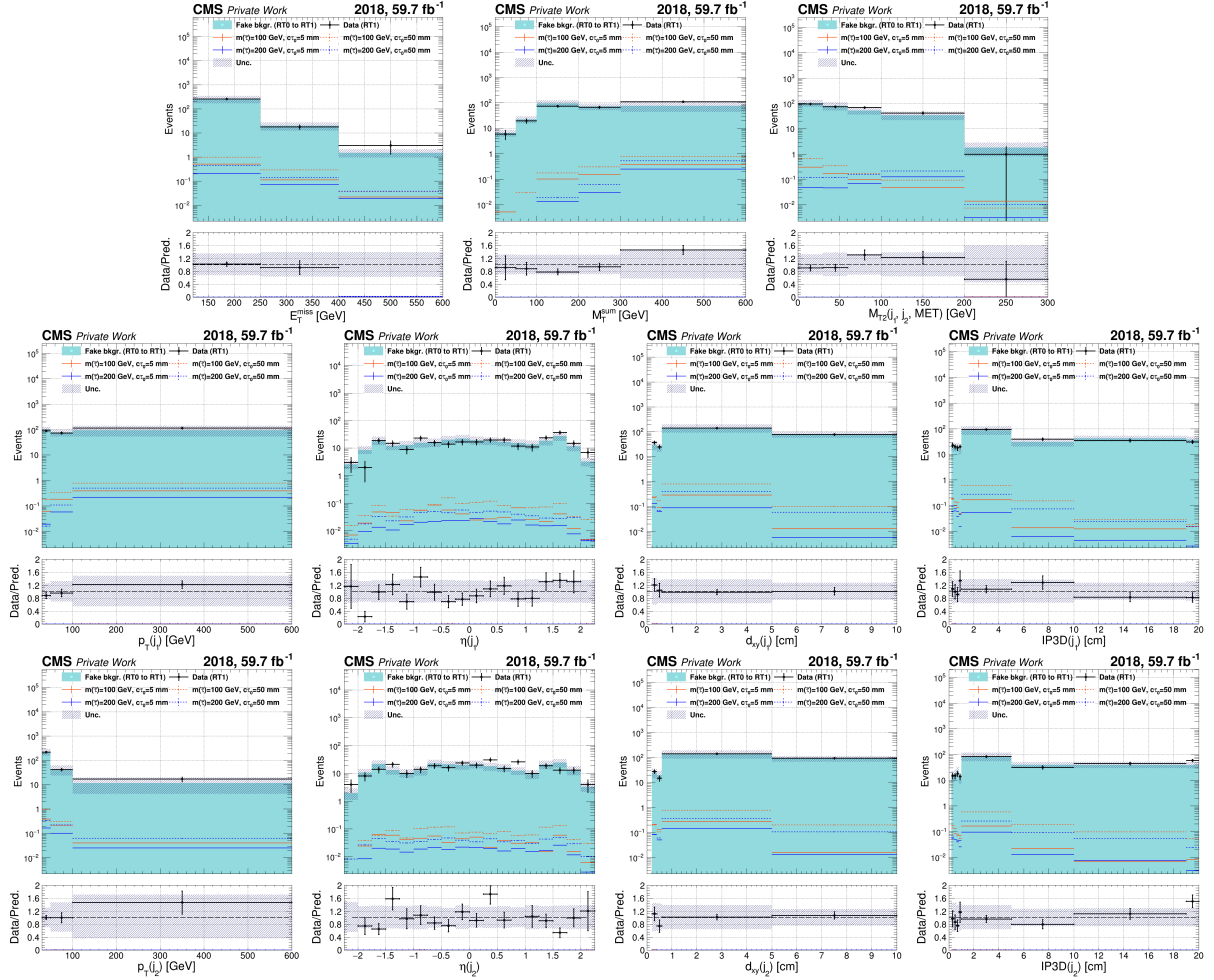
Figure A.8: From left to right and top to bottom: the distributions of $p_\mathrm{T}^\mathrm{miss}$, Σm_T, $m_{\mathrm{T}2}$, $p_\mathrm{T}^{\mathrm{j}1}$, $\eta^{\mathrm{j}1}$, $d_{xy}^{\mathrm{j}1}$, $\mathrm{IP}_{\mathrm{3D}}^{\mathrm{j}1}$, $p_\mathrm{T}^{\mathrm{j}2}$, $\eta^{\mathrm{j}2}$, $d_{xy}^{\mathrm{j}2}$, $\mathrm{IP}_{\mathrm{3D}}^{\mathrm{j}2}$, showing the background prediction in BRT1 from BRT0. The prediction uses $f_\mathrm{W}(p_\mathrm{T}, d_{xy})$, and the plots correspond to the 2018 data-taking period.

A.11   Simulated signal scenarios

The current analysis produces the MC simulations under the maximally mixed scenario. However, it is also possible to reinterpret the limits for the mass degenerate scenario, as the kinematic properties between these scenarios do not differ significantly.

While $\widetilde{\tau}_{\mathrm{L}}$ and $\widetilde{\tau}_{\mathrm{R}}$ in maximally mixed and mass degenerate scenarios have differences at the generator level, mainly due to τ polarization effects, these differences are primarily visible in the $\widetilde{\tau}$ rest frame. However, in the lab frame, where reconstructed variables such as leading and sub-leading jet τ and $p_{\mathrm{T}}^{\mathrm{miss}}$ are analyzed, these differences become significantly smeared out.
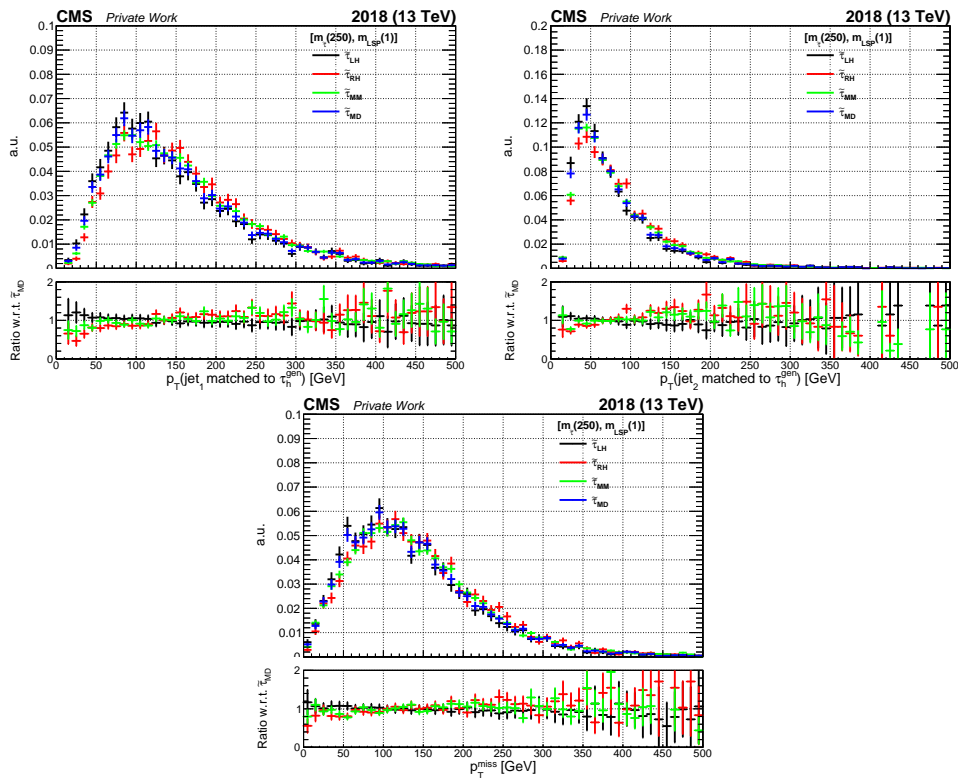
Figure A.9: Reconstructed p_{T} of the leading and subleading jets, $p_{\mathrm{T}}^{\mathrm{miss}}$ shown for the signal scenario of $\widetilde{\tau}$ mass equals 250 GeV and gravitino mass of 1 GeV. Four different scenarios of direct $\tilde{\tau}$ pair production are shown: a purely left-handed $\tilde{\tau}$, a purely right-handed $\tilde{\tau}$, the degenerate production scenario and maximally mixed. The ratio is shown with respect to the maximally mixed scenario.

By explicitly comparing the distributions of these key reconstructed variables, it was observed that the maximally mixed and mass degenerate shapes are practically identical. As a result, the exclusion limits derived using the maximally mixed sample should also be valid for the mass degenerate without requiring additional MC generation.

Acronyms

ALICE A Large Ion Collider Experiment

ATLAS A Toroidal LHC Apparatus

BDT boosted decision tree

BSM beyond the Standard Model

CERN European Organization for Nuclear Research

CHS Charged Hadron Subtraction

CKF combinatorial Kalman filter

CMS Compact Muon Solenoid

CNN Convolutional Neural Networks

CSCs Cathode Strip Chambers

DA deterministic annealing

DNN deep neural network

DTs Drift Tubes

ECAL Electromagnetic Calorimeter

EWSB Electroweak symmetry breaking

FASER Forward Search Experiment

GCT Global Calorimeter Trigger

GMSB gauge mediated supersymmetry breaking

GNN Graph Neural Networks

GSF Gaussian Sum Filter

GUT grand unifying theory

HB Hadron Barrel

HCAL Hadronic Calorimeter

HE Hadron Endcap

HF Hadron Forward

HL-LHC High-Luminosity LHC

HLT High Level Trigger

HO Hadron Outer

HPS hadrons-plus-strips

HSCP Heavy Stable Charged Particle

JEC jet energy correction

JER Jet Energy Resolution

JES Jet Energy Scale

L1 Level 1

LEP Large Electron-Positron

LHC Large Hadron Collider

LHCb Large Hadron Collider beauty

LHCf Large Hadron Collider forward

LO leading order

LSP lightest supersymmetric particle

MC Monte Carlo

ME matrix element

MoEDAL Monopole and Exotics Detector at the LHC

MSSM minimal supersymmetric SM

mSUGRA minimal supergravity

MVA multivariate analysis

NLL next-to-leading logarithmic

NLO next-to-leading order

NLSP next to lightest SUSY particle

PDFs parton distribution functions

PF particle-flow algorithm

pp proton-proton

PS Proton Synchrotron

PS parton shower

PSB Proton Synchrotron Booster

PUPPI pileup per particle identification

PV primary vertex

QCD Quantum chromodynamics

QFT quantum field theory

RCT Regional Calorimeter Trigger

RPCs Resistive Plate Chambers

S&M Shuffle and Merge

SC supercluster

SM Standard Model

SPD Silicon Pixel Detector

SPS Super Proton Synchrotron

SSD Silicon Strip Detector

SUSY Supersymmetry

SV secondary vertex

TEC Tracker Endcaps

TIB Tracker Inner Barrel

TID Tracker Inner Disks

TOB Tracker Outer Barrel

TOTEM TOTal Elastic and diffractive cross section Measurement

TPC Time Projection Chamber

VEV vacuum expectation value

WIMP Weakly Interacting Massive Particle

Bibliography

[1] Grammarly Inc. *Grammarly.* `https : / / www . grammarly . com`. `https : / / www . grammarly.com`. n.d.

[2] GitHub, Inc. *GitHub Copilot.* `https://github.com/features/copilot`. `https://github.com/features/copilot`. n.d.

[3] OpenAI. *ChatGPT (Mar 14 version) [Large language model].* `https : / / chat . openai.com/chat`. Available at `https://chat.openai.com/chat`. Mar. 2023.

[4] Serguei Chatrchyan et al. "Observation of a New Boson at a Mass of 125 GeV with the CMS Experiment at the LHC". In: *Phys. Lett. B* 716 (2012), pp. 30–61. DOI: `10.1016/j.physletb.2012.08.021`. arXiv: `1207.7235 [hep-ex]`.

[5] Georges Aad et al. "Observation of a new particle in the search for the Standard Model Higgs boson with the ATLAS detector at the LHC". In: *Phys. Lett. B* 716 (2012), pp. 1–29. DOI: `10.1016/j.physletb.2012.08.020`. arXiv: `1207.7214 [hep-ex]`.

[6] Stephen P. Martin. "A Supersymmetry primer". In: *Adv. Ser. Direct. High Energy Phys.* 18 (1998). Ed. by Gordon L. Kane, pp. 1–98. DOI: `10.1142/9789812839657_0001`. arXiv: `hep-ph/9709356`.

[7] CSABA CSÁKI. "THE MINIMAL SUPERSYMMETRIC STANDARD MODEL". In: *Modern Physics Letters A* 11.08 (Mar. 1996), pp. 599–613. ISSN: 1793-6632. DOI: `10 . 1142 / s021773239600062x`. URL: `http : / / dx . doi . org / 10 . 1142 / S021773239600062X`.

[8] "Performance of the CNN-based tau identification algorithm with Domain Adaptation using Adversarial Machine Learning for Run 2". In: (2024). URL: `https://cds.cern.ch/record/2904699`.

[9] Huilin Qu and Loukas Gouskos. "Jet tagging via particle clouds". In: *Physical Review D* 101.5 (Mar. 2020). ISSN: 2470-0029. DOI: `10 . 1103 / physrevd . 101 . 056019`. URL: `http://dx.doi.org/10.1103/PhysRevD.101.056019`.

[10] Armen Tumasyan et al. "Search for direct pair production of supersymmetric partners of τ leptons in the final state with two hadronically decaying τ leptons and missing transverse momentum in proton-proton collisions at $\sqrt{s} = 13$ TeV". In: *Phys. Rev. D* 108.1 (2023), p. 012011. DOI: `10 . 1103 / PhysRevD . 108 . 012011`. arXiv: `2207.02254 [hep-ex]`.

[11] Paul A. M. Dirac. "Quantum theory of emission and absorption of radiation". In: *Proc. Roy. Soc. Lond. A* 114 (1927), p. 243. DOI: `10.1098/rspa.1927.0039`.

[12] Wikipedia contributors. *Standard Model — Wikipedia, The Free Encyclopedia.* [Online; accessed 9-February-2025]. 2025. URL: `https://en.wikipedia.org/wiki/Standard_Model`.

[13] F. Englert and R. Brout. "Broken Symmetry and the Mass of Gauge Vector Mesons". In: *Phys. Rev. Lett.* 13 (1964). Ed. by J. C. Taylor, pp. 321–323. DOI: `10.1103/PhysRevLett.13.321`.

[14] Peter W. Higgs. "Broken symmetries, massless particles and gauge fields". In: *Phys. Lett.* 12 (1964), pp. 132–133. DOI: `10.1016/0031-9163(64)91136-9`.

[15] G. S. Guralnik, C. R. Hagen, and T. W. B. Kibble. "Global Conservation Laws and Massless Particles". In: *Phys. Rev. Lett.* 13 (1964). Ed. by J. C. Taylor, pp. 585–587. DOI: `10.1103/PhysRevLett.13.585`.

[16] S. L. Glashow. "Partial Symmetries of Weak Interactions". In: *Nucl. Phys.* 22 (1961), pp. 579–588. DOI: `10.1016/0029-5582(61)90469-2`.

[17] Steven Weinberg. "A Model of Leptons". In: *Phys. Rev. Lett.* 19 (1967), pp. 1264–1266. DOI: `10.1103/PhysRevLett.19.1264`.

[18] Abdus Salam. "Weak and Electromagnetic Interactions". In: *Conf. Proc. C* 680519 (1968), pp. 367–377. DOI: `10.1142/9789812795915_0034`.

[19] G. Arnison et al. "Experimental Observation of Isolated Large Transverse Energy Electrons with Associated Missing Energy at $\sqrt{s} = 540$ GeV". In: *Phys. Lett. B* 122 (1983), pp. 103–116. DOI: `10.1016/0370-2693(83)91177-2`.

[20] M. Banner et al. "Observation of Single Isolated Electrons of High Transverse Momentum in Events with Missing Transverse Energy at the CERN anti-p p Collider". In: *Phys. Lett. B* 122 (1983), pp. 476–485. DOI: `10.1016/0370-2693(83)91605-2`.

[21] W. de Boer. *The Discovery of the Higgs Boson with the CMS Detector and its Implications for Supersymmetry and Cosmology.* 2013. arXiv: `1309.0721 [hep-ph]`. URL: `https://arxiv.org/abs/1309.0721`.

[22] Murray Gell-Mann. "A Schematic Model of Baryons and Mesons". In: *Phys. Lett.* 8 (1964), pp. 214–215. DOI: `10.1016/S0031-9163(64)92001-3`.

[23] H. Fritzsch, Murray Gell-Mann, and H. Leutwyler. "Advantages of the Color Octet Gluon Picture". In: *Phys. Lett. B* 47 (1973), pp. 365–368. DOI: `10.1016/0370-2693(73)90625-4`.

[24] David J. Gross and Frank Wilczek. "Ultraviolet Behavior of Nonabelian Gauge Theories". In: *Phys. Rev. Lett.* 30 (1973). Ed. by J. C. Taylor, pp. 1343–1346. DOI: `10.1103/PhysRevLett.30.1343`.

[25] H. David Politzer. "Reliable Perturbative Results for Strong Interactions?" In: *Phys. Rev. Lett.* 30 (1973). Ed. by J. C. Taylor, pp. 1346–1349. DOI: `10.1103/PhysRevLett.30.1346`.

[26] V. Agrawal et al. "Viable range of the mass scale of the standard model". In: *Phys. Rev. D* 57 (1998), pp. 5480–5492. DOI: `10.1103/PhysRevD.57.5480`. arXiv: `hep-ph/9707380`.

[27] Benjamin D. Wandelt et al. *Self-Interacting Dark Matter.* 2000. arXiv: `astro-ph/0006344 [astro-ph]`. URL: `https://arxiv.org/abs/astro-ph/0006344`.

[28] K. Freese. "Review of Observational Evidence for Dark Matter in the Universe and in upcoming searches for Dark Stars". In: *EAS Publications Series* 36 (2009), pp. 113–126. ISSN: 1638-1963. DOI: 10.1051/eas/0936016. URL: http://dx.doi.org/10.1051/eas/0936016.

[29] Adam G. Riess et al. "Observational Evidence from Supernovae for an Accelerating Universe and a Cosmological Constant". In: *The Astronomical Journal* 116.3 (Sept. 1998), pp. 1009–1038. ISSN: 0004-6256. DOI: 10.1086/300499. URL: http://dx.doi.org/10.1086/300499.

[30] Gian Francesco Giudice. "Naturally Speaking: The Naturalness Criterion and Physics at the LHC". In: (Jan. 2008). Ed. by Gordon Kane and Aaron Pierce, pp. 155–178. DOI: 10.1142/9789812779762_0010. arXiv: 0801.2562 [hep-ph].

[31] Mikhail Shifman. *The Inception, the Concept and the Second Life of Supersymmetry.* 2022. arXiv: 2210.06615 [hep-th]. URL: https://arxiv.org/abs/2210.06615.

[32] Ben Allanach and Howard E. Haber. *Supersymmetry, Part I (Theory).* 2024. arXiv: 2401.03827 [hep-ph]. URL: https://arxiv.org/abs/2401.03827.

[33] Howard E. Haber and Laurel Stephenson Haskins. "Supersymmetric Theory and Models". In: *Anticipating the Next Discoveries in Particle Physics.* WORLD SCIENTIFIC, May 2018, pp. 355–499. DOI: 10.1142/9789813233348_0006. URL: http://dx.doi.org/10.1142/9789813233348_0006.

[34] Yorikiyo Nagashima. *Beyond the standard model of elementary particle physics.* Weinheim, USA: Wiley-VCH, 2014. ISBN: 978-3-527-41177-1, 978-3-527-66505-1.

[35] STEPHEN P. MARTIN. "A SUPERSYMMETRY PRIMER". In: *Perspectives on Supersymmetry.* WORLD SCIENTIFIC, July 1998, pp. 1–98. DOI: 10.1142/9789812839657_0001. URL: http://dx.doi.org/10.1142/9789812839657_0001.

[36] Ian J. R. Aitchison. "Supersymmetry and the MSSM: An Elementary introduction". In: (May 2005). arXiv: hep-ph/0505105.

[37] M. Kuroda. *Complete Lagrangian of MSSM.* 2005. arXiv: hep-ph/9902340 [hep-ph]. URL: https://arxiv.org/abs/hep-ph/9902340.

[38] Essodjolo Kpatcha et al. "Sampling the $\mu\nu$ SSM for displaced decays of the tau left sneutrino LSP at the LHC". In: *The European Physical Journal C* 79.11 (Nov. 2019). ISSN: 1434-6052. DOI: 10.1140/epjc/s10052-019-7412-1. URL: http://dx.doi.org/10.1140/epjc/s10052-019-7412-1.

[39] Jared A. Evans and Jessie Shelton. "Long-lived staus and displaced leptons at the LHC". In: *Journal of High Energy Physics* 2016.4 (Apr. 2016), pp. 1–39. ISSN: 1029-8479. DOI: 10.1007/jhep04(2016)056. URL: http://dx.doi.org/10.1007/JHEP04(2016)056.

[40] Valentin V. Khoze, Alexis D. Plascencia, and Kazuki Sakurai. "Simplified models of dark matter with a long-lived co-annihilation partner". In: *Journal of High Energy Physics* 2017.6 (June 2017). ISSN: 1029-8479. DOI: 10.1007/jhep06(2017)041. URL: http://dx.doi.org/10.1007/JHEP06(2017)041.

[41] G. Bélanger et al. "LHC-friendly minimal freeze-in models". In: *Journal of High Energy Physics* 2019.2 (Feb. 2019). ISSN: 1029-8479. DOI: `10.1007/jhep02(2019)186`. URL: `http://dx.doi.org/10.1007/JHEP02(2019)186`.

[42] Johan Alwall, Philip C. Schuster, and Natalia Toro. "Simplified models for a first characterization of new physics at the LHC". In: *Physical Review D* 79.7 (Apr. 2009). ISSN: 1550-2368. DOI: `10.1103/physrevd.79.075020`. URL: `http://dx.doi.org/10.1103/PhysRevD.79.075020`.

[43] Daniele Alves et al. "Simplified models for LHC new physics searches". In: *Journal of Physics G: Nuclear and Particle Physics* 39.10 (Sept. 2012), p. 105005. ISSN: 1361-6471. DOI: `10.1088/0954-3899/39/10/105005`. URL: `http://dx.doi.org/10.1088/0954-3899/39/10/105005`.

[44] Benjamin Fuks et al. "Revisiting slepton pair production at the Large Hadron Collider". In: *Journal of High Energy Physics* 2014.1 (Jan. 2014). ISSN: 1029-8479. DOI: `10.1007/jhep01(2014)168`. URL: `http://dx.doi.org/10.1007/JHEP01(2014)168`.

[45] Juri Fiaschi and Michael Klasen. "Slepton pair production at the LHC in NLO+NLL with resummation-improved parton densities". In: *Journal of High Energy Physics* 2018.3 (Mar. 2018). ISSN: 1029-8479. DOI: `10.1007/jhep03(2018)094`. URL: `http://dx.doi.org/10.1007/JHEP03(2018)094`.

[46] *SUSY March 2023 Summary Plot Update*. Tech. rep. All figures including auxiliary figures are available at https://atlas.web.cern.ch/Atlas/GROUPS/PHYSICS/PUBNOTES/ATL-PHYS-PUB-2023-005. Geneva: CERN, 2023. URL: `https://cds.cern.ch/record/2852738`.

[47] CMS Collaboration. *CMS Supersymmetry Physics Results*. CMS Public TWiki. Accessed: February 15, 2025. 2025. URL: `https://twiki.cern.ch/twiki/bin/view/CMSPublic/PhysicsResultsSUS`.

[48] CMS Collaboration. "Search for long-lived particles decaying to leptons with large impact parameter in proton–proton collisions at $\sqrt{s} = 13\,\text{TeV}$". In: *The European Physical Journal C* 82.2 (Feb. 2022). ISSN: 1434-6052. DOI: `10.1140/epjc/s10052-022-10027-3`. URL: `http://dx.doi.org/10.1140/epjc/s10052-022-10027-3`.

[49] ATLAS Collaboration. "Search for Displaced Leptons in $\sqrt{s} = 13$ TeV *pp* Collisions with the ATLAS Detector". In: *Phys. Rev. Lett.* 127 (5 July 2021), p. 051802. DOI: `10.1103/PhysRevLett.127.051802`. URL: `https://link.aps.org/doi/10.1103/PhysRevLett.127.051802`.

[50] Freya Blekman et al. "Soft displaced leptons at the LHC". In: *Journal of High Energy Physics* 2020.11 (Nov. 2020). ISSN: 1029-8479. DOI: `10.1007/jhep11(2020)112`. URL: `http://dx.doi.org/10.1007/JHEP11(2020)112`.

[51] Elias Bernreuther and Bogdan A. Dobrescu. "Vectorlike leptons and long-lived bosons at the LHC". In: *Journal of High Energy Physics* 2023.7 (July 2023). ISSN: 1029-8479. DOI: `10.1007/jhep07(2023)079`. URL: `http://dx.doi.org/10.1007/JHEP07(2023)079`.

[52] M. Bahmani et al. "Production of $\tau\tau jj$ final states at the LHC and the TauSpinner algorithm: the spin-2 case". In: *The European Physical Journal C* 78.1 (Jan. 2018). ISSN: 1434-6052. DOI: 10.1140/epjc/s10052-017-5480-7. URL: http://dx.doi.org/10.1140/epjc/s10052-017-5480-7.

[53] Hugues Beauchesne et al. "Uncovering tau leptons-enriched semi-visible jets at the LHC". In: *The European Physical Journal C* 83.7 (July 2023). ISSN: 1434-6052. DOI: 10.1140/epjc/s10052-023-11775-6. URL: http://dx.doi.org/10.1140/epjc/s10052-023-11775-6.

[54] J. Alwall et al. "The automated computation of tree-level and next-to-leading order differential cross sections, and their matching to parton shower simulations". In: *JHEP* 07 (2014), p. 079. DOI: 10.1007/JHEP07(2014)079. arXiv: 1405.0301 [hep-ph].

[55] Torbjörn Sjöstrand et al. "An introduction to PYTHIA 8.2". In: *Comput. Phys. Commun.* 191 (2015), p. 159. DOI: 10.1016/j.cpc.2015.01.024. arXiv: 1410.3012 [hep-ph].

[56] Bo Andersson et al. "Parton Fragmentation and String Dynamics". In: *Phys. Rept.* 97 (1983), pp. 31–145. DOI: 10.1016/0370-1573(83)90080-7.

[57] B. R. Webber. "A QCD Model for Jet Fragmentation Including Soft Gluon Interference". In: *Nucl. Phys. B* 238 (1984), pp. 492–528. DOI: 10.1016/0550-3213(84)90333-X.

[58] S. Agostinelli et al. "GEANT4: A simulation toolkit". In: *Nucl. Instrum. Meth.* A506 (2003), pp. 250–303. DOI: 10.1016/S0168-9002(03)01368-8.

[59] CMS Collaboration. "Extraction and validation of a new set of CMS PYTHIA8 tunes from underlying-event measurements". In: *Eur. Phys. J. C* 80 (2020), p. 4. DOI: 10.1140/epjc/s10052-019-7499-4. arXiv: 1903.12179 [hep-ex].

[60] CMS Collaboration. *CMS Physics: Technical Design Report Volume 1: Detector Performance and Software*. Technical design report. CMS. There is an error on cover due to a technical problem for some items. Geneva: CERN, 2006. URL: https://cds.cern.ch/record/922757.

[61] The CMS Collaboration. "The CMS experiment at the CERN LHC". In: *Journal of Instrumentation* 3.08 (Aug. 2008), S08004. DOI: 10.1088/1748-0221/3/08/S08004. URL: https://dx.doi.org/10.1088/1748-0221/3/08/S08004.

[62] Lyndon Evans and Philip Bryant. "LHC Machine". In: *Journal of Instrumentation* 3.08 (Aug. 2008), S08001. DOI: 10.1088/1748-0221/3/08/S08001. URL: https://dx.doi.org/10.1088/1748-0221/3/08/S08001.

[63] R. Assmann, M. Lamont, and S. Myers. "A brief history of the LEP collider". In: *Nucl. Phys. B Proc. Suppl.* 109 (2002). Ed. by F. L. Navarria, M. Paganoni, and P. G. Pelfer, pp. 17–31. DOI: 10.1016/S0920-5632(02)90005-8.

[64] Esma Mobs. *The CERN accelerator complex - August 2018. Complexe des accélérateurs du CERN - Août 2018*. https://cds.cern.ch/record/2636343. General Photo.

[65] "New Linac + 'old' Booster = many protons. Nouveau Linac + "Booster"' = multiplication des protons". In: *CERN Bulletin* 45 (1978), pp. 1–2. URL: `https://cds.cern.ch/record/1718567`.

[66] K. H. Reich. "The CERN Proton Synchrotron Booster". In: *IEEE Transactions on Nuclear Science* 16.3 (1969), pp. 959–961. DOI: `10.1109/TNS.1969.4325414`.

[67] Donald Cundy and Simone Gilardoni. "The Proton Synchrotron (PS): At the Core of the CERN Accelerators". In: (), pp. 39–85. DOI: `10.1142/9789814749145_0003`. eprint: `https://www.worldscientific.com/doi/pdf/10.1142/9789814749145_0003`. URL: `https://www.worldscientific.com/doi/abs/10.1142/9789814749145_0003`.

[68] J B Adams. "The CERN 400 GeV Proton Synchrotron (CERN SPS)". In: (1977). Talk. URL: `https://cds.cern.ch/record/2048898`.

[69] The ATLAS Collaboration. "The ATLAS Experiment at the CERN Large Hadron Collider". In: *Journal of Instrumentation* 3.08 (Aug. 2008), S08003. DOI: `10.1088/1748-0221/3/08/S08003`. URL: `https://dx.doi.org/10.1088/1748-0221/3/08/S08003`.

[70] The LHCb Collaboration. "The LHCb Detector at the LHC". In: *Journal of Instrumentation* 3.08 (Aug. 2008), S08005. DOI: `10.1088/1748-0221/3/08/S08005`. URL: `https://dx.doi.org/10.1088/1748-0221/3/08/S08005`.

[71] The ALICE Collaboration. "The ALICE experiment at the CERN LHC". In: *Journal of Instrumentation* 3.08 (Aug. 2008), S08002. DOI: `10.1088/1748-0221/3/08/S08002`. URL: `https://dx.doi.org/10.1088/1748-0221/3/08/S08002`.

[72] G. Anelli et al. "The TOTEM experiment at the CERN Large Hadron Collider". In: *JINST* 3 (2008), S08007. DOI: `10.1088/1748-0221/3/08/S08007`.

[73] B. Acharya et al. "The Physics Programme Of The MoEDAL Experiment At The LHC". In: *Int. J. Mod. Phys. A* 29 (2014), p. 1430050. DOI: `10.1142/S0217751X14300506`. arXiv: `1405.7662 [hep-ph]`.

[74] Henso Abreu et al. "The FASER detector". In: *JINST* 19.05 (2024), P05066. DOI: `10.1088/1748-0221/19/05/P05066`. arXiv: `2207.11427 [physics.ins-det]`.

[75] O. Adriani et al. "The LHCf detector at the CERN Large Hadron Collider". In: *JINST* 3 (2008), S08006. DOI: `10.1088/1748-0221/3/08/S08006`.

[76] CMS Collaboration and Thomas Mc Cauley. "Collisions recorded by the CMS detector on 14 Oct 2016 during the high pile-up fill". CMS Collection. 2016. URL: `https://cds.cern.ch/record/2231915`.

[77] Albert M Sirunyan et al. "Pileup mitigation at CMS in 13 TeV data". In: *JINST* 15 (2020), P09018. DOI: `10.1088/1748-0221/15/09/p09018`. arXiv: `2003.00503 [hep-ex]`.

[78] CERN. *High-Luminosity LHC Plan (January 2025)*. Accessed: Month Day, Year. Jan. 2025. URL: `https://hilumilhc.web.cern.ch/sites/default/files/2025-01/HL-LHC_Plan_January2025.pdf`.

[79] CMS Collaboration. "Development of the CMS detector for the CERN LHC Run 3. Development of the CMS detector for the CERN LHC Run 3". In: *JINST* 19.05 (2024). Replaced with the published version. Added the journal reference and the DOI. All the figures and tables can be found at http://cms-results.web.cern.ch/cms-results/public-results/publications/PRF-21-001 (CMS Public Pages), P05064. DOI: `10.1088/1748-0221/19/05/P05064`. arXiv: `2309.05466`. URL: `https://cds.cern.ch/record/2870088`.

[80] Stefanos Dris. *Performance of the CMS Tracker Optical Links and Future Upgrade Using Bandwidth Efficient Digital Modulation*. 2010. arXiv: `1004.5574` `[physics.ins-det]`. URL: `https://arxiv.org/abs/1004.5574`.

[81] L. Viliani. "CMS tracker performance and readiness for LHC Run II". In: *Nuclear Instruments and Methods in Physics Research Section A: Accelerators, Spectrometers, Detectors and Associated Equipment* 824 (2016). Frontier Detectors for Frontier Physics: Proceedings of the 13th Pisa Meeting on Advanced Detectors, pp. 67–69. ISSN: 0168-9002. DOI: `https://doi.org/10.1016/j.nima.2015.09.046`. URL: `https://www.sciencedirect.com/science/article/pii/S0168900215011018`.

[82] The Tracker Group of the CMS Collaboration. *The CMS Phase-1 Pixel Detector Upgrade*. Tech. rep. Geneva: CERN, 2020. URL: `https://cds.cern.ch/record/2745805`.

[83] CMS Collaboration. *CMS Public Tracker Material Budget twiki*. `https://twiki.cern.ch/twiki/bin/view/CMSPublic/TrackerMaterialBudgetPlots`.

[84] Michael Andrews. "The LHC and the CMS Detector". In: *Search for Exotic Higgs Boson Decays to Merged Diphotons: A Novel CMS Analysis Using End-to-End Deep Learning*. Cham: Springer Nature Switzerland, 2023, pp. 7–37. ISBN: 978-3-031-25091-0. DOI: `10.1007/978-3-031-25091-0_2`. URL: `https://doi.org/10.1007/978-3-031-25091-0_2`.

[85] CMS Collaboration. *Calibration of the CMS hadron calorimeters using proton-proton collision data at $\sqrt{s} = 13$ TeV*. Sept. 2019. DOI: `10.48550/arXiv.1910.00079`.

[86] Minos Collaboration. "CMS reconstruction improvement for the muon tracking by the RPC chambers". In: 2012. URL: `https://api.semanticscholar.org/CorpusID:44047517`.

[87] Min Suk Kim. "CMS reconstruction improvement for the muon tracking by the RPC chambers". In: *PoS* RPC2012 (2013). Presented by Minsuk Kim at the XI workshop on Resistive Plate Chambers and Related Detectors - RPC2012, INFN Laboratori Nazionali di Frascati Italy, February 5-10, 2012, p. 045. DOI: `10.1088/1748-0221/8/03/T03001`. arXiv: `1209.2646`. URL: `https://cds.cern.ch/record/1477844`.

[88] Albert M Sirunyan et al. "Performance of the CMS Level-1 trigger in proton-proton collisions at $\sqrt{s} = 13$ TeV". In: *JINST* 15 (2020), P10017. DOI: `10.1088/1748-0221/15/10/P10017`. arXiv: `2006.10165` `[hep-ex]`.

[89] Vardan Khachatryan et al. "The CMS trigger system". In: *JINST* 12 (2017), P01020. DOI: 10.1088/1748-0221/12/01/P01020. arXiv: 1609.02366 [physics.ins-det].

[90] The CMS Collaboration. "Description and performance of track and primary-vertex reconstruction with the CMS tracker". In: *Journal of Instrumentation* 9.10 (Oct. 2014), P10009. DOI: 10.1088/1748-0221/9/10/P10009. URL: https://dx.doi.org/10.1088/1748-0221/9/10/P10009.

[91] The CMS Collaboration. "Alignment of the CMS tracker with LHC and cosmic ray data". In: *Journal of Instrumentation* 9.06 (June 2014), P06009. DOI: 10.1088/1748-0221/9/06/P06009. URL: https://dx.doi.org/10.1088/1748-0221/9/06/P06009.

[92] W. Adam et al. "Stand-alone cosmic muon reconstruction before installation of the CMS silicon strip tracker". In: *Journal of Instrumentation* 4 (Jan. 2009), P05004.

[93] Walaa Elmetenawee. *CMS track reconstruction performance during Run 2 and developments for Run 3*. 2020. arXiv: 2012.07035 [physics.ins-det]. URL: https://arxiv.org/abs/2012.07035.

[94] Felice Pantaleo. "New Track Seeding Techniques for the CMS Experiment". CERN, 2017. URL: https://cds.cern.ch/record/2293435.

[95] "2017 tracking performance plots". In: (2017). URL: https://cds.cern.ch/record/2290524.

[96] "Energy calibration and resolution of the CMS electromagnetic calorimeter in pp collisions at $\sqrt{s}=7$ TeV". In: *Journal of Instrumentation* 8.09 (Sept. 2013), P09009. DOI: 10.1088/1748-0221/8/09/P09009. URL: https://dx.doi.org/10.1088/1748-0221/8/09/P09009.

[97] CMS Collaboration. "Calibration of the CMS hadron calorimeters using proton-proton collision data at $\sqrt{s} = 13$ TeV". In: *Journal of Instrumentation* 15.05 (May 2020), P05002–P05002. ISSN: 1748-0221. DOI: 10.1088/1748-0221/15/05/p05002. URL: http://dx.doi.org/10.1088/1748-0221/15/05/P05002.

[98] CMS Collaboration. "Particle-flow reconstruction and global event description with the CMS detector. Particle-flow reconstruction and global event description with the CMS detector". In: *JINST* 12.10 (2017). Replaced with the published version. Added the journal reference and DOI. All the figures and tables can be found at http://cms-results.web.cern.ch/cms-results/public-results/publications/PRF-14-001 (CMS Public Pages), P10003. DOI: 10.1088/1748-0221/12/10/P10003. arXiv: 1706.04965. URL: https://cds.cern.ch/record/2270046.

[99] Jon Louis Bentley. "Multidimensional binary search trees used for associative searching". In: *Commun. ACM* 18.9 (Sept. 1975), pp. 509–517. ISSN: 0001-0782. DOI: 10.1145/361002.361007. URL: https://doi.org/10.1145/361002.361007.

[100] CMS Collaboration. "Electron and photon reconstruction and identification with the CMS experiment at the CERN LHC". In: *JINST* 16.05 (2021). Replaced with the published version. Added the journal reference and the DOI. All the figures and tables can be found at http://cms-results.web.cern.ch/cms-results/public-results/publications/EGM-17-001 (CMS Public Pages), P05014. DOI: 10.1088/1748-0221/16/05/P05014. arXiv: 2012.06888. URL: https://cds.cern.ch/record/2747266.

[101] W Adam et al. "Reconstruction of electrons with the Gaussian-sum filter in the CMS tracker at the LHC". In: *Journal of Physics G: Nuclear and Particle Physics* 31.9 (July 2005), N9–N20. ISSN: 1361-6471. DOI: 10.1088/0954-3899/31/9/n01. URL: http://dx.doi.org/10.1088/0954-3899/31/9/N01.

[102] CMS Collaboration. "Performance of the CMS muon detector and muon reconstruction with proton-proton collisions at $\sqrt{s}$=13 TeV". In: *Journal of Instrumentation* 13.06 (June 2018), P06015–P06015. ISSN: 1748-0221. DOI: 10.1088/1748-0221/13/06/p06015. URL: http://dx.doi.org/10.1088/1748-0221/13/06/P06015.

[103] "Muon Reconstruction and Identification Performance with Run-2 data". In: (2020). URL: https://cds.cern.ch/record/2727091.

[104] M. Mulders. "Muon Reconstruction and Identification at CMS". In: *Nuclear Physics B - Proceedings Supplements* 172 (2007). Proceedings of the 10th Topical Seminar on Innovative Particle and Radiation Detectors, pp. 205–207. ISSN: 0920-5632. DOI: https://doi.org/10.1016/j.nuclphysbps.2007.08.049. URL: https://www.sciencedirect.com/science/article/pii/S0920563207005932.

[105] Matteo Cacciari, Gavin P. Salam, and Gregory Soyez. "The anti-k_T jet clustering algorithm". In: *JHEP* 04 (2008), p. 063. DOI: 10.1088/1126-6708/2008/04/063. arXiv: 0802.1189 [hep-ex].

[106] Matteo Cacciari, Gavin P. Salam, and Gregory Soyez. "FastJet user manual". In: *Eur. Phys. J. C* 72 (2012), p. 1896. DOI: 10.1140/epjc/s10052-012-1896-2. arXiv: 1111.6097 [hep-ph].

[107] *Pileup Removal Algorithms*. Tech. rep. Geneva: CERN, 2014. URL: https://cds.cern.ch/record/1751454.

[108] Daniele Bertolini et al. "Pileup per particle identification". In: *JHEP* 10 (2014), p. 059. DOI: 10.1007/JHEP10(2014)059. arXiv: 1407.6013 [hep-ph].

[109] Vardan Khachatryan et al. "Jet energy scale and resolution in the CMS experiment in pp collisions at 8 TeV". In: *JINST* 12.02 (2017), P02014. DOI: 10.1088/1748-0221/12/02/P02014. arXiv: 1607.03663 [hep-ex].

[110] Garvita Agarwal. *Jet Energy Scale and Resolution Measurements in CMS*. Tech. rep. 6 pages, 6 figures, Contribution to 41st International Conference on High Energy physics - ICHEP 2022, Accepted for publication in POS. 2022. DOI: 10.22323/1.414.0652. arXiv: 2301.02175. URL: https://cds.cern.ch/record/2847453.

[111] Albert M Sirunyan et al. "Performance of missing transverse momentum reconstruction in proton-proton collisions at $\sqrt{s} = 13\,\text{TeV}$ using the CMS detector". In: *JINST* 14 (2019), P07004. DOI: 10.1088/1748-0221/14/07/P07004. arXiv: 1903.06078 [hep-ex].

[112] CMS Collaboration. *Missing ET (MET) Optional Filters for Run 2.* https://twiki.cern.ch/twiki/bin/view/CMS/MissingETOptionalFiltersRun2. [Online; accessed 22-Feb-2025].

[113] Gian F. Giudice, Riccardo Rattazzi, and James D. Wells. "Quantum gravity and extra dimensions at high-energy colliders". In: *Nuclear Physics B* 544.1–2 (Apr. 1999), pp. 3–38. ISSN: 0550-3213. DOI: 10.1016/s0550-3213(99)00044-9. URL: http://dx.doi.org/10.1016/S0550-3213(99)00044-9.

[114] Martin Schmaltz and David Tucker-Smith. "LITTLE HIGGS THEORIES". In: *Annual Review of Nuclear and Particle Science* 55.1 (Dec. 2005), pp. 229–270. ISSN: 1545-4134. DOI: 10.1146/annurev.nucl.55.090704.151502. URL: http://dx.doi.org/10.1146/annurev.nucl.55.090704.151502.

[115] Ilja Doršner and Admir Greljo. "Leptoquark toolbox for precision collider studies". In: *Journal of High Energy Physics* 2018.5 (May 2018). ISSN: 1029-8479. DOI: 10.1007/jhep05(2018)126. URL: http://dx.doi.org/10.1007/JHEP05(2018)126.

[116] G.C. Branco et al. "Theory and phenomenology of two-Higgs-doublet models". In: *Physics Reports* 516.1–2 (July 2012), pp. 1–102. ISSN: 0370-1573. DOI: 10.1016/j.physrep.2012.02.002. URL: http://dx.doi.org/10.1016/j.physrep.2012.02.002.

[117] Martin L. Perl et al. "Evidence for Anomalous Lepton Production in e+ - e- Annihilation". In: *Phys. Rev. Lett.* 35 (1975), pp. 1489–1492. DOI: 10.1103/PhysRevLett.35.1489.

[118] R. L. Workman et al. "Review of Particle Physics". In: *PTEP* 2022 (2022), p. 083C01. DOI: 10.1093/ptep/ptac097.

[119] *Performance of reconstruction and identification of tau leptons in their decays to hadrons and tau neutrino in LHC Run-2.* Tech. rep. Geneva: CERN, 2016. URL: https://cds.cern.ch/record/2196972.

[120] A.M. Sirunyan et al. "Performance of reconstruction and identification of τ leptons decaying to hadrons and ν_τ in pp collisions at $\sqrt{s} = 13$ TeV". In: *Journal of Instrumentation* 13.10 (Oct. 2018), P10005. DOI: 10.1088/1748-0221/13/10/P10005. URL: https://dx.doi.org/10.1088/1748-0221/13/10/P10005.

[121] Izaak Neutelings. *Hadronic Tau Decay.* https://tikz.net/tau_decay/. Accessed: July 2017. TikZ.net, 2020.

[122] Till Tantau. *The TikZ and PGF Packages. Manual for version 3.0.0.* Dec. 20, 2013. URL: http://sourceforge.net/projects/pgf/.

[123] CMS Collaboration. "Identification of hadronic tau lepton decays using a deep neural network". In: *Journal of Instrumentation* 17.07 (July 2022), P07023. DOI: 10.1088/1748-0221/17/07/P07023. URL: https://dx.doi.org/10.1088/1748-0221/17/07/P07023.

[124] Ian J. Goodfellow, Yoshua Bengio, and Aaron Courville. *Deep Learning*. `http://www.deeplearningbook.org`. Cambridge, MA, USA: MIT Press, 2016.

[125] Ian Goodfellow, Yoshua Bengio, and Aaron Courville. *Deep Learning*. `http://www.deeplearningbook.org`. MIT Press, 2016.

[126] Y. Lecun et al. "Gradient-based learning applied to document recognition". In: *Proceedings of the IEEE* 86.11 (1998), pp. 2278–2324. DOI: `10.1109/5.726791`.

[127] Farhad Mortezapour Shiri et al. *A Comprehensive Overview and Comparative Analysis on Deep Learning Models: CNN, RNN, LSTM, GRU*. 2023. arXiv: `2305.17473 [cs.LG]`. URL: `https://arxiv.org/abs/2305.17473`.

[128] Hyeon-Joong Yoo. "Deep convolution neural networks in computer vision: a review". In: *IEIE Transactions on Smart Processing and Computing* 4.1 (2015), pp. 35–43.

[129] Vanessa Buhrmester, David Münch, and Michael Arens. "Analysis of explainers of black box deep neural networks for computer vision: A survey". In: *Machine Learning and Knowledge Extraction* 3.4 (2021), pp. 966–989.

[130] Shun Miao, Z Jane Wang, and Rui Liao. "A CNN regression approach for real-time 2D/3D registration". In: *IEEE transactions on medical imaging* 35.5 (2016), pp. 1352–1363.

[131] Xu Chen et al. "An enhanced AlexNet-Based model for femoral bone tumor classification and diagnosis using magnetic resonance imaging". In: *Journal of Bone Oncology* (2024), p. 100626.

[132] Min Chen et al. "Disease prediction by machine learning over big data from healthcare communities". In: *Ieee Access* 5 (2017), pp. 8869–8879.

[133] Andre Luckow et al. "Deep learning in the automotive industry: Applications and tools". In: *2016 IEEE International Conference on Big Data (Big Data)*. IEEE. 2016, pp. 3759–3768.

[134] Lei Ren et al. "A data-driven auto-CNN-LSTM prediction model for lithium-ion battery remaining useful life". In: *IEEE Transactions on Industrial Informatics* 17.5 (2020), pp. 3478–3487.

[135] Wenpeng Yin et al. "Comparative study of CNN and RNN for natural language processing". In: *arXiv preprint arXiv:1702.01923* (2017).

[136] Antimo Cagnotta, Francesco Carnevali, and Agostino De Iorio. "Machine Learning Applications for Jet Tagging in the CMS Experiment". In: *Applied Sciences* 12.20 (2022). ISSN: 2076-3417. DOI: `10.3390/app122010574`. URL: `https://www.mdpi.com/2076-3417/12/20/10574`.

[137] Jinmian Li, Tianjun Li, and Fang-Zhou Xu. "Reconstructing boosted Higgs jets from event image segmentation". In: *Journal of High Energy Physics* 2021.4 (Apr. 2021). ISSN: 1029-8479. DOI: `10.1007/jhep04(2021)156`. URL: `http://dx.doi.org/10.1007/JHEP04(2021)156`.

[138] Kaiming He et al. *Delving Deep into Rectifiers: Surpassing Human-Level Performance on ImageNet Classification*. 2015. arXiv: `1502.01852 [cs.CV]`. URL: `https://arxiv.org/abs/1502.01852`.

[139] Kevin P. Murphy. *Probabilistic Machine Learning: An introduction.* MIT Press, 2022. URL: probml.ai.

[140] Tsung-Yi Lin et al. "Focal Loss for Dense Object Detection". In: *Proceedings of the IEEE International Conference on Computer Vision (ICCV)*. Oct. 2017.

[141] Yaroslav Ganin et al. *Domain-Adversarial Training of Neural Networks.* 2016. arXiv: 1505.07818 [stat.ML]. URL: https://arxiv.org/abs/1505.07818.

[142] Eric Tzeng et al. *Adversarial Discriminative Domain Adaptation.* 2017. arXiv: 1702.05464 [cs.CV]. URL: https://arxiv.org/abs/1702.05464.

[143] Mingsheng Long et al. *Learning Transferable Features with Deep Adaptation Networks.* 2015. arXiv: 1502.02791 [cs.LG]. URL: https://arxiv.org/abs/1502.02791.

[144] Lucas Russell. "Identification of Hadronic Tau Lepton Decays with Domain Adaptation using Adversarial Machine Learning at CMS". Presented 28 Jun 2022. Imperial Coll., London, 2022. URL: https://cds.cern.ch/record/2827366.

[145] CMS Collaboration. *TauMLTools,* https://github.com/cms-tau-pog/TauMLTools. 2019.

[146] Adam Paszke et al. "PyTorch: An Imperative Style, High-Performance Deep Learning Library". In: *Advances in Neural Information Processing Systems 32*. Curran Associates, Inc., 2019, pp. 8024–8035. URL: http://papers.neurips.cc/paper/9015-pytorch-an-imperative-style-high-performance-deep-learning-library.pdf.

[147] Timothy Dozat. "Incorporating nesterov momentum into adam". In: (2016).

[148] Kaiming He et al. *Deep Residual Learning for Image Recognition.* 2015. arXiv: 1512.03385 [cs.CV]. URL: https://arxiv.org/abs/1512.03385.

[149] C. G. Lester and D. J. Summers. "Measuring masses of semi-invisibly decaying particle pairs produced at hadron colliders". In: *Phys. Lett. B* 463 (1999), p. 99. DOI: 10.1016/S0370-2693(99)00945-4. arXiv: hep-ph/9906349.

[150] Christopher G. Lester and Benjamin Nachman. "Bisection-based asymmetric M_{T2} computation: a higher precision calculator than existing symmetric methods". In: *JHEP* 03 (2015), p. 100. DOI: 10.1007/JHEP03(2015)100. arXiv: 1411.4312 [hep-ph].

[151] Alan Barr, Christopher Lester, and P. Stephens. "m_{T2}: The Truth behind the glamour". In: *J. Phys. G* 29 (2003), p. 2343. DOI: 10.1088/0954-3899/29/10/304. arXiv: hep-ph/0304226 [hep-ph].

[152] Alan J. Barr and Claire Gwenlan. "The Race for supersymmetry: Using m_{T2} for discovery". In: *Phys. Rev. D* 80 (2009), p. 074007. DOI: 10.1103/PhysRevD.80.074007. arXiv: 0907.2713 [hep-ph].

[153] CMS Collaboration. "Search for direct pair production of supersymmetric partners of τ leptons in the final state with two hadronically decaying τ leptons and missing transverse momentum in proton-proton collisions at $\sqrt{s} = 13$ TeV". In: *Phys. Rev. D* 108 (1 July 2023), p. 012011. DOI: 10.1103/PhysRevD.108.012011. URL: https://link.aps.org/doi/10.1103/PhysRevD.108.012011.

[154]   Dongwook Jang. "Search for MSSM Higgs decaying to τ pairs in $p\bar{p}$ collision at $\sqrt{s}$ = 1.96 TeV at CDF". PhD thesis. Rutgers U., Piscataway, 2006. DOI: 10.2172/892378.

[155]   Armen Tumasyan et al. "Search for long-lived particles using out-of-time trackless jets in proton-proton collisions at $\sqrt{s} = 13$ TeV". In: *JHEP* 07 (2023), p. 210. DOI: 10.1007/JHEP07(2023)210. arXiv: 2212.06695 [hep-ex].

[156]   Andy Buckley et al. "LHAPDF6: parton density access in the LHC precision era". In: *The European Physical Journal C* 75.3 (Mar. 2015). ISSN: 1434-6052. DOI: 10.1140/epjc/s10052-015-3318-8. URL: http://dx.doi.org/10.1140/epjc/s10052-015-3318-8.

[157]   Jon Butterworth et al. "PDF4LHC recommendations for LHC Run II". In: *Journal of Physics G: Nuclear and Particle Physics* 43.2 (Jan. 2016), p. 023001. ISSN: 1361-6471. DOI: 10.1088/0954-3899/43/2/023001. URL: http://dx.doi.org/10.1088/0954-3899/43/2/023001.

[158]   "Procedure for the LHC Higgs boson search combination in Summer 2011". In: (Aug. 2011).

[159]   CMS Collaboration. "Interpretation of searches for supersymmetry with simplified models". In: *Physical Review D* 88.5 (Sept. 2013). ISSN: 1550-2368. DOI: 10.1103/physrevd.88.052017. URL: http://dx.doi.org/10.1103/PhysRevD.88.052017.

[160]   CMS Collaboration. "Tau lepton identification in displaced topologies using machine learning at CMS". In: (2024). URL: https://cds.cern.ch/record/2904366.

[161]   Mykyta Shchedrolosiev. "Tau lepton identification in displaced topologies using machine learning at CMS". In: *Proceedings of 42nd International Conference on High Energy Physics — PoS(ICHEP2024)*. Vol. 476. 2025, p. 996. DOI: 10.22323/1.476.0996.

[162]   *Twiki: Stitching of MC samples*. URL: https://twiki.cern.ch/twiki/bin/view/CMS/MCStitching.

Acknowledgements